THE UNIVERSITY *of* EDINBURGH

Investigating Astrocyte Dysfunction in Mouse Models of Alzheimer's Disease

Monique Hooley

A thesis submitted for the degree of Doctor of Philosophy

2021

Supervisors

Professor Giles Hardingham

Professor Tara Spires-Jones

The Wellcome Trust Translational Neuroscience PhD Programme

The University of Edinburgh

Declaration

I declare that this thesis has been composed solely by myself and that it has not been submitted, in whole or in part, in any previous application for a degree. Except where stated otherwise by reference or acknowledgment, the work presented is entirely my own.

Acknowledgements

I am incredibly grateful for the support and guidance I have received from a number of people during my PhD.

To my supervisors Professor Giles Hardingham, and Professor Tara Spires-Jones, I sincerely thank you for your mentorship throughout these years. I learnt a great deal from you both and thoroughly enjoyed being a member of your labs. I would not be the scientist I am today without your guidance and I'm extremely grateful I had the opportunity to join your labs.

In the Hardingham lab, Zoeb Jiwaji, it was a pleasure working on complimentary projects with you. I really enjoyed getting to know you. Owen Dando, Katie Emelianova and Xin He, thank you for your bioinformatic skills, you are a dream team! Jing Qui, Paul Baxter, Alison Todd, Sean Mckay, Jamie McQueen, Philip Hasel, Jamie Loan, Ying Zhou and Lynsey Dunsmore, thank you for your support over the years, it was such a pleasure to work with you all.

In the Spires-Jones lab, Caitlin Davies- my comrade-in-arms. I've been glad that I met you from the very first interview day. Couldn't have asked for a better pal to spend hours talking about array tomography with, or dancing like fools dressed as retro space hoppers with. Jane Tulloch, I owe a huge debt of gratitude for all of your support throughout the years. I could not have done it without you. Marti Colom-Cadena, thank you for your friendship and your awesome array tomography tool! Jamie Rose, you brought a smile to my face every day, thank you for your support during my PhD. Declan King, thank you for your support and IPA tutelage! Anna, I feel very lucky to have gotten to know you, you are a brilliant scientist, thank you for all your support. Makis Tzorias, it was fun working alongside you, thanks for your support throughout the years. Helen Stirling, thank you for being such a brilliant student and person to work with. Hati Kurudzhu, Chaitra Sathyaprakash, James Catterson, Claire Durrant, Jamie Toombs, Tyler Saunders, Jie Yeap, Kris Holt, Rosie Jackson and Ellie Pickett, it was awesome getting to know you and being part of the spires-lab family. I always promised I would thank the mice as well, none of this would have been possible without them!

I am very grateful to the Wellcome Trust for giving me the opportunity to do this research, as well as the 4 Year Wellcome Trust Translational Neuroscience organisers at Edinburgh University for organising such a brilliant course. The first year was a lot of fun dipping into the different subject areas and it was a great experience to visit the clinics. Most importantly, I want to thank my cohort. The power women Emily Wheater, Liv Hamilton, Tuula Ritakari and the already mentioned Caitlin Davies and Anna Stevenson. I feel very lucky to have been part of such a wonderful cohort. You are all fantastic scientists but most importantly fantastic people. I will cherish many fond memories with you all.

I'd like to thank my parents for providing me with the opportunities they have in life, and for their love and support. My sister and brother, thank you for being the best cheerleaders a sister could wish for, your everlasting support is appreciated. Finally, a big thanks goes to my fiancée Deniz Kent, your belief in me over the years builds me up and encourages me to reach to do great things.

Grandpa papa, this is for you "panya shway aoe luu mkhaoe".

Table of Contents

Abbreviations

A1	Lipopolysaccharide activated reactive astrocyte profile
A2	Middle cerebral artery occlusion activated astrocyte profile
ABCA1	ATP-binding Cassette Transporter
AD	Alzheimer's disease
AICD	Amyloid Precursor Protein Intracellular Domain
ALDH1L1	Aldehyde Dehydrogenase 1 Family Member L1
ANOVA	Analysis of variance
APOE	Apolipoprotein E
APP	Amyloid Precursor Protein
APP/PS1	APPswePS1dE9 transgenic amyloidopathy model
APPNLF	Knock-in amyloidopathy model
AQP4	Aquaporin 4
ARPC1B	Actin Related Protein 2/3 Complex Subunit 1B
AT	Array tomography
ATP6AP1	ATPase H+ Transporting Accessory Protein 1
Aβ	Amyloid-beta
BACE1	β-site APP Cleaving Enzyme
BBB	Blood brain barrier
C1Q	Complement Component 1q
C3	Complement Protein C3
C4B	Complement Component 4B
CAP1	Cyclase Associated Actin Cytoskeleton Regulatory Protein 1
CCL4	Carbon Tetrachloride
CD109	CD109 Antigen
CD44	CD44 Antigen
cDNA	Complementary deoxyribonucleic acid
CLEC7A	C-type Lectin Domain Family 7 Member A
CLU	Clusterin
CNS	Central nervous system
CO_2	Carbon dioxide
COX6C	Cytochrome C Oxidase Subunit 6C
Cp	Ceruloplasmin
CSEA	Cell type specific expression analysis
CSF	Cerebrospinal fluid
CST7	Cystatin F
CTSD	Cathepsin D
CX3CR1	CX3C Chemokine Receptor 1
DAA	Disease associated astrocytes

DAPI	4’-6-diamidino-2-phenylindole
DHPC	1,2-diheptanoyl-sn-glycero-3-phosphocholine
DPBS	Dulbecco's phosphate-buffered saline
DTT	Dithiothreitol
EAAT1/ GLAST	Excitatory Amino Acid Transporter 1
EAAT2/ GLT-1	Excitatory Amino Acid Transporter 2
EIF2	Eukaryotic Initiation Factor 2
ENO2	Enolase 2
ER	Endoplasmic reticulum
F	Female
FACS	Fluorescence activated cell sorting
FAD	Familial Alzheimer's disease
FC	Fold change
FDG	18F-fluorodeoxyglucose
FERMT2	Fermitin Family Member 2
FPKM	Fragments per kilobase of transcript per million mapped reads
FUCA1	Alpha-L-Fucosidase 1
GABA	Gamma-aminobutyric Acid
GAD	Glutamine Acid Decarboxylase
GBP	Guanylate-Binding Protein
GEM	Gel bead emulsions
GFAP	Glial Fibrillary Acidic Protein
GFP	Green fluorescent protein
GJB5	Gap Junction Beta-5 Protein
GLUL	Glutamine Synthetase
GO	Gene ontology
GPC4	Glypican-4
GPC6	Glypican-6
GPX4	Glutathione Peroxidase 4
GSTA4	Glutathione S-Transferase Alpha 4
GULP1	PTB Domain-Containing Engulfment Adaptor Protein 1
GWAS	Genome wide association studies
HEPES	4-(2-hydroxyethyl)-1-piperazineethanesulfonic acid
HET	Heterozygote
HOM	Homozygote
HSP90B1	Heat Shock Protein 90 Beta Family Member 1
HSPA5	Heat Shock Protein Family A Member 5
IBA1	Allograft Inflammatory Factor 1
IFN ɣ	Interferon Gamma
IHC	Immunohistochemistry
IL-1β	Interleukin-1β

IL-6	Interleukin-6
iNOS	Inducible nitric oxide
IPA	Ingenuity pathway analysis
iPSC	Induced pluripotent stem cell
JAK	Janus kinase
KCL	Potassium chloride
KEGG	Kyoto Encyclopedia of Genes and Genomes
LCN2	Lipocalin-2
LPS	Lipopolysaccharide
LRP1	Lipoprotein receptor-related protein 1
m	Male
MAN2B1	Mannosidase Alpha Class 2B Member 1
MAPK	Mitogen-Activated Protein Kinase
MAPT	Microtubule Associated Protein Tau
MAPTP301S	Tauopathy mouse model
MBP	Myelin Basic Protein
MCAO	Middle cerebral artery occlusion
MEGF10	Multiple EGF-like domains 10
MgCl2	Magnesium chloride
miRNAs	Micro ribonucleic acid
mRNA	Messenger ribonucleic acid
MT-RNR2	Mitochondrially encoded 16S RNA
NDS	Normal donkey serum
NDUFA3	NADH:Ubiquinone Oxidoreductase Subunit A3
NDUFA4	Cytochrome C Oxidase Subunit NDUFA4
NF-κB	Nuclear Factor Kappa-Light-Chain-Enhancer of Activated B Cells
NFTs	Neurofibrillary tangles
NMDA	N-Methyl-D-Aspartic Acid (NMDA)
NQO1	NAD(P)H Quinone Dehydrogenase 1
NRF2	Nuclear Factor Erythroid 2-Related Factor 2
NSAIDs	Non-Steroidal Anti-Inflammatory Drugs
OC	Amyloid-beta fibril antibody
ORM2	Alpha-1-acid Glycoprotein 2
P2Y1 receptor	P2Y Purinoceptor 1 Receptor
PCA	Principle component analysis
PDIA6	Protein Disulphide-Isomerase A6 Precursors
PET	Positron emission tomography
PI3K/Akt	Phosphoinositide 3 kinase/Akt
PIGS	Plaque induced genes
PRDX5	Peroxiredoxin 5
PSD95	Post-synaptic density 95
PSEN1	Presenilin 1

PSEN2	Presenilin 2
Q-q plot	Quantile-quantile plot
qPCR	quantitative Polymerase Chain Reaction
RNA	Ribonucleic acid
RNA-seq	Ribonucleic acid sequencing
ROIs	Regions of interest
ROS	Reactive oxygen species
RPL10a	Ribosomal protein L10a
RPL13A	Ribosomal protein L13a
RT	Reverse transcription
RT-PCR	Reverse Transcription Polymerase Chain Reaction
S100B	S100 Calcium-Binding Protein B
sAAPβ	Soluble Amyloid Precursor Protein β
SAD	Sporadic Alzheimer's disease
sAPPα	Soluble Amyloid Precursor Protein α
SD	Standard deviation
SERPINA3N	Serine Protease Inhibitor A3n
SLC1A2	Excitatory Amino Acid Transporter 2
SLC1A3	Excitatory Amino Acid Transporter 1
SORL1	Sortilin-Related Receptor 1
SPARCL1	SPARC-like Protein 1
SPI1	Transcription factor PU.1
STAR	Spliced transcripts alignment to a reference
STAT3	Signal Transducer and Activator of Transcription 3
SY38	Antibody against synaptophysin
TBS	Tris-buffered saline
TGF-β3	Transforming Growth Factor-β3
THBS1	Thrombospondin 1
THBS2	Thrombospondin 2
ThioS	Thioflavin-S
TNF α	Tumor Necrosis Factor alpha
TRAP	Translating ribososome affinity purification
TREM2	Triggering Receptor Expressed on Myeloid Cells 2
TYROBP	TYRO Protein Tyrosine Kinase-Binding Protein
UMAP	Uniform manifold approximation and projection
UMI	Unique molecular identifier
UPR	Unfolded Protein Response
VIM	Vimentin
WT	Wild-type

Declaration

I declare that this thesis has been composed solely by myself and that it has not been submitted, in whole or in part, in any previous application for a degree. Except where stated otherwise by reference or acknowledgment, the work presented is entirely my own.

Acknowledgements

I am incredibly grateful for the support and guidance I have received from a number of people during my PhD.

To my supervisors Professor Giles Hardingham, and Professor Tara Spires-Jones, I sincerely thank you for your mentorship throughout these years. I learnt a great deal from you both and thoroughly enjoyed being a member of your labs. I would not be the scientist I am today without your guidance and I'm extremely grateful I had the opportunity to join your labs.

In the Hardingham lab, Zoeb Jiwaji, it was a pleasure working on complimentary projects with you. I really enjoyed getting to know you. Owen Dando, Katie Emelianova and Xin He, thank you for your bioinformatic skills, you are a dream team! Jing Qui, Paul Baxter, Alison Todd, Sean Mckay, Jamie McQueen, Philip Hasel, Jamie Loan, Ying Zhou and Lynsey Dunsmore, thank you for your support over the years, it was such a pleasure to work with you all.

In the Spires-Jones lab, Caitlin Davies- my comrade-in-arms. I've been glad that I met you from the very first interview day. Couldn't have asked for a better pal to spend hours talking about array tomography with, or dancing like fools dressed as retro space hoppers with. Jane Tulloch, I owe a huge debt of gratitude for all of your support throughout the years. I could not have done it without you. Marti Colom-Cadena, thank you for your friendship and your awesome array tomography tool! Jamie Rose, you brought a smile to my face every day, thank you for your support during my PhD. Declan King, thank you for your support and IPA tutelage! Anna, I feel very lucky to have gotten to know you, you are a brilliant scientist, thank you for all your support. Makis Tzorias, it was fun working alongside you, thanks for your support throughout the years. Helen Stirling, thank you for being such a brilliant student and person to work with. Hati Kurudzhu, Chaitra Sathyaprakash, James Catterson, Claire Durrant, Jamie Toombs, Tyler Saunders, Jie Yeap, Kris Holt, Rosie Jackson and Ellie Pickett, it was awesome getting to know you and being part of the spires-lab family. I always promised I would thank the mice as well, none of this would have been possible without them!

I am very grateful to the Wellcome Trust for giving me the opportunity to do this research, as well as the 4 Year Wellcome Trust Translational Neuroscience organisers at Edinburgh University for organising such a brilliant course. The first year was a lot of fun dipping into the different subject areas and it was a great experience to visit the clinics. Most importantly, I want to thank my cohort. The power women Emily Wheater, Liv Hamilton, Tuula Ritakari and the already mentioned Caitlin Davies and Anna Stevenson. I feel very lucky to have been part of such a wonderful cohort. You are all fantastic scientists but most importantly fantastic people. I will cherish many fond memories with you all.

I'd like to thank my parents for providing me with the opportunities they have in life, and for their love and support. My sister and brother, thank you for being the best cheerleaders a sister could wish for, your everlasting support is appreciated. Finally, a big thanks goes to my fiancée Deniz Kent, your belief in me over the years builds me up and encourages me to reach to do great things.

Grandpa papa, this is for you "panya shway aoe luu mkhaoe".

Table of Contents

Abbreviations

A1	Lipopolysaccharide activated reactive astrocyte profile
A2	Middle cerebral artery occlusion activated astrocyte profile
ABCA1	ATP-binding Cassette Transporter
AD	Alzheimer's disease
AICD	Amyloid Precursor Protein Intracellular Domain
ALDH1L1	Aldehyde Dehydrogenase 1 Family Member L1
ANOVA	Analysis of variance
APOE	Apolipoprotein E
APP	Amyloid Precursor Protein
APP/PS1	APPswePS1dE9 transgenic amyloidopathy model
APPNLF	Knock-in amyloidopathy model
AQP4	Aquaporin 4
ARPC1B	Actin Related Protein 2/3 Complex Subunit 1B
AT	Array tomography
ATP6AP1	ATPase H+ Transporting Accessory Protein 1
Aβ	Amyloid-beta
BACE1	β-site APP Cleaving Enzyme
BBB	Blood brain barrier
C1Q	Complement Component 1q
C3	Complement Protein C3
C4B	Complement Component 4B
CAP1	Cyclase Associated Actin Cytoskeleton Regulatory Protein 1
CCL4	Carbon Tetrachloride
CD109	CD109 Antigen
CD44	CD44 Antigen
cDNA	Complementary deoxyribonucleic acid
CLEC7A	C-type Lectin Domain Family 7 Member A
CLU	Clusterin
CNS	Central nervous system
CO_2	Carbon dioxide
COX6C	Cytochrome C Oxidase Subunit 6C
Cp	Ceruloplasmin
CSEA	Cell type specific expression analysis
CSF	Cerebrospinal fluid
CST7	Cystatin F
CTSD	Cathepsin D
CX3CR1	CX3C Chemokine Receptor 1
DAA	Disease associated astrocytes

DAPI	4’-6-diamidino-2-phenylindole
DHPC	1,2-diheptanoyl-sn-glycero-3-phosphocholine
DPBS	Dulbecco's phosphate-buffered saline
DTT	Dithiothreitol
EAAT1/ GLAST	Excitatory Amino Acid Transporter 1
EAAT2/ GLT-1	Excitatory Amino Acid Transporter 2
EIF2	Eukaryotic Initiation Factor 2
ENO2	Enolase 2
ER	Endoplasmic reticulum
F	Female
FACS	Fluorescence activated cell sorting
FAD	Familial Alzheimer's disease
FC	Fold change
FDG	18F-fluorodeoxyglucose
FERMT2	Fermitin Family Member 2
FPKM	Fragments per kilobase of transcript per million mapped reads
FUCA1	Alpha-L-Fucosidase 1
GABA	Gamma-aminobutyric Acid
GAD	Glutamine Acid Decarboxylase
GBP	Guanylate-Binding Protein
GEM	Gel bead emulsions
GFAP	Glial Fibrillary Acidic Protein
GFP	Green fluorescent protein
GJB5	Gap Junction Beta-5 Protein
GLUL	Glutamine Synthetase
GO	Gene ontology
GPC4	Glypican-4
GPC6	Glypican-6
GPX4	Glutathione Peroxidase 4
GSTA4	Glutathione S-Transferase Alpha 4
GULP1	PTB Domain-Containing Engulfment Adaptor Protein 1
GWAS	Genome wide association studies
HEPES	4-(2-hydroxyethyl)-1-piperazineethanesulfonic acid
HET	Heterozygote
HOM	Homozygote
HSP90B1	Heat Shock Protein 90 Beta Family Member 1
HSPA5	Heat Shock Protein Family A Member 5
IBA1	Allograft Inflammatory Factor 1
IFN ɣ	Interferon Gamma
IHC	Immunohistochemistry
IL-1β	Interleukin-1β

IL-6	Interleukin-6
iNOS	Inducible nitric oxide
IPA	Ingenuity pathway analysis
iPSC	Induced pluripotent stem cell
JAK	Janus kinase
KCL	Potassium chloride
KEGG	Kyoto Encyclopedia of Genes and Genomes
LCN2	Lipocalin-2
LPS	Lipopolysaccharide
LRP1	Lipoprotein receptor-related protein 1
m	Male
MAN2B1	Mannosidase Alpha Class 2B Member 1
MAPK	Mitogen-Activated Protein Kinase
MAPT	Microtubule Associated Protein Tau
MAPTP301S	Tauopathy mouse model
MBP	Myelin Basic Protein
MCAO	Middle cerebral artery occlusion
MEGF10	Multiple EGF-like domains 10
MgCl2	Magnesium chloride
miRNAs	Micro ribonucleic acid
mRNA	Messenger ribonucleic acid
MT-RNR2	Mitochondrially encoded 16S RNA
NDS	Normal donkey serum
NDUFA3	NADH:Ubiquinone Oxidoreductase Subunit A3
NDUFA4	Cytochrome C Oxidase Subunit NDUFA4
NF-κB	Nuclear Factor Kappa-Light-Chain-Enhancer of Activated B Cells
NFTs	Neurofibrillary tangles
NMDA	N-Methyl-D-Aspartic Acid (NMDA)
NQO1	NAD(P)H Quinone Dehydrogenase 1
NRF2	Nuclear Factor Erythroid 2-Related Factor 2
NSAIDs	Non-Steroidal Anti-Inflammatory Drugs
OC	Amyloid-beta fibril antibody
ORM2	Alpha-1-acid Glycoprotein 2
P2Y1 receptor	P2Y Purinoceptor 1 Receptor
PCA	Principle component analysis
PDIA6	Protein Disulphide-Isomerase A6 Precursors
PET	Positron emission tomography
PI3K/Akt	Phosphoinositide 3 kinase/Akt
PIGS	Plaque induced genes
PRDX5	Peroxiredoxin 5
PSD95	Post-synaptic density 95
PSEN1	Presenilin 1

PSEN2	Presenilin 2
Q-q plot	Quantile-quantile plot
qPCR	quantitative Polymerase Chain Reaction
RNA	Ribonucleic acid
RNA-seq	Ribonucleic acid sequencing
ROIs	Regions of interest
ROS	Reactive oxygen species
RPL10a	Ribosomal protein L10a
RPL13A	Ribosomal protein L13a
RT	Reverse transcription
RT-PCR	Reverse Transcription Polymerase Chain Reaction
S100B	S100 Calcium-Binding Protein B
sAAPβ	Soluble Amyloid Precursor Protein β
SAD	Sporadic Alzheimer's disease
sAPPα	Soluble Amyloid Precursor Protein α
SD	Standard deviation
SERPINA3N	Serine Protease Inhibitor A3n
SLC1A2	Excitatory Amino Acid Transporter 2
SLC1A3	Excitatory Amino Acid Transporter 1
SORL1	Sortilin-Related Receptor 1
SPARCL1	SPARC-like Protein 1
SPI1	Transcription factor PU.1
STAR	Spliced transcripts alignment to a reference
STAT3	Signal Transducer and Activator of Transcription 3
SY38	Antibody against synaptophysin
TBS	Tris-buffered saline
TGF-β3	Transforming Growth Factor-β3
THBS1	Thrombospondin 1
THBS2	Thrombospondin 2
ThioS	Thioflavin-S
TNF α	Tumor Necrosis Factor alpha
TRAP	Translating ribososome affinity purification
TREM2	Triggering Receptor Expressed on Myeloid Cells 2
TYROBP	TYRO Protein Tyrosine Kinase-Binding Protein
UMAP	Uniform manifold approximation and projection
UMI	Unique molecular identifier
UPR	Unfolded Protein Response
VIM	Vimentin
WT	Wild-type

Lay Summary

Alzheimer's disease is a neurodegenerative disease and is the most common form of dementia. Patients with dementia typically experience a loss of memory, language and problem-solving skills, leading to behaviour that can affect their ability to perform every day activities. Alzheimer's disease is characterised by the build-up of two proteins in the brain, amyloid-beta (Aβ) and tau. Additional features include a reduction in the number of synapses, the connections between neurons, degeneration of neurons themselves, and alterations to other cell types in the brain such as astrocytes. Astrocytes are star shaped cells which have a number of roles in healthy brain function, such as aiding the formation of synapses and supporting the energy needs of neurons. However, in Alzheimer's disease, it is thought that astrocytes lose the ability to perform a number of these functions and may also gain functions which contribute to the disease worsening. In this state, astrocytes are called 'reactive' astrocytes. In this thesis, I focus on the impact the protein Aβ has on astrocytes. In the hope that understanding how astrocytes are changed in Alzheimer's disease may broaden the therapeutic approaches taken in future clinical trials.

I have used 2 mouse models of Alzheimer's disease which display an accumulation of Aβ. One of the mouse models has been used in Alzheimer's disease research for many years and develops Aβ accumulation relatively quickly. The other mouse model is a newer model of Alzheimer's disease, it develops Aβ accumulation more slowly than the first mouse model. However, the synapse loss and astrocyte reaction to Aβ in this newer mouse model was not well documented. Hence, I used imaging techniques to quantify the synapse loss and reactive astrocyte presence around Aβ aggregates called Aβ plaques. I found that reactive astrocyte burden and synapse loss increased with reduced distance from Aβ plaques.

Next, I measured average gene expression changes occurring in astrocytes in each mouse model. Genes are units which carry information that determine traits. In this case, changes in gene expression were used as a proxy for changes in the functions of astrocytes exposed to Aβ. I found that Aβ exposed astrocytes upregulated genes involved in inflammation, protein processing and degradation, and the antioxidant response. However, genes involved in energy generation appeared to be downregulated. Hence, both protective and toxic changes

in astrocyte function appeared to occur. Interestingly, the gene changes in astrocytes exposed to Aβ were similar to those changed in astrocytes which had been exposed to toxic tau proteins. Hence, astrocytes share similar changes in gene expression when exposed to the two key toxic proteins in Alzheimer's disease. I also found that genes upregulated in Aβ exposed astrocytes overlapped with genes upregulated in astrocytes due to ageing. Additionally, the genes upregulated in Aβ exposed astrocytes overlapped with genes upregulated in astrocytes in models of acute inflammation and stroke. Thus, astrocytes exposed to chronic and acute insults share some similarities in reaction. Notably, changes in astrocyte gene expression in mouse models of AD also showed similarities to genes which were changed in in human post-mortem Alzheimer's disease astrocytes. Hence, the results found in these mice are somewhat translatable to the human condition. The results mentioned above were only found in one of the Alzheimer's disease mouse models. Astrocytes from the newer mouse model showed few changes in gene expression. The slower accumulation of Aβ in this mouse might have led to astrocytes which were not dysfunctioning yet, or perhaps only a small number of astrocytes were dysfunctioning and so when looking at average gene expression across all astrocytes in the mouse model, alterations in gene expression were not found.

In the last section of the thesis, I investigate gene expression changes in individual astrocytes from each mouse model of Alzheimer's disease. This demonstrated that, in both models, astrocytes do not all express the same gene expression changes. Some astrocytes appeared to express genes at similar levels to non-diseased mice, whilst others expressed genes at levels which were distinctly different from non-diseased mice. These astrocytes were termed pathology associated astrocytes. Hence, in both mouse models dysfunctioning astrocytes were found when investigating gene expression at the single cell level. Just as in the previous section, the pathology associated astrocytes upregulated genes related to the antioxidant response in astrocytes, and also displayed changes in expression of genes involved in protein processing and energy support.

These investigations add to our growing understanding of mouse models of Alzheimer's disease and astrocyte dysfunction in Alzheimer's disease. Astrocytes appear to take on both neuroprotective and neurotoxic functions when exposed to Aβ pathology. If given at an

appropriate time point, therapeutics which target dysfunctioning astrocytes and boost their neuroprotective functions, whilst reducing their neurotoxic functions, may prove to alter the course of Alzheimer's disease, especially if given in combination with therapeutics targeting other aspects of the disease, such as the build-up of Aβ.

Abstract

Every 3 seconds someone in the world is diagnosed with dementia. This staggering fact is compounded by another, 60-80% of these patients are suffering from the same disease, Alzheimer's disease (AD). Despite this, we currently have no disease modifying treatments. AD is characterized by an accumulation of extracellular amyloid-beta (Aβ) plaques, intracellular tau neurofibrillary tangles and neuronal loss. Additional pathological features include synapse loss and an increase in reactive astrocytes and microglia, particularly around Aβ plaques. Aβ accumulation is thought to occur early in the disease process and trigger downstream pathology. For this reason, many therapeutics in clinical trials have targeted Aβ accumulation. However, thus far there has been little success, highlighting that pharmaceutical companies need to explore new therapeutic strategies. Genome wide association studies have illustrated the importance of the innate immune system in AD. Astrocytes and microglia are the main cells in the brain involved in innate immunity. In this study, I investigate the impact of Aβ on astrocytes, in the hope that a better understanding of how these cells are affected may lead to novel therapeutic targets.

We have used two mouse models of familial AD which develop amyloid plaque pathology similar to that seen in AD; the well characterized transgenic APP_{swe}/PSEN1dE9 (APP/PS1) mouse model and the less well characterized knock-in APP^{NLF} mouse model. Firstly, we used array tomography and immunohistochemistry to quantify the synapse loss and astrogliosis around plaques in 12-month APP^{NLF} mice. This demonstrated that synapse loss and astrogliosis in the APP^{NLF} mouse is comparable to other mouse models of AD, but is generally confined to within 10μm of the plaque core.

Next, we used translating ribosome affinity purification (TRAP) followed by bulk ribonucleic acid-sequencing (RNA-seq) to assess how astrocytic gene expression changed with increasing Aβ pathology in 6, 12 and 18-month APP/PS1 and APP^{NLF} neocortical astrocytes. Amyloidopathy in APP/PS1 astrocytes exacerbated age dependent gene changes in astrocytes, as well as inducing a profile which resembled acutely induced reactive astrocytes. Thus, highlighting an overlap of acute and chronic reactive astrocyte signatures. APP/PS1 astrocytes also showed overlapping up and down regulation of genes with those changed in

astrocytes in the MAPT^{P301S} tauopathy model, suggesting that the two core proteinopathies in AD induce elements of similar changes in astrocyte phenotype. Pathways related to protein degradation and inflammation appeared to be upregulated due to the AD proteinopathies, whilst pathways related to mitochondrial function and protein synthesis were downregulated. Notably, genes induced in APP/PS1 astrocytes were enriched for genes induced in human post-mortem AD astrocytes, indicating that the results obtained in this mouse model are somewhat translatable to the human condition.

The APP^{NLF} astrocyte bulk RNA-seq showed few differentially expressed genes at the ages tested. However, genes that were upregulated in the APP/PS1 astrocytes demonstrated a positive fold change in the APP^{NLF} astrocytes. This might indicate overlap of astrocytic response to amyloidopathy in both models, but that astrocyte pathology is slower to develop in the APP^{NLF} mouse model, compared to the APP/PS1 mouse model, mirroring the slower development of plaque pathology. It is also possible that some APP^{NLF} astrocytes displayed phenotypes similar to APP/PS1 astrocytes, but the gene expression was obscured when conducting bulk RNA-seq.

To investigate the heterogeneity of astrocytic response to Aβ pathology, we conducted single cell RNA-seq on astrocytes from the neocortex of APP/PS1 and APP^{NLF} mice. This revealed an astrocyte phenotypic state present in both mouse models of amyloidopathy, which was largely absent in 12-month WT mice, but which began to become apparent in 18-month WT astrocytes. Genes involved in oxidative phosphorylation, protein synthesis, the unfolded protein response, and nuclear factor erythroid 2-related factor 2 (NRF2)-mediated oxidative stress response were expressed higher in this pathology associated cluster of astrocytes, compared to astrocytes in other clusters. However, genes involved in synaptogenesis were lowly expressed in the pathology associated cluster of astrocytes compared to other astrocytes, potentially linking Aβ induced astrocyte dysfunction with the reduction in synapses seen in AD. This analysis highlights the benefits of single cell gene expression analysis in identifying heterogeneity of astrocyte response to amyloidopathy, which was lost in the bulk translatome analysis of astrocytes from mouse models of AD.

These investigations add to our growing understanding of mouse models of AD and astrocyte dysfunction in AD. Amyloidopathy appears to induce both neuroprotective and neurotoxic phenotypic alterations in astrocytes. Designing therapeutic strategies which enhance neuroprotective functions of astrocytes, such as NRF2-mediated antioxidant signaling, whilst reducing neurotoxic overactivation of inflammatory responses and the unfolded protein response, may improve AD pathogenesis. Further research defining phenotypic states of astrocytes in AD will enable the design of astrocyte-state targeted therapeutics, which will likely demonstrate superior results to broader astrocyte targeted therapeutics.

Chapter 1

Introduction

1.1 Dementia

Dementia is an urgent global health problem, with 50 million people diagnosed worldwide and a projection of 152 million people to be diagnosed by 2050 (https://www.dementiastatistics.org/statistics-about-dementia). Dementia is a term for diseases characterized by a decline in memory, language, problem solving and other cognitive abilities (Duong et al. 2017). It is distinct from normal ageing, but most notably affects the ageing population (Irwin et al. 2018). The current global cost of dementia is thought to be 1 trillion dollars per year, taking into account direct medical costs, direct social care costs, as well as informal care costs (https://www.alz.co.uk/research/world-report-2019). The impact of dementia does not stop at the staggering financial burden, it also causes profound emotional burden to patients and their families as a lack of independence and alterations in social behaviour develop as dementia progresses. For these reasons, academia, industry, the government and funding institutions have all agreed on making a concerted effort to translate dementia research into therapeutics.

1.2 Alzheimer's Disease

Alzheimer's disease (AD) is the most common form of dementia, affecting approximately 60-80% of dementia patients (Duong et al. 2017). There are two distinct forms of AD, familial AD (FAD) and sporadic AD (SAD). Autosomal dominant mutations in amyloid precursor protein (APP), presenilin 1 (PSEN1) and presenilin 2 (PSEN2) genes are causative of FAD, which accounts for ~5% of AD cases (Wu et al. 2012; Johns 2014). Around 95% of AD cases are sporadic and are thought to develop due to a combination of genetic and environmental factors, in addition to aging (Piaceri et al. 2013; Guerreiro and Bras 2015). However, we do not fully understand the interplay between these contributing factors.

The pathological hallmarks of AD include 'positive' lesions and 'negative' lesions. Positive lesions include extracellular deposits of the protein amyloid-beta (Aβ) in plaques, intracellular aggregates of hyperphosphorylated tau protein in neurofibrillary tangles (NFTs), dystrophic neurites, reactive astrocytes and activated microglia. Characteristic 'negative' lesions include neuron loss and synapse loss (Serrano-Pozo et al. 2011). Currently AD is only definitively diagnosed after death, by linking

cognition scores with examination of brain tissue at autopsy. However, ante-mortem diagnosis integrating blood and cerebrospinal fluid (CSF) biomarkers, non-invasive neuroimaging, cognition scores and genetic background is a budding field of research (Khan 2018; Fisher et al. 2019).

Rivastigmine, galantamine, donepezil and memantine are the medications used presently to treat AD (Yiannopoulou and Papageorgiou 2013). All of these medications reduce the symptoms of AD, but do not affect the underlying pathophysiology of the disease or alter the course of the disease, and so are not disease modifying therapies. A patient with AD lives on average 4-10 years after diagnosis (Zanetti et al. 2009). However, approximately 87% of dementia patients are in the mild-moderate stage of the disease (Prince, M et al. 2014) and could conceivably benefit from a disease modifying therapy, along with those who would benefit from a preventative therapy. Hence, there is a need to better understand early mechanisms underpinning the disease in order to produce these novel disease modifying therapies.

1.3 The Case for Amyloid

There is strong genetic evidence to suggest that Aβ is involved in the pathogenesis of AD. The first piece of evidence is from APP, the protein from which Aβ is formed **(figure 1)**. Mutations in APP have been shown to affect Aβ generation and have 100% penetrance in causing AD (Goate et al. 1991; Weggen and Beher 2012; Cruts et al. 2012; Mullan et al. 1992). Interestingly, a missense mutation in APP (A673T) has been shown to reduce the deposition of Aβ and reduce the risk of developing AD (Jonsson et al. 2012). Secondly, mutations in PSEN1 and PSEN2, which orchestrate the cleavage of APP to Aβ, also have a high degree of penetrance in the development of AD (Cruts et al. 2012; Sherrington et al. 1996; Rogaev et al. 1995; Levy-Lahad et al. 1995; Sherrington et al. 1995). Thirdly, Down Syndrome patients who have an extra copy of the APP gene have an increased risk of developing AD (Wisniewski et al. 1985). It is worth noting that in these cases the genetic evidence has stemmed from FAD. Nevertheless, FAD and SAD share remarkably similar pathophysiology and clinical presentation. A convincing piece of evidence which is directly related to SAD and implicates Aβ in AD pathogenesis comes from SAD patients who possess the ***ε***4 versions of Apolipoprotein E (*APOE*). A single allele of *APOE**ε***4 leads to a 47% chance of developing SAD, and having both alleles leads to a staggering 91% chance of developing SAD (Corder et al. 1993). APOE***ε***4 is a protein which has been shown to increase Aβ deposition and reduce the

clearance of Aβ relative to the other isoforms of APOE (Schmechel et al. 1993; Head et al. 2012; Verghese et al. 2013). Therefore, supporting the notion that Aβ pathology is important in SAD.

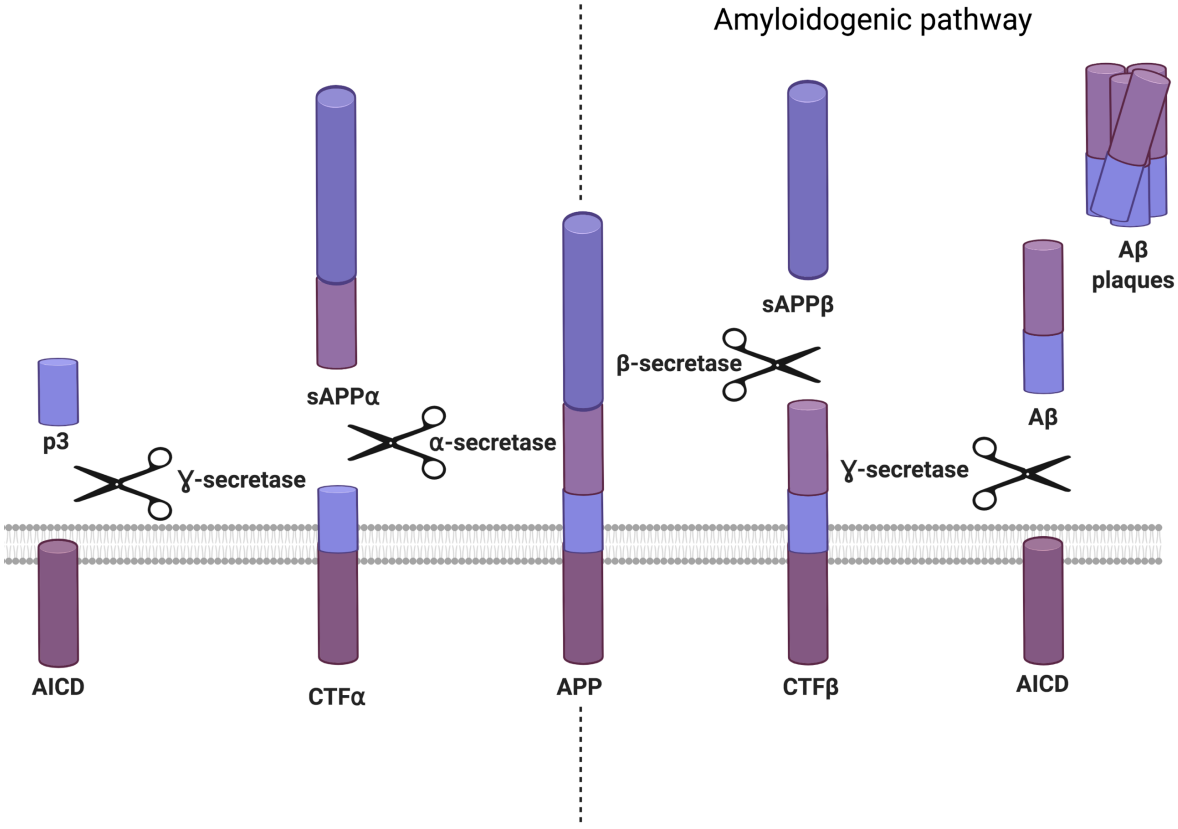

Figure 1. Amyloid precursor protein (APP) cleavage. Cleavage of APP via the β and γ secretase pathway leads to soluble amyloid precursor protein β (sAAPβ), amyloid β (Aβ), and amyloid precursor protein intracellular domain (AICD) formation. Whereas, cleavage of APP via the α and γ secretase pathway leads to soluble amyloid precursor protein α (sAPPα), AICD, and p3 peptide formation. Cleavage sites of enzymes indicated by scissors. Made using Biorender.com.

Along with genetic evidence, the buildup of amyloid pathology early in the disease, decades before symptoms emerge, led to the theory that amyloid pathology may be an important trigger in downstream dysfunction (Jack et al. 2013; Mormino and Papp 2018). The amyloid cascade hypothesis has dominated AD research for the past 30 years. The hypothesis originally postulated that the deposition of amyloid in plaques was the central disease-causing mechanism in AD, with neurofibrillary tangle accumulation, inflammation, neurodegeneration and dementia following suite (Hardy and Higgins 1992; Selkoe 1991).

Studies have since indicated that Aβ plaques may not be pathological in and of themselves as plaque load does not correlate well with cognitive decline (Terry et al. 1991; Aizenstein et al. 2008). Nevertheless, enthusiasm for Aβ as a pathological protein in AD has remained, albeit the with a focus on the synaptotoxic effects of oligomeric Aβ rather than fibrillar plaques **(figure 2)** (Koffie et al. 2012; Hong et al. 2018; Lambert et al. 1998). Ex-vivo studies have shown that Aβ oligomers reduce long term potentiation of synapses in hippocampal slices (Shankar et al. 2008; Lambert et al. 1998; Hong et al. 2018). In vivo studies using amyloidopathy mice have illustrated impairment of synaptic function prior to plaque deposition (Hsia et al. 1999), and Aβ oligomers injected into rat brains caused significant disruptions of complex learned behaviors (Cleary et al. 2005). Additionally, oligomer load has been correlated with the inflammatory response, memory impairment and neurodegeneration in an AD mouse model (DaRocha-Souto et al. 2011). Furthermore, the theory that soluble Aβ oligomers are the pathological culprit is supported by the fact that oligomer load correlates with cognitive decline in humans (Savage et al. 2014; Esparza et al. 2013; Wang et al. 1999), and the presence of Aβ dimers in post brain samples strongly distinguished post-mortem AD, demented non-AD and non-dementia brains(Mc Donald et al. 2010). Importantly, dysregulation of production and clearance of soluble Aβ is thought to be one of the earliest pathological mechanisms in AD (Ingelsson et al. 2004), and a trigger for downstream tau hyperphosphorylation (Ma et al. 2009), gliosis (Sondag et al. 2009; Dhawan et al. 2012; White et al. 2005) and synapse degeneration (Hong et al. 2018; Shankar et al. 2007; Miñano-Molina et al. 2011). **Figure 2** illustrates the current state of the amyloid cascade hypothesis.

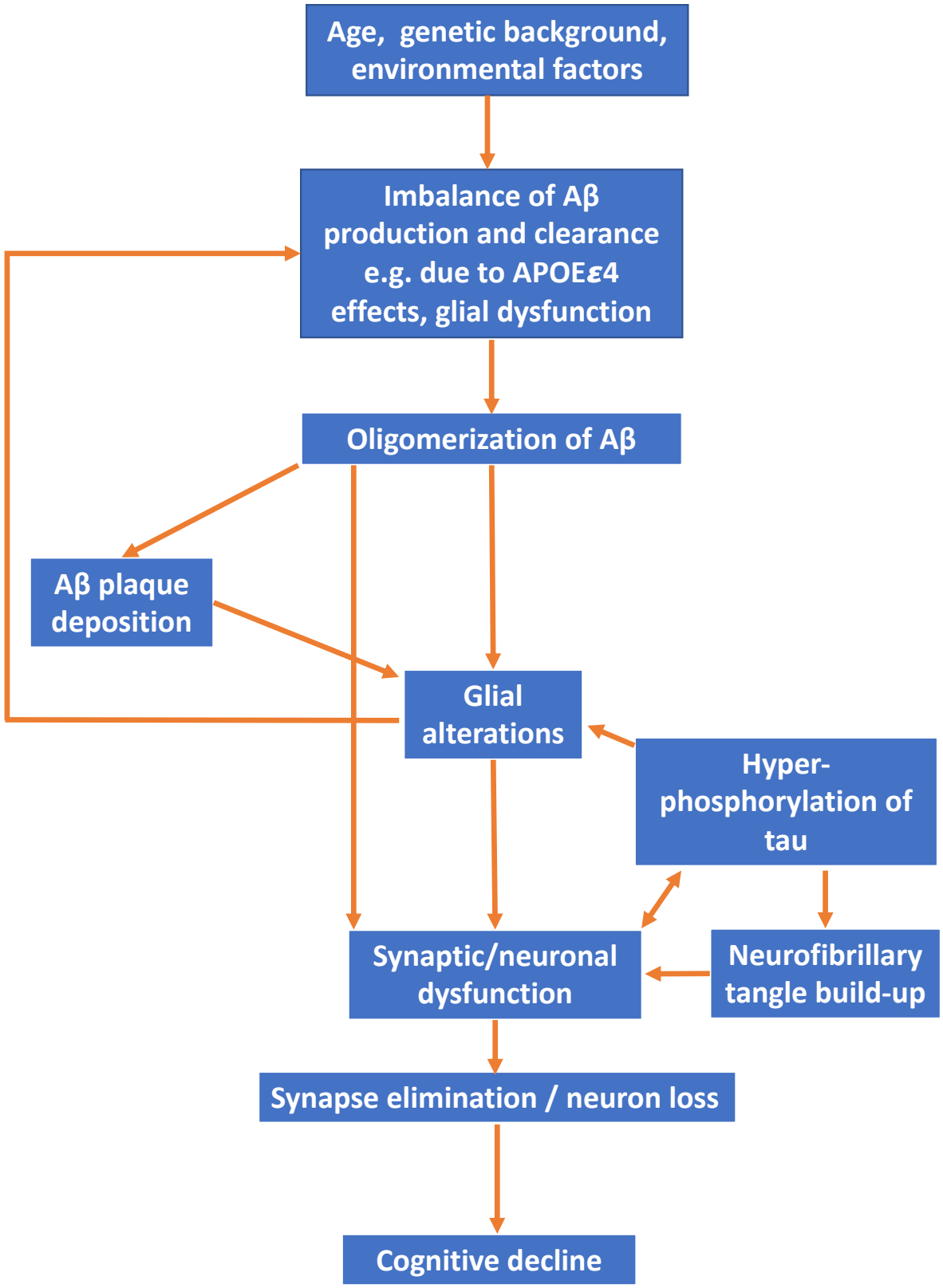

Figure 2. The sequence of major pathological events which leads to cognitive decline in Alzheimer's disease.

1.4 Failure of Clinical Trials Targeting Aβ

Enthusiasm for the amyloid cascade hypothesis has decreased in recent years, largely due to the numerous clinical trials of Aβ targeted therapies which have spectacularly failed (Mehta et al. 2017). Rather than simply writing off a target which has decades of research supporting its importance, it is prudent that we truly understand why these clinical trials failed.

Bapinezumab, Solanezumab, Crenezumab and Gantenerumab are all anti-amyloid monoclonal antibodies designed against different epitopes and forms of amyloid (Mehta et al. 2017). It is now thought that oligomeric Aβ is the primary noxious form. Hence, it is feasible that these antibodies have not been efficacious due to not selectively targeting oligomeric Aβ. Additionally, monoclonal antibodies are relatively large molecules which have a limited ability to cross the blood brain barrier (BBB). It is possible that therapeutically relevant concentrations were not reaching the brain, especially as doses in clinical trials were chosen to limit the threat of vasogenic edema (Sperling et al. 2011). This certainly seemed to be the case in Biogen's recent trial of Aducanumab, where a post-hoc analysis illustrated that there was a beneficial effect of Aducanumab on measured outcomes, but only in groups of patients who had received 10 or more uninterrupted doses of the highest dose of Aducanumab (10mg/kg) (Schneider 2020).

In the case of Solanezumab and Crenezumab, the treatments demonstrated some efficacy in mild AD patients, highlighting a possible temporal issue in these clinical trials (Siemers et al. 2016; Cummings et al. 2018). Perhaps targeting Aβ alone is only useful early in the disease when other pathological cascades have not yet begun. To this end, current clinical trials of Aβ targeted therapies are focusing on high risk currently undiagnosed, prodromal, or mild AD subjects (NCT03443973, NCT02008357). Since Aβ pathology begins more than a decade before clinical presentation (Ingelsson et al. 2004; Villemagne et al. 2013), the challenge has become detecting candidates for therapeutics early enough for the therapies to be efficacious. Companies such as Altoida are developing digital biomarkers which supposedly detect people at high risk of developing dementia 10 years prior to clinical onset and diagnosis (Tarnanas et al. 2015). Until then, it appears that Aβ therapeutics may only be useful years before clinical diagnosis, therefore it seems logical to move our efforts away from targeting

Aβ directly, and focus on the downstream consequences of Aβ pathology, such as the chronic activation of glial cells and the propagation of misfolded tau (Selkoe and Hardy 2016). Indeed, Alector and Abbvie are partnering to conduct phase 1 clinical trials of antibodies against CD33 and TREM2 (Triggering receptor expressed on myeloid cells 2) (NCT03635047, NCT03822208), receptors on microglia which are involved in phagocytosis (Yao et al. 2019; Griciuc et al. 2013). AstronauTx and Astrocyte Pharmaceuticals are two early stage biotech companies focused on developing astrocyte targeted therapeutics, and TauRx is currently conducting a phase 3 clinical trial of LMTX, a tau aggregation inhibitor on patients with mild Alzheimer's disease (NCT03446001).

1.5 Mouse Models of AD

Mouse models of AD have been extremely useful tools for dissecting the molecular mechanisms of pathology in AD. However, the lack of translation of therapeutics from mouse to human led some to question their utility. The mouse models of AD which were first formed overexpress APP and contain autosomal dominant AD mutations (Hsiao et al. 1996; Games et al. 1995). Whilst it could be said that these mice simply model the rare autosomal dominant form of AD, the accumulation of Aβ plaques, gliosis and synapse loss all resemble the pathology in human sporadic AD. Notably, the accumulation of hyperphosphorylated tau aggregates in NFTs were not present in transgenic APP models and the mice often showed limited neurodegeneration. To combat this, other mouse models, such as the 3xTg mouse model were created to investigate the effect of Aβ and tau aggregation (Oddo et al. 2003). Whilst there will be species differences between mouse and human brains, and no mouse model exhibits the full range of clinical and pathological features found in sporadic AD, mouse models can still be extremely helpful in investigating disease mechanisms. Hence, mouse models are best viewed as tools for understanding the effects of genes/proteins that have been implicated in AD, rather than as models which reflect the entire biology of the disease.
Age is an additional factor to consider when using mice to model human disease. Many of the early studies conducted using transgenic mouse models used relatively young mice since pathology begins early (Oddo et al. 2003; Rockenstein et al. 1995; Games et al. 1995). However, evidence suggest that function of innate immune cells changes with aging(Boisvert et al. 2018; Clarke et al. 2018; Soreq et al. 2017). Hence, this might further explain the

discrepancies between therapeutics trialled in mice vs human. Mice aged >10 months are most likely to reflect middle aged and old human biology (Hagan.C 2017).

In this study I used the APP_{swe}PS1dE9 (APP/PS1) (Jankowsky et al. 2004) and APP^{NLF} mouse (Saito et al. 2014) models to investigate the impact of amyloidopathy on astrocytes. The APP/PS1 mouse model expresses a human/mouse chimeric APP. The APP was humanised by mutating 3 amino acids. The Swedish mutation (amino acids KM670/671NL) was also introduced to the APP gene. Additionally, the mouse has a deletion of exon 9 in PSEN1. Together, these mutations lead to increased Aβ generation and impaired Aβ clearance. APP/PS1 mice are transgenic and so the gene is inserted randomly into the genome. The overexpression of mutant APP is driven by the prion promoter rather than the endogenous promoter; hence, it could be argued that this model might lack a degree of physiological relevance in the timing and location of APP expression, as well as in the overexpression of other cleavage products of APP in addition to Aβ. However, the phenotype in this model is strong, with deposits and gliosis developing by 6 months, and large plaques with more pronounced astrogliosis by 9 months (Kamphuis et al. 2015). Hence, this model provides the opportunity to investigate the impact of widespread Aβ pathology on astrocytic gene expression. Additionally, synapse loss, Aβ accumulation and gliosis in the mouse model is well documented, meaning alterations in astrocytic gene expression can be put in the context of pathology (Koffie et al. 2009; Kamphuis et al. 2015).

The APP^{NLF} mouse model avoids possible artifacts introduced by overexpression of APP in transgenic mouse models as a knock-in approach was used to target the construct to the correct location in the mouse genome using the endogenous mouse APP promoter (Saito et al. 2014). Hence, expression of APP occurs at a physiologically relevant time point, in the right cells, and at a level which is similar to wild-type mice. The introduction of the Swedish (KM670/671NL) mutation in APP increases the total amount of Aβ40 and Aβ42, isoforms of Aβ which are thought to be important in AD pathology. The Iberian (I716F) mutation was also introduced, and increases the ratio of Aβ42 to Aβ40. This ratiometric alteration mimics the relative abundance of isoforms found in the CSF of people with AD (Baiardi et al. 2019). Aβ plaque deposition in homozygote APP^{NLF} mice was reported to begin at 6-months of age in the cortex and hippocampus, but are not widespread until 18-months. Glial fibrillary acidic protein (GFAP) positive astrocytes were shown to surround Aβ plaques in 18-month-old mice.

However, quantitative measurements of synapse loss was not performed (Saito et al. 2014). Pathology in this mouse model is slower to progress than in the APP/PS1 mouse model. However, results may be more translatable to the human condition. Hence, investigating astrocyte dysfunction due to amyloidopathy using both models provides the benefits of each of the models and helps to validate results.

The quest for a single 'best' model of AD is likely misguided. However, information from various models will incrementally add to and validate knowledge, moving research towards disease modifying therapeutics. Hence, the information gained from this study of astrocyte dysfunction in mouse models of FAD should be combined with information gained using other experimental methods such as brain organoids, examination of post-mortem tissue, use of novel sporadic AD animal models and non-human primate research.

1.6 Astrocytes

Astrocytes are a type of glial cell, named after their stellate shape under the microscope. They exhibit molecular and functional heterogeneity, particularly in a region and context dependent manner (Morel et al. 2017; Zamanian et al. 2012; Vasile et al. 2017). In humans, cortical astrocytes are broadly categorized into 4 types, interlaminar (layers 1/2), protoplasmic (layers 3/4), varicose-projection (layers 5/6) and fibrous astrocytes (white matter), depending on their location in the brain (Vasile et al. 2017). However, it is acknowledged that classification into 4 subtypes is likely an over-simplification and that astrocyte gene expression and function might exist on a continuum rather than in such distinct categories. In support of this, studies have shown that astrocytes which were located closer together had more similar gene expression profiles (Boisvert et al. 2018; Morel et al. 2017).

Protoplasmic astrocytes are some of the most widely studied astrocytes due to their abundance in the grey matter and their presence in rodent brains. They are thought to occupy non-overlapping domains (Halassa et al. 2007), with their endfeet in contact with synapses, glial cells or blood vessels. The literature around the functionality of these astrocytes is staggering, especially considering that they were once thought of as mere structural support. Nowadays, astrocytes are thought to be involved in the formation (Christopherson et al.

2005), maturation (Risher et al. 2014) and elimination of synapses (Chung et al. 2013), the regulation of blood flow (Mulligan and MacVicar 2004), blood brain barrier integrity (Yao et al. 2014), ion (Hertz and Chen 2016), neurotransmitter (Mahmoud et al. 2019) and water homeostasis (Potokar et al. 2016), clearance of toxic solutes (Iliff et al. 2012), as well as in providing metabolic support to tissues (Rouach et al. 2008) and influencing network activity (Poskanzer and Yuste 2016). Hence, the centrality of astrocytic health to overall brain health is unquestionable.

1.6.1 Comparison of Mouse and Human Astrocytes

Mouse models are extremely useful tools for understanding the molecular mechanisms of astrocytic health and disease. However, it is important to bear in mind the limitations of using such models. Evidence exists to demonstrate that human astrocytes display morphological, transcriptional and functional features that are not present in murine astrocytes. Whilst protoplasmic and fibrous astrocytes have been described in both humans and rodents, interlaminar and varicose-projection astrocytes are thought to only be found in primates (Oberheim et al. 2009). Human protoplasmic astrocytes have a cell volume which is 16.5 times larger than their rodent counterparts, with processes that are longer and larger in number (Oberheim et al. 2009).

Transcriptomic studies have illustrated an overlap in human and mouse astrocyte specific genes, for example, *Gfap*, *Aldh1l1* (Aldehyde Dehydrogenase 1 Family Member L1), *Aqp4* (Aquaporin 4), *Slc1a2* (Excitatory Amino Acid Transporter 2), *Slc1a3* (Excitatory Amino Acid Transporter 2) and *Glul* (Glutamine Synthetase) (Zhang et al. 2016). Notably, Zhang et al (2016) found that only 30% of the most highly expressed genes in human astrocytes were also enriched in mouse astrocytes. The differences in species transcriptomes are in part accounted for by the differing subtypes, as was previously mentioned. Additionally, the difference may be due to the human samples originating from the temporal lobe, whereas the mouse samples were derived from the whole cortex. Interestingly, 52% of mouse astrocyte enriched genes were also enriched in human astrocytes. Hence, mouse models of astrocytic function do provide some valuable insight despite there being differences between the species.

As is to be expected, the transcriptomic differences in human and murine astrocytes also leads to functional differences. For example, both human and mouse astrocytes signal using calcium waves. However, the calcium waves in human astrocytes were shown to be approximately 5 times quicker than mouse astrocytic calcium waves (Oberheim et al. 2009). Additionally, the differences in human and mouse astrocytes appear to impact cognition, as human astrocytes transplanted into a mouse brain enhanced contextual learning (Han et al. 2013). Despite these differences, mouse models remain a valuable tool for dissecting mechanisms of health and the consequences of specific disease pathologies.

1.7 Astrocytes in AD

AD has long been associated with alterations in astrocyte morphology and function, with the literature containing suggestions of both neuroprotective and neurotoxic contributions of astrocytes to AD (Perez-Nievas and Serrano-Pozo 2018). Genome wide association studies (GWAS) have indicated that much of the risk for developing Alzheimer's disease is associated with genes expressed in glial cells (Karch and Goate 2015). Among these, *CLU* (Clusterin), *SORL1* (Sortilin-related Receptor 1), *FERMT2* (Fermitin Family Member 2) and *APOE*, are mainly expressed by astrocytes (Arranz and De Strooper 2019; Zhang et al. 2014), suggesting that astrocyte functions not only alter as a consequence of AD pathology, but also play a causative role in the development of AD.

Just as astrocytes in a healthy brain are thought to exhibit morphological, molecular and functional heterogeneity in a context dependent manner, so do astrocytes exposed to injury/disease. Astrocytes in AD have been broadly categorized into 'reactive' astrocytes, often located around plaques and 'atrophic' astrocytes which are often found distant from plaques (Verkhratsky, Parpura, et al. 2019). However, this is an oversimplification of the complex alterations occurring in astrocytes in AD. Thinking about astrocyte phenotype as a continuum seems more appropriate. For the purposes of therapeutically targeting astrocytes, it is important to understand the spectrum of changes occurring in astrocytes in a context dependent manner. Taking a systems biology approach, where by information from ribonucleic acid-sequencing (RNA-seq), proteomics, studies of morphology, proliferation, function and cellular interactions are combined in a context specific manner will be the best way to define therapeutically targetable subtypes/states of astrocytes in AD.

1.7.1 Morphology of Astrocytes in AD

Alois Alzheimer documented an abundance of glia surrounding Aβ plaques. Since then, many studies of post-mortem Alzheimer's disease patients, induced pluripotent stem cell (iPSC) derived astrocytes from human AD patients and mouse models of AD have corroborated this finding, demonstrating the presence of both reactive and atrophic astrocytes (Jones et al. 2017; Olabarria et al. 2010; Verkhratsky, Parpura, et al. 2019).

Reactive astrocytes classically overexpress two intermediate filament proteins, GFAP and vimentin (VIM) (Yamada et al. 1992; Olsen et al. 2018; Kamphuis et al. 2014). They are hypertrophic and have thick processes which encircle Aβ plaques, without substantially altering their distribution of cell bodies (Galea et al. 2015; Wilhelmsson et al. 2006). This indicates a reorientation of astrocyte processes, rather than migration of astrocytes towards plaques, or a proliferation of astrocytes near plaques. This theory is supported by the fact that reactive astrocyte load does not correlate with plaque size (Serrano-Pozo, Muzikansky, et al. 2013) and stereological quantification of astrocytes in AD and control brains, using the pan-astrocytic marker ALDH1L1, demonstrated no difference in abundance (Serrano-Pozo, Gómez-Isla, et al. 2013). Notably, reactive astrocytes have also been associated with the other core pathology in AD, tau NFTs. Astrocytic processes have been shown to penetrate 'ghost' NFTs present in the neuropil once the neuron has degenerated (Perez-Nievas and Serrano-Pozo 2018).

Astrocytes which display a reduced soma volume, and a decreased number of processes have been termed 'atrophic astrocytes' (Verkhratsky, Rodrigues, et al. 2019; Olabarria et al. 2010). It is possible that these astrocytes are senescent. Whilst reactive and atrophic astrocytes are not exclusive features of Alzheimer's disease, evidence would suggest their presence begins early in the disease and contributes to disease pathogenesis (Ingelsson et al. 2004). Importantly, the classification of astrocytes into reactive and atrophic subtypes is likely an oversimplification of the cellular states that astrocytes adopt over the course of AD development.

1.7.2 Alterations to Astrocyte Function in AD

Several lines of evidence suggest that astrocytes undergo functional changes in AD. Whilst some alterations have been attributed to enhancing neuroprotection, many indicate astrocytes are contributing to the neuropathology, either through neurotoxic gains of function or detrimental loss of functions.

1.7.2.1 Neuroinflammation

A sustained inflammatory response has become a cardinal, albeit non-exclusive, hallmark of AD (Gomez-Nicola and Boche 2015; Knezevic and Mizrahi 2018). Astrocytes and microglia are the two immune cell types in the brain which play pivotal roles in the neuroinflammatory response in AD. Aβ is thought to bind directly to astrocytes via receptors such as the N-Methyl-D-aspartic acid (NMDA) receptor and the P2Y purinoceptor 1 (P2Y1) receptor (Delekate et al. 2014; Mota et al. 2014). Binding to these receptors alters downstream signaling through the calcium/calcineurin/nuclear factor of activated T cells pathway, leading to a reactive astrocyte phenotype and enhanced production of pro-inflammatory cytokines such as interleukin-1β (IL-1β), interleukin-6 (IL-6) and tumour necrosis factor α (TNFα), inducible nitric oxide (iNOS) and complement protein C3 (C3), amongst other molecules (Liddelow et al. 2017; Lian et al. 2016; Perez-Nievas and Serrano-Pozo 2018; Norris et al. 2005; Abdul et al. 2009). This leads to a detrimental feed forward cycle of further glial activation and neuroinflammation.

Reactive microglia have also been shown to exacerbate glial activation and neuroinflammation by secreting cytokines such as TNF-α, IL-1β, IL-6, which bind to receptors on astrocytes (Liddelow et al. 2017) and activate pathways such as the Janus kinase (JAK)-signal transducer and activator of transcription 3 (STAT3) and nuclear factor kappa-light-chain-enhancer of activated B cells (NF-κB) pathway, again leading a reactive astrocyte phenotype (Bales et al. 1998; Ben Haim et al. 2015; Perez-Nievas and Serrano-Pozo 2018).

Importantly, glia driven inflammation has been proposed to be a link between the two core proteinopathies in AD (Yoshiyama et al. 2007; Meda et al. 2001). For example, Aβ binding to glia leads to enhanced production of pro-inflammatory cytokines. When IL-6 was exogenously

applied to rat to hippocampal neuronal cultures, this led to activation of cyclin dependent kinase 5 (CDK5), and hyperphosphorylation of tau, as measured by increased immunoreaction with the tau AT8 antibody (Quintanilla et al. 2004). Therefore, providing a possible mechanistic link between Aβ accumulation and tau hyperphosphorylation.

1.7.2.2 Aβ clearance / plaque formation

Astrocytes are thought to be providing a neuroprotective function against Aβ pathology in AD. Firstly, by secreting extracellular Aβ chaperones, such as apolipoproteins, α2macrogloblulin, and α1-antichymotrypsin, which facilitate the clearance of Aβ across the BBB. Secondly, by secreting Aβ proteases which degrade Aβ extracellularly. Thirdly, by internalizing Aβ either through phagocytosis or receptor mediated endocytosis and degrading Aβ intracellularly (Ries and Sastre 2016), and fourthly, by forming a physical barrier between the plaque and surrounding neuropil, limiting the damage of diffusible soluble oligomeric Aβ. This notion of a neuroprotective role of astrocytes is strengthened by the demonstration that primary human adult astrocytes preferentially engulf the more neurotoxic oligomeric Aβ over fibrillar Aβ (Nielsen et al. 2010). However, questions have risen over the ability of astrocytes to effectively clear Aβ across the BBB in AD, since AQP4, a water channel involved in the transport of soluble Aβ across the BBB, appears to lose its perivascular localization with increasing Aβ burden in post-mortem AD brains (Zeppenfeld et al. 2017). Additionally, APOE***ε***4, is thought to bind Aβ less efficiently than the ***ε***2 and ***ε***3 isoforms, which may influence clearance (Wildsmith et al. 2013). However, others believe APOE does not bind Aβ, but instead competes with Aβ for low density lipoprotein receptor-related protein 1 (LRP-1) binding in astrocytes. Nevertheless, this would still impact astrocyte mediated Aβ clearance. The capacity of astrocytes to phagocytose also appears to decrease with progressive AD pathology (Iram et al. 2016). Hence, a loss of astrocytic functions may contribute to Aβ accumulation in AD.

An alternative hypothesis is that astrocytes are actively contributing to Aβ production, secretion and aggregation. Primary cultures of mouse astrocytes exposed to $A\beta_{42}$ and inflammatory stressors lipopolysaccharide (LPS), TNF-α, interferon γ (IFN-γ), and IL-1β have been shown to increase expression of APP and β-site APP cleaving enzyme (BACE1), two

essential components in the production of Aβ. Additionally, Aβ40 was increased in the culture medium, indicating enhanced secretion of Aβ from astrocytes (Zhao et al. 2011). These in vitro findings are supported by immunohistochemical studies in human AD patients which demonstrated enhanced astrocytic BACE1 immunoreactivity in proximity to Aβ plaques (Hartlage-Rübsamen et al. 2003). Furthermore, some studies have suggested that APOE, especially APOEε4 may play a role in Aβ aggregation (Hashimoto et al. 2012; Cerf et al. 2011; Castano et al. 1995; Ma et al. 1994).

The ground truth is likely that astrocytes are involved in both the production and clearance of Aβ. In AD the equilibrium appears disrupted in favour of a surplus of Aβ, which contributes to a detrimental feed forward cycle of activating astrocytes, further Aβ production, neuroinflammation and neurodegeneration.

1.7.2.3 Metabolic Compromise

Reduced brain glucose uptake as measured by ^{18}F-fluorodeoxyglucose positron emission tomography (FDG-PET) is an early indication of AD (Bloudek et al. 2011). Since astrocytes are one of the most abundant cell types in the brain, a portion of the signal is likely caused by reduced astroglial glucose uptake (Zimmer et al. 2017). Indeed, a study in AD patients combining longitudinal PET data of astrocyte function using ^{11}C-deuterium-L-deprenyl, and glucose metabolism using FDG uptake, showed significant association between astrocyte function and progressive hypometabolism (Carter et al. 2019). Reduced astroglial glucose uptake would impact the ability of astrocytes to perform the myriad of homeostatic functions attributed to them. In particular, their ability to metabolise glucose to lactate which is utilised by neurons as a fuel source.

Astrocytes positioned at the BBB also contribute to energy availability in the brain by playing a critical role in sensing energy requirements and modulating cerebral blood flow and thus glucose availability accordingly (Howarth 2014). In an amyloid mouse model of AD, astrocytic endfeet surrounding parenchymal Aβ deposits were shown to swell and detach from the BBB, thus compromising their ability to regulate blood flow (Merlini et al. 2011).

1.7.2.4 Synaptic Formation Function and Elimination

Astrocytes are thought to be intrinsically involved in synapse formation, function and elimination. Since synapse loss and reactive astrocytes around plaques are key pathological features of Alzheimer's disease, this begs the question, what role do astrocytes play in synaptic pathology?

Thrombospondin 1 and 2 (THBS1, THBS2) (Christopherson et al. 2005), Sparc-like protein 1 (SPARCL1) (Kucukdereli et al. 2011), and glypican4 and 6 (GPC4 and GPC6) (Allen et al. 2012) are some of the astrocyte secreted factors known for their involvement in excitatory synapse formation. Liddelow et al. (2017) recently demonstrated that reactive astrocytes, exposed to LPS, exhibit reduced expression of *Gpc6* and *Sparcl1*, whilst simultaneously showing increased expression of *Thbs1* and *Thbs2*. Whilst one would expect enhanced expression of Thbs1 and 2 to increase synapse formation, these reactive astrocytes promoted less synapse formation than resting astrocytes. Additionally, when neurons were cultured with resting astrocytes to induce synapse formation and were subsequently cultured with these reactive astrocytes, synapse number decreased by approximately 40% (Liddelow et al. 2017). Thus, indicating the reactive astrocytes were either unable to maintain the synapses or were actively toxic to the synapses. Culturing neurons with reactive astrocyte conditioned medium revealed that the reactive astrocytes secrete soluble toxin(s) which kill a subset of central nervous system (CNS) neurons and mature oligodendrocytes (Liddelow et al. 2017). Whilst the astrocytes in this study were acutely induced reactive astrocytes, the results highlight the potential for reactive astrocytes induced by chronic pathology to be contributing to synapse pathology via similar mechanisms of a reduced ability to form and maintain synapses, or secretion of molecules which lead to synapse and neuronal loss. Several studies have suggested that Aβ oligomers, which may be produced by activated astrocytes in Alzheimer's disease, are directly synaptotoxic (Hong et al. 2018; Ferreira et al. 2015; Frost and Li 2017). Other astrocyte secreted molecules, such as transforming growth factor-β3 (TGF-β3) (Bialas and Stevens 2013) and C3 (Shi et al. 2017; Hong et al. 2016) may be indirectly synaptotoxic by increasing microglia mediated synapse engulfment.

APOE is a cholesterol carrier predominantly synthesized and secreted by astrocytes. Cholesterol is thought to be important in synapse formation and function (Pfrieger 2003). The

presence of the APOE***ε***4 allele has been associated with increased risk of AD (Corder et al. 1993). Intriguingly, Zhao et al. found that iPSC derived neurons cultured with *APOE* ***ε***4/***ε***4 astrocytes demonstrated reduced synaptic protein abundance compared to ***ε***3/***ε***3 astrocytes. Therefore, suggesting that astrocyte derived APOE***ε***4 may contribute to AD pathology via a reduced capacity to support synaptogenesis or maintain synapses (Zhao et al. 2017). Another study investigating the effect of APOE isoform on astrocytic phagocytic ability revealed APOE ***ε***4 was associated with a reduced rate of synaptic pruning by astrocytes compared to APOE ***ε***2. Furthermore, complement component 1q (C1q) accumulation was higher in *Apoe****ε***4 knock-in animals compared to *Apoe****ε***2 or ***ε***3. They proposed that AD susceptibility of APOE may in part be due to defective pruning of senescent synapses, which leads to an accumulation of C1q coated senescent synapses, and enhances susceptibility to complement cascade mediated degeneration (Chung et al. 2016). Further research will help to determine whether the phagocytic ability of astrocytes change in the context of AD and contribute to synapse pathology and neurodegeneration.

In addition to synapse formation and elimination, astrocytes play a fundamental role in regulating excitatory glutamate and inhibitory gamma-aminobutyric acid (GABA) neurotransmission in the brain. Excitatory amino acid transporter 1 (EAAT1/GLAST) and excitatory amino acid transporter2 (EAAT2/GLT-1) are glutamate transporters present on astrocytes which facilitate removal of glutamate from the synaptic cleft (Anderson and Swanson 2000). However, in AD this critical astrocyte function appears to be disrupted. Aβ oligomers have been shown to reduce the expression of GLT-1 in primary rat astrocyte cultures (Abdul et al. 2009), additionally astrocytes surrounding plaques demonstrated reduced GLT-1 expression in the APP/PS1 amyloid mouse model, and finally this observation translated to the human condition, where EAAT2 expression was found to decrease with increasing amyloid pathology in post-mortem AD brains (Simpson et al. 2010). Impaired reuptake of glutamate likely contributes to neuronal excitotoxicity through excessive activation of extrasynaptic NMDA receptors, promoting pro-death and oxidative stress signaling and leading to neurodegeneration (Hardingham et al. 2002). Notably, astrocytes also express NMDA receptors (Verkhratsky and Kirchhoff 2007). Hence, it is conceivable that excessive glutamate also disrupts astrocytic NMDA receptor signaling and astrocytic function. However, this is a relatively understudied field.

Another mechanism by which astrocytes might contribute to glutamatergic excitotoxicity in AD is through the downregulation of glutamine synthetase. Glutamine synthetase is an enzyme located in astrocytes which converts glutamate to glutamine, so that glutamine can be recycled back to neurons for conversion into neurotransmitters. Studies conducted in the 3xTg AD mouse model have shown reduced expression of glutamine synthetase in the hippocampus and medial prefrontal cortex, in particular in areas where Aβ deposits are abundant (Olabarria et al. 2011; Kulijewicz-Nawrot et al. 2013). Whether this observation translates to the human condition is unclear (Robinson 2000; Le Prince et al. 1995; Serrano-Pozo, Gómez-Isla, et al. 2013). However, if it does, reduced glutamine synthetase expression would substantially inhibit astrocytes from performing glutamate recycling, which would contribute to glutamate excitotoxicity in AD. Notably, Robinson (2000) and Serrano-Pozo et al. (2013) have demonstrated expression of glutamine synthetase in pyramidal neurons in the cortex of AD patients, perhaps highlighting a compensatory mechanism (Serrano-Pozo, Gómez-Isla, et al. 2013; Robinson 2000).

Astrocytes are also involved in the removal and recycling of the inhibitory neurotransmitter GABA from the synapse. Studies would suggest that reactive astrocytes may be contributing to neurotoxicity through an enhancement of GABAergic tone. The activity of glutamate decarboxylase, an enzyme involved in GABA production, was found to be doubled in the cortex of Aβ plaque bearing APP/PS1 mice, compared to age matched control mice. Importantly, this increase in glutamine acid decarboxylase (GAD) activity was found to be predominantly of glial origin (Mitew et al. 2013). Similarly, GABA content of astrocytes has repeatedly been reported to be increased in other studies of mouse models of AD and in human post-mortem AD brains (Wu et al. 2014; Jo et al. 2014). Enhanced astrocyte derived GABAergic tone may contribute to memory impairment in AD.

The ground truth is likely that astrocytes develop both neurotoxic and neuroprotective functions in AD. However, the equilibrium appears in favour of neurotoxic functions which contribute to a detrimental feed forward cycle of activating astrocytes, further Aβ production, neuroinflammation and neurodegeneration.

1.7.3 Transcriptomic Studies of Astrocytes in AD

Whether reactive astrocytes in AD are the villain, displaying neurotoxic gains of functions, the hero, displaying neuroprotective gains of functions, or the damsel in distress, displaying loss of functions, is unclear. Transcriptomic studies provide an opportunity to assess alterations in astrocytic phenotype in AD in an unbiased and information rich manner.

There have been two key investigations of laser captured astrocytes from human post-mortem AD patients. Simpson et al. conducted a microarray analysis comparing astrocytes from early (I/II), mid (III-IV) and late (V/VI) Braak staged brains (Simpson et al. 2011). Genes involved with the cytoskeleton, immune response, apoptosis and ubiquitin-mediated proteolysis were dysregulated in mid compared to early Braak staged astrocytes. In late Braak staged astrocytes, genes involved in insulin, phosphoinositide 3 kinase/Akt (PI3K/Akt) and mitogen-activated protein kinase (MAPK) signalling pathways were downregulated. These results might indicate that astrocytes contribute to disease pathology and lose their ability to perform their usual functions, especially later in the disease. A caveat to this study is that *GFAP* is only expressed in a subset of astrocytes and is often not expressed at detectable levels in resting state astrocytes (Zhang et al. 2019). Hence, comparison of high pathology astrocytes to low pathology astrocytes is impeded. Additionally, microarrays require pre-specified transcript probes and have a limited dynamic range compared to RNA-seq technologies, meaning investigations are inherently somewhat biased and genes with low expression may not be detected.

Sekar et al. addressed the issues above by conducting RNA-seq analysis on astrocytes micro-dissected using ALDH1L1 as a marker from the posterior cingulate of AD and control postmortem brains (Sekar et al. 2015). ALDH1L1 is thought to be a widely expressed astrocyte specific marker and so subtle differences in gene expression between diseased and control brains should be identified (Cahoy et al. 2008). Sekar et al. found that the most impacted pathway was the immune response, with 82.4% of significantly changed genes in this pathway demonstrating upregulated expression. These studies provide an excellent basis for our understanding of the phenotype of astrocytes in AD. However, it is difficult to dissect the impact of amyloid pathology on the astrocyte transcriptome due to there also being tau pathology in human AD, as well as the potential for co-morbidities in subjects. Additionally,

human transcriptomic studies may be affected by the period of disease prior to death, the cause of death and the post-mortem interval.

Transcriptomic studies on transgenic mice provide a good method of gathering data to disentangle some of these questions. Amyloid pathology in mice can be studied in isolation, with tighter control on post-mortem interval. Orre et al. used a microarray to investigate transcriptomic alterations in GLT-1 fluorescence activated cell sorted (FACS) astrocytes from 15-18-month APP/PS1 and control mice (Orre et al. 2014). APP/PS1 mice are transgenic mice which begin displaying amyloid plaque pathology at 6-months, with abundant plaques at 9-months (Jankowsky et al. 2004). The top 5 upregulated genes in APP/PS1 mice were *Cst7* (Cystatin F), *Ccl4* (Carbon Tetrachloride), *Il-1β*, *Clec7a* (C-type lectin-like domain) and *Tyrobp* (TYRO protein tyrosine kinase-binding protein), all of which are involved in immune signaling, highlighting the similarity of astrocyte responses in an amyloidopathy model as in human post-mortem AD astrocytes. Interestingly, 21% of the genes which the group had previously identified as highly enriched in astrocytes were downregulated in APP/PS1 astrocytes, which might indicate an impairment of normal astrocytic function. Notably, this included reduced expression of genes involved in cholesterol biosynthesis, synapse organization and synaptic transmission. The limitations of this study include the fact that transcript probes were pre-specified and that the APP/PS1 mouse is a transgenic mouse model, meaning the mutated gene is inserted randomly into the genome which can affect the pattern and level of gene expression. Furthermore, it is difficult to untangle the effects of elevated Aβ from APP overexpression. Hence, it would be beneficial to investigate alterations in astrocyte gene expression in a knock-in mouse model of amyloidopathy.

Finally, all of the aforementioned studies investigated transcriptomic alterations in astrocytes due to AD pathology. Whilst the transcriptome provides a good indication of genes which are being expressed under different conditions, the translating messenger RNA (mRNA) profile likely reflects the protein content and thus function of the cell more closely (Schwanhäusser et al. 2011). Hence, it would be beneficial to assess alterations in the astrocyte translatome due to amyloidopathy.

1.8 Overview:

In this thesis I explore how astrocytes change in models of amyloidopathy. I use two amyloidopathy models, the transgenic APP/PS1 mouse model, and the knock-in APP^{NLF} mouse model. Whilst the APP/PS1 mouse model is very well characterized and widely used in Alzheimer's disease research, the APP^{NLF} model was relatively new and needed better characterization.

1.8 Aims and Hypotheses:

1) Characterize synapse pathology and astrogliosis in the knock-in APP^{NLF} amyloidopathy model.

   I hypothesize that this knock-in model exhibits plaque associated synapse loss which is comparable to other models of Alzheimer's disease.

2) Investigate alterations in the astrocyte translatome in mouse models of amyloidopathy.

   I am testing the hypothesis that the astrocyte translatome changes temporally over the course of the progression of amyloidopathy models.

3) Investigate heterogeneity of astrocytic gene expression in mouse models of amyloidopathy.

   I am testing the hypothesis that astrocytes display heterogeneous gene expression within models of amyloidopathy, which includes a cluster(s) of astrocytes associated with pathology.

Chapter 2

Materials & Methods

2.1 Animals

Mouse models were used throughout the experiments presented in this thesis.

All animal experiments conformed to national and institutional guidelines including the Animals [Scientific Procedures Act] 1986 (UK), and the Council Directive 2010/63EU of the European Parliament and the Council of 22 September 2010 on the protection of animals used for scientific purposes, and had full Home Office ethical approval. Mice were group housed according to sex, in a 12h/12-hour light/dark cycle with *ad libitum* access to food and water. Here, I present an overview of the genetically engineered animals used.

2.1.1 APP^{NLF} Mice

APP^{NLF} mice obtained from Dr. Takaomi Saido were bred in house and maintained on a C57BL/6N background. These mice express a humanized Aβ region in the APP knock-in construct, along with two pathogenic mutations, the Swedish "NL" and the Iberian "F", which lead to increased total Aβ and Aβ42 respectively. Aβ plaques and gliosis begin to accumulate in these animals around six months of age. However, they aren't widespread until 18-24-months (Saito et al. 2014). In this thesis we used mice at 6, 12 and 18-months in order to have sampled changes in astrocyte phenotype throughout pathology development.

2.1.2 APP/PS1 Mice

APP/PS1 mice carrying a chimeric mouse/human APP (Mo/HuAPP695$_{swe}$), and a mutant human presenilin 1 (PS1-$_{dE9}$) (Borchelt et al. 1997; Jankowsky et al. 2004), were purchased from The Jackson Laboratory (B6.Cg-Tg(APPswe,PSEN1dE9)85Dbo/Mmjax; MMRRC Stock No: 34832-JAX) and were bred onto a C57BL/6J background. APP/PS1 mice develop Aβ plaques around 6-months old, and pathology is widespread by 12-months. In this thesis we used mice at 6, 12 and 18-months in order to have sampled changes in astrocyte phenotype throughout pathology development, and to match APP^{NLF} time points.

2.1.3 MAPT^{P301S} Mice

Whilst I did not personally conduct experiments using the MAPT^{P301S} mice, I did compare alterations in astrocytic gene expression in the amyloidopathy APP/PS1 mouse model with a

dataset collected by Zoeb Jiwaji on astrocytic gene expression changes in the $MAPT^{P301S}$ tauopathy mouse model. $MAPT^{P301S}$ mice accumulate hyperphosphorylated filamentous tau. This drives progressive neurodegeneration in the spinal cord and upper cortical layers. Pathology begins around 3-months, and is widespread by 5-months. The $MAPT^{P301S}$ mice are on a C57BL6J background. Zoeb had previously shown that substantial alterations in the spinal cord astrocyte translatome occur at 5-months. In the cortex, where degeneration only takes place in upper layers, numbers of significantly changed genes was lower than in the spinal cord, although, the fold-change (up and down) correlated well with the spinal cord data r=0.77 (data not shown). This is indicative of a similar qualitative response of cortical and spinal astrocytes to tau pathology, albeit weaker in the cortex. Hence, in this study I used the spinal cord data for enrichment analyses, since the larger numbers of significant genes provided greater power for these studies.

2.1.4 Aldh1l1-eGFP-rpl10a (TRAP) Mice

Aldh1l1-eGFP-Rpl10a (TRAP) mice which express eGFP tagged ribosomal protein L10a under the astrocyte-specific *Aldh1l1* promoter were generated as previously described by the laboratory of Nathaniel Heintz (Doyle et al. 2008) and re-derived on a C57BL/6J background from frozen sperm imported from Jackson Laboratories (Mouse Strain Number – 030248).

Reagents were obtained from Sigma (St. Louis, Missouri) unless stated otherwise.

2.2 Characterization of Synapse Density, Plaque Load and Astrogliosis in 12-month APP^{NLF} Mice

2.2.1 Sample Size Estimation with Power Analysis

A power analysis was conducted on a historical data set to determine group sizes for synapse density studies using G*Power 3.1. Data on synapse density in relation to distance from plaque in APP/PS1 mice revealed ~50% reduction in synapse density close to plaques (within the halo of Aβ surrounding the core), with a standard deviation (SD) of ~20% (Koffie et al. 2009). Hence, the effect size was 2.5. To detect this at high power (98%) a sample size (n) = 5 is necessary. Since I was also investigating the impact of sex, I used n=10. This sample size was adequate to measure plaque burden and astrogliosis using immunohistochemistry, based on

the APP^{NLF} immunohistochemical data collected by Saito et al (2014), where the difference in GFAP expression between HOM and WT mice was ~0.35%, with a SD of ~0.05% of the mean. To detect this at a power of 98% we would require n=4. Tissue from the same animals was used to detect synapse density, plaque burden and astrogliosis around plaques in order to reduce the number of experimental animals, in line with the 3Rs (replacement, reduction, refinement).

2.2.2 Animals

10 APP^{NLF} homozygote (HOM) mice, 10 heterozygote (HET) and 10 wild-type (WT) mice, balanced for sex **(table 1)**, were aged to 12 months. One hemisphere was fixed in 4% paraformaldehyde, transferred to 15% glycerol and stored at 4^{o}C for measurement of astrogliosis and plaque burden using immunohistochemistry (IHC). The other hemisphere was used to make tissue blocks for analysis of synaptic density by array tomography.

Animal ID	Genotype	Sex	Age (months, days)	AT/ IHC
AP183	HOM	m	12m, 4d	AT
AP202	HOM	m	12m, 17d	AT
AP174	HOM	m	12m, 9d	AT, IHC
AP197	HOM	m	11m, 21d	AT, IHC
AP198	HOM	m	11m, 21d	AT, IHC
AP182	HOM	m	12m, 4d	IHC
AP175	HOM	m	12m, 9d	IHC
AP176	HOM	f	12m, 9d	AT, IHC
AP184	HOM	f	12m, 4d	AT, IHC
AP192	HOM	f	12m, 5d	AT, IHC
AP206	HOM	f	12m, 14d	AT, IHC
AP270	HOM	f	12m,17d	AT, IHC
AP178	WT	m	12m, 4d	AT, IHC
AP196	WT	m	12m, 1d	AT, IHC
AP181	WT	m	12m, 4d	AT, IHC
AP180	WT	m	12m, 4d	AT, IHC
AP179	WT	m	12m, 4d	AT, IHC
AP187	WT	f	12m, 4d	AT, IHC
AP194	WT	f	12m, 1d	AT, IHC
AP225	WT	f	12m, 9d	AT, IHC
AP224	WT	f	12m, 9d	AT, IHC
AP226	WT	f	12m, 9d	AT, IHC
AP172	HET	m	12m, 9d	IHC
AP177	HET	m	12m, 4d	IHC
AP191	HET	m	12m, 15d	IHC
AP193	HET	m	12m, 1d	IHC
AP203	HET	m	12m, 1d	IHC
AP185	HET	f	12m, 4d	IHC
AP186	HET	f	12m, 4d	IHC
AP188	HET	f	12m, 4d	IHC
AP189	HET	f	12m, 4d	IHC
AP195	HET	f	12m,1d	IHC

Table 1. Mice included in the array tomography (AT) and immunohistochemistry (IHC) study. Homozygote (HOM), Heterozygote (HET), wild-type (WT) mice. Studies were balanced for male (m) and female (f) mice.

2.2.3 Array Tomography Tissue Embedding

Array tomography experiments were largely carried out as previously described (Kay et al. 2013; Micheva and Smith 2007). Briefly, small blocks of somatosensory cortex tissue were fixed in 4% paraformaldehyde. Samples were then dehydrated in ascending concentrations of ethanol (50%, 70%, 95%,100%, 100%), each for 5 minutes. Following this, samples were incubated in 50:50 LRWhite resin, ethanol for 5 minutes. Finally, samples were incubated in 100% LRWhite resin for 5 minutes, then covered with fresh LRWhite resin overnight 4^{o}C. Blocks were embedded in LRWhite resin in gelatin capsules by baking at 56^{o}C for 24 hours. Blocks were stored at room temperature.

2.2.4 Array Tomography Ribbon Cutting

Thickness No. 1 glass coverslips (VWR International, Randor, Pennsylvania) were coated with 0.1% fish skin gelatin and 0.01% chromium potassium sulphate, and allowed to dry to facilitate adhesion of array tomography sections to coverslips. Approximately 30 70nm serial sections from APP^{NLF} somatosensory cortex blocks were cut using an Ultracut Ultramicrotome (Leica, Wetzlar, Germany) with a Histo Jumbo Diamond Knife (Diatome, Hatfield, Pennsylvania) and collected on the coverslips. Ribbons were stained and imaged within 3 months of cutting, as previous members of the lab had found antigens appear to degrade with longer term storage.

2.2.5 Staining Array Tomography Ribbons

Ribbons were outlined in a hydrophobic pen, baked at 53^{o}C for 30 minutes and then incubated with 50mM glycine in tris-buffered saline (TBS) for 5 minutes at room temperature. The tissue was washed with TBS and antigen retrieval was performed by pressure cooking the slides in citrate buffer (pH 6) for 2 minutes. Ribbons were washed again in TBS and incubated with 50mM glycine for a further 5 minutes at room temperature. Array tomography block buffer (0.1% fish skin gelatine, 0.05% tween in TBS) was then applied for 30 minutes at room temperature. Following this, ribbons were incubated with a solution of primary antibodies **(table 2)** diluted in AT block buffer overnight at 4°C. The next day ribbons were washed with

TBS and incubated in a solution of secondary antibodies **(table 2)** in AT block buffer for 30 minutes at room temperature and in the dark. Ribbons were washed with TBS and stained with 0.001 mg/ml 4'-6-diamidino-2-phenylindole (DAPI) for 5 minutes at room temperature and in the dark. Finally, ribbons were washed with TBS and mounted on microscope slides (VWR international) using Immu-Mount media (Thermo Scientific, Waltham, Massachusetts).

A negative control omitting the primary antibodies and a positive control from an APP/PS1 mouse with known extensive plaque and synapse pathology were included to validate the experimental procedure.

Target	Antibody	Species	Supplier	Catalogue number	Concentration
Synaptophysin	SY38	Mouse	Abcam	ab8049	1:50
Post-synaptic density 95	PSD95	Guinea-pig	Synaptic Systems	124014	1:50
Amyloid fibrils	OC (amyloid)	Rabbit	Merck Millipore	ab2286	1:1000
GFAP	GFAP	Rabbit	Dako	Z0334	1:3000
	IgG (H+L) cross-adsorbed secondary antibody, Alexa Fluor 647	Goat anti-mouse	Thermo-fisher scientific	A-21235	1:50
	IgG H&L Cy3 preadsorbed	Goat anti-guinea pig	Abcam	ab102370	1:50
	IgG (H+L) highly cross-adsorbed secondary antibody, Alexa fluor 488	Goat anti-rabbit	Invitrogen	A-11034	1:50
	IgG, Alexa Fluor 647	Donkey anti-Rabbit	Abcam	ab150075	1:500

Table 2. Primary and secondary antibodies used in array tomography and immunohistochemistry study.

2.2.6 Array Tomography Image Acquisition and Analysis

Tissue from HOM APP^{NLF} and WT animals were stained and imaged in parallel. All staining, imaging and analysis was performed blind to genotype.

A Zeiss Axio Imager Z2 epifluorescent microscope fitted with a Coolsnap digital camera and Axio Imager software was used to obtain the images (Carl Zeiss Ltd., Cambridge, UK). The same nuclei on consecutive slices of the ribbon were imaged using a 63X objective. A minimum of 16 slices within the ribbon were imaged. For ribbons which contained plaques,

two image stacks near the plaque and one without a plaque in view were taken. For ribbons that did not contain plaques, two image stacks were taken.

2.2.6.1 Aligning Images

Consecutive images were aligned and segmented using a MATLAB script custom built by Dr. Marti Colom Cadena, a member of the Spires-Jones lab, and Jordi Pegueroles, a member of the Lleo lab (https://github.com/arraytomographyusers/Array_tomography_analysis_tool).

The synaptophysin channels in each image stack were aligned first. This alignment was then used to align the other channels in the same image stack. The synaptophysin stain was chosen to set the alignment parameters since the small size of the puncta increased the accuracy of alignment. Additionally, the synaptophysin stain did not contain spurious nucleic staining, unlike the post-synaptic density 95 (PSD95) stain.

2.2.6.2 Segmenting Images

The array tomography analysis tool (link above) was used to segment the images.

The auto local threshold function was used to isolate the SY38 and PSD95 staining. After optimization, the following parameters were chosen (see **section 4.2.4** for details on optimization of image analysis):

- Window size: 6 for both SY38 and PSD95
- C factor: 3 for SY38, 2 for PSD95
- Mean intensity measured
- Minimum pixel size: 3
- Maximum pixel size: 500

Since synapses are larger than 70nm in depth, it was assumed that puncta which only appear in one slice was noise. Hence, puncta which were not found in consecutive slices were removed in the segmented images.

Thresholds for plaque cores and whole plaques (core and halo) were determined manually using ImageJ. Dense staining at the centre of the plaque was defined as the plaque core.

Values for the plaque thresholds determined in ImageJ were used in the MATLAB tool fixed threshold function, and segmented images were output. The fixed threshold function is better for large irregular shaped objects, as the auto local threshold function tended to break the plaque into many small pieces, which would have affected the boundaries used to quantify synapses and the colocalisation of synaptic puncta and Aβ.

2.2.6.3 Quantification and Statistical Analysis of Synaptic Density Over the Whole Image and Around the Aβ Plaque Core

An in-house Python tool built by Dr. Lewis Wilkins (https://github.com/lewiswilkins/Array-Tomography-Tool) was used to identify presynaptic SY38 puncta that were within 500µm of a PSD95 puncta and so were considered a synaptic pair. Unpaired and paired synaptic density were quantified using the MATLAB tool. A neuropil mask generated using the synaptophysin channel was applied in order to exclude nucleic staining.

Statistical analysis was performed in R. A linear mixed effects model was used to analyse unpaired SY38, unpaired PSD95 and paired synapse density in the neuropil. The fixed effects were image type (WT, HOM_Near (containing a plaque) and HOM_far (not containing a plaque)) and sex. The random effects accounted for the fact that multiple images were taken from the same mouse and that experiments were done in batches.

```
Formula: MEPairedUnpaired<-
lmer(Puncta_density~Image_type*Puncta_type*Sex+(1|Mouse_ID:stack_number) +
(1|batch), data=paired_vs_unpaired_R)
anova(MEPairedUnpaired)
```

A type III analysis of variance (ANOVA) on the linear mixed effects model was run, which revealed there were no significant interactions between puncta type, image type or sex **(table 5A)**, so the model was re-run without interactions.

```
Formula: MEPairedUnpaired <-
lmer(Puncta_density~Image_type+Puncta_type+Sex+(1|Mouse_ID:stack_number) +
(1|batch), data=paired_vs_unpaired_R)
anova(MEPairedUnpaired)
```

Qunatile-quantile (q-q) plot of the residuals of the linear mixed effects model **(figure 3)** indicated that most of the points lay within the 95% error intervals represented by the dashed lines. Hence, the data fit the model reasonably well.

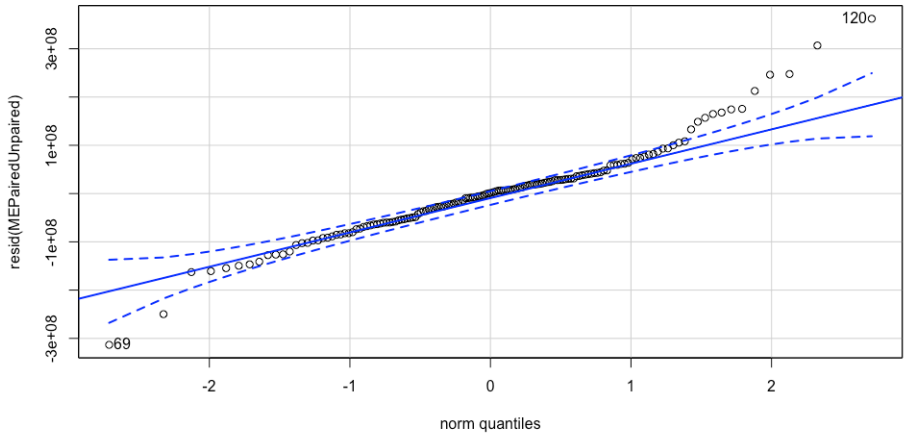

Figure 3. Q-Q plot of the residuals of the linear mixed effects model used to assess differences in synaptic protein density over the whole image between WT, HOM_near and HOM_far images.

A type III ANOVA run on the revised linear mixed effects model revealed there was no main effect of image type (F=0.77, p=0.47) or sex (F=0.84, p=0.37) **(table 5B)**, so a post-hoc Tukey corrected pairwise comparison was run to assess differences in synaptic puncta density between all the puncta types **(table 5C)**.

Formula: emmeans(MEPairedUnpaired, list(pairwise ~ Puncta_type), adjust = "tukey")

In image stacks which contained dense core plaques (APP^{NLF} HOM), paired SY38 density was also measured in 2µm concentric rings, from the boundary of the plaque core to 40µm from the boundary of the plaque core using the MATLAB tool. The density of paired SY38 puncta was expressed as a percentage of paired SY38 puncta at 40µm from the plaque core boundary, the furthest measured distance from the plaque. The mixed model below was run:

Formula: MM<-
lmer(Percentage_paired_SY38~Dist+Sex+(1|Mouse_ID:stack_number)+(1|Batch), data=AT_HOM_PD_PairedSY38_R).

The fixed effects were distance and sex, the random effects accounted for the fact that 2 images were taken from the same mouse and that experiments were done in batches. On inspection of the q-q plot of the residuals **(figure 4A)**, several transformations of the data were trialed in order to better fit the assumptions of the model. Squaring the data appeared to improve the fit of the data to the model assumptions **(figure 4B)**. Hence, the mixed model was re-run using the transformed data.

Formula: MM<-
lmer(Square_Percentage_paired_SY38~Dist+Sex+(1|Mouse_ID:stack_number)+(1|Batch),
data=AT_HOM_PD_PairedSY38_R).

A type III ANOVA on the linear mixed effects model **(table 6A)** revealed no main effect of sex. Hence, sex was removed from the model. Paired synapse density at each distance was compared to the paired synapse density measured furthest from the plaque (40µm).

Formula: MM<-
lmer(Square_Percentage_paired_SY38~Dist+(1|Mouse_ID:stack_number)+(1|Batch),
data=AT_HOM_PD_PairedSY38_R).

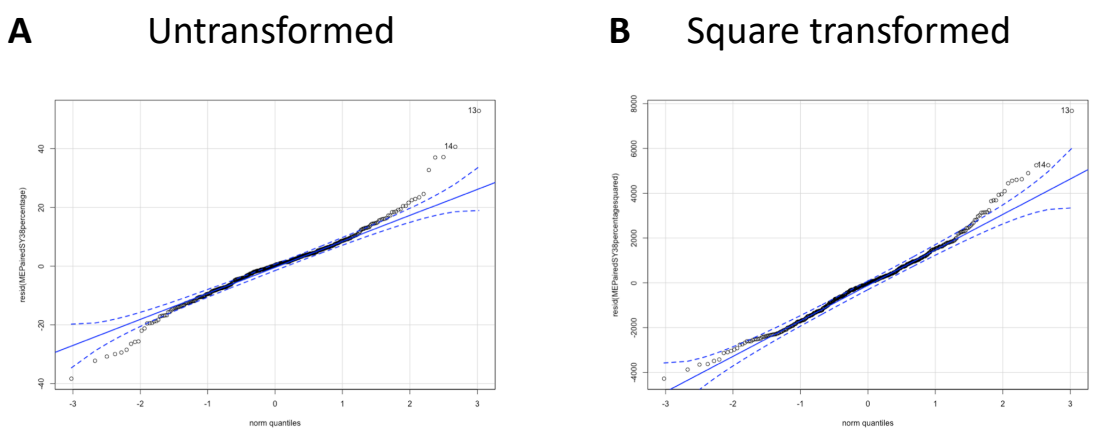

Figure 4. Q-Q plots of the residuals of the linear mixed effects models run on the percentage of paired SY38 at different distances from the plaque core. (A) The residuals of the mixed model using the untransformed data. **(B)** The residuals of the mixed model using the square transformed data. Square transforming the data appeared to better fit the assumptions of the model.

2.2.6.4 Quantification and Statistical Analysis of Colocalisation of Paired Synapses with Aβ

The python tool was used to isolate paired pre and/or post-synaptic puncta where 50% or more of the puncta overlapped with the OC stain for Aβ. The MATLAB script was then used to quantify the isolated puncta in 2µm concentric rings around the plaque core. The amount of paired synaptic puncta which colocalize with OC is expressed as a percentage of paired synaptic puncta in the ring. The linear mixed effects model below was run. The fixed effects were distance and sex. The random effects accounted for the fact that 2 images were taken from the same mouse and that experiments were done in batches.

Formula:MM<-lmer(Density~Dist+Sex+(1|Mouse:Image_number)+(1|Batch), data=coloc_PSY38_OC or coloc_PSD95_OC)

Anova(MM)

On inspection of the q-q plots of the residuals **(figure 5A, C)**, several transformations of the data were trialed in order to better fit the assumptions of the model. The Log(data+1) transformation appeared to improve the fit of the data to the model in both the SY38 and PSD95 colocalisation datasets **(figure 5B, D)**. Hence, the linear mixed effects models were re-run using the transformed data.

Formula: MM<-logdensityplusone~ Dist + Sex (1 | Mouse_ID:Image_number) + (1|Batch).

The ANOVA results revealed that sex did not impact the model. Hence, sex was removed from the model when investigating the main effect of distance.

Formula: MM<- logdensityplusone~ Dist + (1 | Mouse_ID:Image_number) + (1|Batch).

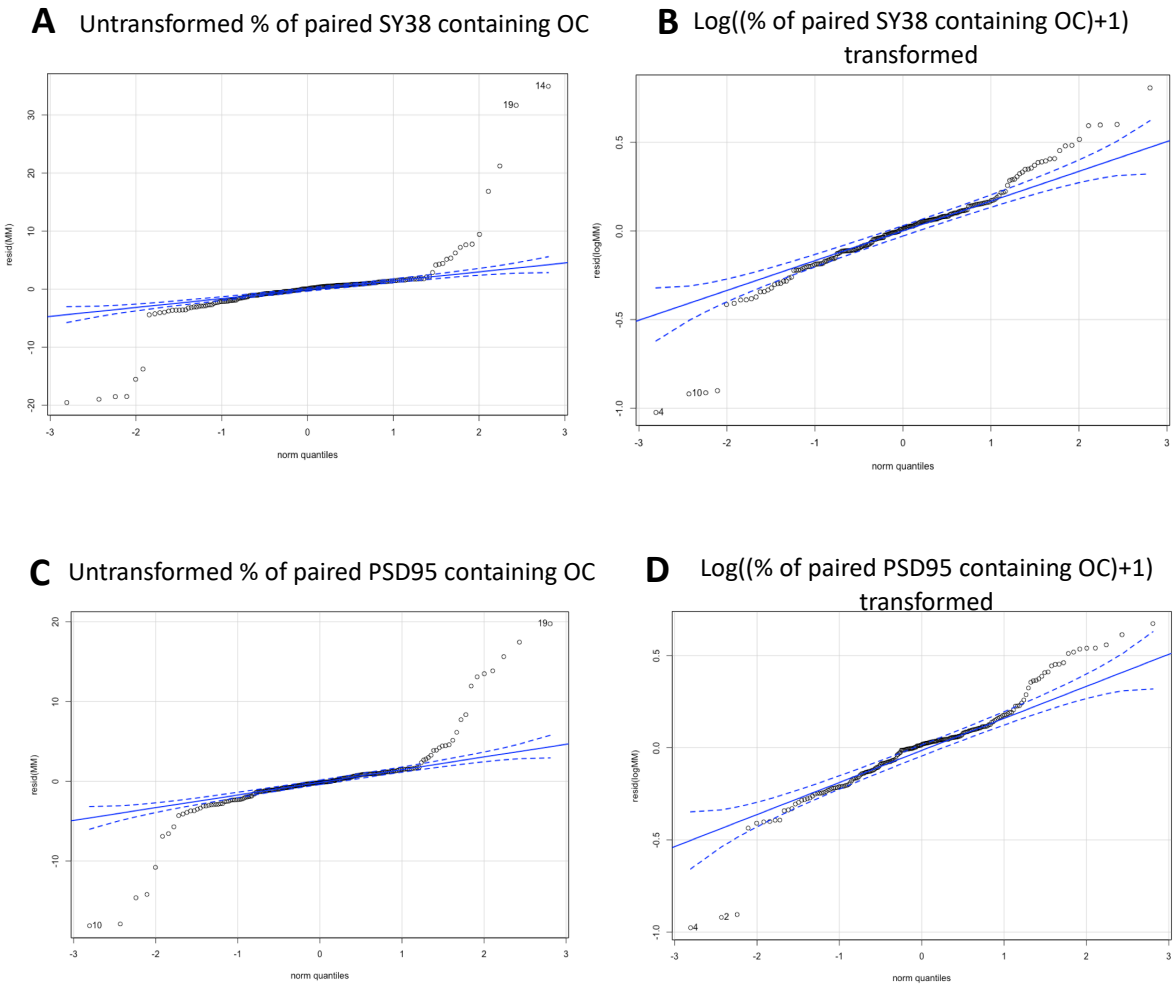

Figure 5. Q-Q plots of the residuals of the linear mixed effects models run on the percentage (%) of paired synaptic puncta which overlap with OC. (A) The residuals of the linear mixed effects model using the untransformed percentage of paired SY38 containing OC data. **(B)** The residuals of the linear mixed effects model using the log ((percentage of paired SY38 containing OC)+1) data. **(C)** The residuals of the linear mixed effects model using the untransformed percentage of paired PSD95 containing OC data. **(D)** The residuals of the linear mixed effects model using the log ((percentage of paired PSD95 containing OC)+1) data.

2.2.6.5 Visualization of Images

ImageJ and Imaris 3D viewer were used to prepare representative images.

2.2.7 Immunohistochemical Staining of Plaque Load and Astrogliosis.

Helen Stirling, an undergraduate student I supervised in the Spires-Jones lab conducted the immunohistochemistry experiments and aspects of the analysis. Fixed hemispheres were coronally sectioned using a sliding microtome (Leica SM 2010R) at 50µm and stored at -20^{o}C until required. From each mouse, 3 sections were chosen at approximately -1mm, -2mm and -3mm from Bregma **(figure 6)** to sample throughout the cortex and hippocampus. In this study, Thioflavin-S (ThioS) and GFAP **(table 2)** were used to measure Aβ plaque and reactive astrocyte burden respectively.

Free floating sections were pre-treated with citrate buffer (95^{o}C for 20 minutes) to retrieve antigens. Subsequently sections were permeabilised with 0.5% Triton X-100 at room temperature for 20 minutes. Sections were blocked with 5% normal donkey serum (NDS) for 1 hour and the anti-GFAP primary antibody **(table 2)** was applied in 1% NDS (4^{o}C overnight). The donkey anti-rabbit AlexaFluor 647 secondary antibody **(table 2)** was applied in 1% NDS at room temperature for 1.5 hours. Sections were counter-stained with 0.001 mg/mL DAPI in order to stain nuclei. Sections were mounted on polysine adhesion slides and stained with 0.05% ThioS in 50% ethanol then differentiated in 80% ethanol before being coverslipped with Immu-Mount (Thermo Scientific). All washes were performed with TBS.

A negative control omitting the primary anti-GFAP antibody and a positive control from an APP/PS1 mouse with known extensive plaque pathology and GFAP positive astrocytes were included to validate the experimental procedure.

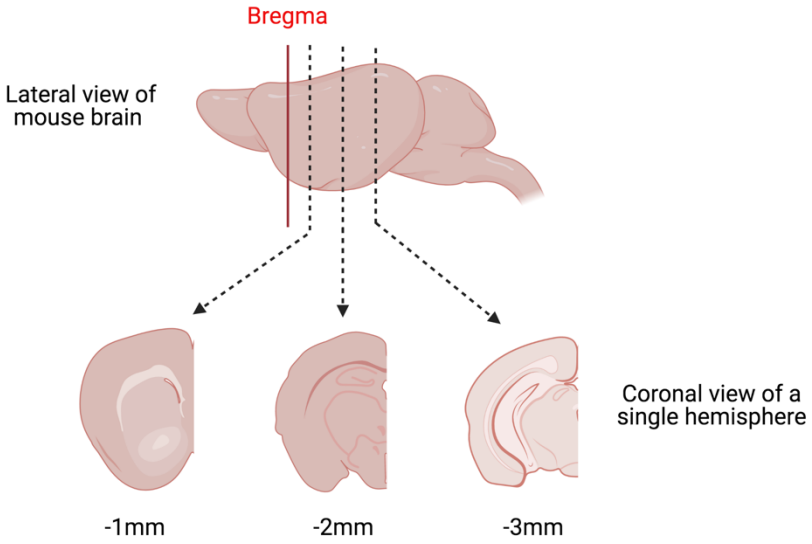

Figure 6. Schematic illustrating approximate position of Bregma, and the 3 coronal sections used from each mouse for immunohistochemical study of plaque and GFAP load. Image made using Biorender.com.

2.2.8 Imaging of Plaque Load and Astrogliosis.

Images were obtained with a ZEISS Axio Scan.Z1 slide-scanner using a 20x objective lens. Slides were imaged at 465nm, 517nm and 668nm to capture the DAPI, ThioS and GFAP signals respectively. A single focus layer without Z stacking was applied with 6 coarse and 6 fine focal points set across the tissue. Exposure times for each channel were set automatically and remained constant for all images taken on that day. Images were manually inspected for focusing problems and re-imaged accordingly.

2.2.9 Analysis of Plaque Load

Regions of interest (ROIs) were defined by outlining cortical boundaries in all three sections and hippocampal boundaries in sections approximately -2mm and -3mm from Bregma in ImageJ using the Allen Mouse Brain Atlas as a guide (Atlas.brain- map.org). The ThioS channel was thresholded using the MaxEntropy algorithm in ImageJ. The ImageJ analyse particles function was used to calculate the percentage area of the ROI occupied by ThioS staining.

The mixed model below was used to investigate the impact of genotype, region and sex on the percent area covered by ThioS stain. The fixed effects were genotype, region and sex. The random effect accounted for the fact that multiple images were taken from the same mouse. Data on experimental batch was not collected.

ThioS_MM<-lmer(ThioS~Genotype*Region+Sex+(1|Mouse:Image_number), data=ThioS_data_MH)

Anova(ThioS_MM)

On inspection of the q-q plot of the residuals **(figure 7)**, several transformations of the data were trialed in order to better fit the assumptions of the model. The cube root transformation appeared to improve the fit of the data to the model. A type III ANOVA revealed no effect of sex and an interaction of genotype and region.

Formula: transformed_ThioS_MM<-
lmer(cuberootthios~Genotype*Region+Sex+(1|Mouse:Image_number), data=ThioS_data_MH)

Anova(transformed_ThioS_MM)

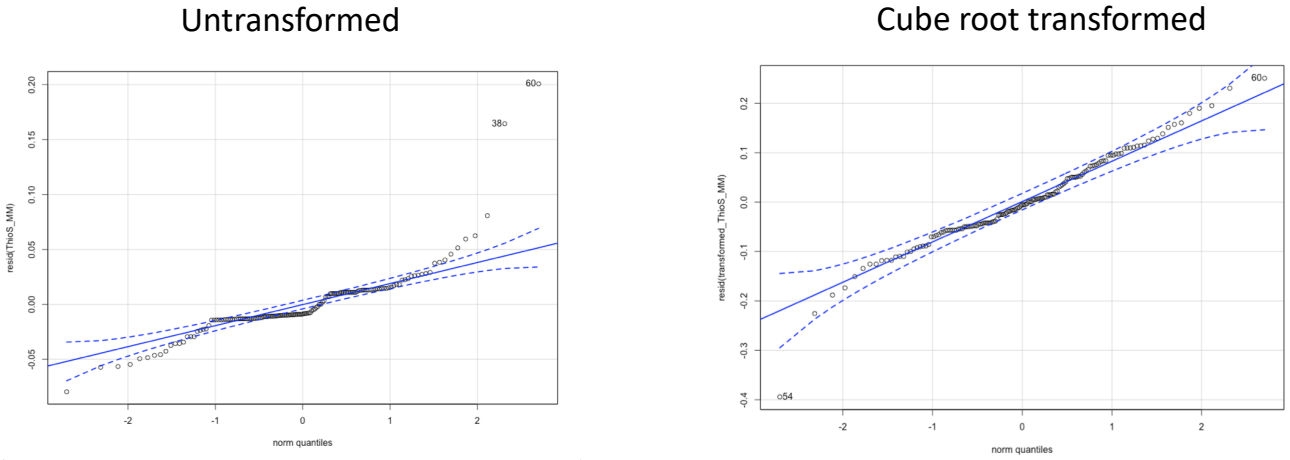

Figure 7. Q-Q plots of the residuals of the mixed models run on the ThioS data (A) The residuals of the mixed model using the untransformed ThioS data. **(B)** The residuals of the mixed model using the cube root transformed ThioS data. Cube root transformation appeared to improve the fit of the data to the model assumptions.

A post-hoc Tukey corrected pairwise comparison of the main effects of genotype and region was performed. The effects deemed to have biological relevance are shown. Differences found between WT/HET values in the cortex and hippocampus were removed since these values were thought to be noise as no plaques were present in these mice.

Formula: emmeans(transformed_ThioS_MM, list(pairwise ~ Genotype*Region), adjust = "tukey")

2.2.10 Analysis of Astrogliosis

7 crops containing ThioS positive plaques and the surrounding neuropil per APP^{NLF} HOM mouse cortex, and 7 crops per WT cortex were isolated. This enabled more accurate manual thresholding of the GFAP channel. ROIs were manually drawn around the boundary of the ThioS stain, marking the boundary of the core of the plaque. The percentage area covered by GFAP stain was measured in 20µm concentric circles around the ThioS positive plaque core, up to 200µm using a macro made in ImageJ. The linear mixed effects model below was run to investigate the impact of distance from plaque core on GFAP burden. The fixed effects were distance and sex. The random effect accounted for the fact that multiple image crops were taken from the same mouse.

```
MEGFAPrings<-lmer(GFAP~Dist+Sex+(1|Mouse_ID:plaque_number),
data=GFAP_in_concentric_rings_)

Anova(MEGFAPrings)
```

On inspection of the q-q plot of the residuals **(figure 8)**, several transformations of the data were trialed in order to better fit the model assumptions. The cube root transformation appeared to improve the fit of the data to the model assumptions. Whilst not all the residuals in the q-q plot lay within the 95% error lines, most of the residuals did. Hence, the mixed model was re-run on the transformed data. A type III ANOVA revealed that sex did not impact the model, so sex was removed when interrogating the main effect of distance.

Formula: transformedMEGFAPrings<-lmer(cube_root~Dist+(1|Mouse_ID:plaque_number), data=GFAP_in_concentric_rings_)

GFAP burden at each distance was compared to the furthest distance from the plaque (200µm).

Untransformed

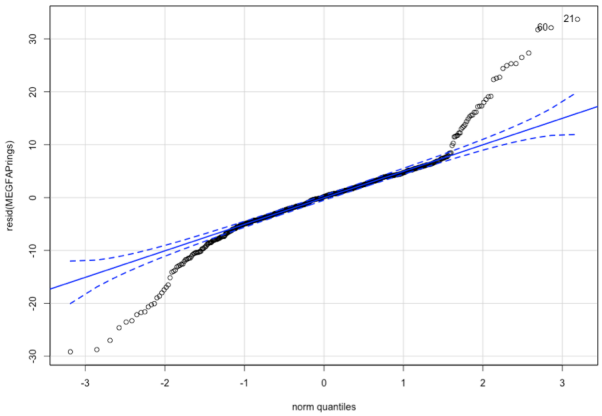

Cube root transformed

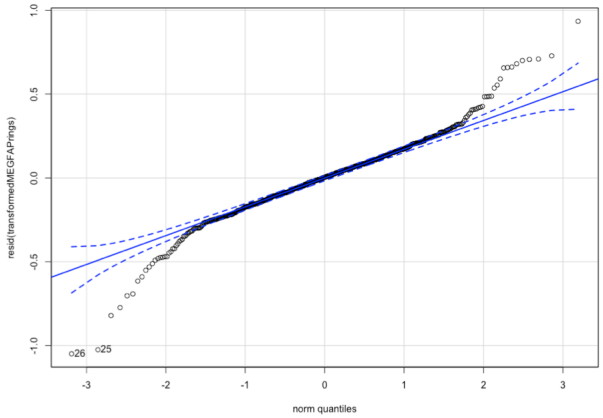

Figure 8. Q-Q plots of the residuals of the linear mixed effects models run on the GFAP burden (percentage area) in concentric rings around plaque data (A) The residuals of the linear mixed effects model using the untransformed GFAP data. **(B)** The residuals of the linear mixed effects model using the cube root transformed GFAP data. Cube root transformation appeared to improve the fit of the data to the model assumptions.

The linear mixed effects model below was used to compare the GFAP burden over the whole crop in APP^{NLF} HOM cortex crops (which contained plaques), with crops taken from WT cortices. The fixed effects were distance and sex. The random effects accounted for the fact that multiple image crops were taken from the same mouse.

Formula: MM<-lmer(GFAP~Genotype+Sex+(1|Mouse_ID), data=GFAP_over_whole_image_R)

anova(MM)

On inspection of the q-q plot of the residuals **(figure 9)**, several transformations of the data were trialed in order to better fit model assumptions. The cube root transformation appeared to improve the fit of the data to the model assumptions.

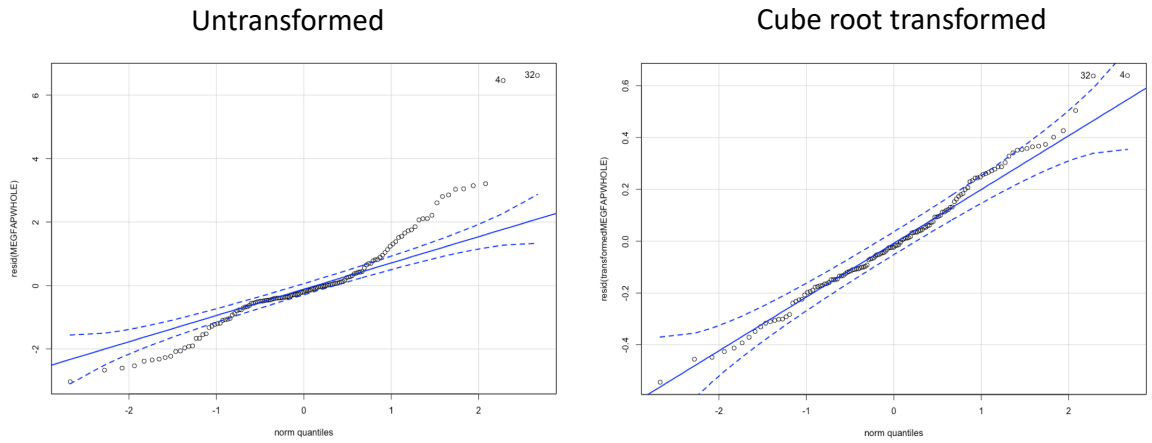

Figure 9. Q-Q plots of the residuals of the linear mixed effects models run on the GFAP burden (percentage area) over the whole image crop data (A) The residuals of the linear mixed effects model using the untransformed GFAP data. **(B)** The residuals of the linear mixed effects model using the cube root transformed GFAP data. Cube root transformation appeared to improve the fit of the data to the model assumptions.

2.3 Bulk RNA-Sequencing of Astrocytes in AD models

2.3.1 Animals

TRAP mice **(see section 2.1.4)** were cross-bred with HET APP/PS1 mice **(see section 2.1.2)** and HOM APP^{NLF} mice **(see section 2.1.1)** to form mice which were HET/HET for the TRAP and APP/PS1 genes and HET/HOM for the TRAP and APP^{NLF} genes. Mice which were HET for the TRAP gene and WT for APP and PSEN1 genes were bred as controls. Genotypes were determined using real time PCR with specific probes (Transnetyx, Memphis, Tennessee). Mice were aged to 6,12 and 18 months for experimentation.

The creators of the TRAP mice investigated gene expression in specific cell types using the TRAP methodology followed by microarray analysis. They detected 2 fold enrichment in gene expression in the purified cells vs the entire sample using 3-6 mice (Doyle et al. 2008). We intended to use TRAP followed by RNA-seq. The dynamic range of array technology is limited by background at low expression and signal saturation at high expression and was estimated

to be ~10^3. Whereas, RNA-seq has a wider dynamic range (>10^5), with low background signal and discrete digital read count enabling highly expressed genes to be accurately counted (Wang et al. 2009). Hence, we decided n=3-6 mice per genotype per time point would allow us to detect alterations in astrocyte gene expression.

2.3.2 Translating Ribosome Affinity Purification (TRAP)

Isolation of astrocyte specific translating mRNA was carried out as previously described (Heiman et al. 2014). Briefly, 6, 12 or 18-month amyloidopathy and WT mice were subject to isoflurane followed by decapitation. Carbon dioxide (CO_2) was not used in order to avoid confounding effects on gene expression. Neocortices were dissected and lysed in ice-cold lysis buffer (20mM 4-(2-hydroxyethyl)-1-piperazineethanesulfonic acid (HEPES), 10mM magnesium chloride ($MgCl_2$), 150mM potassium chloride (KCl), 0.5mM dithiothreitol (DTT), 100 µg/mL cycloheximide, cOmplete ULTRA protease inhibitors and RNAse inhibitors Superasin (Life Technologies,Carlsbad, California) and RNAsin (Promega, Madison, Wisconsin). Cell lysates were centrifuged to clear debris and solubilised with 1% NP40 and 30mM 1,2-diheptanoyl-*sn*-glycero-3-phosphocholine (DHPC) (Avanti Polar Lipids, Alabaster, Alabama). Samples were further centrifuged, 50µl of the supernatants were taken as the input samples which represent the total RNA. The remainder of the supernatants were incubated with pre-prepared anti-GFP beads. Antibodies 19C8 and 19F7 (Sloan Kettering Memorial Centre, New York City, New York) coated Dynabeads MyOne Streptavadin T1 magnetic beads (Life Technologies). Samples were kept at 4^oC with continuous rotation overnight. Beads were washed 4 times with wash buffer (20mM HEPES, 5mM $MgCl_2$, 350mM KCl, 1% NP40, 0.5mM DTT and 100 µg/mL cycloheximide). Cell-type specific mRNAs attached to immunoprecipitated GFP-tagged ribosomes were isolated and purified using the Agilent technologies Nanoprep kit, as per the manufacturer's instructions. Briefly, samples were lysed in 100 µL of lysis buffer with β-mercaptoethanol. 80% sulfolane was mixed in equal volume with the sample and filtered with silica-based fibre filter columns. DNAse treatment was carried out for 15 minutes, columns were washed and dried, and RNA eluted in 20 µL of pre-warmed RNase free water.

2.3.3 Reverse Transcription Polymerase Chain Reaction (RT-PCR)

Complimentary deoxyribose nucleic acid (cDNA) was generated using the SuperScript Vilo cDNA Synthesis Kit (Thermofisher, Waltham, Massachusetts). 2µl of RNA was added to an enzyme and buffer mixture as per the manufacturer's instructions. RT-PCR was carried out with the following programme: 10 minutes at 25°C, 30 minutes at 55°C and 5 minutes at 85°C.

2.3.4 Quantitative Polymerase Chain Reaction (qPCR)

Primers were designed for cell type specific genes and a gene translated on mitochondrial ribosomes **(table 3)**. Genes were counted as cell type specific if they demonstrated >10-fold higher expression in a particular cell type vs other cell types as determined using https://www.brainrnaseq.org/ (Zhang et al. 2014). FastStart Universal SYBR Green qPCR Master Rox reagent (Roche, Basel, Switzerland), along with 6 ng of cDNA, the forward and reverse primers were used for each reaction. qPCR reactions were carried out in duplicate, along with no template controls and no RT controls where appropriate. qPCRs were performed on a Mx3000P qPCR machine (Agilent Technologies, Santa Clara) using the following cycling programme: 10 minutes at 95°C; 40 cycles of: 30 s at 95°C, 40 s at 60°C, 1 minute at 72°C; ending with the dissociation curve: 1 minute at 95°C and 30 s at 55°C with a ramp up to 30s at 95°C. All data was normalised to house-keeping gene controls (ribosomal protein L13a (*Rpl13a*)).

Gene	Forward	Reverse
Rpl13a	GATGAATACCAACCCCTCC	CGAACAACCTTGAGAGCAG
Cx3cr1	CTGGTGGTCTTTGCCTTC	GCACTTCCTATACAGGTGTCC
Eno2	GCCATCTCCTGTAACTCTCC	ATTCTGTAAAGTTCCGAGCTTC
Mbp	CCAGTCTAATAATGTCCATCGAC	CAGATTAACAAGATGCAGTATTGG
Aldh1l1	GCCCTGAGTAATGTGAAGAAG	ACTGGTCATGGATGGAGTC
Mt-rnr2	CGAGCTTGGTGATAGCTCGT	GAGCTGTCCCTCTTTTGGCT

Table 3. Primer sequences of cell type specific genes and mitochondrial ribosome translated gene. Ribosomal Protein L13a (*Rpl13a*), CX3C Chemokine Receptor 1 (*Cx3cr1*), Enolase 2 (*Eno2*), Myelin Basic Protein (*Mbp*), Aldehyde Dehydrogenase 1 Family Member L1 (*Aldh1l1*), Mitochondrially Encoded 16S RNA (*Mt-rnr2*).

2.3.5 Analysis of RNA Integrity

The Agilent RNA 6000 Pico Kit was used to check the concentration and integrity of the RNA (RIN) (**table 4**), according to manufacturer's protocol. Briefly, aliquots of the RNA were heat denatured at 70°C for 2 minutes and returned to ice. Gel/dye mix was loaded onto pico microfluidic chips along with a ladder and the RNA samples. The reaction was run on the Agilent Bioanalyzer. We were aiming for RINs above 7. However, the samples with RINs below 7 did not appear abnormal when assessing the sequencing and so were kept in the analysis.

Age (months)	Genotype	Sex	TRAP/INPUT	Sample_ID	Concentration (ng/ul)	RIN
6	ASRIBO HET APPNLF HOM	m	TRAP	TAN2-144	9	7.4
6	ASRIBO HET APPNLF HOM	m	TRAP	TAN2-110	12	8.2
6	ASRIBO HET APPNLF HOM	f	TRAP	TAN2-79	5	7.2
6	ASRIBO HET APPNLF HOM	f	TRAP	TAN2-80	6	7.7
6	ASRIBO HET APPNLF WT	m	TRAP	TAN2-54	3	7
6	ASRIBO HET APPNLF WT	m	TRAP	TAN2-121	5	7.6
6	ASRIBO HET APPNLF WT	f	TRAP	TAN2-22	7	8
6	ASRIBO HET APPNLF WT	f	TRAP	TAN2-59	6	6.6
6	ASRIBO HET APPNLF HOM	m	INPUT	iAN2-144	6	7.6
6	ASRIBO HET APPNLF HOM	m	INPUT	iAN2-110	6	8.4
6	ASRIBO HET APPNLF HOM	f	INPUT	iAN2-79	4	8.1
6	ASRIBO HET APPNLF HOM	f	INPUT	iAN2-80	5	7.5
6	ASRIBO HET APPNLF WT	m	INPUT	iAN2-54	6	7.8
6	ASRIBO HET APPNLF WT	m	INPUT	iAN2-121	5	7.5
6	ASRIBO HET APPNLF WT	f	INPUT	iAN2-22	4	8.4
6	ASRIBO HET APPNLF WT	f	INPUT	iAN2-59	6	7
6	ASRIBO HET APP/PS1 HET	m	TRAP	TAAP-66	10	7.9
6	ASRIBO HET APP/PS1 HET	m	TRAP	TAAP-27	12	8.1
6	ASRIBO HET APP/PS1 HET	f	TRAP	TAAP-48	5	7.8
6	ASRIBO HET APP/PS1 HET	f	TRAP	TAAP-52	6	7.7
6	ASRIBO HET APP/PS1 WT	m	TRAP	TAAP-26	8	8.1
6	ASRIBO HET APP/PS1 WT	m	TRAP	TAAP-39	2	7.9
6	ASRIBO HET APP/PS1 WT	f	TRAP	TAAP-36	11	7.9
6	ASRIBO HET APP/PS1 WT	f	TRAP	TAAP-37	7	7.7
6	ASRIBO HET APP/PS1 HET	m	INPUT	iAAP-66	11	7.9
6	ASRIBO HET APP/PS1 HET	m	INPUT	iAAP-27	13	8.1
6	ASRIBO HET APP/PS1 HET	f	INPUT	iAAP-48	6	7.9
6	ASRIBO HET APP/PS1 HET	f	INPUT	iAAP-52	5	7.1
6	ASRIBO HET APP/PS1 WT	m	INPUT	iAAP-26	7	8.2
6	ASRIBO HET APP/PS1 WT	m	INPUT	iAAP-39	3	7.7
6	ASRIBO HET APP/PS1 WT	f	INPUT	iAAP-36	9	7.9
6	ASRIBO HET APP/PS1 WT	f	INPUT	iAAP-37	9	7.8

Age (months)	Genotype	Sex	TRAP/INPUT	Sample_ID	Concentration (ng/ul)	RIN
12	ASRIBO HET APPNLF HOM	m	TRAP	TAN2-7	23	8.4
12	ASRIBO HET APPNLF HOM	m	TRAP	TAN2-26	7	5.8
12	ASRIBO HET APPNLF HOM	f	TRAP	TAN2-10	10	8.7
12	ASRIBO HET APPNLF HOM	f	TRAP	TAN2-12	25	8
12	ASRIBO HET APPNLF WT	m	TRAP	TAN2-46	8	6
12	ASRIBO HET APPNLF WT	m	TRAP	TAN2-48	11	6.2
12	ASRIBO HET APPNLF WT	f	TRAP	TAN2-16	19	4.5
12	ASRIBO HET APPNLF WT	f	TRAP	TAN2-17	15	4.9
12	ASRIBO HET APPNLF WT	f	TRAP	TAN2-156	16	5.7
12	ASRIBO HET APPNLF WT	f	TRAP	TAN2-157	5	7.3
12	ASRIBO HET APPNLF HOM	m	INPUT	iAN2-7	19	7.5
12	ASRIBO HET APPNLF HOM	m	INPUT	iAN2-26	10	5.6
12	ASRIBO HET APPNLF HOM	f	INPUT	iAN2-10	10	7.9
12	ASRIBO HET APPNLF HOM	f	INPUT	iAN2-12	8	7.5
12	ASRIBO HET APPNLF WT	m	INPUT	iAN2-46	9	6.2
12	ASRIBO HET APPNLF WT	m	INPUT	iAN2-48	7	6.6
12	ASRIBO HET APPNLF WT	f	INPUT	iAN2-16	14	5.1
12	ASRIBO HET APPNLF WT	f	INPUT	iAN2-17	8	4.8
12	ASRIBO HET APPNLF WT	f	INPUT	iAN2-156	10	7
12	ASRIBO HET APPNLF WT	f	INPUT	iAN2-157	8	7
12	ASRIBO HET APP/PS1 HET	m	TRAP	TAAP-2	6	7.3
12	ASRIBO HET APP/PS1 HET	m	TRAP	TAAP-5	15	6.6
12	ASRIBO HET APP/PS1 HET	f	TRAP	TAAP-24	17	5.1
12	ASRIBO HET APP/PS1 HET	f	TRAP	TAAP-29	13	5.5
12	ASRIBO HET APP/PS1 WT	m	TRAP	TAAP-1	1	7.9
12	ASRIBO HET APP/PS1 WT	m	TRAP	TAAP-3	16	7.9
12	ASRIBO HET APP/PS1 WT	f	TRAP	TAAP-9	11	5
12	ASRIBO HET APP/PS1 WT	f	TRAP	TAAP-43	12	7.3
12	ASRIBO HET APP/PS1 HET	m	INPUT	iAAP-2	6	7
12	ASRIBO HET APP/PS1 HET	m	INPUT	iAAP-5	14	4.6
12	ASRIBO HET APP/PS1 HET	f	INPUT	iAAP-24	11	5.5
12	ASRIBO HET APP/PS1 HET	f	INPUT	iAAP-29	14	5.6
12	ASRIBO HET APP/PS1 WT	m	INPUT	iAAP-1	6	7.1
12	ASRIBO HET APP/PS1 WT	m	INPUT	iAAP-3	9	7.7
12	ASRIBO HET APP/PS1 WT	f	INPUT	iAAP-9	16	4.9
12	ASRIBO HET APP/PS1 WT	f	INPUT	iAAP-43	12	7.1

Age (months)	Genotype	Sex	TRAP/INPUT	Sample_ID	Concentration (ng/ul)	RIN
18	ASRIBO HET APPNLF HOM	m	TRAP	TAN2-71	13	5.1
18	ASRIBO HET APPNLF HOM	m	TRAP	TAN2-74	7	7.5
18	ASRIBO HET APPNLF HOM	f	TRAP	TAN2-78	3	9.7
18	ASRIBO HET APPNLF HOM	f	TRAP	TAN2-97	7	8.9
18	ASRIBO HET APPNLF WT	m	TRAP	TAN2-53	6	5.8
18	ASRIBO HET APPNLF WT	f	TRAP	TAN2-52	7	7.9
18	ASRIBO HET APPNLF WT	f	TRAP	TAN2-18	8	8.3
18	ASRIBO HET APPNLF HOM	m	INPUT	iAN2-71	5	8
18	ASRIBO HET APPNLF HOM	m	INPUT	iAN2-74	4	7.8
18	ASRIBO HET APPNLF HOM	f	INPUT	iAN2-78	2	8.4
18	ASRIBO HET APPNLF HOM	f	INPUT	iAN2-97	4	8.2
18	ASRIBO HET APPNLF WT	m	INPUT	iAN2-53	4	7.7
18	ASRIBO HET APPNLF WT	f	INPUT	iAN2-52	4	7.7
18	ASRIBO HET APPNLF WT	f	INPUT	iAN2-18	4	7.8
18	ASRIBO HET APP/PS1 HET	m	TRAP	TAAP-7	9	8.9
18	ASRIBO HET APP/PS1 HET	f	TRAP	TAAP-42	9	7.7
18	ASRIBO HET APP/PS1 HET	f	TRAP	TAAP-53	11	7.7
18	ASRIBO HET APP/PS1 WT	m	TRAP	TAAP-4	2	9.4
18	ASRIBO HET APP/PS1 WT	m	TRAP	TAAP-12	6	9.1
18	ASRIBO HET APP/PS1 WT	f	TRAP	TAAP-16	6	9.2
18	ASRIBO HET APP/PS1 WT	f	TRAP	TAAP-31	5	8.2
18	ASRIBO HET APP/PS1 HET	m	INPUT	iAAP-7	7	7.8
18	ASRIBO HET APP/PS1 HET	f	INPUT	iAAP-42	2	7.5
18	ASRIBO HET APP/PS1 HET	f	INPUT	iAAP-53	4	7.7
18	ASRIBO HET APP/PS1 WT	m	INPUT	iAAP-4	3	8.6
18	ASRIBO HET APP/PS1 WT	m	INPUT	iAAP-12	3	8.2
18	ASRIBO HET APP/PS1 WT	f	INPUT	iAAP-16	3	8.2
18	ASRIBO HET APP/PS1 WT	f	INPUT	iAAP-31	3	8.2

Table 4. Checking the concentration and integrity of the RNA being sent for sequencing. An Agilent 2100 Bioanalyser was used to quality check the TRAP and input samples being sent for sequencing.

2.3.6 TRAP-Sequencing and Processing of Data

6-month samples were prepped and sequenced by Edinburgh Genomics. The library was prepped using the SMARTer stranded pico input kit (Takara, Kyoto, Kyoto), and sequencing was performed on the Illumina NovaSeq 6000 platform (Illlumina, San Diego, California). 12 and 18-month samples were prepped and sequenced by Cambridge Genomics using the Clonetech - SMART-Seq v4 Ultra Low input RNA library preparation (Takara), along with sequencing on the Illumina Nextseq 500 platform. All sequencing utilised 75 paired-end reads at approximate sequencing depths of 60 million reads per sample for mixed RNA samples (input) and 30 million reads per sample for TRAP-seq.

Dr Owen Dando and Dr Xin He, postdocs in the Hardingham lab, mapped RNA-seq reads and analysed using Spliced Transcripts Alignment to a Reference (STAR) version 2.5.3a. Subsequently, per-gene read counts were summarised using featureCounts version 1.5.2. For read-mapping and feature counting, genome sequences and gene annotations were downloaded from Ensembl version 94. Differential expression analysis was then performed using DESeq2 (R package version 1.18.1), with a significance threshold calculated at a Benjamini–Hochberg-adjusted P value of <0.05.

2.3.7 TRAP-Sequencing Analysis

An expression cut-off of 1 fragments per kilobase of transcript per million mapped reads (FPKM), and a filter for protein coding genes was applied to all the datasets. The EnrichR platform (Kuleshov et al. 2016) was used to conduct gene ontology (GO) and Kyoto Encyclopedia of Genes and Genomes (KEGG) pathway analysis on selected gene sets. In order to identify potential transcription factors regulating gene expression, the ENCODE and ChEA consensus target genes from Chip-X database was interrogated using EnrichR, along with the TFEA.ChiP platform (https://www.iib.uam.es/TFEA.ChIP/). Ingenuity pathway analysis (IPA) (Qiagen, Hilden, Germany) was also used to identify alterations in expression of pathways. Gene sets altered in these experiments were compared to previously collected/published data as described in chapter 4. Two-sided Fisher's exact tests were used to assess enrichment of gene sets in candidate gene lists.

2.3.7.1 Generation of Expanded Lipopolysaccharide (LPS), Middle Cerebral Artery Occlusion (MCAO) and Pan-reactive Gene Sets

The original sets of A1 (LPS-specific), A2 (MCAO-specific) and pan-reactive gene sets comprised groups of 12-13 genes (Liddelow et al. 2017) and although they were derived from the microarray data previously published (Zamanian et al. 2012), the rationale behind their selection was not stated. To generate larger gene sets, the microarray data from GSE accession number GSE35338 previously published (Zamanian et al. 2012) was analysed in GEO2R and fold change gene expression for the acute-LPS and acute-MCAO sets were calculated. For both stimulation paradigms, fully annotated genes were ranked by fold change (highest fold change ranked highest). For genes featuring within the top 250 for either stimuli and for which there were multiple probe sets, the average fold-change for the probe sets was

taken as the final value. To generate LPS and MCAO gene sets, we required the gene be ranked in the top 100 genes for one stimulation paradigm, and ranked at least 50 places lower for the other stimulation paradigm. Using this approach 70 genes were obtained both for the LPS and MCAO sets. To generate pan-reactive gene sets we wanted robustly induced genes that were of similar ranking across both stimulation paradigms, so we required that genes be in the top 250 ranked genes, and no more than 50 ranking positions between the two stimulation paradigms. This yielded a pan-reactive set of 42 genes. Of the 37 'A1' (LPS), 'A2' (MCAO) and pan-reactive genes previously employed (Liddelow et al. 2017), 8 were found in different categories using our method. For example, we classed one previously stated A1/LPS gene (*Gbp* - guanylate-binding protein) as a pan-reactive gene since it was ranked 8th in the LPS stimulation and 26th in the MCAO stimulation. Conversely, the gene *Serpina3n* (Serine Protease Inhibitor A3n) was previously classed as a pan-reactive gene, but we classed it as an A1 gene since it was ranked 6th in the LPS stimulation and 61st in the MCAO stimulation. Of note, when interrogating TRAP-seq data with these gene sets, only genes within these sets expressed >1 FPKM across all conditions were included in the analysis.

2.4 Single Cell RNA Sequencing of Astrocytes in AD models

2.4.1 Animals

Mice which were HET/HET and HET/WT for the TRAP and APP/PS1 genes were grown to 12 and 18-months. Mice which were HET/HOM for the TRAP and APP^{NLF} genes respectively were grown to 18-months. Keren-Shaul et al. (2017) had previously conducted a single-cell RNA sequencing experiment where they identified a disease associated population of microglia in a transgenic mouse model of AD using n=3 mice per genotype (Keren-Shaul et al. 2017). Hence, in this study 3-4 mice per genotype per age were used.

2.4.2 Gentle Dissociation of Tissue

Mice were anesthetised using isoflurane and decapitated. CO_2 was not used in order to avoid confounding effects on gene expression. The neocortices were dissected and placed in ice cold Dulbecco's phosphate-buffered saline (DPBS) (ThermoFisher). Tissue was enzymatically and mechanically dissociated using the Adult Brain Tissue Dissociation Kit, as per the

manufacturer's instructions (Miltenyi Biotec, Bergisch Gladbach, Germany). Briefly, tissue was combined with the enzyme cocktails. The gentleMACS Octo Dissociator with Heaters (Miltenyi Biotec) was used to mechanically dissociate the tissue at 37°C for 30 minutes (program 37C_ABDK_01). The digested tissue was filtered (70 µm) with DPBS. Myelin and cell debris were removed using the Debris Removal Solution and centrifugation steps. Erythrocytes were removed using the Red Blood Cell Removal Solution and centrifugation steps. Cells were transported to the FACS facility in PBS containing 0.5% bovine serum albumin.

2.4.3 Fluorescence Activated Cell Sorting (FACS) of Astrocytes

FACS of astrocytes was carried out by the University of Edinburgh FACS facility on a BD Aria II. In collaboration with Lizzie Freyer, the facility manger, gates were set up to gate out debris and dead cells, along with clumps and auto fluorescent cells. GFP positive cells were collected.

2.4.4 10x Genomics Single Cell Sequencing

Lizzie Freyer conducted the 10x Genomics sample preparation using the 10x Genomics Single Cell 3' Reagent kits V3 (10x Genomics, Pleasanton, California) according to the manufacturer's instructions. Briefly, gel bead emulsions (GEMs) were generated by combining unique molecular identifier (UMI)-barcoded gel beads, cells, and partitioning oil onto a chromium chip. To achieve single cell resolution, cells were delivered at a limiting dilution, such that the majority (~90-99%) of generated GEMs contain no cell, while the remainder largely contain a single cell. The gel bead is subsequently dissolved, primers are released, along with a master mix containing RT reagents. Incubation of the GEMs produces barcoded cDNA from poly-adenylated mRNA. GEMs are then broken and pooled fractions are recovered. Silane magnetic beads are used to purify the first-strand cDNA from the post GEM-RT reaction mixture, which includes leftover biochemical reagents and primers. Barcoded, full-length cDNA is amplified via PCR to generate sufficient mass for library construction. The integrity and concentration of the DNA was checked using the Agilent High Sensitivity Kit and Bioanalyzer. Richard Clark at the Edinburgh Clinical Research Facility conducted the sequencing, which was performed on the NextSeq 550 (Illumina). Approximately 50,000 reads per cell we carried out.

2.4.5 Single Cell Sequencing Data Processing and Analysis

Processing of the single cell sequencing data was conducted by Dr. Katie Emelianova, a postdoc in the Hardingham lab, except for the section on defining the population of cells which were likely astrocytes, which I performed. I also performed the preliminary analysis of the single cell data presented in this thesis.

2.4.5.1 Cell calling

Cell Ranger, a set of 10x Genomics pipelines to process 10x Genomics single cell data, was used to demultiplex raw base call files to produce forward, reverse and index FASTQ files. Reads were aligned to a 10x formatted reference genome using STAR, a splice aware aligner. Reads which align to an exonic position on the correct strand uniquely were considered for downstream UMI counting. Reads were grouped by cell barcode, UMI and gene annotation, and after a process of error correction to resolve sequencing errors and barcode collisions, each cell barcode, UMI and gene annotation combination was recorded as a UMI count. The UMI counts were used to predict which cells were empty or ambient RNA containing cells, which were excluded from further analysis. Cells with expression profiles that strongly deviated from the background were deemed cell containing droplets that were used in downstream analysis.

2.4.5.2 Normalisation

Total UMI counts for each cell were normalised towards the median of UMI counts for all cells. The count matrices were log-transformed, mean centred and scaled. These normalised counts were used for clustering and uniform manifold approximation and projection (UMAP) dimensionality reduction. For differential expression, for larger count sizes, an asymptotic beta test was used to test for differential expression. This is based on the exactTest from edgeR. This equalizes library sizes prior to running the test for differential expression, thereby internally normalizing for library size (in this case each cell is a library).

2.4.5.3 Dimensionality reduction

Principle component analysis (PCA) was run on the normalised and filtered feature-barcode matrices, computing the top 10 dimensions by default. Using this reduced representation of the matrices, UMAP was used to visualise the data in 2D space.

2.4.5.4 Defining the Astrocyte Populations in the Single Cell RNA-Seq

Using the UMAP representation of all cells sorted and sequenced, groups of cells were manually segmented based on position in UMAP space. Gene sets which were significantly enriched in each cluster of cells were imported into the cell type specific expression analysis tool produced by the Dougherty lab http://genetics.wustl.edu/jdlab/csea-tool-2/ (Dougherty et al. 2010), in order to identify which populations of cells were likely astrocytes.

2.4.5.5 Clustering

Following selection of astrocyte populations, clustering was performed on the UMAP reduced points in PCA space. K-means clustering was performed, which generated K centroids and assigned each cell a cluster membership based on the nearest centroid. A clustering quality metric called the Davies-Bouldin Index was used to estimate the initial value of K.

2.4.5.6 Ingenuity Pathway Analysis (IPA)

Genes which were significantly enriched or de-enriched in each cluster relative to other clusters were imported into IPA. Pathways upregulated or downregulated in each cluster relative to other clusters were visualised using heatmaps.

2.4.5.7 Visualisation of Featured Genes

The 10x Genomics Loupe browser was used to visualise expression of featured genes.

Chapter 3

Characterising Synapse Pathology and Astrogliosis in APP^{NLF} Mice

3.1 Chapter Introduction

Saito et al. generated the knock-in APP^{NLF} mouse in order to combat the fact that studies of Alzheimer's disease pathology had largely relied upon transgenic mice which overexpress APP (Saito et al. 2014). Initial characterization of the APP^{NLF} model demonstrated plaque deposition beginning at 6-months of age, increased microgliosis and astrogliosis compared to WT mice, a qualitative reduction in pre-synaptic protein synaptophysin and PSD95 around plaques, and memory impairment in the y maze at 18-months. Quantitative examination of synapse pathology and astrogliosis in relation to plaque distance was not carried out.

At the beginning of this chapter I investigate synapse pathology in 12-month APP^{NLF} mice in a quantitative manner. Synapse pathology is the strongest correlate of cognitive decline and therefore is a central pathology in AD (Terry et al. 1991). Plaque- associated synapse loss and synaptic accumulation of oligomeric Aβ also occur in AD and are accurately modelled by many of the overexpressing transgenic FAD mouse models (Koffie et al. 2012; Koffie et al. 2009; Pickett et al. 2016; Spires et al. 2005). Quantifying pathology not only identifies how well the mouse model recapitulates aspects of human AD, but also allows other molecular, cellular and behavioural studies of the APP^{NLF} mouse to be put in the context of pathology.

3.1.1 Imaging the Synapse Using Array Tomography

Typically, a confocal microscope achieves a resolution of approximately 800nm in the z-direction and approximately 250nm in the x-y direction (Pawley 1995). This z resolution is inadequate to accurately quantify synaptic bouton density, since synaptic boutons have a diameter of approximately 400nm (Ballesteros-Yáñez et al. 2006). Additionally, the z resolution of a confocal microscope limits the ability to identify whether proteins such as Aβ are inside the pre/post-synaptic terminals or simply near them. In order to overcome this, Micheva and Smith developed the high-resolution imaging technique array tomography, which has since been adapted for use in mouse models of AD and human post-mortem tissue (Micheva and Smith 2007; Micheva et al. 2010; Kay et al. 2013).

The process of array tomography **(figure 10)** involves embedding tissue into an acrylic resin and physically sectioning the tissue into ribbons of 70nm thick serial sections. These ribbons

are stained with antibodies and each section is imaged using a fluorescent light microscope. The images are processed and a 3D reconstruction of the tissue is formed, giving a resolution 250nm in the x-y direction and 70nm in z direction. This allows for synaptic density and colocalization of synaptic puncta with Aβ to be conducted with greater confidence than standard confocal microscopy. There are several studies published using this technique to quantify synaptic proteins in mouse (Pickett et al. 2019; Koffie et al. 2009) and human (Henstridge et al. 2015; Kay et al. 2013; Colom-Cadena et al. 2017; Jackson et al. 2019).

Due to limitations on time, I decided to only investigate synaptic density and colocalization of Aβ in synaptic terminals in 12-month APP^{NLF} mice, since this was the middle time point for the TRAP-sequencing experiments described in chapter 4. I used the somatosensory cortex since Saito et al. had demonstrated cortical plaque deposition at 12 -months in APP^{NLF} HOM mice (Saito et al. 2014) and because Koffie et al. had previously used array tomography to investigate synapse loss around plaques in the somatosensory cortex of APP/PS1 mice (Koffie et al. 2009), the other amyloidopathy model I used in chapters 4 and 5. Hence, a comparison of synapse loss in the two mouse models could be made.

1. Dissect somatosensory cortex

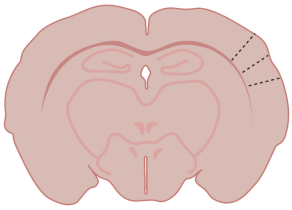

2. Embed tissue in resin

3. Cut 70nm serial sections

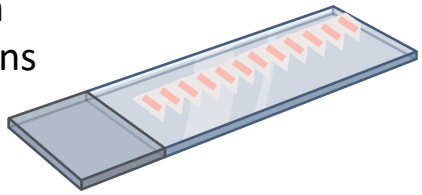

4. Antigen retrieval and stain

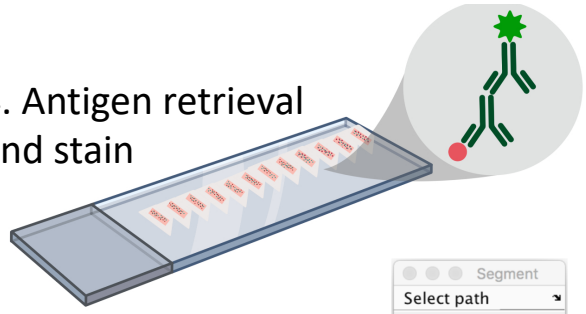

5. Image, reconstruct z stack, align images

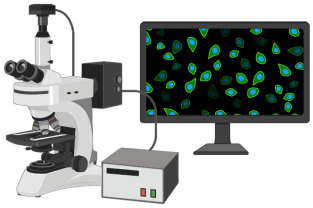

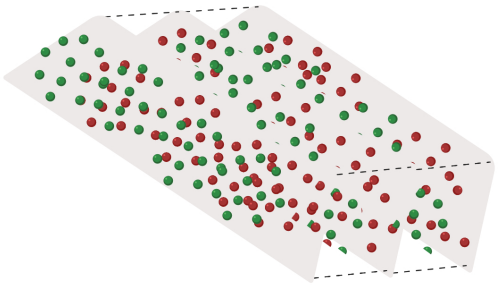

6. Segment

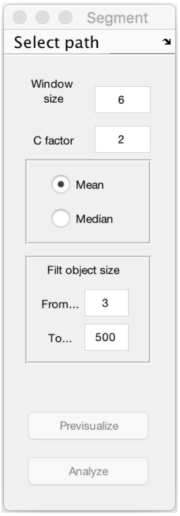

7. Pair synapses

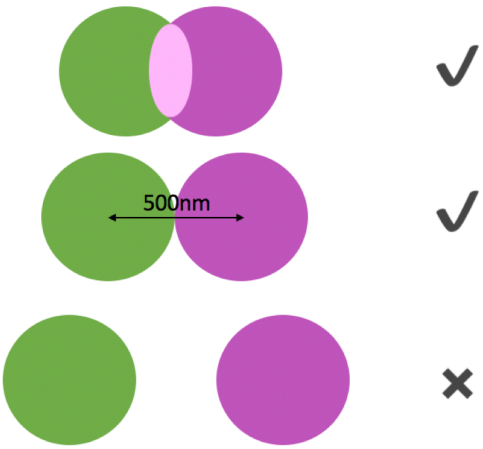

8. Measure density and colocalization

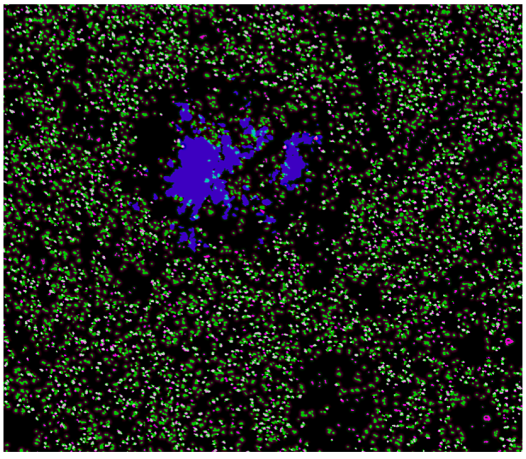

Figure 10. The process of array tomography.

3.1.2 Plaque and Reactive Astrocyte Load in 12-month APP^{NLF} Mice

This chapter also investigates plaque load and associated reactive astrocyte load in the 12-month APP^{NLF} mice. Enhanced expression of the intermediate filament protein GFAP is widely used as a marker of astroglial activation (Eng and Ghirnikar 1994; Kamphuis et al. 2014). However, the diversity of the reactive astrocyte phenotype is being realized (Zamanian et al. 2012). Hence, GFAP alone is unlikely to mark all reactive astrocytes. Nevertheless, Saito et al. previously illustrated that GFAP occupied more cortical area in 18-month-old APP^{NLF} HOM mice compared to WT mice. They also qualitatively show that GFAP load increases around plaques. However, they did not quantify the relationship between GFAP load and distance from plaque. Hence, the extent to which GFAP positive reactive astrocytes surround Aβ plaques in this model is not known.

Whilst array tomography is very useful for visualising individual synaptic proteins, only a small portion of tissue is sampled. In order to get an idea of plaque load over the whole cortex and hippocampus, as well as the presence of activated astrocytes. I designed experiments conducted by Helen Stirling, an undergraduate student I supervised in the Spires-Jones lab. Analysis of plaque load and GFAP load was conducted by both Helen and myself.

3 coronal sections approximately -1mm, -2mm and -3mm from Bregma were sampled from 10 APP^{NLF} HOM mice, 10 HET mice and 9 WT mice. The sections were stained for nuclei using DAPI, activated astrocytes using a GFAP antibody, and dense Aβ plaque cores were stained with ThioS (as described in **section 2.1.7**).

3.2 Results

3.2.1 Optimisation of Array Tomography Stain – Choosing Markers of Synaptic Proteins and Aβ

Synapsin-1 and synaptophysin are both considered markers of pre-synaptic terminals (Brachya et al. 2006). Trial staining experiments were carried out to decide which pre-synaptic marker to use **(figure 11A)**. Synaptophysin was chosen since the stain appeared more punctate and therefore was thought to better label individual synaptic boutons. It is not surprising that the synaptophysin stain was better for distinguishing synaptic boutons, since synaptophysin is a synaptic vesicle glycoprotein thought to constitute part of the pore complex which forms when the vesicle fuses with the presynaptic membrane (Adams et al. 2015). On the other hand, synapsin-1 is a phosphoprotein involved in axonogenesis as well as synaptogenesis (Chin et al. 1995).

PSD95 is thought to be a good marker for excitatory post-synaptic terminals as it is involved in the formation of scaffolds for the clustering of receptors, ion channels and signaling proteins at post-synaptic terminals (Sheng and Kim 2011). Additionally, many other studies have used the expression of this protein as a proxy for post-synaptic density (Koffie et al. 2009; Saito et al. 2014). The trial stains **(figure 11B)** showed that a guinea-pig PSD95 antibody labelled the nuclei of cells as well as what was thought to be post-synaptic terminals. Nuclear staining is a common artefact when using polyclonal antibodies for array tomography for unknown reasons (unpublished data).

In order to determine whether the neuropil puncta staining was reliable, I co-stained mouse tissue with a guinea-pig PSD95 antibody and a rabbit PSD95 antibody **(figure 11B)**. 78% of the rabbit PSD95 stain colocalized with the guinea-pig PSD95, n=2. On inspection of the images, it appeared that the non-nucleic puncta were the major source of colocalization. Hence, both PSD95 antibodies were thought to reliably label post-synaptic densities. The Aβ antibody needed in this study was raised in a rabbit, so experiments went ahead with the guinea-pig PSD95 antibody.

In order to overcome the issue of nucleic PSD95 antibody staining affecting density measurements, I implemented 3 tools when analysing the data:

1) Only puncta which were present in adjacent images were included in the segmented image which was used to quantify puncta density. Synaptic puncta have a diameter of approximately 400nm, hence real puncta would be present in more than one 70nm slice; excluding puncta only present in one slice reduces the noise in the data.
2) A neuropil mask which is based on the synaptophysin stain was applied to the PSD95 images. This excluded blood vessels and cell bodies, including nucleic staining, giving more accurate neuropil PSD95 density measurements.
3) I decided to only measure the density of paired synaptic puncta, i.e. only measure PSD95 puncta that are within 500nm of a synaptophysin puncta.

Previous studies which used array tomography to measure synaptic density around plaques in transgenic mice illustrated that a significant reduction in synapse density occurs in the core of the plaque, in the Aβ oligomer halo region around the plaque, and 20μm beyond the halo (Koffie et al. 2009). Hence, the OC antibody was chosen to mark plaques as it marks amyloid fibrils which constitute the plaque core and fibrillar oligomers which are often found in halos around the plaque core.

3.2.2 Optimisation of Array Tomography Stain- Testing Antigen Retrieval

Most of the array tomography studies carried out in the Spires-Jones lab use pressure cooking in citrate buffer (pH6) as a method of antigen retrieval. This is necessary due to the tissue embedding process masking epitopes. Before starting my study, I wanted to check whether this antigen retrieval method was affecting my PSD95 stain. **Figure 11C** shows that there was less PSD95 antibody bound to the plaque and nuclei with antigen retrieval compared to without antigen retrieval. Hence, I decided to keep the citrate buffer antigen retrieval step.

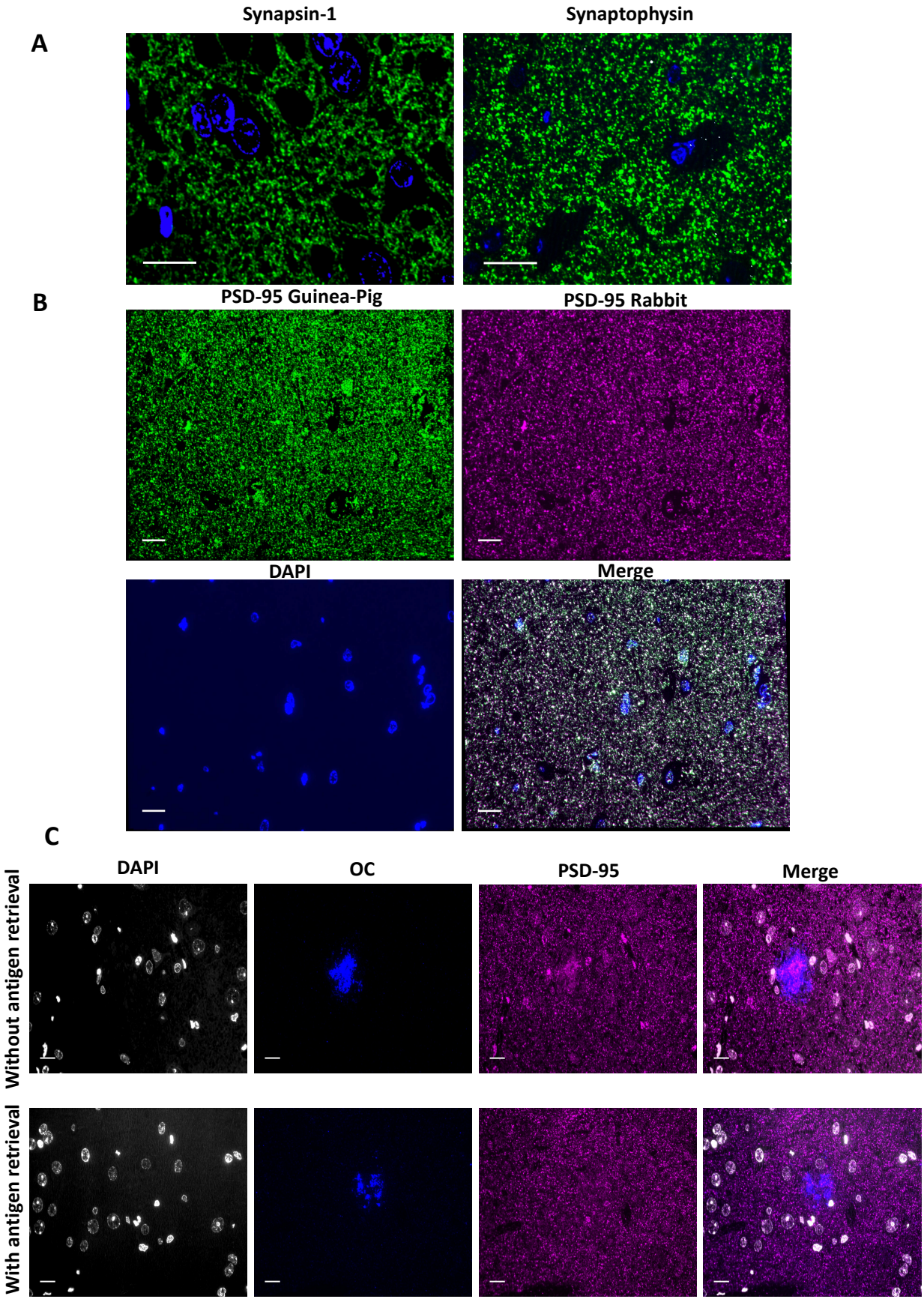
A
Synapsin-1
Synaptophysin
B
PSD-95 Guinea-Pig
PSD-95 Rabbit
DAPI
Merge
C
DAPI
OC
PSD-95
Merge
Without antigen retrieval
With antigen retrieval

Figure 11. Optimisation of array tomography stain. Array tomography ribbons from the cortex of spare mouse array tomography blocks were cut and stained. Images shown are maximum intensity z projections of 4 serial sections (aligned raw images). **(A)** Synapsin-1 and synaptophysin are labelled. Scale bar = 5µm. **(B)** The PDZ PSD95 domain was labelled using guinea-pig primary antibody (green), residues surrounding Gln53 of PSD95 was labelled using rabbit primary antibody (magenta) and nuclei were labelled with DAPI (blue). In the merged tile, white indicates colocalization of PSD95 antibodies. Scale bar = 10µm. **(C)** testing PSD95 stain with and without citrate buffer pH6 antigen retrieval. DAPI labels nuclei (white), OC antibody labels amyloid fibrils and fibrillar oligomers (blue), PSD95 labelled with the guinea-pig primary antibody (magenta). Scale bar = 10µm.

3.2.3 Investigating Synaptic Density Around Plaques in 12-month APP^{NLF} Somatosensory Cortex – Staining Tissue and Aligning Images.

The array tomography procedure described in **figure 10** was carried out, using an SY38 antibody to mark presynaptic protein synaptophysin, PSD95 antibody to mark the post-synaptic protein PSD95, OC to mark amyloid fibrils and fibrillar oligomers and DAPI to mark nuclei. 2 stacks of images were taken per WT mouse. For HOM mice, 2 stacks including a plaque in the field of view (classed as near plaque), plus 1 stack without a plaque in the field of view (classed as far from plaque) were taken per mouse. The z stacks were reconstructed and consecutive images were aligned using rigid body and affine transformations. Example images from the array tomography study are shown in **figure 12**. Qualitatively, there appears to be less synaptophysin and PSD95 stain in the region of the plaque (indicated by white arrows). However, I wanted to assess this quantitatively.

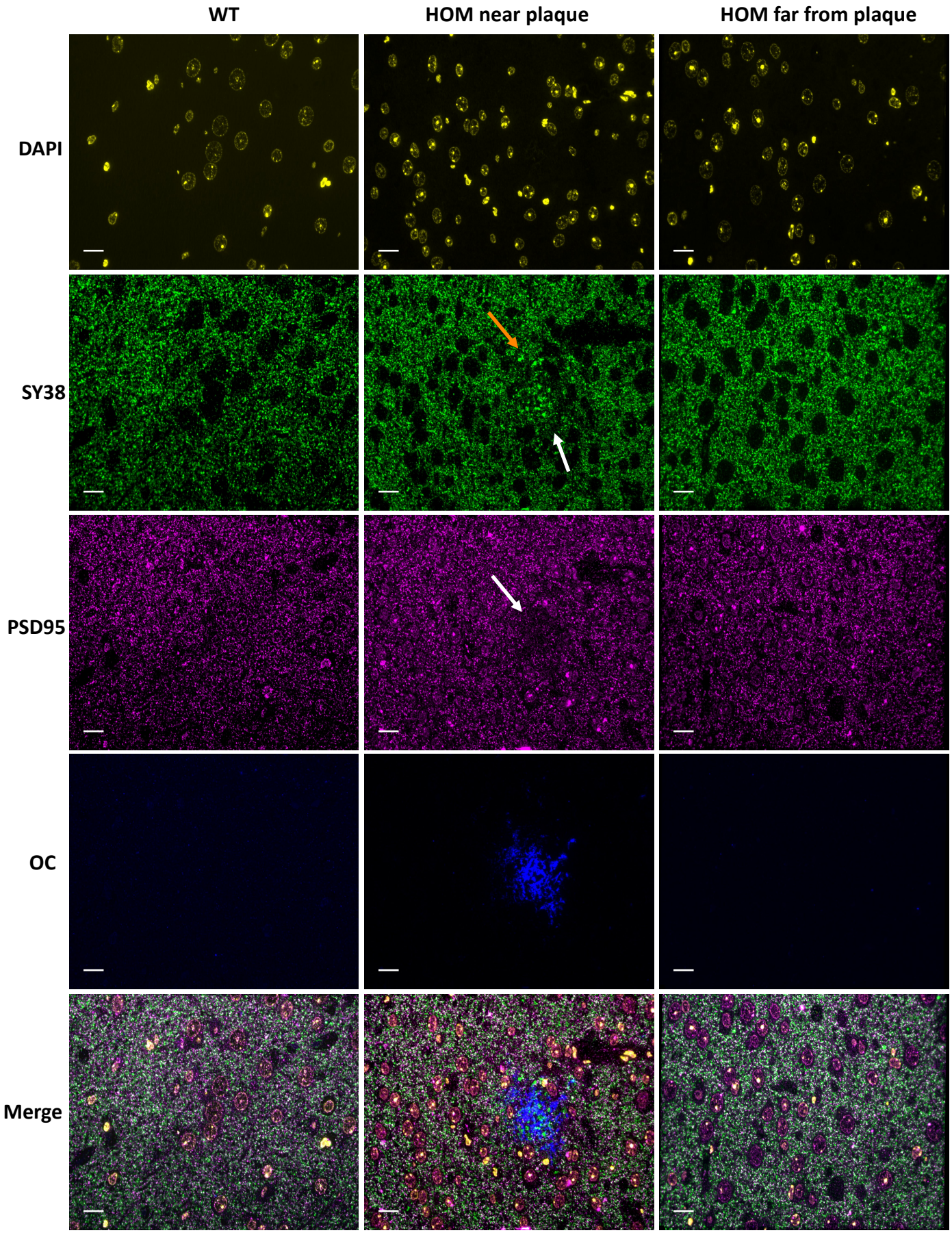
WT
HOM near plaque
HOM far from plaque
DAPI
SY38
PSD95
OC
Merge

Figure 12. Representative images of array tomography staining of 12-month WT and HOM APP^{NLF} somatosensory cortex. Array tomography ribbons from WT and HOM APP^{NLF} mice were stained with DAPI to mark nuclei (yellow), SY38 to mark presynaptic synaptophysin proteins (green), PSD95 to mark post-synaptic proteins (magenta). Orange arrow indicates SY38 positive dystrophic neurite, white arrow indicates reduced SY38 and PSD95 stain around the plaque. If the field of view contained a plaque, this was counted as being 'near plaque', if the field of view did not contain a plaque, this was counted as being 'far from plaque'. Channels are shown separately, followed by the merged image. Images shown here are maximum intensity z projections of 5 slices of raw image. However, between 15-20 slices per mouse were imaged and used for quantification. Scale bar = 10µm.

3.2.4 Investigating Synaptic Density Around Plaques in 12-month APP^{NLF} Somatosensory Cortex – Image Segmentation.

In order to quantitatively assess synaptic density around plaques, I first needed to segment the channels. This allows isolation of 3D objects to be counted. For the synaptic puncta I used the auto local threshold function in the MATLAB script **(see section 2.1.6.2),** which is ideal for segmenting small, regular shaped objects. There were 4 parameters which could be chosen:

1) window size - the sampling window, should be slightly bigger than the size of the object of interest, in this case a single synaptic punctum. Window size 6 was chosen for both pre and post synaptic puncta.
2) c factor - a correction factor, the higher it is, the more permissive the detection is of lower intensity objects. **Figure 13A** illustrates how I determined the c factor for each channel. I tried a range of c factors and decided whether the segmented image accurately represented the original image. I chose c factor 3 for synaptophysin as when zooming in on individual synaptic puncta that tracked through multiple images, c factor 2 was underrepresenting the synaptic puncta and c factor 4 was merging what I believed to be 2 individual puncta into one object. I chose c factor 2 for the PSD95 puncta as c factor 3 was too permissive, detecting objects that were not in consecutive images, were low intensity and most likely noise.

3) Mean intensity- the mean or median intensity of the same object in different slices could be chosen, there did not appear to be a difference between the results of mean or median, so the default mean was chosen.
4) Minimum and maximum pixel size- a filter to ensure only relevant objects are detected. I chose 3-500nm.

Importantly, only objects that were in at least two consecutive images were segmented.
The segmentation of synaptic puncta was checked by overlaying the original image with the segmented image and scrolling through the stack to check that puncta present in consecutive slices were segmented and vice versa **(figure 13B)**.

In order to segment the plaques, I used ImageJ to manually choose a threshold. This threshold value was then input into the fixed value threshold function in the MATLAB script. This function is better for large irregular shaped objects compared to the auto local threshold function. I segmented both the core of the plaque and the whole plaque (core and halo) by eye, based on the density of the stain. I checked the segmentation by overlaying the original image with the segmented image **(figure 13B)**.

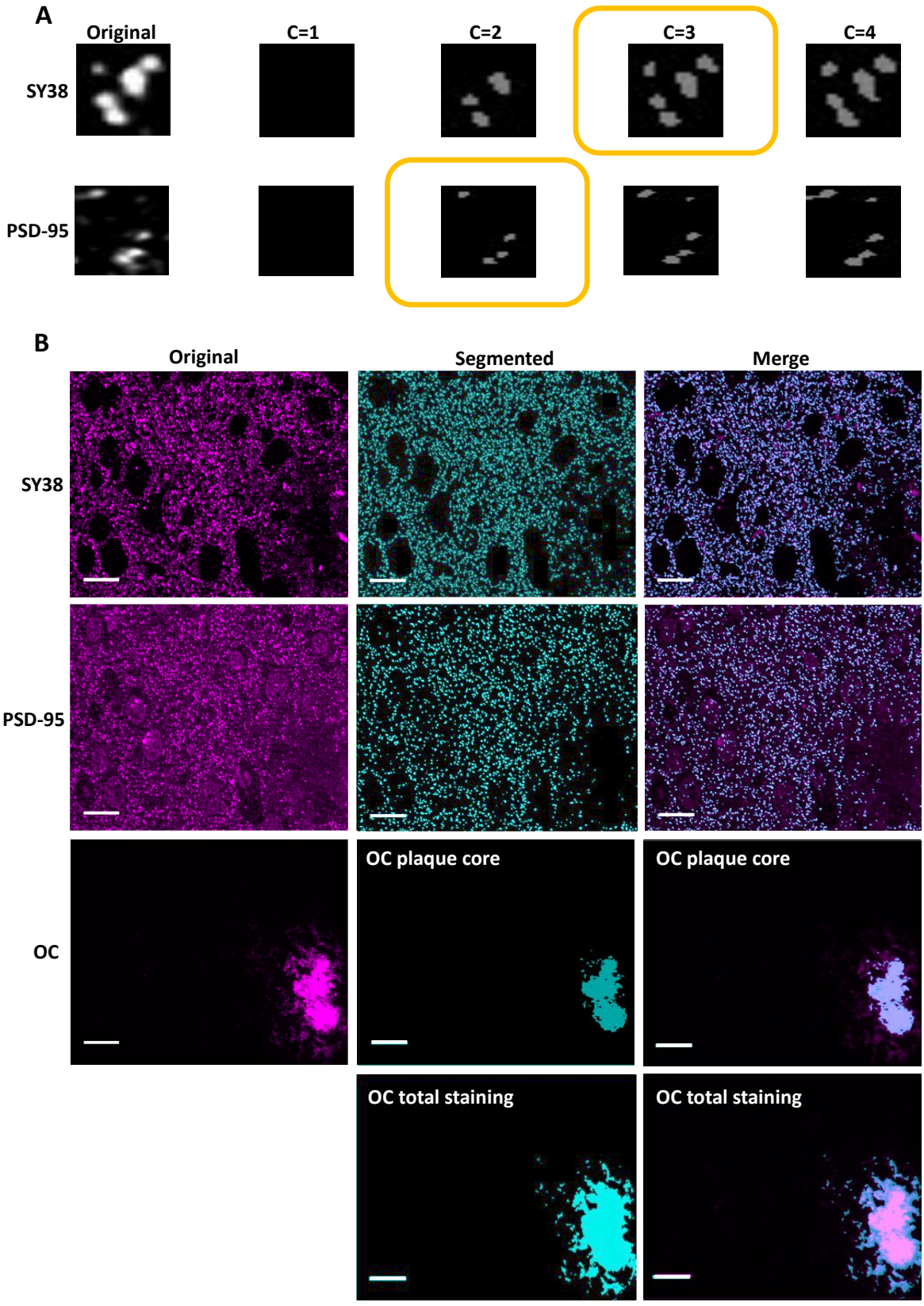
A
Original
C=1
C=2
C=3
C=4
SY38
PSD-95
B
Original
Segmented
Merge
SY38
PSD-95
OC
OC plaque core
OC plaque core
OC total staining
OC total staining

Figure 13. Image segmentation. Array tomography ribbons were stained with SY38 to mark presynaptic synaptophysin proteins, PSD95 to mark post-synaptic PSD95 proteins and OC to mark amyloid fibrils and fibrillar oligomers. Images were aligned, and maximum intensity z projections of 5 slices are presented. **(A)** The auto local threshold function in the MATLAB script was used to segment the SY38 and PSD95 stain. A variety of correction factors (c factors) were trialled. Yellow rings highlight the c factors chosen as they best represented the original images. **(B)** Original images (magenta) and segmented images (cyan) were merged to investigate the how accurately the segmented channels represent the original image. Scale bar = 10µm.

3.2.5 Investigating Synaptic Density Around Plaques in 12-month APP^{NLF} Somatosensory Cortex – Quantifying Synaptic Density

I used a custom-built python script **(see section 2.1.6.2)** to identify presynaptic SY38 puncta that were paired with post-synaptic PSD95 puncta, i.e. the puncta were within 500µm of each other. 500µm was chosen as it is slightly larger than the diameter of a synaptic bouton (Ballesteros-Yáñez et al. 2006). Following this I used the MATLAB script to quantify unpaired pre and post-synaptic protein density, as well as paired synaptic density in the segmented image stacks of WT and HOM mice (HOM images with plaques were labelled HOM_Near and without plaques were labelled HOM_Far **(figure 14A)**). A neuropil mask based on the SY38 segmented images was applied when quantifying synaptic protein density in order to exclude nucleic PSD95 staining.

Pairing synaptic proteins reduced the mean synaptic density in all image types (WT, HOM_Near, HOM_Far), when compared to unpaired SY38. This could be because synaptophysin is thought to be present in all synapses, whether they are excitatory or inhibitory (Sarnat 2013). Whereas, PSD95 is thought to only be present in a portion of excitatory post-synaptic terminals, with other markers such as SAP102 also marking excitatory post-synaptic terminals (Zhu et al. 2018), hence only counting paired synaptophysin was likely to reduce the quantity measured. A linear mixed effects model was constructed to determine whether the density of different puncta type (unpaired SY38, unpaired PSD95 or paired puncta) differed with image type (WT, HOM_Near, HOM_Far), and

sex over the whole image. Image type, puncta type and sex were the fixed effects and the random effects accounted for the fact that multiple images were taken from the same mouse, and experiments were done in batches. A type III ANOVA on the linear mixed effects model revealed there were no significant interactions between puncta type, image type or sex **(table 5A)**, so the model was re-run without interactions. This revealed there was no main effect of image type (F=0.77, p=0.47) or sex (F=0.84, p=0.37) **(table 5B)**. Post-hoc Tukey corrected pairwise comparisons revealed significant differences in synaptic puncta density between all the puncta types **(table 5C)**.

I focused on paired synaptic protein density when investigating synaptic density at various distances from the boundary of the core of the plaque as this was the most conservative way to measure synaptic density. **Figure 14B** illustrates the paired synaptic proteins in 2µm bins surrounding the plaque up to 40µm. **Figure 14Ci and ii** is the quantification of APP^{NLF} HOM paired pre- and post-synaptic proteins as a percentage of the paired puncta measured at 40µm from the core of the plaque. WT shaded bar represents the standard deviation of WT values which are also expressed as a percentage of the density at 40µm, but the 2µm bins were averaged over the area since distance from plaque did not apply. I chose to measure synaptic density from the edge of the core of the plaque as historically this is where a large proportion of the synapse loss occurs and it seemed to be true when qualitatively inspecting images with plaques. I used a linear mixed effects model to investigate the fixed effects of distance and sex on paired puncta density. The random effects accounted for the fact that multiple images were taken from the same mouse and experiments were done in batches. An ANOVA on the linear mixed effects model **(table 6A)** revealed no main effect of sex. Hence, sex was removed from the model. The linear mixed effects model revealed paired synaptic density was significantly lower within 10µm of the boundary of the plaque compared to 40µm from the plaque core boundary (p<2.0E-05, linear mixed effects model on square transformed data, **see table 6B**). A maximal paired synapse loss of 50% was reached 2µm from the edge of the core of the plaque. There was no significant difference in paired synaptic density between 12µm and 40µm from the plaque core boundary.

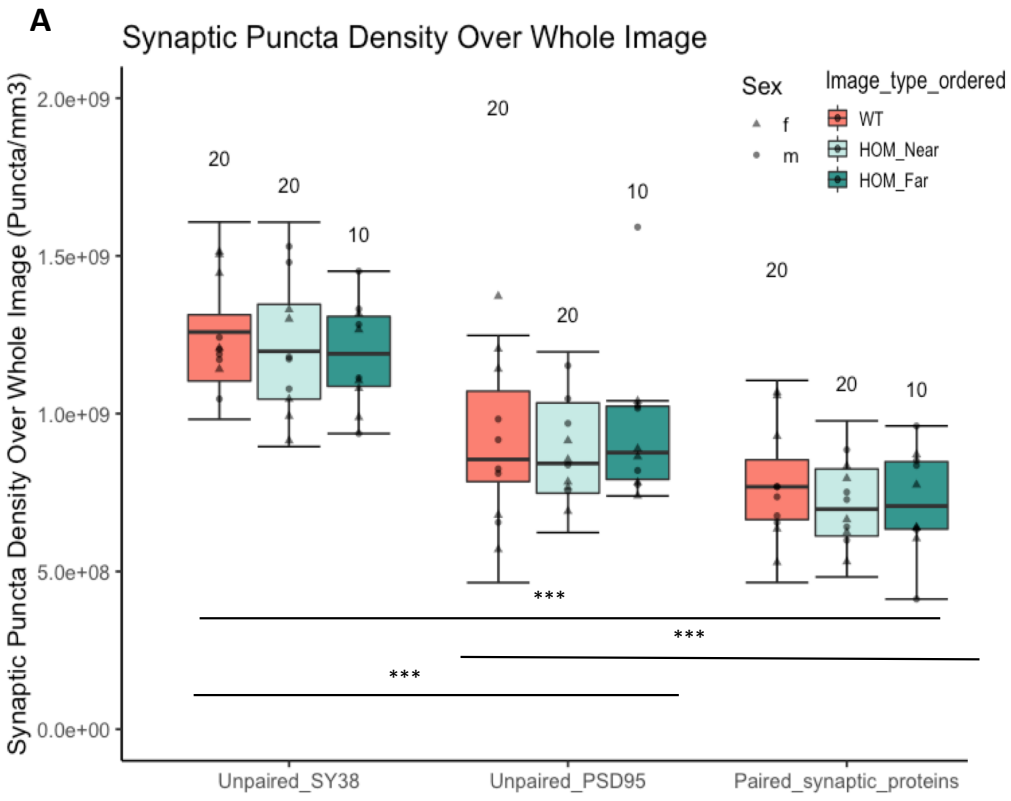
A
Synaptic Puncta Density Over Whole Image
Synaptic Puncta Density Over Whole Image (Puncta/mm3)
2.0e+09
1.5e+09
1.0e+09
5.0e+08
0.0e+00
Sex
f
m
Image_type_ordered
WT
HOM_Near
HOM_Far
20
20
10
20
20
10
20
20
10
***
***
***
Unpaired_SY38
Unpaired_PSD95
Paired_synaptic_proteins

B

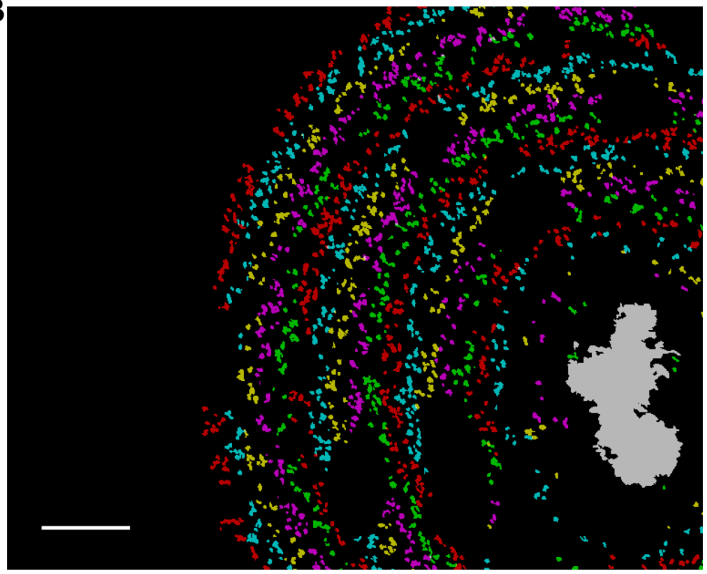

Ci

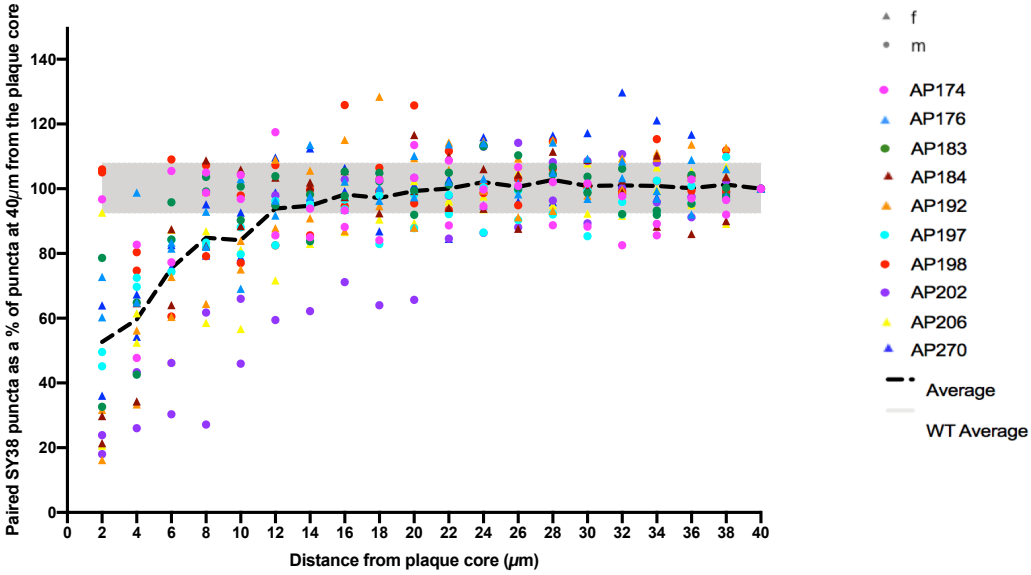
Paired SY38 puncta as a % of puncta at 40μm from the plaque core
Distance from plaque core (μm)
Sex
f
m
AP174
AP176
AP183
AP184
AP192
AP197
AP198
AP202
AP206
AP270
Average
WT Average

Cii

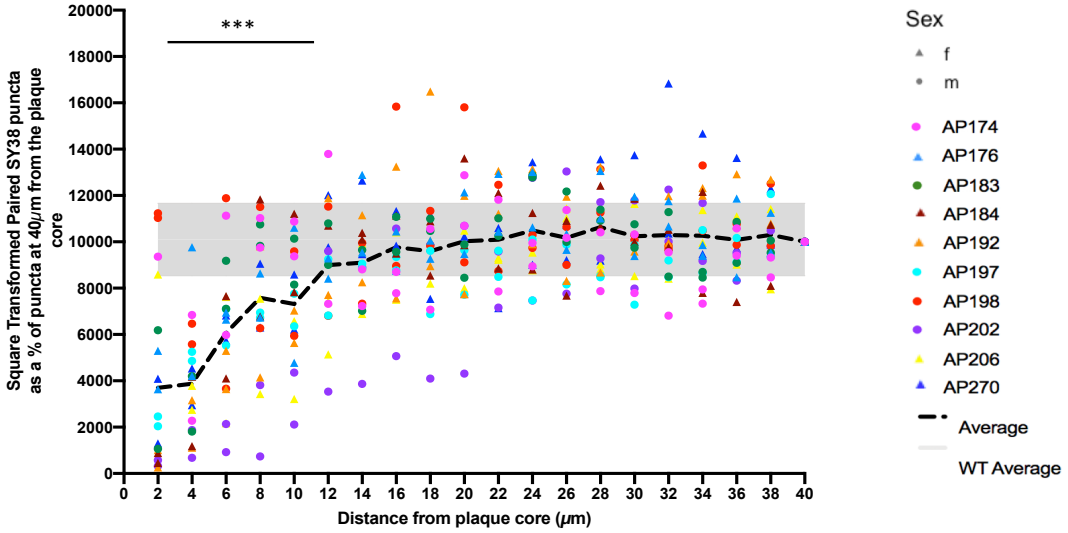
***
Square Transformed Paired SY38 puncta as a % of puncta at 40μm from the plaque core
Distance from plaque core (μm)
Sex
f
m
AP174
AP176
AP183
AP184
AP192
AP197
AP198
AP202
AP206
AP270
Average
WT Average

Figure 14. Quantifying synaptic density. Array tomography ribbons of somatosensory cortex of 12-month HOM APP^{NLF} and WT mice were stained with SY38 to measure presynaptic synaptophysin, PSD95 to measure post-synaptic PSD95 and OC to measure amyloid fibrils and fibrillar amyloid oligomers. n= 10 WT (2 image stacks per mouse), 10 HOM (2 image stacks containing a plaque per mouse (HOM_Near), 1 image stack not containing a plaque, (HOM_Far). Female (f), male (m). **(A)** Density of different puncta type (unpaired presynaptic SY38 puncta, unpaired post-synaptic PSD95 puncta and SY38 puncta paired with PSD95 puncta) were measured over the whole image. SY38 puncta were considered paired if within 500nm of a PSD95 puncta. Upper and lower bounds of the box plot represent the 1^{st} and 3^{rd} quartile, median line shown. Whiskers illustrate 1.5x the interquartile range. Each point represents the mean value from a mouse. Numbers indicate the number of observations. A linear mixed effects model was constructed to investigate the fixed effects of image type (WT, HOM_Near, HOM_Far), puncta type (unpaired SY38, unpaired PSD95, paired synaptic proteins) and sex on density of puncta. The random effects accounted for the fact that multiple images were taken from the same mouse and experimentation was done in batches. A type III ANOVA on the linear mixed effects model revealed were no significant interactions between puncta type, image type or sex **(table 5A)**, so the model was re-run without interactions. This revealed there was no main effect of image type ($F=0.77$, $p=0.47$) or sex ($F=0.84$, $p=0.37$) **(table 5B)**. Post-hoc Tukey corrected pairwise comparisons revealed significant differences in synaptic puncta density between all the puncta types **(table 5C)**. **(B)** Example image of paired synaptic puncta in 2µm concentric circles around the edge of the core of the plaque (core was determined by eye). Scale bar = 10µm. **(Ci)** The density of paired SY38 puncta (expressed as a percentage of paired SY38 at 40µm from the plaque core), measured in 2µm bands around the edge of the plaque core. Each colour represents a different mouse and each dot represents a different image. Black dashed line represents the average density over all images. Grey shade represents the standard deviation of WT paired synaptic density averaged over 40µm and expressed as a percentage of paired SY38 at 40µm. **(Cii)** Square transforming the data appeared to improve the fit of the linear mixed effects model **(see section 2.1.6.3)**. There is a significant reduction in paired synapses in HOM mice between 2-10µm from the plaque core boundary when compared to synaptic pairs 40µm from the plaque core ($p<0.001$, linear mixed effects model on square transformed data, see **table 6B**). '***'$p<0.001$.

A

```
Type III Analysis of Variance Table with Satterthwaite's method
                               Sum Sq    Mean Sq NumDF DenDF  F value Pr(>F)
Image_type                  1.2832e+16 6.4160e+15     2    41   0.5098 0.6044
Puncta_type                 5.3442e+18 2.6721e+18     2   Inf 212.3303 <2e-16 ***
Sex                         9.2008e+13 9.2008e+13     1     9   0.0073 0.9338
Image_type:Puncta_type      5.5531e+16 1.3883e+16     4   Inf   1.1031 0.3530
Image_type:Sex              5.7597e+16 2.8799e+16     2    39   2.2884 0.1148
Puncta_type:Sex             3.4805e+16 1.7403e+16     2   Inf   1.3828 0.2509
Image_type:Puncta_type:Sex 7.3365e+16 1.8341e+16     4   Inf   1.4574 0.2122
---
Signif. codes:  0 ‘***’ 0.001 ‘**’ 0.01 ‘*’ 0.05 ‘.’ 0.1 ‘ ’ 1
```

B

```
Type III Analysis of Variance Table with Satterthwaite's method
                Sum Sq    Mean Sq NumDF DenDF  F value Pr(>F)
Image_type  1.9830e+16 9.9149e+15     2    44   0.7697 0.4693
Puncta_type 6.0760e+18 3.0380e+18     2   Inf 235.8364 <2e-16 ***
Sex         1.0789e+16 1.0789e+16     1    30   0.8375 0.3674
---
Signif. codes:  0 ‘***’ 0.001 ‘**’ 0.01 ‘*’ 0.05 ‘.’ 0.1 ‘ ’ 1
```

C

```
$`pairwise differences of Puncta_type`
 1                                      estimate       SE df t.ratio p.value
 Paired_synaptic_proteins - Unpaired_PSD95 -1.69e+08 22699590 98  -7.433 <.0001
 Paired_synaptic_proteins - Unpaired_SY38  -4.86e+08 22699590 98 -21.389 <.0001
 Unpaired_PSD95 - Unpaired_SY38            -3.17e+08 22699590 98 -13.956 <.0001

Results are averaged over the levels of: Image_type, Sex
Degrees-of-freedom method: kenward-roger
P value adjustment: tukey method for comparing a family of 3 estimates
```

Table 5. Results from type III ANOVAs on linear mixed effects models investigating synaptic puncta density over the whole image. The fixed effects were image type, puncta type and sex. The random effects accounted for the fact that multiple images were taken from the same mouse and experiments were done in batches. **(A)** The results demonstrated no interaction between image type (WT, HOM_Near, HOM_Far), puncta type (Unpaired_SY38, Unpaired_PSD95, Paired_synaptic_proteins), or sex. Hence the model was re-run without the interactions. **(B)** The results demonstrated no significant main effects of image type or sex. **(C)** Post-hoc Tukey adjusted multiple comparisons test revealed significant differences between synaptic puncta density of all the different puncta types.

Formula in A: MEPairedUnpaired<-
lmer(Puncta_density~Image_type*Puncta_type*Sex+(1|Mouse_ID:stack_number) +
(1|batch), data=paired_vs_unpaired_R)
anova(MEPairedUnpaired)

Formula in B: MEPairedUnpaired<-
lmer(Puncta_density~Image_type+Puncta_type+Sex+(1|Mouse_ID:stack_number) +
(1|batch), data=paired_vs_unpaired_R)
anova(MEPairedUnpaired)

Formula in C:emmeans(MEPairedUnpaired, list(pairwise ~ Puncta_type), adjust = "tukey")

A

```
Type III Analysis of Variance Table with Satterthwaite's method
         Sum Sq  Mean Sq NumDF  DenDF F value Pr(>F)
Dist 1700249384 89486810    19 360.01 28.5895 <2e-16 ***
Sex     1413369  1413369     1   7.77  0.4515 0.5211
---
Signif. codes:  0 ‘***’ 0.001 ‘**’ 0.01 ‘*’ 0.05 ‘.’ 0.1 ‘ ’ 1
```

B

```
Linear mixed model fit by REML. t-tests use Satterthwaite's method ['lmerModLmerTest']
Formula: Square_Percentage_paired_SY38 ~ Dist + (1 | Mouse_ID:stack_number) +      (1 | Batch)
   Data: AT_HOM_PD_PairedSY38_R

REML criterion at convergence: 6851.2

Scaled residuals:
    Min      1Q  Median      3Q     Max
-2.4125 -0.6598  0.0013  0.5331  4.3368

Random effects:
 Groups                Name        Variance Std.Dev.
 Mouse_ID:stack_number (Intercept) 1613760  1270.3
 Batch                 (Intercept)  144478   380.1
 Residual                          3130055  1769.2
Number of obs: 399, groups:  Mouse_ID:stack_number, 20; Batch, 7

Fixed effects:
            Estimate Std. Error       df t value Pr(>|t|)
(Intercept)  9978.69     511.13    30.59  19.523  < 2e-16 ***
Dist2       -6354.43     567.13   360.09 -11.205  < 2e-16 ***
Dist4       -6126.82     559.47   360.00 -10.951  < 2e-16 ***
Dist6       -3937.04     559.47   360.00  -7.037 9.97e-12 ***
Dist8       -2418.50     559.47   360.00  -4.323 2.00e-05 ***
Dist10      -2682.11     559.47   360.00  -4.794 2.40e-06 ***
Dist12      -1002.40     559.47   360.00  -1.792    0.074 .
Dist14       -902.93     559.47   360.00  -1.614    0.107
Dist16       -230.44     559.47   360.00  -0.412    0.681
Dist18       -406.35     559.47   360.00  -0.726    0.468
Dist20         23.13     559.47   360.00   0.041    0.967
Dist22         93.03     559.47   360.00   0.166    0.868
Dist24        493.89     559.47   360.00   0.883    0.378
Dist26        172.84     559.47   360.00   0.309    0.758
Dist28        632.57     559.47   360.00   1.131    0.259
Dist30        239.31     559.47   360.00   0.428    0.669
Dist32        295.32     559.47   360.00   0.528    0.598
Dist34        262.16     559.47   360.00   0.469    0.640
Dist36         88.60     559.47   360.00   0.158    0.874
Dist38        302.57     559.47   360.00   0.541    0.589
---
Signif. codes:  0 ‘***’ 0.001 ‘**’ 0.01 ‘*’ 0.05 ‘.’ 0.1 ‘ ’ 1
```

Table 6. The results of the linear mixed effects model comparing square transformed paired SY38 puncta in 12-month APP^{NLF} HOM mice at different distances from the plaque core. (A) The fixed effects in the linear mixed effect model were distance and sex. The random effects accounted for the fact that multiple images were taken from the same mouse and experiments were done in batches. An ANOVA on the linear mixed effects model revealed that there was a main effect of distance on paired synaptic density. However, there was no effect of sex. Hence, sex was subsequently removed from the linear mixed effects model. **(B)** The linear mixed effects model revealed a significant reduction in paired synaptic density between 2-10µm from the plaque core when compared to 40µm from the plaque core.
Formula in A: MM<-
lmer(Square_Percentage_paired_SY38~Dist+Sex+(1|Mouse_ID:stack_number)+(1|Batch), data=AT_HOM_PD_PairedSY38_R).
Anova(MM)
Formula in B: MM<-
lmer(Square_Percentage_paired_SY38~Dist+(1|Mouse_ID:stack_number)+(1|Batch), data=AT_HOM_PD_PairedSY38_R).

3.2.6 Investigating the Colocalization of Aβ in Synaptic Puncta Around Plaques in 12-month APP^{NLF} Somatosensory Cortex

The presence of Aβ oligomers in synapses is thought to contribute to synapse dysfunction and loss. Hence, I wanted to investigate the proportion of paired synaptic puncta which contained Aβ surrounding the plaque. To do this, I used the segmented SY38, PSD95 and whole plaque images, along with the python script to isolate the paired synaptic puncta where 50% or more of the pre and/or post-synaptic puncta overlapped with OC. 50% was chosen in order to be relatively stringent with colocalisation parameters. However, it is acknowledged that varying this percentage would impact the data. In the future, more investigation of how varying this parameter affects the data could be carried out. I used the MATLAB script to quantify the colocalised objects in 2µm bins surrounding the boundary of the plaque core. The boundary was based upon the manually thresholded plaque core images. **Figure 15A** is an Imaris 3D rendering of an array tomography image stack taken of a 12-month APP^{NLF} HOM mouse somatosensory cortex (5 slices visualised). The synapse loss around the plaque is clear. In

order to visually illustrate the colocalization of synaptic puncta and OC, I zoomed in further using Imaris viewer **(figure 15B)**. The bottom panels show synaptophysin (green), PSD95 (magenta) and OC (blue) colocalising. I quantified the number of paired synapses containing OC **(figure 16)** and found that pre and post synaptic puncta show similar levels of colocalization with OC between 2-20µm from the plaque core, with both SY38 and PSD95 displaying an average maximum of 20% of paired synapses within a 2µm bin colocalizing with OC. The colocalization of OC with pre and post paired synaptic puncta decreased with distance from the plaque core, with no synaptic pairs colocalising with OC beyond 12µm from the plaque core. Notably, OC only marks fibrillar Aβ oligomers and Aβ fibrils, hence it is conceivable that smaller Aβ oligomers are present in synaptic puncta prior to and beyond 12µm from the plaque core. Furthermore, studies indicate that it is actually the smaller soluble oligomers which appear to be the most toxic form of Aβ (Hong et al. 2018; Ferreira et al. 2015; Shankar et al. 2007). Hence, in the future it would be useful to use an antibody to label soluble Aβ and assess its colocalisation with synaptic puncta over time.

Linear mixed effects models were performed on log (data+1) transformed paired SY38 colocalization with OC data, and log (data+1) transformed paired PSD95 colocalization with OC data. The fixed effects were distance and sex. The random effects accounted for the fact that multiple images were taken from the same mouse and experimentation was done in batches. An ANOVA was run on the linear mixed effects models to reveal the main effects. For both SY38 and PSD95, there was a significant main effect of distance ($p<2e-16$), but no effect of sex ($F=0.95$, $p= 0.34$ for SY38 **table 7A**, $F=0.01$, $p=0.92$ for PSD95 **table 7C** respectively). Hence, sex was removed from the linear mixed effects models. There was a significant increase in OC colocalising with synaptic puncta close to the plaque core, between 2-6µm for SY38 ($p<0.01$ **table 7B**) and 2-8µm for PSD95 ($p<0.05$ **table 7D**), when compared to the colocalization at 20µm from the plaque core.

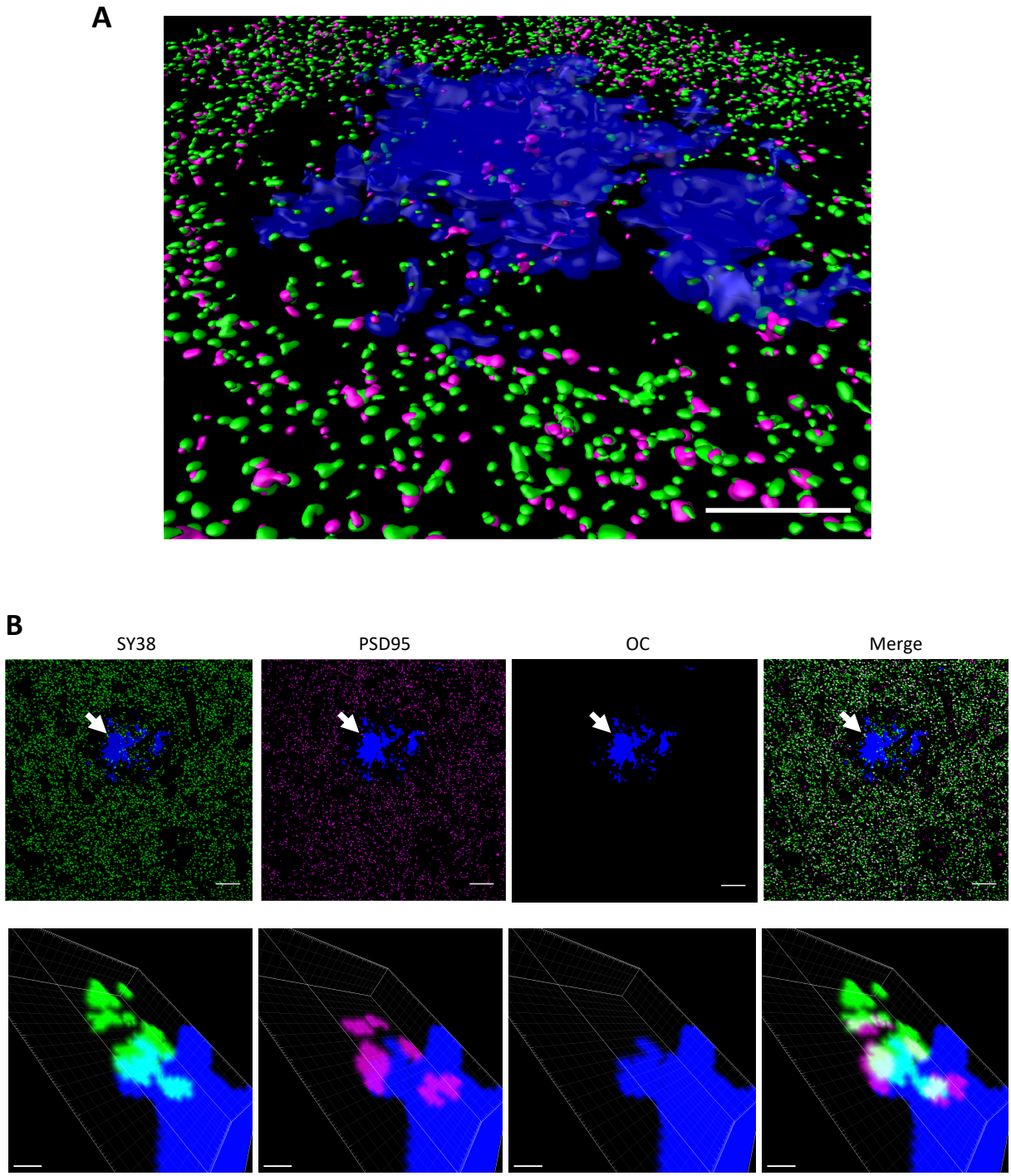

Figure 15. Investigating colocalization of Aβ in synapses. Array tomography ribbons were stained with SY38 to mark presynaptic synaptophysin, PSD95 to mark postsynaptic PSD95, and OC to mark fibrillar Aβ oligomers and Aβ fibrils. Images were segmented using ImageJ and the MATLAB script **(A)** a 3D rendering of an image stack taken from a HOM APP^{NLF} mouse somatosensory cortex, 5 slices visualised. Scale bar = 10µm. **(B)** Separated channels and merged image illustrating colocalization of SY38, PSD95 and OC. White arrow indicates the zoomed section in the panel below. Scale bar of top panel = 10µm. Scale bar of bottom panel = 0.5µm.

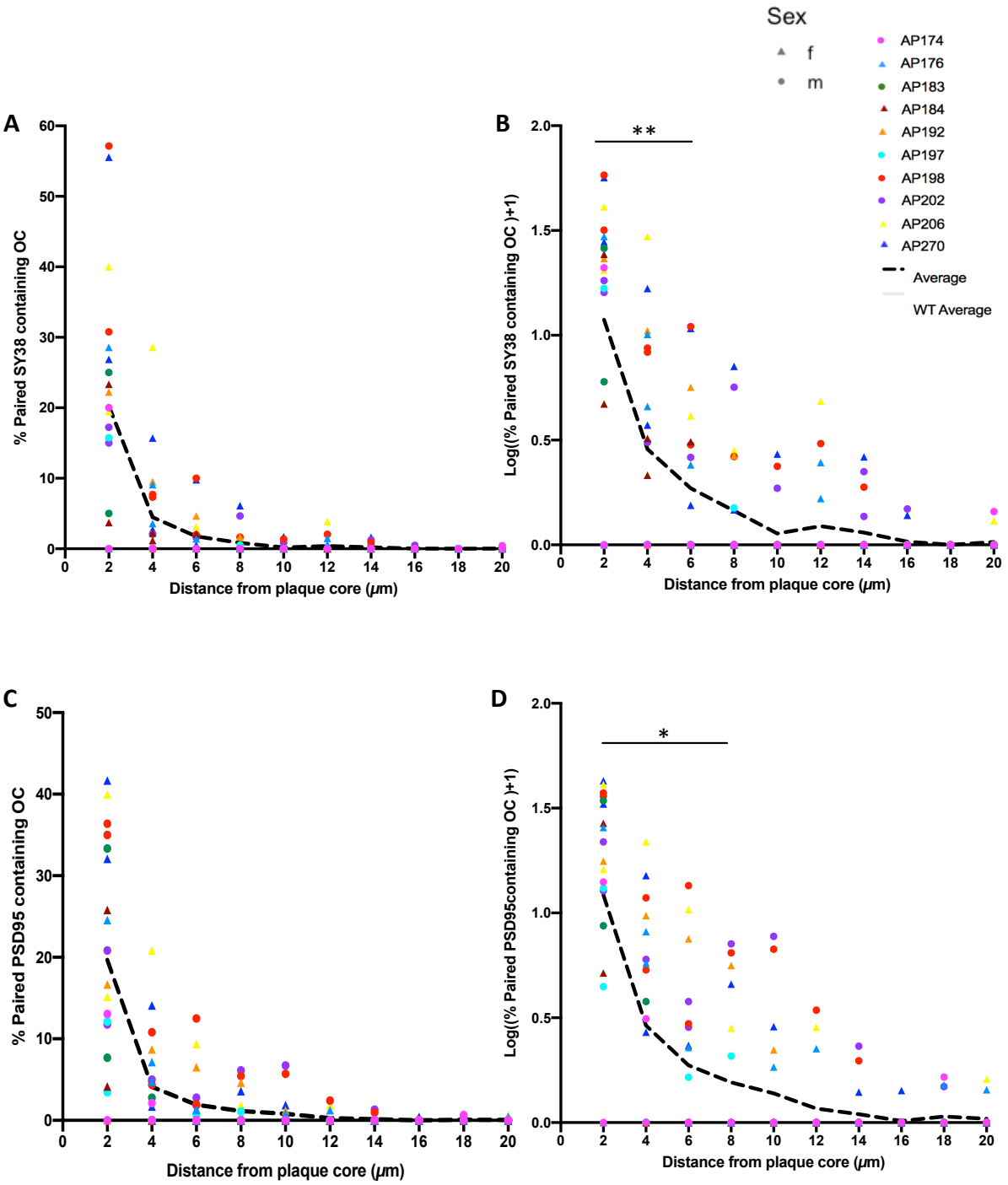
A
% Paired SY38 containing OC
Distance from plaque core (μm)
B
Log((% Paired SY38 containing OC)+1)
**
Distance from plaque core (μm)
Sex
f
m
AP174
AP176
AP183
AP184
AP192
AP197
AP198
AP202
AP206
AP270
Average
WT Average
C
% Paired PSD95 containing OC
Distance from plaque core (μm)
D
Log((% Paired PSD95containing OC)+1)
*
Distance from plaque core (μm)

Figure 16. Quantification of colocalization of OC with paired synaptic puncta in HOM APP^{NLF} array tomography images. Each coloured point is an individual mouse, 2 images per mouse were analysed and are displayed. Female (f), male (m). **(A)** The percentage of paired SY38 puncta (SY38 puncta within 500nm of a PSD95 puncta) where 50% of the SY38 puncta area overlaps with OC. **(B)** A linear mixed effects model was constructed using the Log((data)+1) transformed data, since transformed data better fit the assumptions of the model. Distance and sex were the fixed effects and the random effects accounted for the fact that multiple images were taken from the same mouse, and experimentation was done in batches. An ANOVA on the linear mixed effects model revealed there was no main effect of sex. Hence, it was removed from the model. The subsequent linear mixed effects model identified significant differences in colocalization of OC with paired SY38 puncta between 2-6µm from the plaque core when compared to 20µm from the plaque core ($p<0.01$ **See table 7B, C**). The percentage of paired PSD95 puncta where 50% of the PSD95 puncta area overlaps with OC. **D)** The data in **figure 16C** was log(data+1) transformed and a linear mixed effects model was constructed as in **figure 16B**. The linear mixed effects model was used to identify significant differences in the colocalization of OC with paired PSD95 puncta between 2-8µm from the plaque core, when compared to 20µm from the plaque core. ($p<0.05$ **See table 7D**). **'*'**$p<0.05$, '**' $p<0.01$.

A

```
Type III Analysis of Variance Table with Satterthwaite's method
     Sum Sq Mean Sq NumDF DenDF F value Pr(>F)
Dist 19.907 2.21191     9   171 32.0125 <2e-16 ***
Sex   0.066 0.06597     1    18  0.9548 0.3415
---
Signif. codes:  0 ‘***’ 0.001 ‘**’ 0.01 ‘*’ 0.05 ‘.’ 0.1 ‘ ’ 1
```

B

```
Linear mixed model fit by REML. t-tests use Satterthwaite's method ['lmerModLmerTest']
Formula: logdensityplusone ~ Dist + (1 | Mouse:Image_number) + (1 | Batch)
   Data: coloc_PSY38_OC

REML criterion at convergence: 87.6

Scaled residuals:
    Min      1Q  Median      3Q     Max
-3.8600 -0.4435  0.0192  0.4012  3.1055

Random effects:
 Groups              Name        Variance Std.Dev.
 Mouse:Image_number (Intercept) 0.02055  0.1433
 Batch              (Intercept) 0.00000  0.0000
 Residual                       0.06910  0.2629
Number of obs: 200, groups:  Mouse:Image_number, 20; Batch, 7

Fixed effects:
             Estimate Std. Error         df t value Pr(>|t|)
(Intercept)  0.013613   0.066949 128.997510   0.203  0.83919
Dist2        1.060743   0.083124 171.000006  12.761  < 2e-16 ***
Dist4        0.443392   0.083124 171.000006   5.334 3.01e-07 ***
Dist6        0.256300   0.083124 171.000006   3.083  0.00239 **
Dist8        0.148612   0.083124 171.000006   1.788  0.07557 .
Dist10       0.040266   0.083124 171.000006   0.484  0.62871
Dist12       0.075481   0.083124 171.000006   0.908  0.36513
Dist14       0.045354   0.083124 171.000006   0.546  0.58604
Dist16       0.001988   0.083124 171.000006   0.024  0.98094
Dist18      -0.013613   0.083124 171.000006  -0.164  0.87010
---
Signif. codes:  0 ‘***’ 0.001 ‘**’ 0.01 ‘*’ 0.05 ‘.’ 0.1 ‘ ’ 1
```

C

```
Type III Analysis of Variance Table with Satterthwaite's method
      Sum Sq Mean Sq NumDF DenDF F value Pr(>F)
Dist 19.9351 2.21501     9   171 33.4464 <2e-16 ***
Sex   0.0007 0.00072     1    18  0.0109 0.9182
---
Signif. codes:  0 ‘***’ 0.001 ‘**’ 0.01 ‘*’ 0.05 ‘.’ 0.1 ‘ ’ 1
```

D

```
Linear mixed model fit by REML. t-tests use Satterthwaite's method ['lmerModLmerTest']
Formula: logdensityplusone ~ Dist + (1 | Mouse_ID:Image_number) + (1 |      Batch)
   Data: coloc_PSD95_OC

REML criterion at convergence: 81.9

Scaled residuals:
    Min      1Q  Median      3Q     Max
-3.7976 -0.5123  0.0626  0.3934  2.6327

Random effects:
 Groups                Name        Variance Std.Dev.
 Mouse_ID:Image_number (Intercept) 0.02309  0.1520
 Batch                 (Intercept) 0.00000  0.0000
 Residual                          0.06623  0.2573
Number of obs: 200, groups:  Mouse_ID:Image_number, 20; Batch, 7

Fixed effects:
            Estimate Std. Error        df t value Pr(>|t|)
(Intercept)  0.01817    0.06683 118.63336   0.272  0.78613
Dist2        1.06828    0.08138 171.00002  13.127  < 2e-16 ***
Dist4        0.44469    0.08138 171.00002   5.464 1.62e-07 ***
Dist6        0.25527    0.08138 171.00002   3.137  0.00201 **
Dist8        0.17377    0.08138 171.00002   2.135  0.03415 *
Dist10       0.12103    0.08138 171.00002   1.487  0.13879
Dist12       0.04901    0.08138 171.00002   0.602  0.54778
Dist14       0.02205    0.08138 171.00002   0.271  0.78674
Dist16      -0.01053    0.08138 171.00002  -0.129  0.89720
Dist18       0.01027    0.08138 171.00002   0.126  0.89969
---
Signif. codes:  0 '***' 0.001 '**' 0.01 '*' 0.05 '.' 0.1 ' ' 1
```

Table 7. Results from the linear mixed effects model log (data +1) transformed data comparing colocalisation of OC with paired SY38 or paired PSD95 puncta between 2-20µm from the plaque core. (A) A linear mixed effects model to investigate colocalisation of OC with paired SY38 puncta was constructed. The fixed effects were distance and sex. The random effects accounted for the fact that multiple images were taken from the same mouse, and experiments were done in batches. An ANOVA on the linear mixed effects model revealed a significant main effect of distance, and no main effect of sex. Consequently, sex was removed from the linear mixed effects model. **(B)** The subsequent linear mixed effects model demonstrated significant colocalisation of OC with paired SY38 puncta between 2-6µm from the plaque core, when compared to 20µm from the plaque core. **(C)** A linear mixed effects model to investigate colocalisation of OC with paired PSD95 puncta was constructed. The fixed effects were distance and sex. The random effects accounted for the fact that multiple images were taken from the same mouse, and experiments were done in batches. An ANOVA on the linear mixed effects model revealed a significant main effect of distance, and no main effect of sex. Consequently, sex was removed from the linear mixed effects model. **(D)** The

linear mixed effects model demonstrated significant colocalisation of OC with paired PSD95 puncta between 2-8µm from the plaque core, when compared to 20µm from the plaque core. Formula in A and C: MM<-logdensityplusone~ Dist + Sex (1 | Mouse_ID:Image_number) + (1|Batch).

Anova(MM)

Formula in B and D: MM<-logdensityplusone~ Dist + (1 | Mouse_ID:Image_number) + (1|Batch).

3.2.7 Diversity of Plaque Formations in the APP^{NLF} Mouse

Whilst analysing the array tomography images I noticed that the plaques I sampled were a range of shapes, sizes and densities **(figure 17)**. This was interesting as diversity in plaque formation is also seen in human AD post-mortem brains (Liebmann et al. 2016), but was not found in the common transgenic APP/PS1 amyloidopathy model, where all the plaques sampled showed little deviation in ThioS positive plaque cores or AW7 positive halos (Jackson et al. 2016). Additionally, some studies have proposed a link between plaque morphology and disease pathogenesis (D'Andrea and Nagele 2010; Delaère et al. 1991). Thus, the APP^{NLF} mouse may be more appropriate to use to investigate this further, compared to the APP/PS1 mouse.

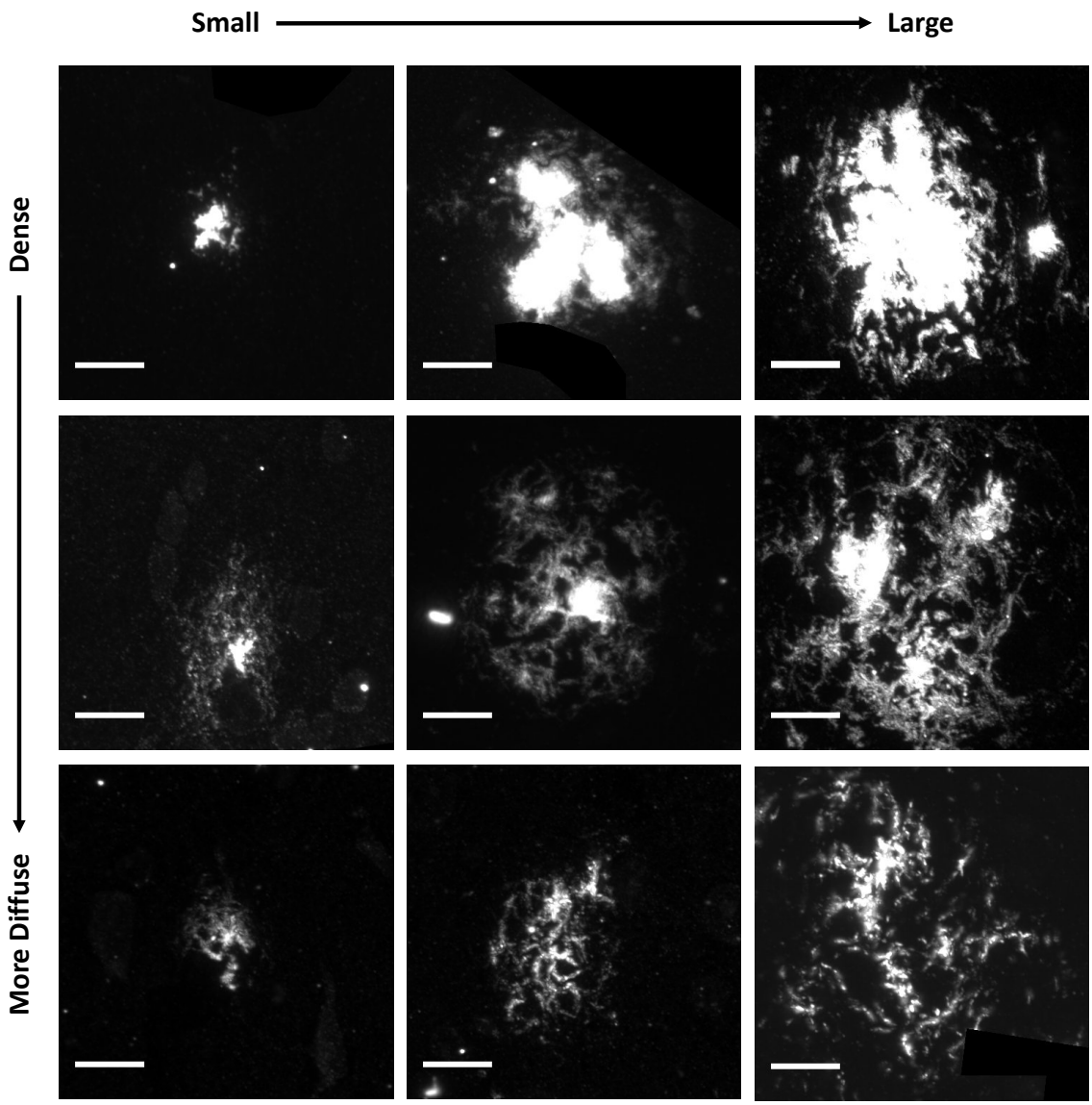

Figure 17. Diversity of plaque formations in 12-month HOM APP^{NLF} mice. Somatosensory cortex tissue from 12-month HOM APP^{NLF} mice was processed for array tomography. The OC antibody was used to label amyloid fibrils and fibrillar oligomers. Example images of the amyloid plaques sampled are shown here, illustrating diversity in size, shape and density of plaques. Scale bar = 10µm.

3.2.8 Plaque Burden Greatest in 12-month HOM APP^{NLF} Mice

Coronal sections approximately -1mm, -2mm and -3mm from Bregma were sampled from 10 APP^{NLF} HOM mice, 10 HET mice and 9 WT mice. The sections were stained for nuclei using DAPI, activated astrocytes using a GFAP antibody, and dense Aβ plaque cores were stained with ThioS. **Figure 18** displays representative raw images of the plaque load in APP^{NLF} HOM, HET and WT mice. HOM mice displayed dense core plaques in the cortex and hippocampus. HET and WT mice did not display any plaques. In order to quantify plaque burden, the regions of interest were manually outlined in 3 slices for the cortex and 2 slices for the hippocampus **(figure 19A)**, the ThioS stains were thresholded using the max entropy algorithm in ImageJ and the percentage area covered by the stain was calculated. **Figure 19Bi** shows boxplots of the ThioS burden in the cortex and hippocampus of WT, APP^{NLF} HET and APP^{NLF} HOM brains. Upper and lower bounds of the boxplot represent the 1st and 3rd quartile of the data, the median line shown. Whiskers illustrate 1.5x the interquartile range. Each point represents the median value from a mouse.

A linear mixed effects model was constructed. The fixed effects were genotype, region and sex. The random effects accounted for the fact that multiple images were taken from the same mouse. Data was cube root transformed in order to better fit model assumptions. A type III ANOVA on cube root transformed ThioS data found a significant interaction between genotype and region ($F=9.28$, $p<0.001$), and no effect of sex ($F=0.23$, $p=0.63$) **(table 8A)**. A post-hoc Tukey adjusted pairwise multiple comparisons test revealed significant differences between ThioS burden in HOM cortex and WT cortex (p=3.11e-14), HOM cortex and HET Cortex (p=2.66e-15), HOM hippocampus and WT hippocampus (p=6.27e-10), HOM hippocampus and HET hippocampus (p=1.65e-09), and HOM cortex and HOM hippocampus (p=4e-07) **(table 8B)**. Hence, in all comparisons between genotypes, the HOM mice had higher plaque burdens than the other genotypes and the plaque burden in the cortex of the HOM mice was higher than in the hippocampus of the HOM mice. The ThioS burden values for WT and HET mice approach 0 and there are no differences in any comparisons between them, indicating negligible ThioS positive stain in these genotypes.

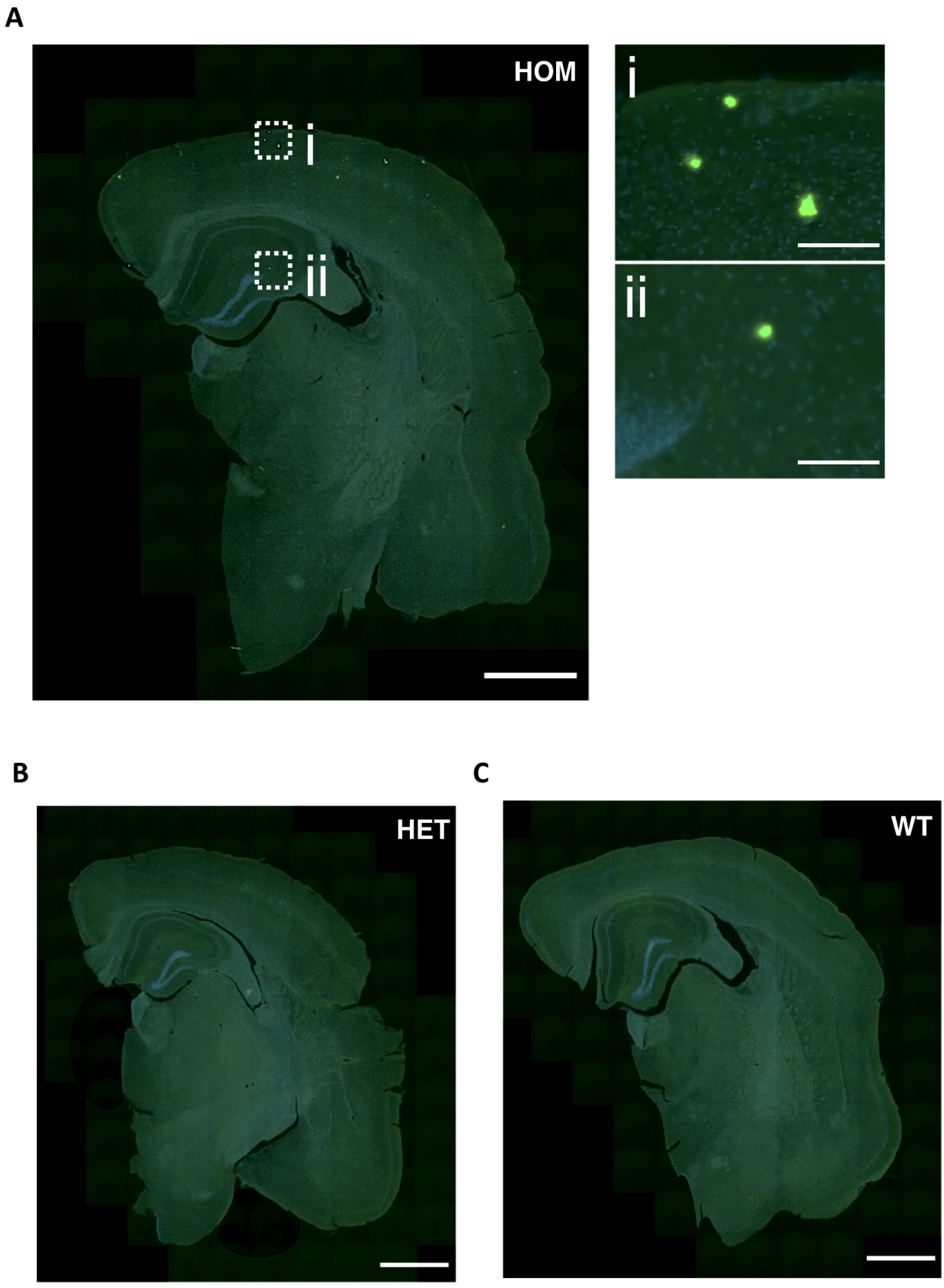
A
HOM
i
ii
i
ii
B
HET
C
WT

Figure 18. Representative images of plaque load in APP^{NLF} HOM, HET and WT mice. 50µm coronal sections from mice were cut and stained with DAPI (blue) to mark nuclei, ThioS (green) to mark dense plaque cores and GFAP (not shown). Images were taken using a 20x objective on a ZEISS Axio Scan Z1 slide-scanner. **(A)** APP^{NLF} HOM slices displayed dense cored Aβ plaques in the cortex and the hippocampus n=10. **(i)** and **(ii)** are zooms of the cortex and hippocampus respectively. (B) The APP^{NLF} HET slices, n=10 and (C) the WT slices, n=9 displayed no plaques. Scale bar = 1mm, inset scale bar = 50µm.

Ai

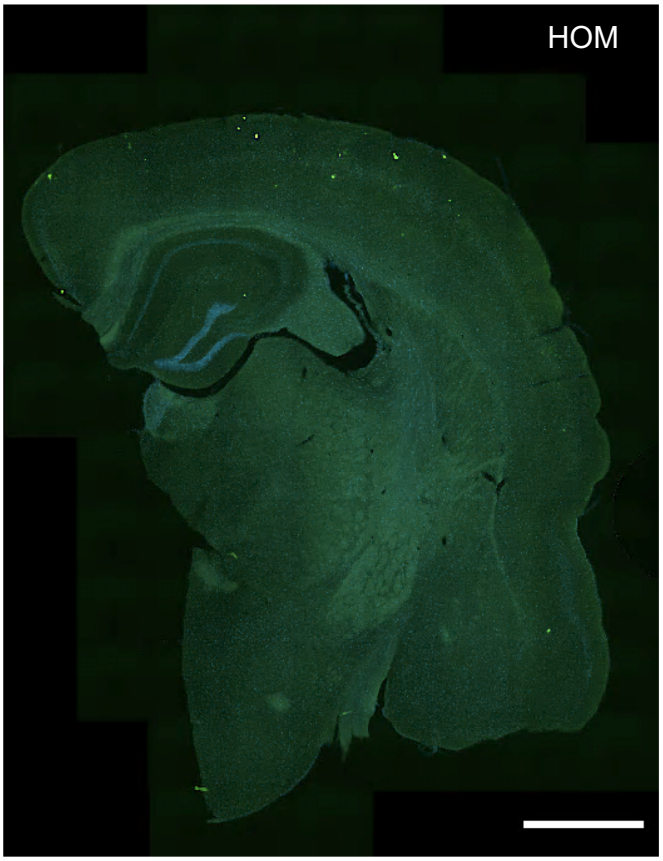
HOM

Aii

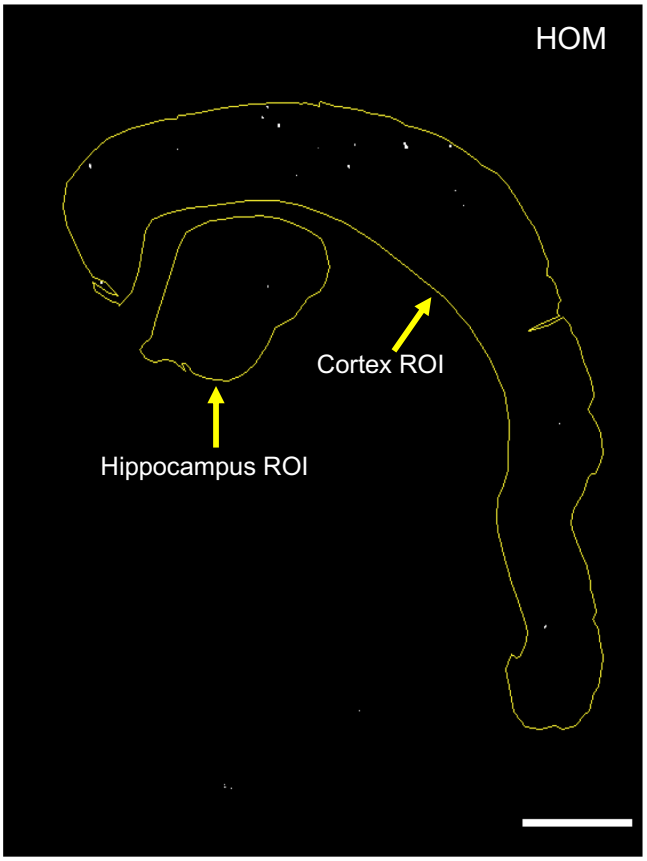
HOM
Cortex ROI
Hippocampus ROI

Bi

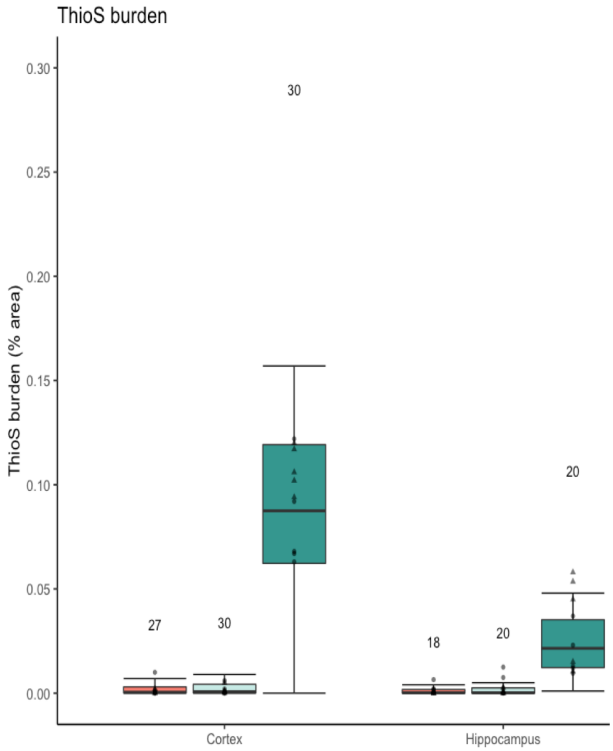
ThioS burden
ThioS burden (% area)
0.30
0.25
0.20
0.15
0.10
0.05
0.00
27
30
30
18
20
20
Cortex
Hippocampus

Bii

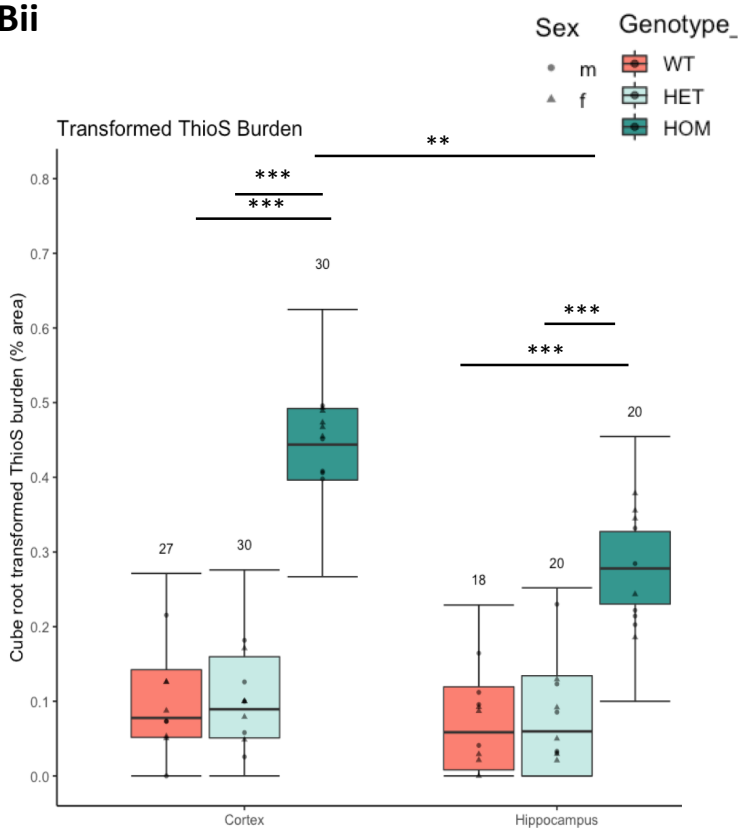
Sex
m
f
Genotype_
WT
HET
HOM
Transformed ThioS Burden
Cube root transformed ThioS burden (% area)
**
***
***
***
***
0.8
0.7
0.6
0.5
0.4
0.3
0.2
0.1
0.0
27
30
30
18
20
20
Cortex
Hippocampus

Figure 19. Quantifying plaque load. (Ai) A representative image of a HOM mouse brain. **(Aii)** Thresholded version of the image in Ai, indicating the manually outlined regions of interest. **(Bi)** Quantification of the percentage of area containing ThioS in WT, HET and HOM mouse slices. Boxplots of the data are shown. The upper and lower bounds of the boxplot represent the 1st and 3rd quartile of the data, the median line is shown. Whiskers illustrate 1.5x the interquartile range. Each point represents the median value from a mouse. Numbers denote number of observations. **(Bii)** A linear mixed effects model was constructed. The fixed effects were genotype, region and sex. The random effects accounted for the fact that multiple images were taken from the same mouse. The data was cube root transformed in order to meet the assumptions of the model. An ANOVA on the linear mixed effects model demonstrated a significant interaction between genotype and region ($F=9.28$, $p<0.001$), and no effect of sex ($F=0.23$, $p=0.63$). A post-hoc Tukey adjusted pairwise multiple comparisons test revealed significant differences between ThioS burden in HOM cortex and WT cortex ($p=3.11e-14$), HOM cortex and HET cortex ($p=2.66e-15$), HOM hippocampus and WT hippocampus ($p=6.27e-10$), HOM hippocampus and HET hippocampus ($p=1.65e-09$), and HOM cortex and HOM hippocampus ($p=4e-07$). Boxplots of the cube root transformed data are shown. The upper and lower bounds of the boxplot represent the 1st and 3rd quartile of the data, the median line is shown. Whiskers illustrate 1.5x the interquartile range. Each point represents the median value from a mouse. Numbers denote number of observations. Female (f), male (m). Scale bar = 1mm. '**' $p<0.01$, '***' $p<0.001$.

A

```
Type III Analysis of Variance Table with Satterthwaite's method
                Sum Sq Mean Sq NumDF DenDF  F value    Pr(>F)
Genotype        2.22318 1.11159     2   138 146.0520 < 2.2e-16 ***
Region          0.15735 0.15735     1   138  20.6737  1.18e-05 ***
Sex             0.00175 0.00175     1   138   0.2304 0.6319603
Genotype:Region 0.14123 0.07062     2   138   9.2781 0.0001657 ***
---
Signif. codes:  0 '***' 0.001 '**' 0.01 '*' 0.05 '.' 0.1 ' ' 1
```

B

Pairwise Differences of Genotype*Region	Estimate	SE	df	t.ratio	p.value
WT Cortex - HET Cortex	-0.0055784	0.023156813	137.9920011	-0.2409	0.999887
WT Cortex - HOM Cortex	-0.3357962	0.023156813	137.9920011	-14.501	3.11E-14
HET Cortex - HOM Cortex	-0.33021779	0.022525431	137.9941306	-14.6598	2.66E-15
WT Hippocampus - HET Hippocampus	-0.01061867	0.028528124	137.9927469	-0.37222	0.999051
WT Hippocampus - HOM Hippocampus	-0.20448964	0.028528124	137.9927469	-7.168	6.27E-10
HET Hippocampus - HOM Hippocampus	-0.19387097	0.027756072	137.9941306	-6.98481	1.65E-09
WT Cortex - WT Hippocampus	0.02523588	0.026643684	76.73847409	0.947162	0.932742
HET Cortex - HET Hippocampus	0.02019561	0.025276418	76.73847409	0.79899	0.96686
HOM Cortex - HOM Hippocampus	0.15654243	0.025276418	76.73847409	6.193221	4E-07

Table 8. Results of the linear mixed effects model on cube root transformed ThioS burden in WT, APP^{NLF} HET and HOM cortex and hippocampus. (A) A linear mixed effects model using the cube root transformed ThioS data was constructed. The fixed effects were genotype, region and sex. The random effects accounted for the fact that multiple images were taken from the same mouse. A type III ANOVA on the linear mixed effects model revealed a significant interaction between genotype and region, and no effect of sex. **(B)** A post-hoc Tukey adjusted pairwise comparison revealed significant differences between HOM ThioS burden and HET and WT ThioS burden, as well as HOM ThioS burden in the cortex vs HOM ThioS burden in the hippocampus.

Formula in A: transformed_ThioS_MM<-

lmer(cuberootthios~Genotype*Region+Sex+(1|Mouse:Image_number),

data=ThioS_data_MH)

Anova(transformed_ThioS_MM)

Formula in B: emmeans(transformed_ThioS_MM, list(pairwise ~ Genotype*Region), adjust = "tukey")

3.2.9 GFAP Load Increases Close to Plaques

Since only HOM mice displayed plaques, analysis of GFAP positive astrocyte load in relation to distance from plaque was only measured in HOM cortices. **Figure 20A** is a representative image of a 12-month APP^{NLF} HOM mouse brain slice. 3 slices at approximately -1mm, -2mm and -3mm from Bregma were sampled.

It was difficult to threshold GFAP accurately over the whole slice. Therefore, cortical plaques were Isolated **(figure 20Bi)**, thresholded and the percentage area covered by GFAP was measured in 20µm concentric rings, up to 200µm from the edge of the plaque core, measured by ThioS **(figure 20Bii and figure 21A)**. 7 plaques per mouse were isolated. A linear mixed effects model was used to compare GFAP load at varying distances from the edge of the plaque core. The fixed effects were distance and sex. The random effects accounted for the fact that multiple images were taken from the same mouse. The data was cube root transformed in order to improve the fit of the data to the model **(figure 21B)**. A type III ANOVA on the linear mixed effects model revealed there was a main effect of distance from the plaque core ($F=390.41$, $p<2e-16$), but no effect of sex ($F=0.146$, $p=0.70$) **(table 9A)**. Hence, sex was removed from the model. There was a significant increase in GFAP load between 2-180µm from the plaque core, when compared to 200µm from the plaque core ($p<0.001$, linear mixed effects model on transformed data, **table 9B**), indicating a concentration of GFAP positive astrocytes close to plaques. In the future, it would be beneficial to sample even further from the plaque in order to identify the distance from the plaque core where there is no significant difference in GFAP load.

I also measured total GFAP load over the entire plaque containing crops from HOM mice and crops of the same size from WT mice (isolated whilst blind to the GFAP channel) **(figure 21C)**. The GFAP load in HOM crops containing plaques was approximately 4 times larger than in WT crops. A linear mixed effects model was constructed using cube root transformed GFAP data in order to better fit the assumptions of the model. The fixed effects were genotype and sex. The random effects accounted for the fact that multiple images were taken from the same mouse. A type III ANOVA on the linear mixed effects model **(table 10)** demonstrated a

significant difference in GFAP load between genotypes (F= 209.91, p=1.28e-10), and no effect of sex (F=0.06, p=0.81).

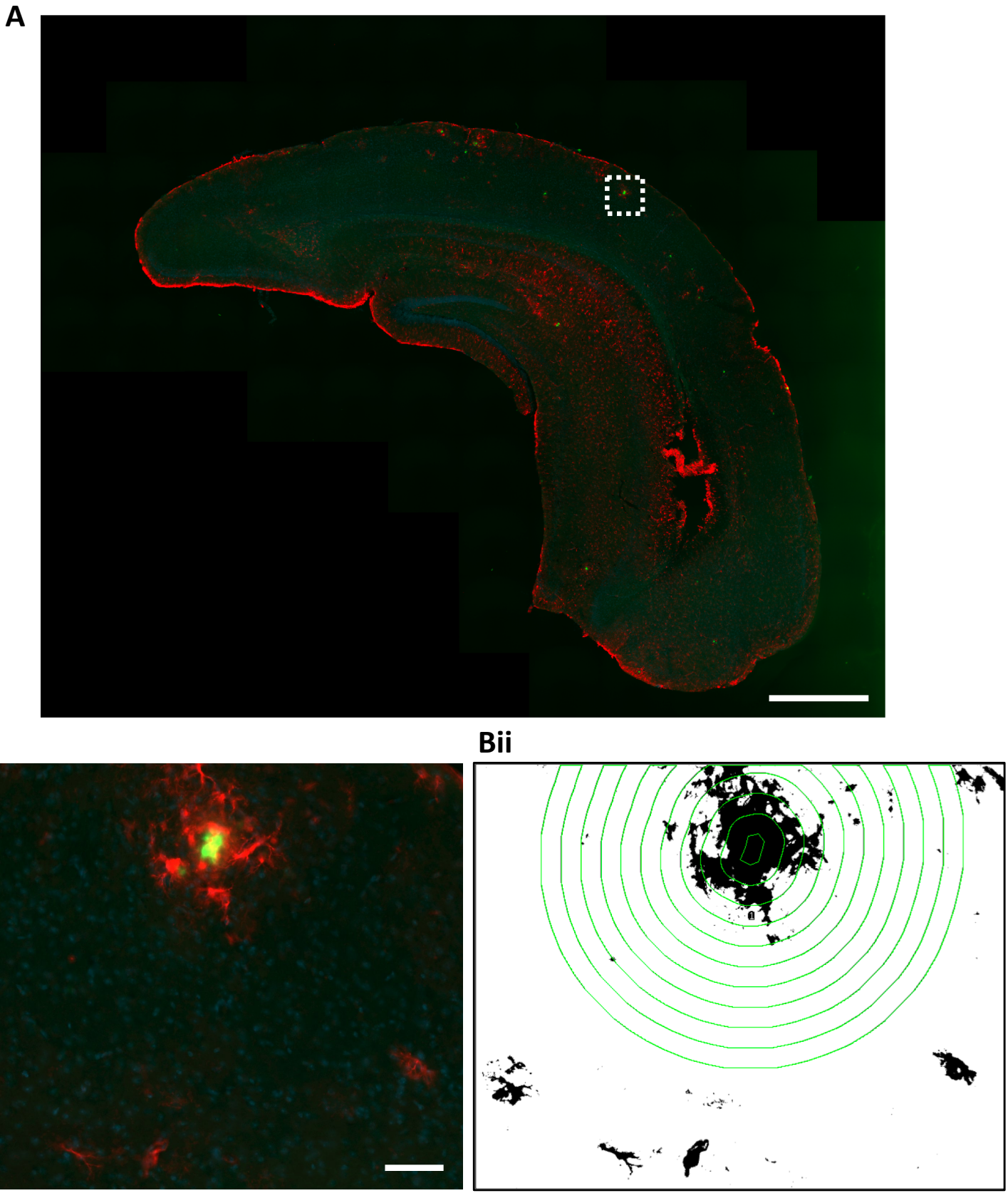
A
Bi
B
Bii

Figure 20. Representative images illustrating GFAP load increases around plaques. Coronal sections of HOM APP^{NLF} mouse brain were stained with ThioS to mark fibrillar Aβ plaques (green), DAPI to mark nuclei (blue), and GFAP to mark activated astrocytes (red). **(A)** a representative image. An example plaque that was isolated and analysed is marked by the white dashed box. Scale bar = 1mm. **(Bi)** An enlarged image of the example plaque highlighted by the white dashed line. Scale bar = 100µm. **(Bii)** Manually thresholded GFAP in image in Bi (black). The innermost region of interest indicates the boundary of the plaque core which was manually defined. Percentage GFAP was measured in 20µm concentric rings around the boundary of the plaque core (green) using ImageJ.

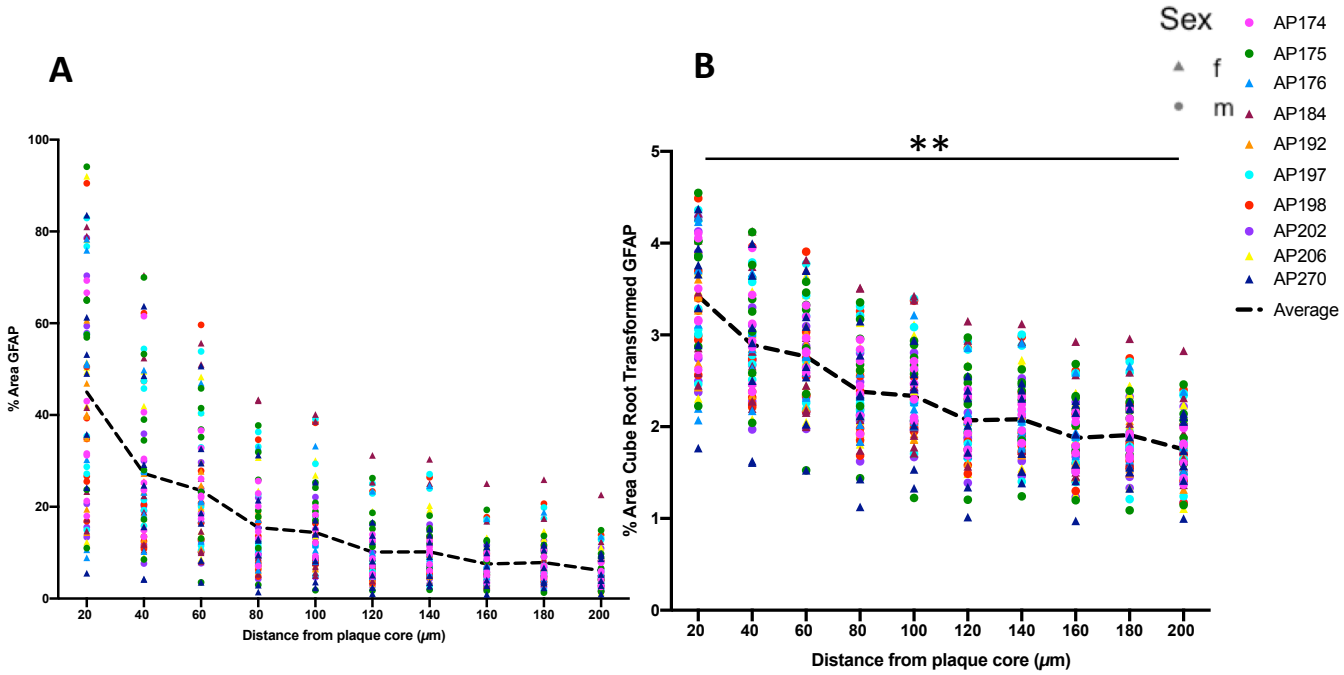
A
B
% Area GFAP
Distance from plaque core (μm)
% Area Cube Root Transformed GFAP
**
Distance from plaque core (μm)
Sex
f
m
AP174
AP175
AP176
AP184
AP192
AP197
AP198
AP202
AP206
AP270
Average

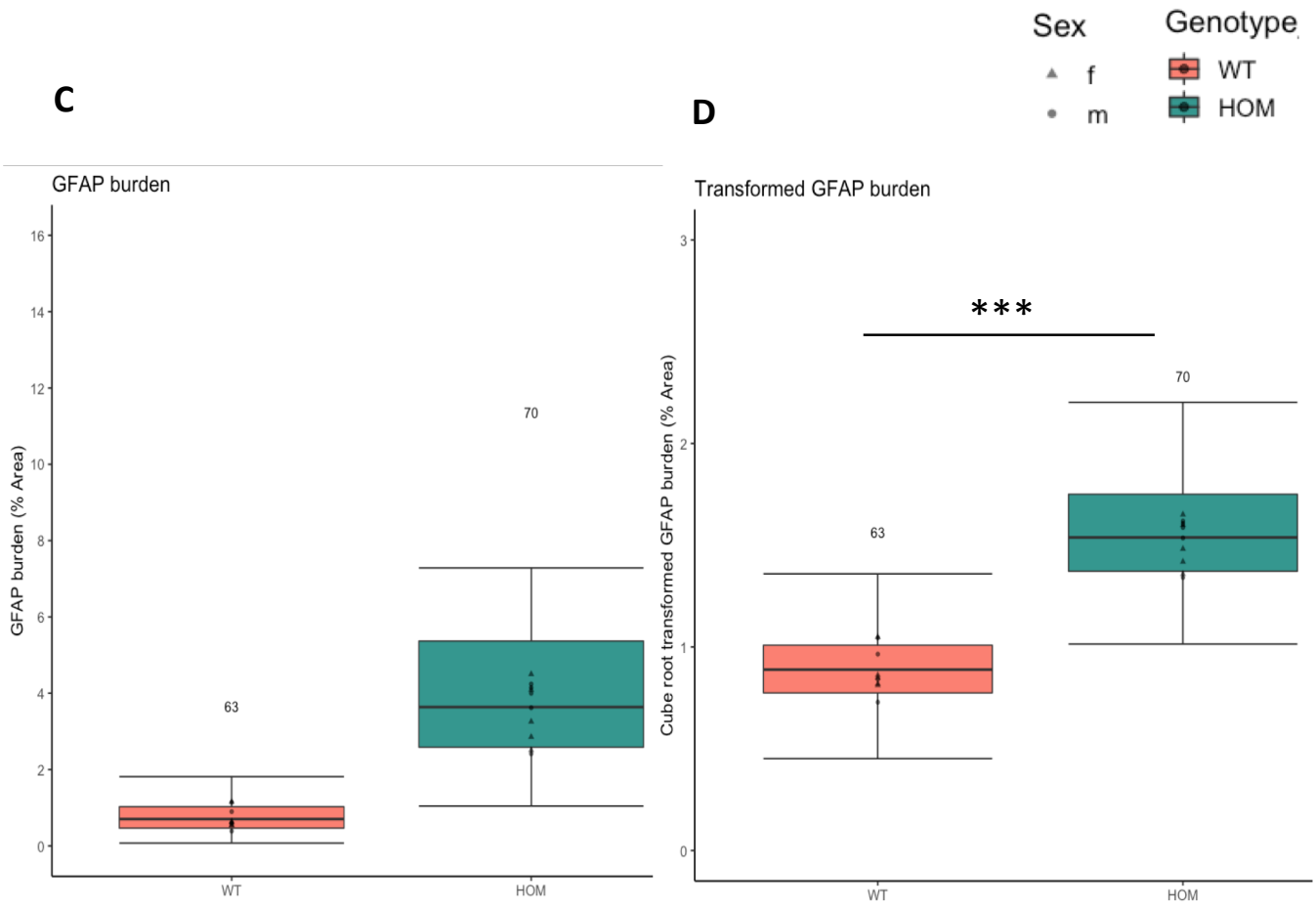
C
D
Sex
f
m
Genotype
WT
HOM
GFAP burden
GFAP burden (% Area)
63
70
WT
HOM
Transformed GFAP burden
Cube root transformed GFAP burden (% Area)
***
63
70
WT
HOM

Figure 21. Quantifying GFAP load in 12-month APP^{NLF} HOM mice. (A) GFAP load was measured in 20µm concentric rings around the edge of plaque cores, manually outlined according to the ThioS stain, up to 200µm. Plaques were sampled from 3 coronal slices of mouse brain, at approximately -1mm, -2mm and -3mm from Bregma. Each coloured dot represents a different mouse. n=10 mice, 7 plaques per mouse. The black dashed line indicates the average percentage (%) area covered by GFAP at each distance. GFAP load decreased with distance from the plaque core. **(B)** A linear mixed effects model was performed on cube root transformed data from **figure 21A** in order to satisfy the assumptions of the model**.** The fixed effects were distance and sex. The random effects accounted for the fact that multiple images were taken from the same mouse. An ANOVA on the linear mixed effects model **(table 9A)** revealed there was no effect of sex (F=0.146, p=0.70). Hence, it was removed from the model. The linear mixed effects model revealed GFAP load significantly increased between 20-180µm from the plaque core when compared to 200µm from the plaque core **(table 9B)**. **(C)** The total GFAP load over crops made from HOM and WT mice was measured. Upper and lower bounds of the boxplot represent the 1st and 3rd quartile of the data, the median line shown. Whiskers illustrate 1.5x the interquartile range. Each point represents the median value from a mouse. Numbers denote the number of observations.
HOM mice displayed more GFAP load than WT mice. **(D)** A linear mixed effects model was performed on cube root transformed data from **figure 21C** in order to satisfy the assumptions of the model**.** The fixed effects were genotype and sex. The random effects accounted for the fact that multiple images were taken from the same mouse. A type III ANOVA was performed on cube root transformed GFAP load over the whole image, GFAP load was significantly different between HOM and WT crops (F=209.91, p=1.28e-10). Boxplot as described in **figure 21C**. Female (f), male (m).

A

```
Type III Analysis of Variance Table with Satterthwaite's method
      Sum Sq Mean Sq NumDF DenDF F value Pr(>F)
Dist 177.895 19.7661     9   621 390.417 <2e-16 ***
Sex    0.007  0.0074     1    68   0.146 0.7036
---
Signif. codes:  0 '***' 0.001 '**' 0.01 '*' 0.05 '.' 0.1 ' ' 1
```

B

```
Linear mixed model fit by REML. t-tests use Satterthwaite's method ['lmerModLmerTest']
Formula: cube_root ~ Dist + (1 | Mouse_ID:plaque_number)
   Data: GFAP_in_concentric_rings_

REML criterion at convergence: 197.2

Scaled residuals:
    Min      1Q  Median      3Q     Max
-4.6678 -0.5225  0.0156  0.5103  4.1480

Random effects:
 Groups                 Name        Variance Std.Dev.
 Mouse_ID:plaque_number (Intercept) 0.19889  0.446
 Residual                           0.05063  0.225
Number of obs: 700, groups:  Mouse_ID:plaque_number, 70

Fixed effects:
            Estimate Std. Error        df t value Pr(>|t|)
(Intercept)  1.75319    0.05970 102.70438  29.365  < 2e-16 ***
Dist20       1.67004    0.03803 621.00000  43.910  < 2e-16 ***
Dist40       1.13793    0.03803 621.00000  29.920  < 2e-16 ***
Dist60       1.01098    0.03803 621.00000  26.582  < 2e-16 ***
Dist80       0.62899    0.03803 621.00000  16.538  < 2e-16 ***
Dist100      0.58234    0.03803 621.00000  15.312  < 2e-16 ***
Dist120      0.31615    0.03803 621.00000   8.312 5.92e-16 ***
Dist140      0.32806    0.03803 621.00000   8.626  < 2e-16 ***
Dist160      0.12467    0.03803 621.00000   3.278   0.0011 **
Dist180      0.15653    0.03803 621.00000   4.116 4.38e-05 ***
---
Signif. codes:  0 '***' 0.001 '**' 0.01 '*' 0.05 '.' 0.1 ' ' 1
```

Table 9. Results of the linear mixed effects model investigation of cube root transformed percentage (%) GFAP in concentric rings around a plaque. (A) A linear mixed effects model using the cube root transformed GFAP data was constructed. Fixed effects were distance and sex. The random effects accounted for the fact that multiple images were taken from the same mouse. A type III ANOVA on the linear mixed effects model revealed a main effect of distance and no effect of sex. Hence, sex was removed from the model. (**B**) The revised linear mixed effects model demonstrated significant increase in GFAP load between 20-180µm from the plaque core when compared to 200µm from the plaque core.

Formula in A:

transformedMEGFAPrings<-lmer(cube_root~Dist+Sex+(1|Mouse_ID:plaque_number), data=GFAP_in_concentric_rings_)

Anova(transformedMEGFAPrings)

Formula in in B: transformedMEGFAPrings<-lmer(cube_root~Dist+(1|Mouse_ID:plaque_number), data=GFAP_in_concentric_rings_)

```
Type III Analysis of Variance Table with Satterthwaite's method
          Sum Sq Mean Sq NumDF DenDF  F value    Pr(>F)
Genotype 11.2971 11.2971     1    16 209.9127 1.284e-10 ***
Sex       0.0034  0.0034     1    16   0.0629    0.8051
---
Signif. codes:  0 '***' 0.001 '**' 0.01 '*' 0.05 '.' 0.1 ' ' 1
```

Table 10. Results from linear mixed effects model investigation of cube root transformed percentage GFAP over whole image crop. (A) A linear mixed effects model using the cube root transformed GFAP data was constructed. Fixed effects were distance and sex. The random effects accounted for the fact that multiple images were taken from the same mouse. A type III ANOVA on the linear mixed effects model revealed a main effect genotype and no effect of sex.

Formula: transformedgfapwholeMM<-
lmer(cube_root_gfap_whole~Genotype+Sex+(1|Mouse_ID),
data=GFAP_over_whole_image_R)
Anova(transformedgfapwholeMM)

3.3 Discussion

3.3.1 Summary of Findings

This chapter characterised synapse pathology in 12-month APP^{NLF} HOM and WT mice, and plaque load and astrogliosis in 12-month APP^{NLF} HOM, HET and WT mice. Paired synaptic density in the somatosensory cortex of HOM and WT mice did not differ when measured over the whole image, irrespective of the presence of a plaque. However, paired synapse density did reduce close to the plaque core boundary. Aβ was found in paired pre and post synaptic puncta within 6µm and 8µm from the plaque core respectively. Plaques were present in many shapes, sizes and densities in APP^{NLF} HOM mice. Finally, GFAP positive astrocyte load increased close to plaque cores in APP^{NLF} HOM mice, and overall GFAP load was larger in APP^{NLF} HOM cortical cropped images compared to WT cortical cropped images.

3.3.2 Synapse Density in the APP^{NLF} Mouse

The APP^{NLF} mouse model is a knock-in amyloidopathy model created by Saito et al. (Saito et al. 2014). The expression of APP is driven by the endogenous promoter; hence, the APP is expressed at a physiologically relevant concentration, location and timing, with increased Aβ expression due to the NLF mutations. This model of amyloidopathy can be seen as an improvement on previous transgenic mouse models, where the effects of Aβ pathology cannot be distinguished from inadvertent effects of overexpression of APP or other APP cleavage products. Saito et al. indicated that synaptic protein density reduces close to the plaque. However, no quantitative analysis was done. Since synapse pathology is the strongest correlate of cognitive decline (Terry et al. 1991) and is fundamental to AD pathology, we decided use array tomography to quantify synaptic density and Aβ colocalization with synaptic puncta.

We found no difference in synaptic density over the whole image when comparing APP^{NLF} HOM images with and without plaque and WT images **(figure 14A)**. This is not surprising since previous studies using array tomography to analyse synaptic density have shown that the synapse loss is found in the plaque proximal region (Jackson et al. 2016; Koffie et al. 2009).

I showed that in 12-month APP^{NLF} HOM somatosensory cortex, there is a significant reduction in paired synaptic density between 2-10µm from the plaque core boundary when compared to 40µm from the plaque core boundary, with a maximum density reduction of 50% 2µm from the plaque core **(figure 14Ci)**. There was no significant difference in synaptic density between 12µm from the plaque core boundary to 40µm from the boundary **(figure 14Cii)**. These findings concur with the current hypothesis that oligomeric Aβ, which can be found close to plaque cores, is the most toxic form of Aβ and is a key driver of synapse loss (Shankar et al. 2007; Ferreira and Klein 2011).

Other array tomography studies conducted on 8-10-month APP/PS1 transgenic mice showed similar plaque proximal reduction in synaptic puncta (Koffie et al. 2009; Jackson et al. 2016). For example, Jackson et al., demonstrated a 1.5-fold reduction in synapsin-1 density and a 1.2-fold reduction in PSD95 density from >50µm from the plaque to < 20 µm from the plaque (Jackson et al. 2016). Notably, the synapse loss in 8-10-month old APP/PS1 mice appears to extend further beyond the plaque than in 12-month APP^{NLF} mice, where the synapse loss is confined to 10µm from the core of the plaque. This more extensive synapse loss could be explained by the APP/PS1 mice having greater Aβ pathology, with a quicker onset (Jankowsky et al. 2004). Alternatively, this could be due to the more conservative criteria for synapse density implemented in this study, since Koffie et al. and Jackson et al. both measure unpaired synaptic puncta. In this study, we chose to measure paired synapse density in order to avoid potential fluorescence artefacts, and also because a reduction in paired synapse density may be more indicative of functional deficits.

Synapse loss proximal to plaques has also been observed in human array tomography studies. For example, Koffie et al. demonstrated a reduction in presynaptic synapsin-1 from $1.3x10^9$ puncta/mm^3 at more than 50µm from the plaque to $8x10^8$ puncta/mm^3 at 20µm from than plaque and $6x10^8$ puncta/mm^3 next to the plaque core (Koffie et al. 2012). Notably, the magnitude of reduction in synapse density close to plaques were similar in the human AT study (2.2 fold), the aforementioned APP/PS1 AT study (1.5 fold) and this APP^{NLF} AT study (1.9 fold). Additionally, the WT and APP^{NLF} HOM mice displayed similar densities of unpaired pre-synaptic synaptophysin over the whole image as the presynaptic synapsin-1 measured far from plaque in human AT studies (Koffie et al. 2012; Jackson et al. 2019). This could indicate

that although humans have more synapses overall, the cortical pre-synaptic densities (puncta/mm^2) over mouse and human cortex might be similar. A thorough examination of different areas of the human and mouse cortex, along with multiple markers of pre and post-synapses would need to be carried out.

Most interestingly, Sauerbeck et al. have just published a study where they used a super-resolution imaging and analysis workflow called SEQUIN to investigate synapse density around plaques in 18-month APP^{NLF} HOM mice (Sauerbeck et al. 2020). According to Sauerbeck et al., SEQUIN offers a similar resolution as array tomography. However, the process is somewhat more efficient. Rather than physically sectioning the tissue to achieve adequate resolution and later reconstructing the 3D image, SEQUIN uses an Airyscan unit on a confocal microscope to acquire data simultaneously on 32 detectors, achieving adequate resolution without ultra-thin sectioning. Sauerbeck et al. found a reduction of synapse density within 25µm of the centre of the plaque, when compared to 100µm from the centre of the plaque, reaching a maximal reduction in synapse density of ~50% at 0µm from the plaque centre. This result is very similar to the synapse loss measured in this study, where significant synapse loss was seen within 10µm of the edge of the core of the plaque, and a maximal reduction in synapse density of ~50% was measured at 2µm from the edge of the plaque core. This might indicate that whilst plaque load has been shown to increase between 12 and 18-month APP^{NLF} mice (Saito et al. 2014), perhaps synapse loss around individual plaques does not advance.

Plaque associated synapse loss is a common finding in all of these studies. This suggests that Aβ plaques are not simply inert structures, as some have suggested (Martins et al. 2008). In fact, it seems likely that Aβ plaques could be a source of synaptotoxic oligomeric species, resulting in vulnerable peri-plaque synapses. Additionally, the synapses around plaques may be subject to enhanced elimination by astrocytes and microglia. Indeed, Chen et al. demonstrated that astrocytes and microglia in the APP^{NLGF} amyloidopathy model display plaque induced gene expression changes, upregulating genes such as *C1q* and *C4b* (Complement Component 4B) which are associated with synapse elimination, as well as genes associated with endocytosis and lysosomal function (Chen et al. 2019). Hence, I would argue the pathological effects of Aβ plaques warrants therapeutic consideration.

3.3.3 Colocalisation of Aβ in Synaptic Puncta

Aβ colocalised with pre and post-synaptic puncta close to the plaque core, with a maximum of 20% colocalization of OC with paired pre or post-synaptic puncta. The colocalization reduced with distance from the plaque core boundary, and no significant increase in colocalization could be seen beyond 8µm when compared to 20µm from the plaque. Importantly, OC only marks Aβ fibrils and fibrillar oligomers, and so smaller soluble oligomer load was not identified. A halo of fibrillar oligomers usually surrounds dense core plaques and so this decrease in colocalization of OC with synaptic puncta is in accordance with the Aβ plaque halos becoming more diffuse. Whilst soluble oligomers are thought to be the most toxic form of Aβ, fibrillar oligomers are also thought to be toxic (Sengupta et al. 2016), hence it is possible that the synapses we have captured colocalising with OC would have been lost if the animal was given more time, certainly the region of the majority of synaptic loss and the region of colocalization of OC with synapses was the same.

3.3.4 Plaques

The APP^{NLF} mouse displayed a variety of plaque shapes, sizes and densities.

This finding is important as diversity in plaque formation is also seen in human AD post-mortem brains (Liebmann et al. 2016), but was not found in the common transgenic APP/PS1 amyloidopathy model, where all the plaques sampled showed little deviation in ThioS positive plaque cores or AW7 positive halos (Jackson et al. 2016). Hence, the knock-in APP^{NLF} mouse might better model Aβ accumulation and downstream consequences. The events leading to, and the significance of, the diversity in plaque shape, size and density is not thoroughly understood. However, some studies have indicated that dense core plaques are likely to contain dystrophic neurites in their central mass, whereas diffuse plaques lack a morphologically identifiable substructure, mainly composed of extracellular aggregates of Aβ (Dickson and Vickers 2001). Additionally, dense core plaques are surrounded by reactive glia, whereas diffuse plaques are most often not (Serrano-Pozo et al. 2011), and have been associated with less severe disease pathogenesis compared to dense core plaques (D'Andrea and Nagele 2010; Delaère et al. 1991). Thus, perhaps neurodegeneration in AD leads to the formation of dense cores at the centre of plaques, encouraging Aβ sequestration, followed by enhanced presence of toxic soluble Aβ oligomers, reactive glia, more synapse loss around

dense core plaques and thus worse disease pathogenesis. Alternatively, perhaps diffuse plaques are simply early-stage dense core plaques, and with time both Aβ accumulation, the presence of reactive glia and synapse loss would progress. One could test this theory by staining for diffuse plaques using the OC antibody and dense core plaques using a combination of the OC antibody and ThioS in the APP^{NLF} mouse at several early time points, identifying whether diffuse plaques appear first, whether there are intermediate stage plaques, and whether there appears to be a link between diffuse and dense core plaque number. Understanding the significance of diffuse and dense core plaques may prove to be important in designing more targeted Aβ therapeutics alongside other therapeutics which target other aspects of AD such as tauopathy and reactive gliosis.

The dense core plaque burden measured in this study was approximately 0.1% in the cortex and 0.03% in the hippocampus. This is comparable to Saito's original characterisation of this mouse model, where the mice exhibited <0.5% plaque burden in the cortex and hippocampus, with the hippocampus containing fewer plaques than the cortex (Saito et al. 2014). Transgenic mouse models tend to have a much higher dense core plaque burden. For example, 12-month 5xFAD transgenic mice exhibit over 5% and 4% cortical and hippocampal plaque burden, and 11-month APP/PS1 transgenic mice exhibit over 2% and 1% cortical and hippocampal plaque burden. On the other hand, dense core plaque burden in human Braak Stage 5/6 AD cases has been reported to be between 0.03% and 0.5% depending on the location (Liu et al. 2017). Hence, the APP^{NLF} mouse model, mimics amyloid deposition in humans.

3.3.5 Astrogliosis

Increased expression of the intermediate filament protein GFAP in astrocytes is widely acknowledged as a marker of astroglial activation (Eng and Ghirnikar 1994). GFAP positive astrocytes have been shown to surround Aβ plaques in the human brain (Kamphuis et al. 2014) and in many mouse models of amyloidopathy (Ruan et al. 2009; Sakakibara et al. 2019). Saito et al had previously shown that GFAP positive astrocytes surround Aβ plaques in the APP^{NLF} mouse model (Saito et al. 2014). However, a quantitative analysis of GFAP load in relation to plaque distance was not carried out. Here, I show that GFAP load significantly

increases between 20-180µm from the plaque core, when compared 200µm from the plaque core. Bouvier et al. found a similar result in human AD tissue, where they measured how the number of GFAP positive astrocytes varied with distance from the centre of the plaque core, demonstrating a peak in GFAP positive astrocytes at 40µm (Bouvier et al. 2016). In the future it would be useful to quantify GFAP burden over the whole cortex, and quantify the number of GFAP positive astrocytes around the plaque so that GFAP load in the APP^{NLF} mouse can be directly compared to other amyloidopathy mouse models and human AD.

Previous work has shown that the number of GFAP positive astrocytes around plaques does not correlate with plaque size in humans (Serrano-Pozo et al. 2013), and in mice the spatial distribution of astrocyte cell bodies was not altered by the presence of plaques (Galea et al. 2015). Hence, it appears that astrocytes in the vicinity of a plaque most likely alter their phenotype, increasing expression of GFAP and re-orientating their processes towards plaques, rather than there being a migration of GFAP positive astrocytes. The function of this increase in GFAP expression remains unclear. Deletion of GFAP and vimentin in APP/PS1 mice increased amyloid plaque and dystrophic neurite load, suggesting a protective role in limiting neurite damage and plaque pathogenesis (Kraft et al. 2013). However, if you were to take the stance that plaques sequester the more toxic oligomers, then a reduced plaque load in the presence of GFAP positive astrocytes might be seen as harmful. The reality is that the phenotypic changes occurring in astrocytes around plaques are complex and many more factors beyond alterations in GFAP expression are important. Single cell RNA-seq analysis of astrocytes in the vicinity of plaques and far from plaques would help us identify the multifarious phenotypic changes occurring in astrocytes in AD.

3.3.6 Limitations and Future Work

This chapter characterises pathology in a knock-in mouse model of AD. Whilst the knock-in mouse models avoids some of the limitations associated with transgenic models, there are still inherent limitations mouse models. Firstly, the mice are genetically engineered and so are models of the rarer familial form of AD, rather than sporadic AD. Secondly, the APP^{NLF} model is an amyloidopathy model, and so does not express tau pathology, the other major pathological hallmark of AD. Hence, even though the focus of this study is amyloidopathy, any

interaction between Aβ and tau pathology is not modelled. Thirdly, studies have indicated that mouse and human synapses and astrocytes exhibit elements of morphological, transcriptional and functional differences (Bayés et al. 2012; Oberheim et al. 2009; Zhang et al. 2016). Nevertheless, there are conserved features of synapses and astrocytes between mice and humans (Curran et al. 2020; Zhang et al. 2016). Hence, mouse models remain a valuable tool for dissecting mechanisms of health and disease.

A technical limitation of this work is the core of plaques used to measure synapse density with distance were approximations manually chosen based on the density of signal. In the future, it would be useful to double stain tissue with ThioS and OC in order to measure dense core and halo size more accurately. Additionally, the slices used in the immunohistochemistry study were relatively thick (50µm), meaning it was difficult to image and threshold GFAP over the whole cortex. In the future, thinner sections will be cut in order to measure this.

This chapter illustrated that there is a reduction in synapse density and an increase in GFAP positive astrocytes around plaques. However, the interaction of the two have not been investigated. Most studies attribute synapse pruning to microglia (Hong et al. 2016). However, some have indicated that astrocytes might have phagocytic properties and thus play an active role in synapse loss and Aβ clearance around plaques (Gomez-Arboledas et al. 2018). Hence, it would be interesting to use immunohistochemistry and array tomography to investigate the colocalization of Aβ and synaptic puncta with astrocytes and microglia in mouse and human, e.g. by looking at ThioS, OC, SY38 and GFAP/ IBA1 (allograft inflammatory factor 1) colocalization.

The studies in this chapter are descriptive experiments. Understanding the functional consequences of activated astrocytes will be fundamental to designing novel AD therapies.

3.4 Chapter Conclusion

The studies in this chapter illustrate a reduction in synapse density and an increase in GFAP positive astrocytes around morphologically identified dense core plaques in 12-month APP^{NLF} mice. Quantifying synapse loss and GFAP positive astrogliosis around diffuse plaques was not in the scope of this study. Nevertheless, others have reported surprisingly little synapse loss

and reactive gliosis around diffuse plaques (Masliah et al. 1990; Serrano-Pozo et al. 2011). This indicates substantial pathological differences between diffuse and dense core plaques. Unlike previous reports of plaque morphology in the APP/PS1 transgenic amyloidopathy model (Jackson et al. 2016), the APP^{NLF} mouse displayed a range of plaque shapes, sizes and densities, mirroring the diversity of plaque morphology seen in humans (Liebmann et al. 2016). In the future, the APP^{NLF} mouse model could be used to dissect how diffuse and dense core plaques form, why they display such pathological differences and how to best target amyloid therapeutics towards the more pathological dense form.

Whilst this study found differences in plaque morphology between the APP^{NLF} and APP/PS1 amyloidopathy mouse models, the magnitude of maximal reduction in synapse density close to dense core plaques was similar in this APP^{NLF} AT study (1.9 fold) as AT studies of APP/PS1 cortex (1.5 fold) and human cortex (2.2 fold) (Koffie et al. 2012). This suggests that dense core plaque associated synapse loss is a robust finding and emphasises the fact that Aβ plaques are not simply inert structures, as some have suggested (Martins et al. 2008). The debate about which mouse model to use is more complex than simply understanding which model best mimics the human condition. Ultimately, it will depend on the question being asked and the resources (time and money) available. Whilst the APP^{NLF} mouse model may better mimic the diversity of plaque formation seen in human AD, the trade-off compared to using the transgenic APP/PS1 mouse model is time and money. The APP^{NLF} mouse takes considerably longer to develop plaque pathology than the APP/PS1 model, and given the end result of plaque associated synapse loss is similar between the two mouse lines, some may still favour the APP/PS1 mouse. However, if one was investigating plaque morphology or comparing synapse and dendrite vulnerability at the very early stages of AD, it may be more beneficial to use the APP^{NLF} mouse model.

In addition to Aβ load, synapse loss around plaques may be affected by astrocyte and microglia load, since both cell types have been implicated in phagocytosis of synapses. In this study I demonstrated that GFAP positive reactive astrocyte load was inversely proportional to distance from the plaque core boundary. Similar results have been shown in the APP/PS1 mouse model (Ruan et al. 2009) and human AD brain (Kamphuis et al. 2014). Nevertheless, the diversity of the reactive astrocyte phenotype is being realized (Zamanian et al. 2012).

Hence, GFAP alone is unlikely to mark all reactive astrocytes. In the future, it will be useful to conduct similar IHC experiments, but stain for a range of reactive astrocyte markers which are identified later in this thesis, such as *Nqo1* (NAD(P)H Quinone Dehydrogenase 1), *Gsta4* (Glutathione S-Transferase Alpha 4) and *Prdx5* (Peroxiredoxin 5) - genes involved in the NRF2 response and upregulated in pathology associated astrocytes in our study. Additionally, one could stain for *Atp6ap1* (ATPase H+ Transporting Accessory Protein 1), *Ctsd* (Cathepsin D) and *Fuca1* (Alpha-L-Fucosidase 1)- genes involved in autophagy, or *Arpc1b* (Actin Related Protein 2/3 Complex Subunit 1B), *Gpx4* (Glutathione Peroxidase 4), and *Man2b1* (Mannosidase Alpha Class 2B Member 1) - genes reported to be expressed highly in plaque associated glia in Chen et al. (2020) and which are also highly expressed in pathology associated astrocytes in our study.

Chapter 4

Genomic Analysis of Astrocytes in Mouse Models of AD

4.1 Chapter Introduction

In the previous chapter I described the presence of GFAP positive astrocytes around plaques. However, GFAP expression is simply a marker protein, indicating activated astrocytes (Pekny and Pekna 2004). Previous research has shown that activated astrocytes encompass a spectrum of phenotypes, dependent on aspects such as stimuli (Zamanian et al. 2012), age (Clarke et al. 2018) and location (Tsai et al. 2012). Hence, GFAP expression alone cannot predict astrocytic phenotype. RNA-seq analysis of gene expression in astrocytes provides a much richer understanding of activated astrocyte phenotypes.

Microarray and RNA-seq analysis of human post-mortem AD astrocytes has indicated that genes involved in the immune response, proteolysis and mitochondria function are dysregulated (Sekar et al. 2015; Simpson et al. 2011). Whilst these studies are useful, post-mortem studies only reflect advanced AD stages and the molecular changes that occur in astrocytes after years of patho-progression. RNA-seq analysis of astrocytes from mouse models of AD offer the opportunity to understand earlier pathological mechanisms and have the potential to reveal therapeutic targets. In this chapter I compare gene expression changes in astrocytes in amyloidopathy models (APP/PS1 and APP^{NLF}) and a tauopathy model ($MAPT^{P301S}$), relating these gene changes to those seen in human AD. Extraction, sequencing and initial analysis of the astrocyte translatome from the $MAPT^{P301S}$ mice was carried by Dr Zoeb Jiwaji, a member of the Hardingham lab, I carried out the rest of the data collection and analysis.

4.1.1 Translating Ribosome Affinity Purification (TRAP)

The amyloidopathy and tauopathy gene expression datasets were obtained using a technique called TRAP **(figure 22)**. TRAP enables cell type specific isolation of translating RNA (Heiman et al. 2014). The *Aldh1l1* promoter drives expression of green fluorescent protein (GFP) tagged ribosomes in astrocytes, and immunoprecipitation of these ribosomes allows translating RNA to be extracted.

TRAP offers a number of benefits over other methods of cell type specific isolation. For example, FACS involves the dissociation of cells into single cell suspension, and laser-capture microdissection involves excision of cells from tissue, both of which can introduce

experimental noise into gene/protein expression profiles and also only reflect the profile of the soma (Heiman et al. 2014). TRAP does not require a single cell suspension and allows profiling of mRNA from the entire cell (Heiman et al. 2014). This is particularly important in astrocytes, where local translation in the fine processes of astrocytes is fundamental to synapse modulation (Sakers et al. 2017). A further advantage of TRAP compared to whole cell RNA isolation is that the translating mRNA profile likely reflects the protein content of the cell more closely than the total mRNA content, since cellular abundance of proteins was found to be predominantly controlled at the level of translation (Schwanhäusser et al. 2011). Hence, translatome analysis may provide a more accurate picture of astrocyte function than transcriptome analysis, and offers the ability to extract cell type specific information without the harsh isolation procedures which would be necessary for proteomic analysis. A limitation of TRAP is that it requires genetic strategies to extract cell type specific information, hence, the technique cannot be used on human tissue (Heiman et al. 2014). For the purposes of these studies where we are using mouse models to dissect the impact of individual pathologies, TRAP is particularly useful.

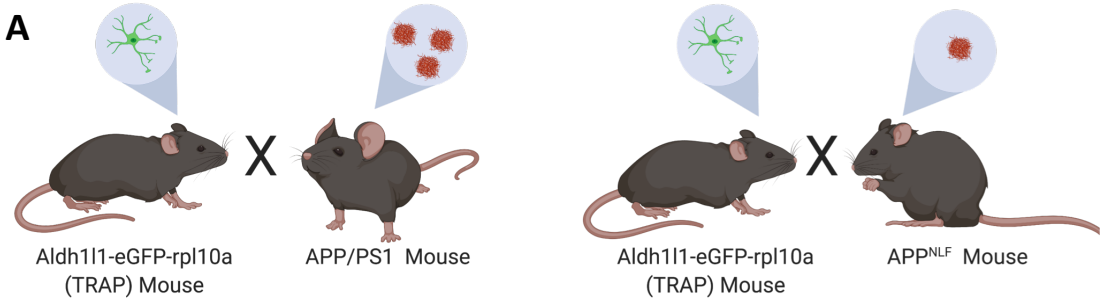

1. Cross bred Aldh1l1-eGFP-rpl10a (TRAP) mice with APP/PS1 or APP^{NLF} mice, resulting in mice with GFP tagged ribosomes in astrocytes and amyloid pathology.

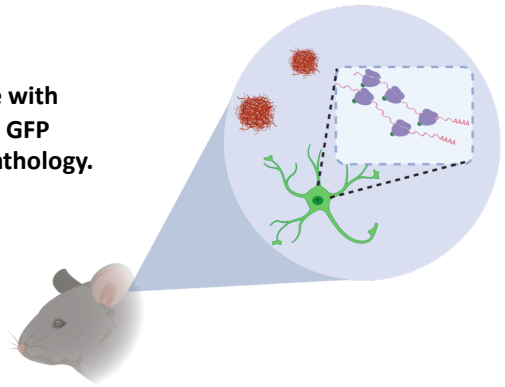

6/12/18 month

2. Homogenised the neocortex. Took RNA as 'input' – RNA from all cells.

3. Ribosomal pulldown of astrocyte RNA

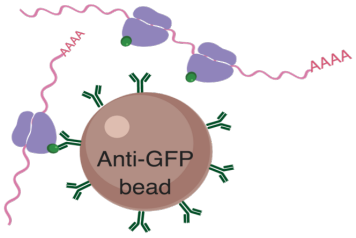

4. Purify RNA. Quality check using a bioanalyser and qPCR then RNA-seq.

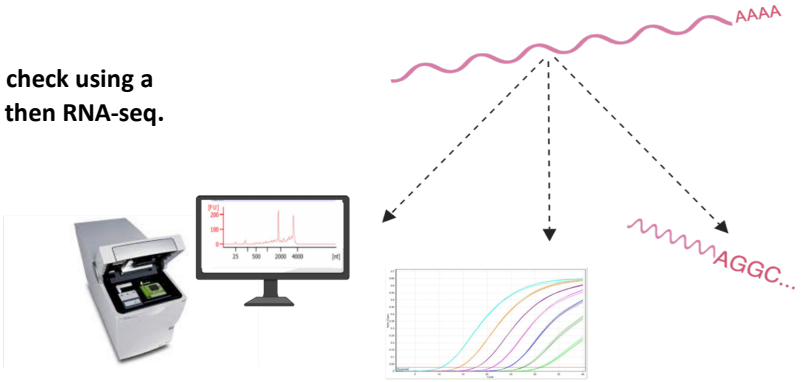

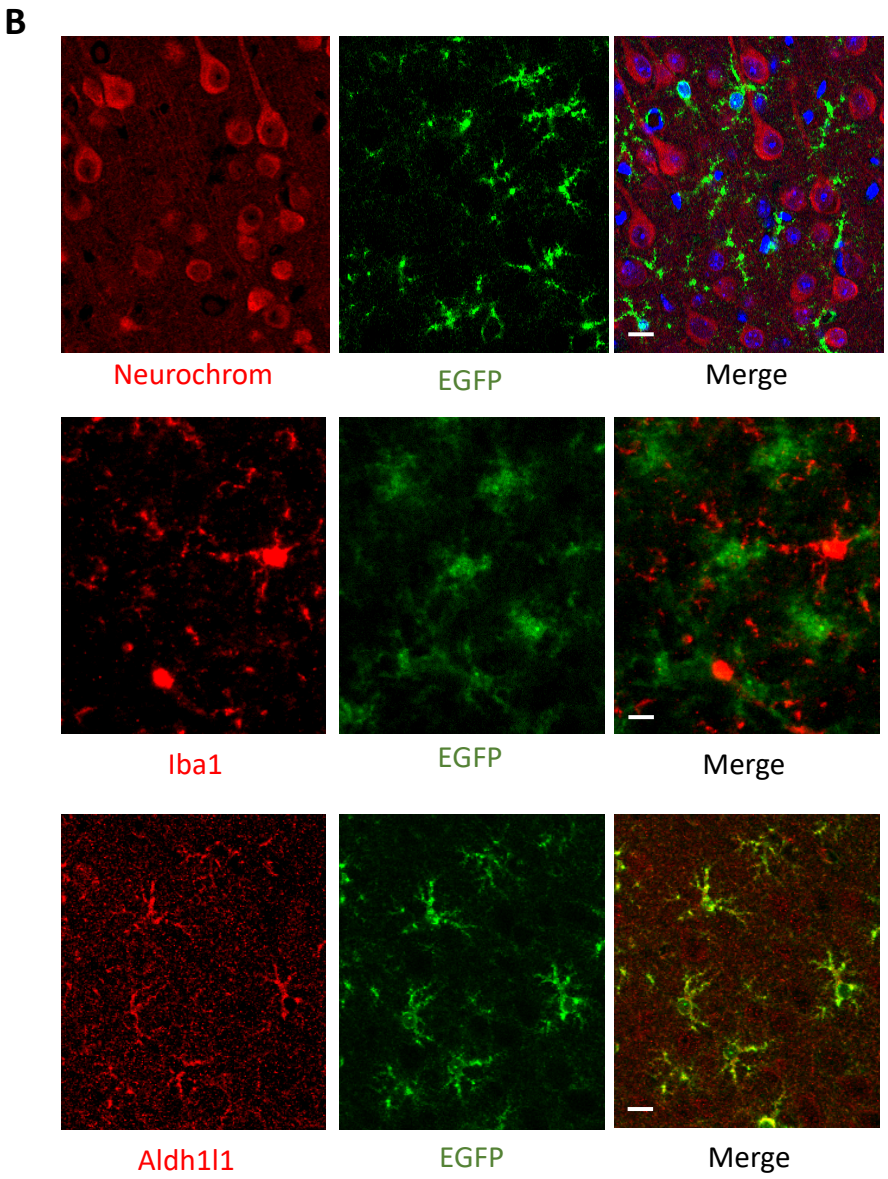

Figure 22 (A) The process of TRAP. Made using Biorender.com **(B)** Immunohistochemical stain of Aldh1l1-eGFP-RPL10a TRAP cortical slices indicated eGFP did not co-localise with Neurochrom positive neurons, or IBA1 positive microglia, but did colocalise with ALDH1L1 positive astrocytes, also confirmed by morphology. Scale bar = 100µm.

4.2 Results

4.2.1 Quality Check of Astrocyte RNA-seq Samples

TRAP was used to extract RNA from astrocytes, using a previously generated transgenic mouse line (Heiman et al. 2008) which was re-derived from frozen sperm on a C57BL/6 background **(see section 2.1)**. Expression of eGFP-RPL10a was driven by the *Aldh1l1* promoter, an astrocyte specific marker, known to be enriched in astrocytes vs other CNS cell types (Srinivasan et al. 2016; Zhang et al. 2014). The *Aldh1l1* promoter has previously demonstrated the best sensitivity and specificity for astrocytes, when compared to other astrocyte markers such as *Gfap*, *S100β* (S100 Calcium-Binding Protein B), *Slc1a3* and *Gjb6* (Gap Junction Protein Beta 6) (Srinivasan et al. 2016). Additionally, extensive validation of the expression profile of eGFP in the Aldh1l1-eGFP-RPL10a TRAP mice was carried out by Dr Zoeb Jiwaji, a member of the Hardingham lab. Briefly, immunohistochemical stains on cortical slices indicated eGFP did not co-localise with Neurochrom positive neurons, or IBA1 positive microglia, but did colocalise with ALDH1L1 positive astrocytes, also confirmed by morphology **(figure 22B)**. Additionally, eGFP positive cells were FACS sorted and the gene expression profiles of GFP positive and GFP negative cells were determined by qPCR. Expression of astrocyte specific genes *Aldh1l1*, *Gfap* and *Slc1a2* were all enriched to similar levels in GFP positive cells compared to GFP negative cells (data not shown).

I carried out a similar qPCR validation of gene expression in all of the amyloidopathy TRAP samples (astrocyte specific RNA) and input samples (RNA from all cell types) that were sent for sequencing **(figure 23)**. Cell type specific markers from Zhang et al (2014) were chosen. Genes were counted as highly selective if they demonstrated >10-fold higher expression in a particular cell type vs other cell types. The APP/PS1 TRAP RNA samples and the APP^{NLF} TRAP RNA samples at all ages showed high expression of *Aldh1l1* compared to input samples, and low expression of *Eno2, Mbp and Cx3cr1*, neuron, oligodendrocyte and microglial specific genes respectively, indicating isolation of astrocyte specific mRNA was successful. Mitochondrial encoded mRNAs are translated by mitochondrial ribosomes (not tagged with eGFP in this model) rather than cytoplasmic ribosomes (Greber and Ban 2016). Therefore, as an additional quality check I investigated the expression of the mitochondrial gene *Mt-rnr2* in

the TRAP and input samples. As expected, expression of *Mt-rnr2* in the TRAP samples was low compared to the input samples **(figure 23)**. This indicated that even within astrocytes, which are densely packed with mitochondria (Agarwal et al. 2017), only the ribosomes tagged with eGFP were being isolated.

To check the concentration and integrity of the RNA being sent for sequencing, I used an Agilent 2100 Bioanalyser **(see section 2.3.5)**. One of the advantages of this microfluidics-based automated electrophoresis system over traditional gel electrophoresis is that a dramatically smaller sample amount is needed, 1ng vs 200ng (Thermo Fisher Scientific - UK 2020). This is especially important when conducting TRAP experiments, since the experiment yields low RNA concentrations.

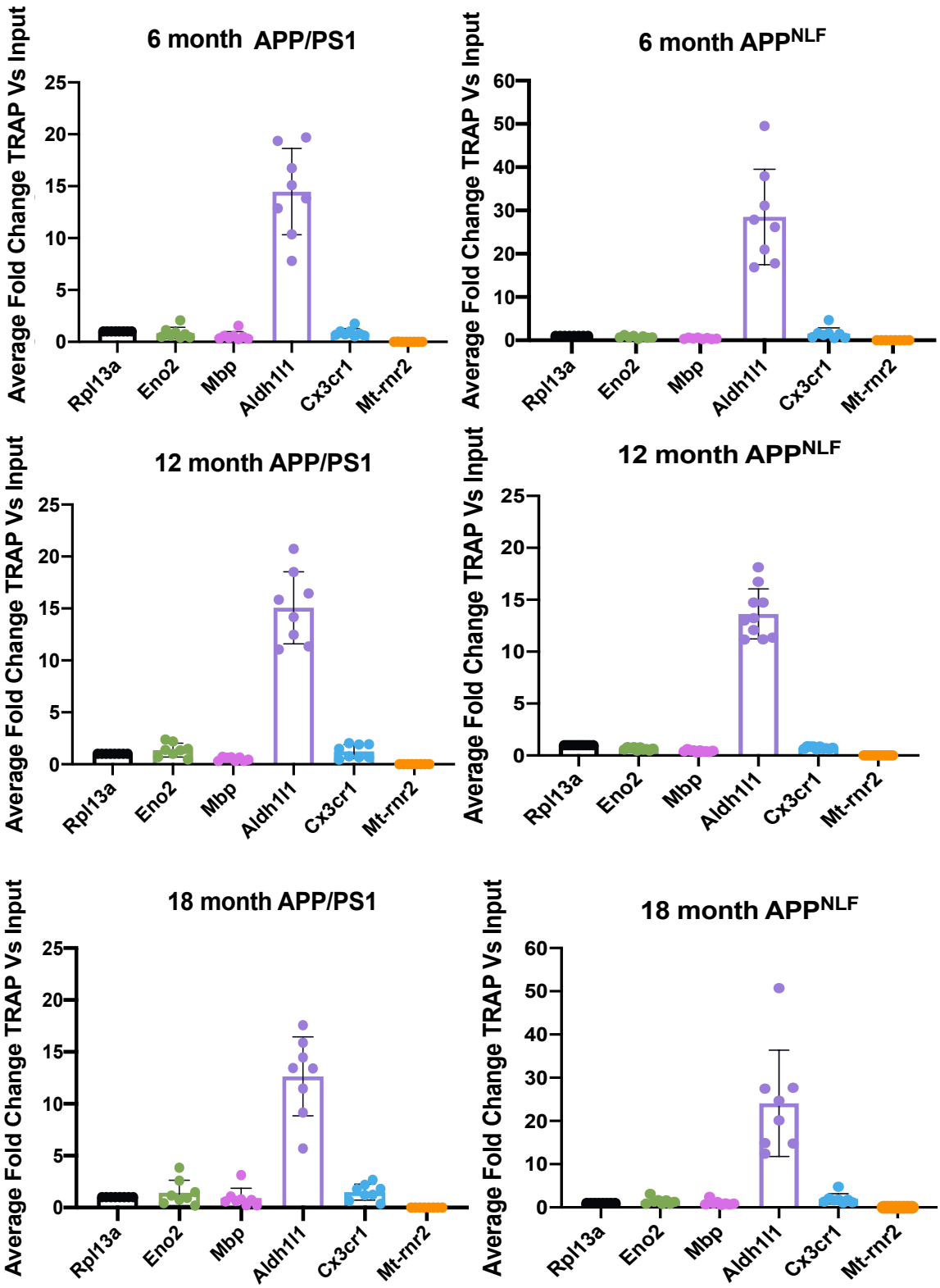
6 month APP/PS1
Average Fold Change TRAP Vs Input
25
20
15
10
5
0
Rpl13a
Eno2
Mbp
Aldh1l1
Cx3cr1
Mt-rnr2
6 month APPNLF
Average Fold Change TRAP Vs Input
60
50
40
30
20
10
0
Rpl13a
Eno2
Mbp
Aldh1l1
Cx3cr1
Mt-rnr2
12 month APP/PS1
Average Fold Change TRAP Vs Input
25
20
15
10
5
0
Rpl13a
Eno2
Mbp
Aldh1l1
Cx3cr1
Mt-rnr2
12 month APPNLF
Average Fold Change TRAP Vs Input
25
20
15
10
5
0
Rpl13a
Eno2
Mbp
Aldh1l1
Cx3cr1
Mt-rnr2
18 month APP/PS1
Average Fold Change TRAP Vs Input
25
20
15
10
5
0
Rpl13a
Eno2
Mbp
Aldh1l1
Cx3cr1
Mt-rnr2
18 month APPNLF
Average Fold Change TRAP Vs Input
60
50
40
30
20
10
0
Rpl13a
Eno2
Mbp
Aldh1l1
Cx3cr1
Mt-rnr2

Figure 23. qPCR validation of enrichment of astrocyte RNA in TRAP samples. RNA extracted from 6,12 and 18-month APP/PS1, APP^{NLF} and corresponding WT astrocytes was sampled for expression of the cell type specific markers. The Zhang et al. (2014) dataset was used to select genes that demonstrated >10-fold higher expression in a particular cell type vs other cell types. All TRAP samples demonstrated enrichment for *Aldh1l1* (astrocyte marker), and low expression of *Eno2* (neuronal marker), *Mbp* (oligodendrocyte marker), and *Cx3cr1(*microglia marker), compared to input samples which contained RNA from all cell types. As expected, *Mt-rnr2* (mitochondrial gene translated on mitochondrial ribosomes) also demonstrated a low expression in TRAP samples compared to input samples. *Rpl13a* was used as the house-keeping gene. Bars represent average fold change in amyloidopathy and WT samples, points represent expression in individual mice.

4.2.2 Summary of Alterations to the Astrocyte Translatome in APP/PS1 Mice

TRAP-seq was conducted on 6, 12 and 18-month APP/PS1 mice. The 6-month APP/PS1 translatome only displayed 10 significantly induced genes and 12 significantly repressed genes compared to WT littermate controls (FPKM>1, p_adj<0.05) **(figure 24A)**. This is to be expected if changes are associated with plaque formation as plaque deposition is reported to only begin at 6-months (Ruan et al. 2009) and astrocytic GFAP immunoreactivity, a marker of activated astrocytes (Eng and Ghirnikar 1994; Kamphuis et al. 2014), becomes evident around 9-months (Kamphuis et al. 2012). However, one might expect pre-plaque gene expression changes in the astrocytes with rising oligomer load, perhaps these not captured when conducting bulk RNA-seq. By 12-months there were 1704 significantly induced (red) and 1151 significantly repressed (blue) genes in the APP/PS1 astrocyte translatome (FPKM>1, p_adj<0.05) **(figure 24B)**, which is consistent with the known progression of amyloid pathology, reactive gliosis and cognitive decline in these mice (Kamphuis et al. 2012; Fu et al. 2018; Garcia-Alloza et al. 2006). At 18-months **(figure 24C)**, there were 861 significantly induced genes and 525 significantly repressed genes (FPKM>1, p_adj<0.05). A possible explanation for the reduction in significantly changed genes at 18-months compared to 12-months is that genotype dependent effects may be occluded by age dependent changes in WT translatomes at 18-months. Indeed, the sample-by-sample heatmap of genes induced (red) or repressed (blue) >1.5 fold (p_adj<0.05) in 12-month **(figure 24D)** and 18-month **(figure 24E)** APP/PS1 astrocytes indicates that WT gene expression may be slightly more variable at 18-months compared to 12-months.

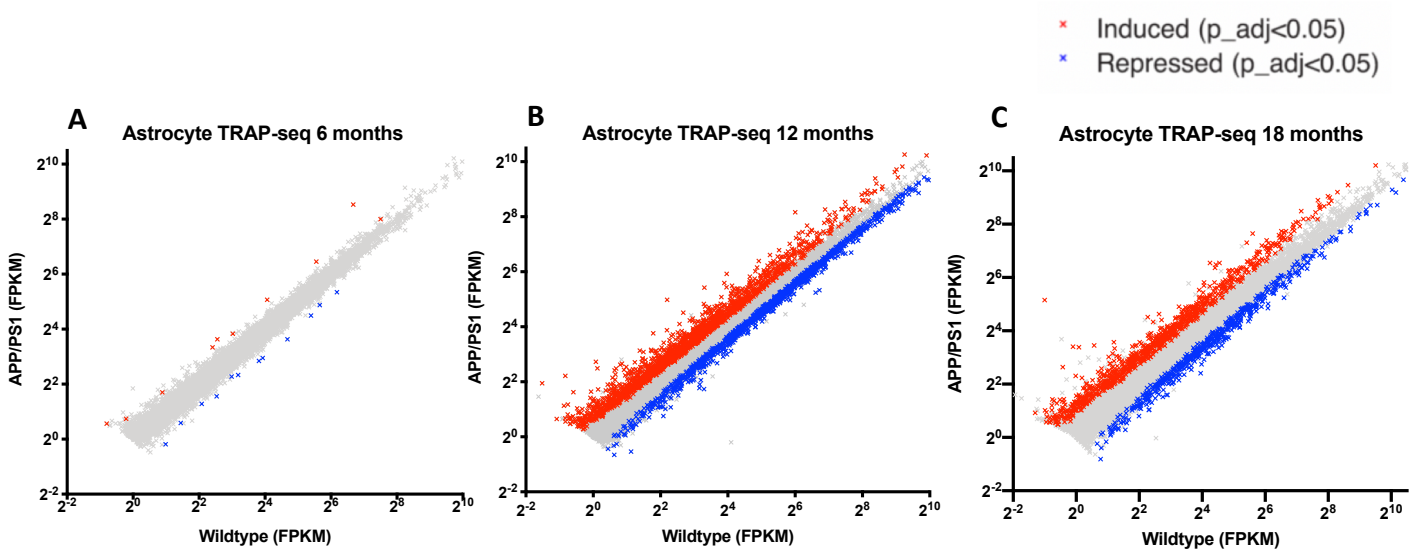

D Genes induced/repressed >1.5 fold in 12-month APP/PS1 astrocytes

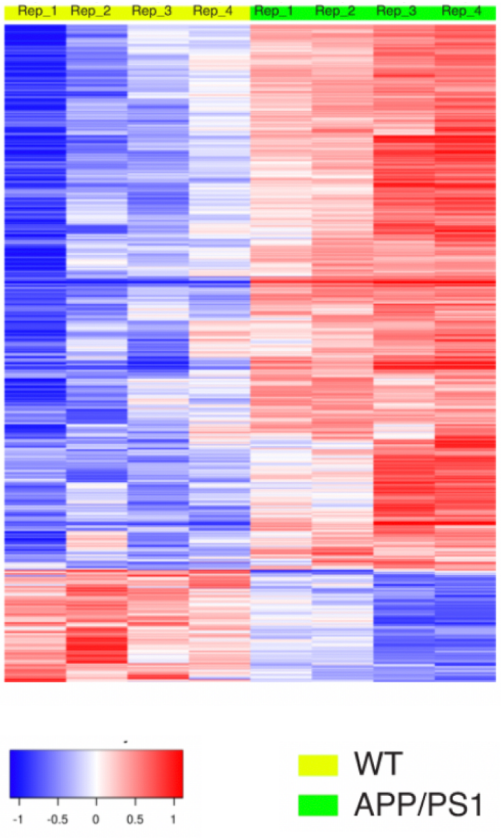

E Genes induced/repressed >1.5 fold in 18-month APP/PS1 astrocytes

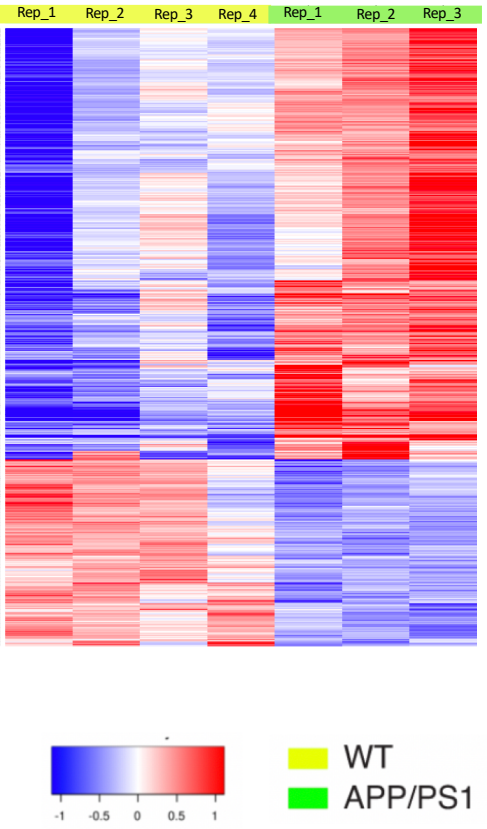

Figure 24. The APP/PS1 astrocyte translatome. Astrocyte TRAP-seq was performed on APP/PS1 vs WT mice (both carrying the Aldh1l1_eGFP-RPL10a allele) at 6-months **(A)**, 12-months **(B)**, and 18-months **(C)** in the neocortex. Genes induced (red), genes repressed (blue) and genes not significantly changed (grey) are shown (expression cut-off 1FPKM, p_adj<0.05, protein coding); n=4 mice per age and genotype, except 18-month HET mice where n=3. **(D)** Sample-by-sample heat map of genes induced (red) or repressed (blue) >1.5 fold (FPKM>1, p_adj<0.05) in 12-month APP/PS1 astrocytes. **(E)** Sample-by-sample heat map of genes induced (red) or repressed (blue) >1.5 fold (FPKM>1, p_adj<0.05) in 18-month APP/PS1 astrocytes.

Investigating the genes which are induced in both the 12 and 18-month APP/PS1 astrocytes enhances the reliability of the gene changes attributed to amyloidopathy. 400 genes were significantly induced in both the 12 and 18-month APP/PS1 astrocytes, and 144 genes were significantly repressed in both the 12 and 18-month APP/PS1 astrocytes (p_adj<0.05). Orre et. al (2014) had previously conducted a microarray analysis of genes induced/repressed in 15-18-month FACS isolated APP/PS1 astrocytes. Their full dataset was not published. However, they did publish lists of the top 50 induced and top 50 repressed genes. The genes significantly induced/repressed in 12 and 18-month APP/PS1 astrocytes demonstrated enrichment for the top induced/repressed gene sets from the Orre et al. paper respectively **(figure 25)**. This indicates somewhat robust gene expression changes due to amyloidopathy across different studies, isolation and sequencing methods.

Genes Induced/Repressed in 12 and 18-month APP/PS1 Astrocytes

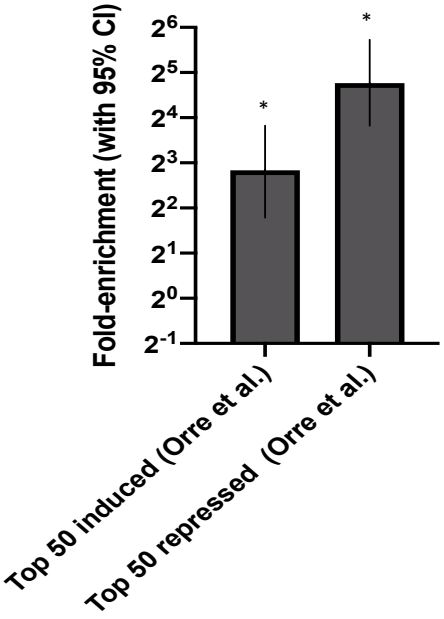

Figure 25. Comparing genes induced/repressed in 12 and 18-month APP/PS1 astrocytes with Orre et al. 2014 top 50 induced/repressed genes. Enrichment of genes induced/repressed in 12 and 18-month APP/PS1 astrocytes for genes in the top 50 induced/repressed in the Orre et al. 2014 dataset. P value <0.0001 (two-sided Fisher's exact test).

I performed GO and KEGG pathway analyses on the genes which were significantly induced **(figure 26A)** or repressed **(figure 26B)** in both the 12-month and 18-month APP/PS1 astrocytes (p_adj<0.05). When investigating the gene set induced by amyloidopathy, the top KEGG pathways enriched were phagosome and lysosome, indicating astrocytes are upregulating pathways involved in protein degradation, potentially a protective mechanism in response to Aβ pathology. Alternatively, perhaps increased astrocyte phagocytosis is contributing to synapse loss in AD (Chung et al. 2015; Chung et al. 2013; Chung et al. 2016). Notably, pathways involved in immune responses such as antigen processing and presentation, and natural killer cell mediated cytotoxicity were also enriched. Interestingly, a number of terms related to synaptic transmission and neuron development were enriched in the KEGG and GO analysis of genes induced by amyloidopathy, suggesting an upregulation of mechanisms to sustain synaptic transmission at a stage when synapse degeneration around plaques has been found (Koffie et al. 2009).

When investigating the KEGG and GO terms enriched by genes repressed in both 12 and 18-month APP/PS1 astrocytes, there appears to be a repression of negative regulation of neurogenesis and differentiation, which may indicate that astrocytes are attempting to aid the production of new neurons in response to the neurodegeneration caused by increasing amyloidopathy. However, one should exercise caution when interpreting this analysis, since only 144 genes were repressed, meaning terms may not be very reliable if the number of genes in each category are low.

Ingenuity pathway analysis is an alternative knowledge base of curated literature. A positive activation z-score >2 (orange) indicates pathways are significantly upregulated in that sample, a negative activation z-score <-2 (blue) indicates pathways are significantly downregulated in that sample. I analysed the genes that were induced/repressed >1.5 fold (p_adj<0.05) in the 6, 12, or 18-month APP/PS1 astrocytes **(figure 27)**. This revealed an upregulation of pathways related to synaptogenesis and synaptic transmission in the 12 and 18-month APP/PS1 astrocytes, but not the 6-month astrocytes. Therefore, this analysis mirrored aspects of the terms enriched in the set of genes upregulated in both the 12 and 18-month astrocytes. Analysing the data via two methods increased the reliability of results. Interestingly, the insulin secretion pathway and opioid signalling pathway were highlighted in the IPA analysis,

both of which have been implicated in Alzheimer's disease (Salarinasab et al. 2020; Stanley et al. 2016; Gabbouj et al. 2019; Hölscher 2019).

A Genes Induced in 12 and 18-Month APP/PS1 Astrocytes

KEGG_2019_Mouse_Table

Term	Overlap	P-value	Adjusted P-value	Odds Ratio
Phagosome	16/180	7.17E-07	9.12E-05	4.9380
Lysosome	13/124	1.24E-06	9.12E-05	5.8979
Synaptic vesicle cycle	10/77	3.04E-06	1.67E-04	7.4753
Antigen processing and presentation	10/90	1.26E-05	5.55E-04	6.2564
Endocrine and other factor-regulated calcium reabsorption	7/55	1.08E-04	3.12E-03	7.2553
Natural killer cell mediated cytotoxicity	10/118	1.31E-04	3.12E-03	4.6277
Glycerophospholipid metabolism	9/97	1.42E-04	3.12E-03	5.1037
Cell adhesion molecules (CAMs)	12/170	1.66E-04	3.33E-03	3.8057
Insulin secretion	8/86	3.25E-04	5.50E-03	5.1078
GABAergic synapse	8/90	4.43E-04	6.50E-03	4.8576

GO_Biological_Process_2018_Table

Term	Overlap	P-value	Adjusted P-value	Odds Ratio
chemical synaptic transmission (GO:0007268)	25/289	9.42E-10	1.99E-06	4.8828
positive regulation of neuron projection development (GO:0010976)	14/97	8.10E-09	5.91E-06	8.5286
modulation of chemical synaptic transmission (GO:0050804)	13/82	8.63E-09	5.91E-06	9.5084
nervous system development (GO:0007399)	30/455	1.23E-08	5.91E-06	3.6582
plasma membrane bounded cell projection organization (GO:0120036)	15/118	1.40E-08	5.91E-06	7.3750
neuron projection development (GO:0031175)	17/167	4.48E-08	1.57E-05	5.7554
neutrophil mediated immunity (GO:0002446)	30/487	5.63E-08	1.69E-05	3.3964
anterograde trans-synaptic signaling (GO:0098916)	20/240	8.57E-08	2.26E-05	4.6364
neutrophil degranulation (GO:0043312)	29/479	1.36E-07	3.19E-05	3.3264
neutrophil activation involved in immune response (GO:0002283)	29/483	1.62E-07	3.42E-05	3.2964

GO_Molecular_Function_2018_Table

Term	Overlap	P-value	Adjusted P-value	Odds Ratio
calcium ion binding (GO:0005509)	20/284	1.27E-06	5.39E-04	3.8549
tubulin binding (GO:0015631)	18/255	4.16E-06	7.46E-04	3.8498
amyloid-beta binding (GO:0001540)	8/49	5.25E-06	7.46E-04	9.7357
syntaxin binding (GO:0019905)	9/77	2.27E-05	2.42E-03	6.6116
spectrin binding (GO:0030507)	5/19	2.88E-05	2.45E-03	17.7089
metalloendopeptidase inhibitor activity (GO:0008191)	4/12	6.87E-05	4.40E-03	24.7374
transmitter-gated ion channel activity involved in regulation of postsynaptic membrane potential (GO:1904315)	6/36	7.22E-05	4.40E-03	9.9340
metal ion binding (GO:0046872)	22/442	9.04E-05	4.82E-03	2.6578
microtubule binding (GO:0008017)	13/195	1.59E-04	7.54E-03	3.5840
MHC class II protein complex binding (GO:0023026)	4/16	2.37E-04	1.01E-02	16.4882

GO_Cellular_component_2018_Table

Term	Overlap	P-value	Adjusted P-value	Odds Ratio
axon (GO:0030424)	18/141	4.62E-10	7.81E-08	7.4615
dendrite (GO:0030425)	20/215	1.36E-08	1.15E-06	5.2375
integral component of plasma membrane (GO:0005887)	60/1463	8.08E-08	4.55E-06	2.2888
node of Ranvier (GO:0033268)	5/12	2.20E-06	9.30E-05	35.4304
lytic vacuole (GO:0000323)	15/183	4.37E-06	1.48E-04	4.5065
lysosomal lumen (GO:0043202)	10/86	8.38E-06	2.36E-04	6.5870
main axon (GO:0044304)	6/33	4.32E-05	1.04E-03	11.0395
secretory granule lumen (GO:0034774)	18/317	7.66E-05	1.62E-03	3.0417
ficolin-1-rich granule (GO:0101002)	13/184	8.89E-05	1.67E-03	3.8167
vacuolar lumen (GO:0005775)	12/161	9.94E-05	1.68E-03	4.0374

B Genes Repressed in 12 and 18-Month APP/PS1 Astrocytes

KEGG_2019_Mouse_Table

Term	Overlap	P-value	Adjusted P-value	Odds Ratio
Signaling pathways regulating pluripotency of stem cells	7/137	6.11E-05	8.13E-03	7.7531
Hippo signaling pathway	7/159	1.55E-04	1.03E-02	6.6235
Pathways in cancer	11/535	1.73E-03	7.66E-02	3.0513

GO_Biological_Process_2018_Table

Term	Overlap	P-value	Adjusted P-value	Odds Ratio
negative regulation of neuron differentiation (GO:0045665)	9/64	7.95E-10	8.79E-07	24.0012
negative regulation of gene expression (GO:0010629)	19/618	1.03E-07	3.75E-05	4.8866
negative regulation of neurogenesis (GO:0050768)	6/33	1.18E-07	3.75E-05	31.9308
negative regulation of cell differentiation (GO:0045596)	10/150	1.36E-07	3.75E-05	10.5096
embryonic digestive tract development (GO:0048566)	5/20	2.56E-07	5.67E-05	47.5803
neuron differentiation (GO:0030182)	9/139	7.49E-07	1.38E-04	10.1159
negative regulation of mitotic cell cycle (GO:0045930)	6/48	1.20E-06	1.90E-04	20.5114
negative regulation of transcription, DNA-templated (GO:0045892)	20/813	1.57E-06	2.17E-04	3.8773
regulation of neuron differentiation (GO:0045664)	7/84	2.47E-06	3.04E-04	13.1248
negative regulation of nucleic acid-templated transcription (GO:1903507)	14/444	4.10E-06	4.27E-04	4.8652

GO_Molecular_Function_2018_Table

Term	Overlap	P-value	Adjusted P-value	Odds Ratio
core promoter sequence-specific DNA binding (GO:0001046)	5/73	1.83E-04	1.56E-02	10.4676
transcription factor activity, RNA polymerase II core promoter proximal region sequence-specific binding (GO:0000982)	9/280	1.99E-04	1.56E-02	4.8180
transcriptional repressor activity, RNA polymerase II transcription factor binding (GO:0001191)	4/47	3.61E-04	1.89E-02	13.1648
enhancer binding (GO:0035326)	3/26	8.42E-04	3.30E-02	18.3469
protein serine/threonine kinase inhibitor activity (GO:0030291)	3/30	1.29E-03	4.04E-02	15.6257
transcriptional activator activity, RNA polymerase II core promoter proximal region sequence-specific binding (GO:0001077)	6/175	1.70E-03	4.12E-02	5.0648
RNA polymerase II transcription factor binding (GO:0001085)	5/121	1.84E-03	4.12E-02	6.1213
transcription regulatory region DNA binding (GO:0044212)	8/374	5.78E-03	1.13E-01	3.1324
RNA polymerase II transcription factor activity, sequence-specific transcription regulatory region DNA binding (GO:0001133)	2/19	8.12E-03	1.42E-01	16.4366
protein serine/threonine phosphatase activity (GO:0004722)	3/61	9.70E-03	1.49E-01	7.2627

GO_Cellular_component_2018_Table

Term	Overlap	P-value	Adjusted P-value	Odds Ratio
mitochondrial matrix (GO:0005759)	6/308	2.42E-02	6.38E-01	2.8151
sex chromosome (GO:0000803)	1/6	4.24E-02	6.38E-01	27.7636
messenger ribonucleoprotein complex (GO:1990124)	1/7	4.93E-02	6.38E-01	23.1352
centrosome (GO:0005813)	7/461	4.95E-02	6.38E-01	2.1836
RISC complex (GO:0016442)	1/9	6.30E-02	6.38E-01	17.3497
RNAi effector complex (GO:0031332)	1/9	6.30E-02	6.38E-01	17.3497
microtubule organizing center (GO:0005815)	7/507	7.42E-02	6.38E-01	1.9780
CD40 receptor complex (GO:0035631)	1/11	7.64E-02	6.38E-01	13.8783
nuclear transcription factor complex (GO:0044798)	2/71	9.28E-02	6.38E-01	4.0390
integral component of peroxisomal membrane (GO:0005779)	1/14	9.62E-02	6.38E-01	10.6740

Figure 26. **Ontological analysis of genes induced or repressed in both 12 and 18-month APP/PS1 astrocytes (p_adj<0.05)**. **(A)** Ontological analysis of genes induced, or **(B)** repressed in both 12 and 18-month APP/PS1 astrocytes. For KEGG pathway analysis, the number of genes required was ≥5, disease pathways were removed. For KEGG and GO ontology analysis the top 10 pathways are shown, unless fewer than 10 satisfied the criteria (p_adj<0.05).

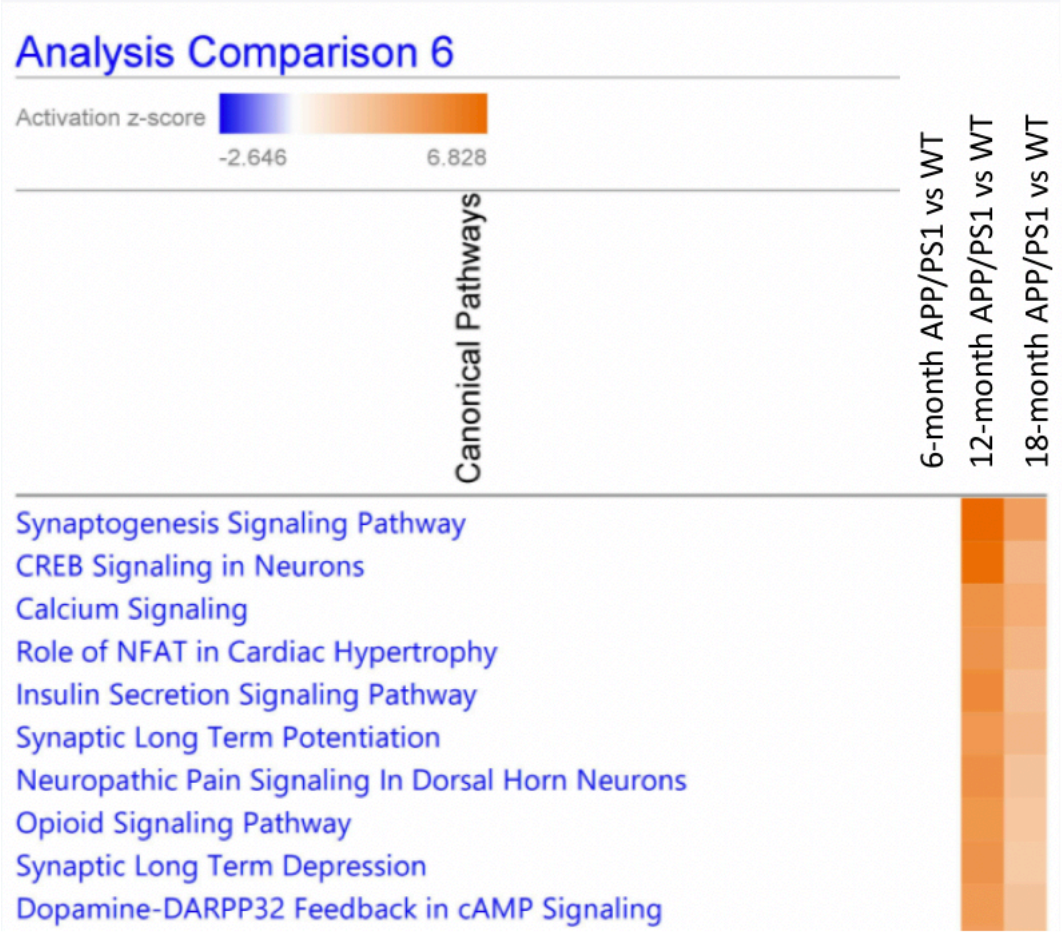

Figure 27. Ingenuity Pathway Analysis of genes induced >1.5 fold (p_adj<0.05) in the 6, 12 or 18- month APP/PS1 astrocytes. A positive activation z-score >2 (orange) indicates pathways are significantly upregulated in that sample, a negative activation z-score <-2 (blue) indicates pathways are significantly downregulated in that sample. The top 10 pathways are shown.

4.2.3 Summary of Alterations to the Astrocyte Translatome in APP^{NLF} Mice

TRAP-seq was conducted on 6, 12 and 18-month APP^{NLF} mice. The 6-month APP^{NLF} astrocyte translatome displayed no significant differentially expressed genes compared to the WT astrocyte translatome (FPKM>1, p_adj<0.05) **(figure 28A)**. At 12 months, only 1 gene (*Cap1* (Cyclase Associated Actin Cytoskeleton Regulatory Protein 1)) was significantly changed in the APP^{NLF} mouse (FPKM>1, p_adj<0.05**) (figure 28B)**. This is not that surprising since plaque load in APP^{NLF} mice is still relatively low at these ages (Saito et al. 2014). By 18 months, 71 genes were significantly upregulated and no genes were significantly downregulated in APP^{NLF} astrocytes **(figure 28C).** Plaque load is much more substantial at this age (Saito et al. 2014), hence, this increase in genes induced in APP^{NLF} astrocytes may be due to increases in reactive astrocytes surrounding plaques. Nevertheless, 71 differentially expressed genes is still not a large number of genes. It is likely that if astrocytes were sampled from APP^{NLF} mice at later time points, when plaques are even more abundant, there would be more differentially expressed genes. Additionally, single cell RNA-seq analysis may illuminate alterations in astrocytic gene expression that are lost due to bulk sequencing of astrocytes close to and far from plaques. **Figure 28D** illustrates a sample-by-sample heatmap of genes significantly induced >1.5 fold (FPKM>1, p_adj<0.05). No genes were significantly repressed.

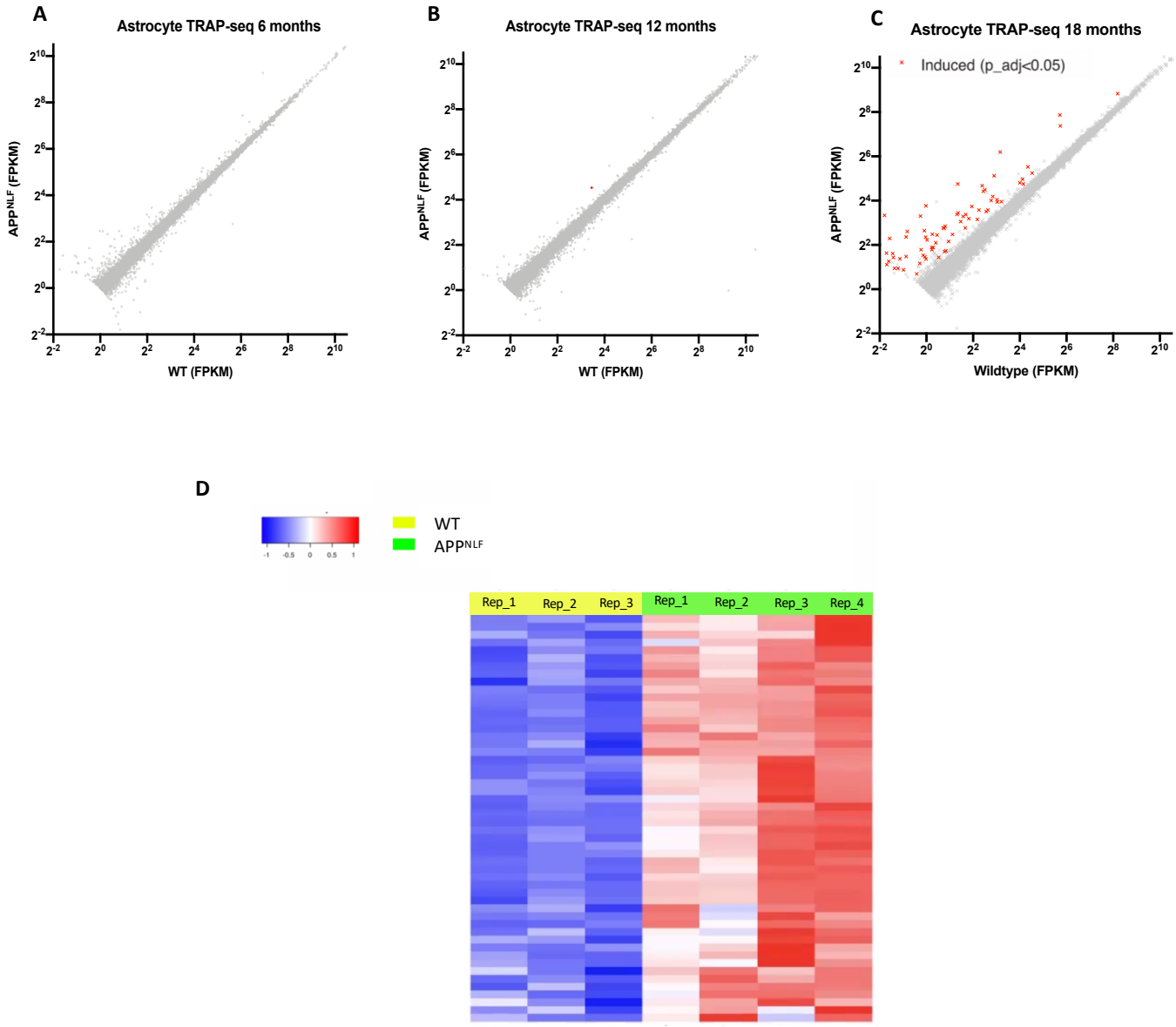

Figure 28. The APP^{NLF} astrocyte translatome. Astrocyte TRAP-seq was performed on APP^{NLF} vs WT mice (both carrying the Aldh1l1_eGFP-RPL10a allele) at **(A)** 6-months (n=4 HOM, 4 WT), **(B)** 12-months (n=4 HOM, 6 WT), and **(C)** 18-months (n=4 HOM, 3 WT) in the neocortex. 1 gene was significantly induced at 12 months and 71 genes were significantly induced at 18 months (red). Genes in grey were not significantly changed and no genes were significantly repressed at any of the time points (expression cut-off 1FPKM, p_adj<0.05); **(D)** Sample-by-sample heatmap of genes significantly induced >1.5 fold at 18-months (FPKM>1, p_adj<0.05). No genes were significantly repressed.

Since there were only 71 genes significantly induced in 18 month-APP^{NLF} astrocytes, I did not use any fold change cut off when exploring the dataset. GO analysis was performed on the 71 genes induced **(figure 29)**. Only one biological process (copper ion transport) and one molecular function term (oxidoreductase activity) was significant, no cellular component terms were significant (p_adj<0.05). KEGG pathway analysis was also performed, however no pathways were significant (p_adj<0.05). This is understandable as 71 genes is a small gene set, and so GO/ KEGG analysis is not that powerful. Genes related to astrocytic phagocytosis such as *Abca1* (ATP-Binding Cassette Transporter), *Megf10* (Multiple EGF-like Domains 10) and *Gulp1* (PTB Domain-Containing Engulfment Adaptor Protein 1) (Morizawa et al. 2017) were not present in the significantly induced gene set, nor were genes related to microglia-astrocyte cross talk, such as *Orm2* (Alpha-1-acid Glycoprotein 2), *Lcn2* (Lipocalin-2) and *C3* (Jha et al. 2019).

GO_Biological_Process_2018_table

Term	Overlap	P-value	Adjusted P-value	Odds Ratio
copper ion transport (GO:0006825)	3/14	1,52E+11	0,04	6,04E+15

GO_Molecular_Function_2018_table

Term	Overlap	P-value	Adjusted P-value	Odds Ratio
oxidoreductase activity, oxidizing metal ions, NAD or NADP as acceptor (GO:0016723)	3/10	5,05E+09	0,01	8,45E+15

Figure 29. Ontological analysis of genes significantly induced (FPKM>1, p_adj<0.05) in astrocytes in 18-month APP^{NLF}. No GO Cellular Compartment terms were significant, nor were any KEGG Pathway terms (p_adj<0.05).

4.2.4 Examining Differential Expression Associated with Amyloid Pathology in Older Animals in Young Animals

To determine whether the gene changes evident in 12-month APP/PS1 astrocytes were beginning to occur earlier in the APP/PS1 model, I examined the genes that were significantly induced or repressed >1.5-fold in 12-month APP/PS1 astrocytes (FPKM>1, p_adj<0.05) and determined the fold change in 6-month APP/PS1 astrocytes **(figure 30A, B)**. The majority of the genes that were significantly induced at 12-months demonstrated a positive fold change at 6-months, and the majority of genes that were repressed at 12-months demonstrated a negative fold change at 6-months. I then repeated this analysis, examining the genes that were significantly induced or repressed >1.5-fold in 12-month and 18-month APP/PS1 astrocytes (FPKM>1, p_adj<0.05) and determining the fold change in 6-month APP/PS1 astrocytes **(figure 30C, D)**. The relationship held. Whilst most of these gene expression changes were not significantly changed at 6-months, the directionality is the same for most. Hence, gene expression changes due to chronic amyloid pathology appear to begin early in disease pathogenesis in APP/PS1 mice.

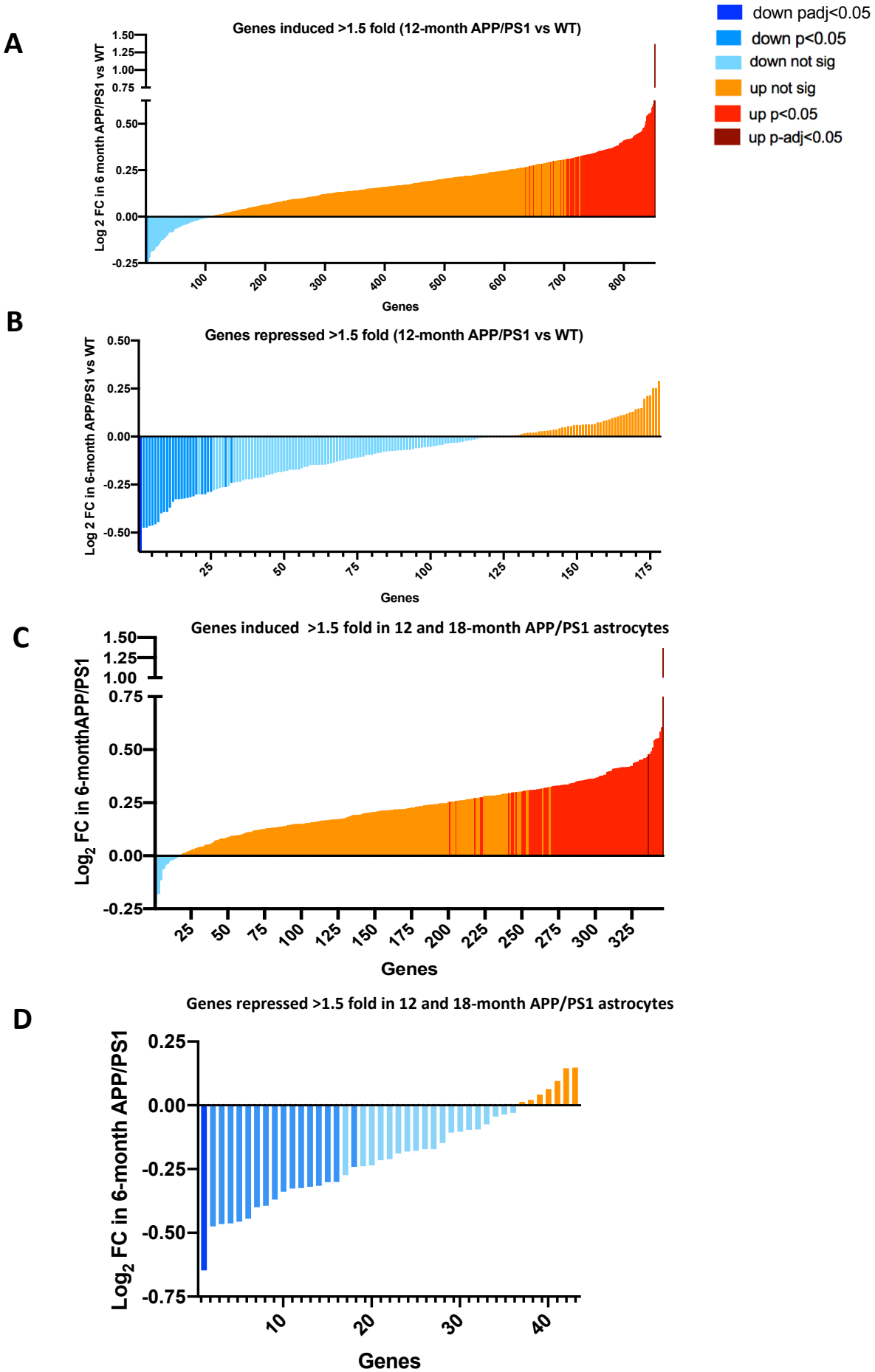
A
Genes induced >1.5 fold (12-month APP/PS1 vs WT)
Log 2 FC in 6 month APP/PS1 vs WT
Genes
B
Genes repressed >1.5 fold (12-month APP/PS1 vs WT)
Log 2 FC in 6-month APP/PS1 vs WT
Genes
C
Genes induced >1.5 fold in 12 and 18-month APP/PS1 astrocytes
Log2 FC in 6-monthAPP/PS1
Genes
D
Genes repressed >1.5 fold in 12 and 18-month APP/PS1 astrocytes
Log2 FC in 6-month APP/PS1
Genes
down padj<0.05
down p<0.05
down not sig
up not sig
up p<0.05
up p-adj<0.05

Figure 30. Investigating whether gene expression changes which occur late in pathology begin earlier in APP/PS1 mouse. (A) Log_2-fold change (FC) of the genes induced > 1.5-fold in 12-month APP/PS1 astrocytes when examined at 6-months in APP/PS1 astrocytes. t=24.88, df=850, p<0.0001 (ratio paired t-test of FPKM (WT) vs FPKM (APP/PS1). **(B)** Log_2 FC of the genes repressed > 1.5-fold in 12-month APP/PS1 astrocytes when examined at 6-months in APP/PS1 astrocytes. t=6.884, df=177, p<0.0001 (ratio paired t-test of FPKM (WT) vs FPKM (APP/PS1)**. (C)** Log_2 FC of the genes induced > 1.5-fold in 12 and 18-month APP/PS1 astrocytes when examined at 6-months in APP/PS1 astrocytes. t=14.66, df=387, p<0.0001 (ratio paired t-test of FPKM (WT) vs FPKM (APP/PS1). **(D)** Log_2 FC of the genes repressed > 1.5-fold in 12 and 18-month APP/PS1 astrocytes when examined at 6-months in APP/PS1 astrocytes. t=6.927, df=42, p<0.0001 (ratio paired t-test of FPKM (WT) vs FPKM (APP/PS1).

I conducted a similar analysis in the APP^{NLF} astrocytes, investigating the expression of genes which were induced >1.5 fold in 18-month APP^{NLF} astrocytes at 12-months **(figure 31)**. The genes induced in the later staged APP^{NLF} astrocytes did not appear to be induced in the earlier staged astrocytes. A reasonable deduction is that these genes begin to be induced post 12-months, whilst pathology is worsening. It is likely that if one was to compare genes induced/repressed in 24-month APP^{NLF} astrocytes with gene expression changes occurring in 18-month APP^{NLF} astrocytes, that the same pattern of earlier indications of gene expression alterations would be found. Notably, when comparing gene expression changes across time points in either model, it is impossible to dissect batch effects from age group effects as the experiments were not done concurrently.

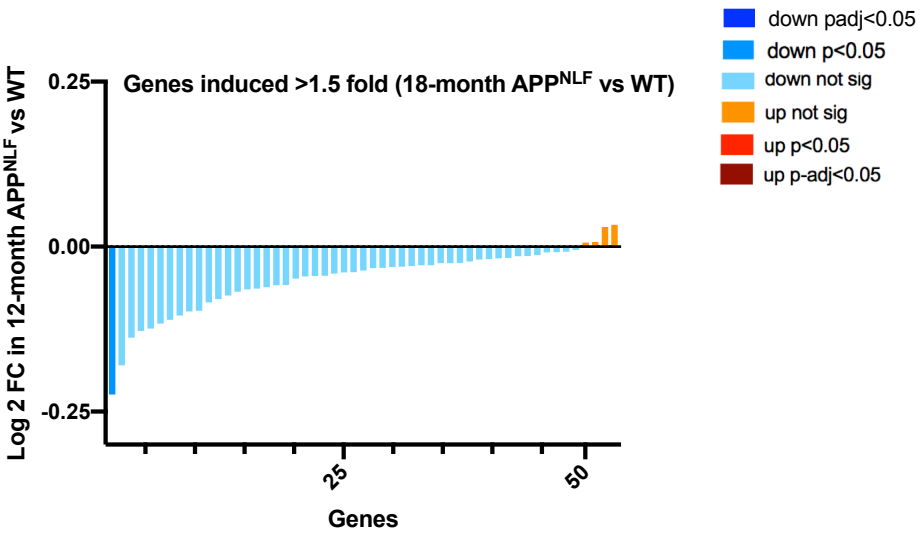

Figure 31. Investigating whether gene expression changes which occur later in pathology begin earlier in APP^{NLF} astrocytes. Log_2-fold change (FC) of the genes induced > 1.5-fold in 18-month APP^{NLF} astrocytes when examined at 12-months in APP^{NLF} astrocytes. t=7.912, df=52, p<0.0001 (ratio paired t-test of FPKM (WT) vs FPKM (APP^{NLF}).

Since the transgenic APP/PS1 mouse model is considered a mouse model with stronger pathology than the knock-in APP^{NLF} mouse model, I wondered whether the genes which were strongly induced in 12 and 18-month APP/PS1 astrocytes (p_adj<0.05, fold change>1.5), showed a trend for increasing expression in the 6, 12 and 18-month APP^{NLF} astrocytes. **Figure 32** demonstrates that most of the genes which are induced in 12 and 18-month APP/PS1 astrocytes are non-significantly downregulated in 6-month APP^{NLF} astrocytes. However, as the APP^{NLF} mouse ages, the expression of this gene set increases, and by 18-months, the majority are showing a positive fold change. This indicates that the two mouse models display similarities in alterations of gene expression with increasing Aβ pathology.

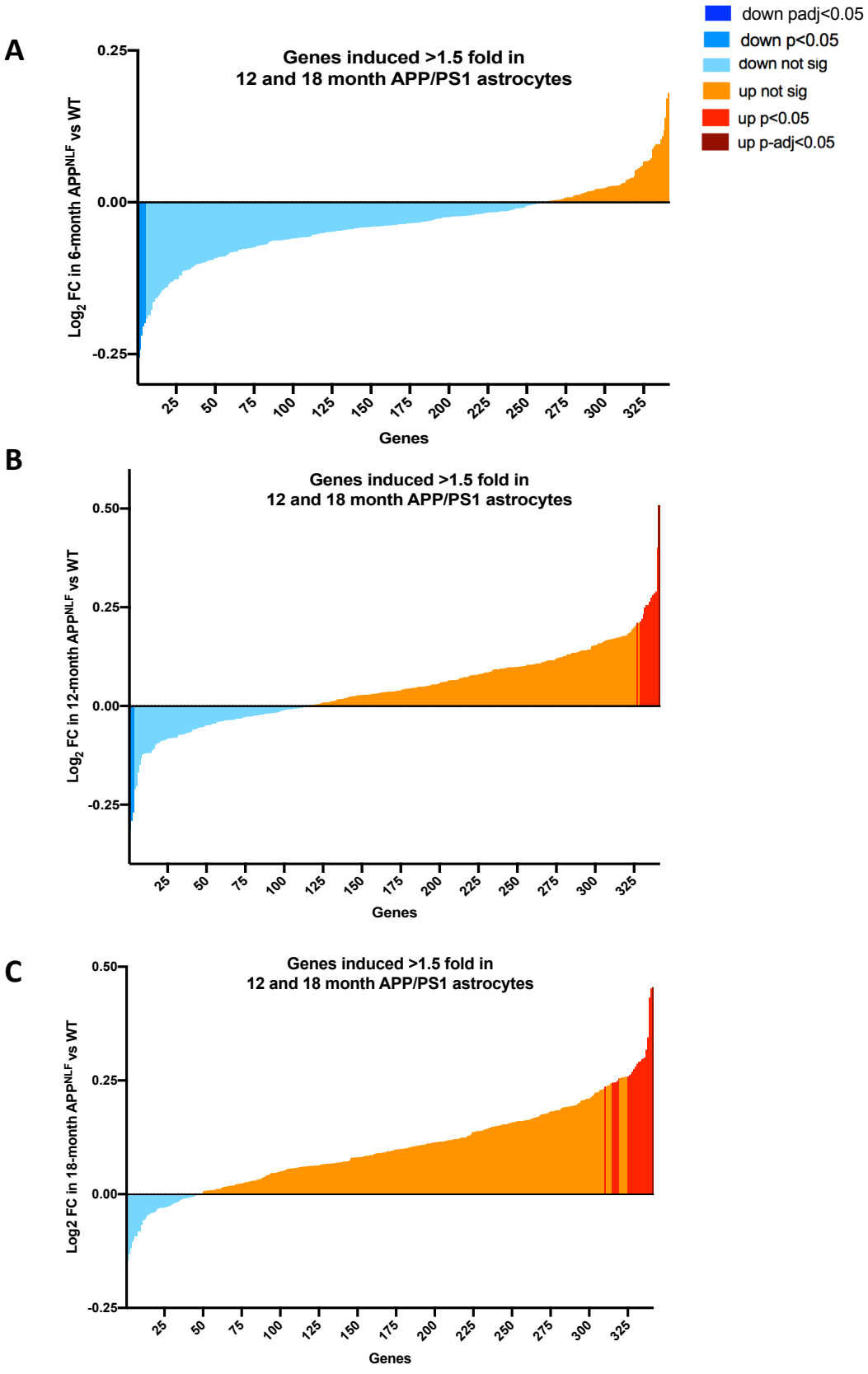
A
Genes induced >1.5 fold in
12 and 18 month APP/PS1 astrocytes
Log2 FC in 6-month APPNLF vs WT
0.25
0.00
-0.25
25 50 75 100 125 150 175 200 225 250 275 300 325
Genes
B
Genes induced >1.5 fold in
12 and 18 month APP/PS1 astrocytes
Log2 FC in 12-month APPNLF vs WT
0.50
0.25
0.00
-0.25
25 50 75 100 125 150 175 200 225 250 275 300 325
Genes
C
Genes induced >1.5 fold in
12 and 18 month APP/PS1 astrocytes
Log2 FC in 18-month APPNLF vs WT
0.50
0.25
0.00
-0.25
25 50 75 100 125 150 175 200 225 250 275 300 325
Genes
down padj<0.05
down p<0.05
down not sig
up not sig
up p<0.05
up p-adj<0.05

Figure 32. Examining the expression of genes which are induced >1.5 fold in 12 and 18-month APP/PS1 mice in APP^{NLF} mice. Log_2-fold change (FC) of the genes induced >1.5-fold in 12 and 18-month APP/PS1 astrocytes when examined at 6-months in APP^{NLF} astrocytes. t=13.20, df=339, p<0.0001 (ratio paired t-test of FPKM (WT) vs FPKM (APP^{NLF}). **(B)** Log_2 FC of the genes induced >1.5-fold in 12 and 18-month APP/PS1 astrocytes when examined at 12-months in APP^{NLF} astrocytes. t=6.010, df=340, p<0.0001 (ratio paired t-test of FPKM (WT) vs FPKM (APP^{NLF}). **(C)** Log_2 FC of the genes induced >1.5-fold in 12 and 18-month APP/PS1 astrocytes when examined at 18-months in APP^{NLF} astrocytes. t=12.15, df=340, p<0.0001 (ratio paired t-test of FPKM (WT) vs FPKM (APP^{NLF}).

In order to dig deeper into the differences and similarities of genes expressed in the APP/PS1 and APP^{NLF} mouse models of amyloidopathy, I split the genes in the graph in **figure 32C** (which examines the expression of genes induced >1.5 fold in 12 and 18-month APP/PS1 mice in 18-month APP^{NLF} mice) into quartiles **(figure 33A)**, and performed ontological analysis on the bottom **(figure 33B)** and top quartiles **(figure 33C)**. The top KEGG pathways in the bottom quartile were antigen processing and presentation, and phagosome. This indicates that the whilst the APP/PS1 astrocytes upregulate immune pathways in response to increased amyloid load, the APP^{NLF} astrocytes did not. This is likely due to the slower pathological progression in the APP^{NLF} mouse. It would be interesting to see if these immune related pathways were induced later in pathology, e.g. in 24-month-old APP^{NLF} mice. Ontological analysis of the top quartile indicated that both models are upregulating a number of processes related to ion transport, an important astrocytic homeostatic function.

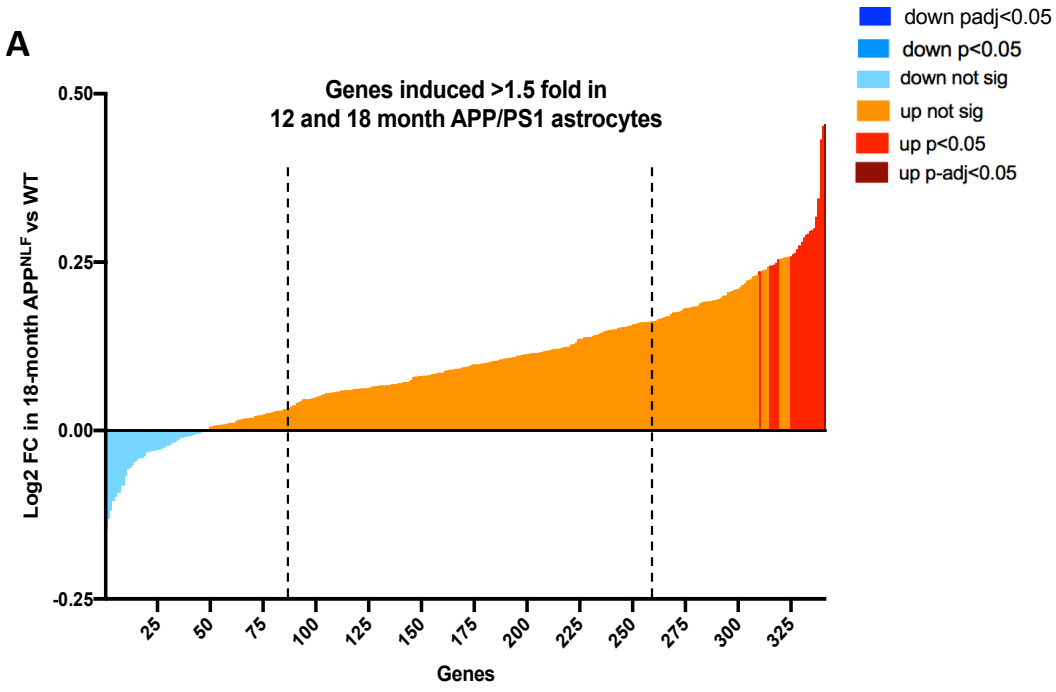

B Bottom Quartile Ontological Analysis

KEGG_2019_Mouse_Table

Term	Overlap	P-value	Adjusted P-value	Odds Ratio
Antigen processing and presentation	6/90	2.31E-06	2.44E-04	17.9304
Phagosome	7/180	1.16E-05	4.11E-04	10.2411

GO_Biological_Process_2018_Table

Term	Overlap	P-value	Adjusted P-value	Odds Ratio
cellular response to peptide (GO:1901653)	4/41	2.73E-05	1.27E-02	26.5305
regulation of peptidyl-tyrosine phosphorylation (GO:0050730)	5/85	3.09E-05	1.27E-02	15.4961
regulation of amyloid-beta formation (GO:1902003)	3/18	5.77E-05	1.58E-02	48.5366
neuron projection development (GO:0031175)	6/167	7.86E-05	1.61E-02	9.3187
cellular response to amyloid-beta (GO:1904646)	3/23	1.23E-04	1.87E-02	36.3933
plasma membrane bounded cell projection organization (GO:0120036)	5/118	1.48E-04	1.87E-02	10.9524
response to amyloid-beta (GO:1904645)	3/25	1.59E-04	1.87E-02	33.0815
positive regulation of catecholamine secretion (GO:0033605)	2/6	2.65E-04	2.40E-02	119.9458
neuron projection maintenance (GO:1990535)	2/6	2.65E-04	2.40E-02	119.9458
regulation of dendritic spine maintenance (GO:1902950)	2/7	3.70E-04	2.40E-02	95.9518

GO_Molecular_Function_2018_Table

Term	Overlap	P-value	Adjusted P-value	Odds Ratio
calcium:sodium antiporter activity (GO:0005432)	2/6	2.65E-04	3.63E-02	119.9458
calcium:cation antiporter activity (GO:0015368)	2/12	1.15E-03	3.68E-02	47.9639
amyloid-beta binding (GO:0001540)	3/49	1.19E-03	3.68E-02	15.8025
hexose transmembrane transporter activity (GO:0015149)	2/13	1.35E-03	3.68E-02	43.6013
serine-type endopeptidase activity (GO:0004252)	5/196	1.49E-03	3.68E-02	6.4542
DNA polymerase binding (GO:0070182)	2/16	2.06E-03	3.68E-02	34.2530
MHC class II protein complex binding (GO:0023026)	2/16	2.06E-03	3.68E-02	34.2530
serine-type peptidase activity (GO:0008236)	5/220	2.47E-03	3.68E-02	5.7267
ankyrin binding (GO:0030506)	2/18	2.61E-03	3.68E-02	29.9684
MHC protein complex binding (GO:0023023)	2/19	2.91E-03	3.68E-02	28.2041

Term	Overlap	P-value	Adjusted P-value	Odds Ratio
integral component of plasma membrane (GO:0005887)	17/1463	1.21E-04	1.15E-02	3.1931
axon (GO:0030424)	5/141	3.38E-04	1.61E-02	9.0896
axon initial segment (GO:0043194)	2/9	6.30E-04	2.00E-02	68.5301
node of Ranvier (GO:0033268)	2/12	1.15E-03	2.72E-02	47.9639
endosome lumen (GO:0031904)	2/24	4.64E-03	8.66E-02	21.7886
perinuclear region of cytoplasm (GO:0048471)	6/378	5.47E-03	8.66E-02	3.9900
main axon (GO:0044304)	2/33	8.65E-03	1.17E-01	15.4559
secretory granule lumen (GO:0034774)	5/317	1.13E-02	1.34E-01	3.9269
dendrite (GO:0030425)	4/215	1.34E-02	1.34E-01	4.6115
polymeric cytoskeletal fiber (GO:0099513)	4/221	1.46E-02	1.34E-01	4.4827

C Top Quartile Ontological Analysis

KEGG_2019_Mouse_Table

Term	Overlap	P-value	Adjusted P-value	Odds Ratio
Cardiac muscle contraction	5/78	2.16E-05	2.07E-03	16.7774
Lysosome	5/124	1.97E-04	4.73E-03	10.2682
Adrenergic signaling in cardiomyocytes	5/148	4.46E-04	8.57E-03	8.5345
cAMP signaling pathway	5/211	2.17E-03	2.09E-02	5.9055

GO_Biological_Process_2018_Table

Term	Overlap	P-value	Adjusted P-value	Odds Ratio
positive regulation of neuron projection development (GO:0010976)	7/97	1.99E-07	1.68E-04	19.5173
positive regulation of cell projection organization (GO:0031346)	5/63	7.55E-06	3.18E-03	21.1324
sodium ion export from cell (GO:0036376)	3/13	2.13E-05	3.58E-03	71.9422
sodium ion export (GO:0071436)	3/13	2.13E-05	3.58E-03	71.9422
cellular potassium ion homeostasis (GO:0030007)	3/13	2.13E-05	3.58E-03	71.9422
cell communication by electrical coupling involved in cardiac conduction (GO:0086064)	3/14	2.70E-05	3.79E-03	65.3987
cellular sodium ion homeostasis (GO:0006883)	3/15	3.36E-05	4.05E-03	59.9458
cellular monovalent inorganic cation homeostasis (GO:0030004)	3/17	5.00E-05	5.26E-03	51.3769
positive regulation of neuron differentiation (GO:0045666)	5/98	6.48E-05	6.07E-03	13.1561
positive regulation of cell motility (GO:2000147)	6/179	1.23E-04	1.03E-02	8.5582

GO_Molecular_Function_2018_Table

Term	Overlap	P-value	Adjusted P-value	Odds Ratio
sodium:potassium-exchanging ATPase activity (GO:0005391)	3/11	1.24E-05	1.05E-03	89.9367
potassium-transporting ATPase activity (GO:0008556)	3/11	1.24E-05	1.05E-03	89.9367
potassium ion binding (GO:0030955)	2/12	1.17E-03	4.98E-02	47.3905
sodium ion binding (GO:0031402)	2/12	1.17E-03	4.98E-02	47.3905
alkali metal ion binding (GO:0031420)	2/16	2.11E-03	7.17E-02	33.8435
sodium ion transmembrane transporter activity (GO:0015081)	3/71	3.55E-03	9.49E-02	10.5489
acetylcholine receptor activity (GO:0015464)	2/23	4.36E-03	9.49E-02	22.5544
syntaxin binding (GO:0019905)	3/77	4.46E-03	9.49E-02	9.6907
purine ribonucleoside triphosphate binding (GO:0035639)	6/396	7.22E-03	1.30E-01	3.7546
calcium ion binding (GO:0005509)	5/284	7.62E-03	1.30E-01	4.3442

GO_Cellular_Component_2018_Table

Term	Overlap	P-value	Adjusted P-value	Odds Ratio
lytic vacuole (GO:0000323)	6/183	1.39E-04	1.09E-02	8.3631
lysosome (GO:0005764)	8/422	4.64E-04	1.83E-02	4.8309
dendrite (GO:0030425)	5/215	2.36E-03	4.85E-02	5.7919
secretory granule lumen (GO:0034774)	6/317	2.46E-03	4.85E-02	4.7274
axon (GO:0030424)	4/141	3.21E-03	5.08E-02	7.0418
vacuolar lumen (GO:0005775)	4/161	5.15E-03	6.78E-02	6.1386
lysosomal lumen (GO:0043202)	3/86	6.08E-03	6.80E-02	8.6359
azurophil granule lumen (GO:0035578)	3/90	6.89E-03	6.80E-02	8.2372
integral component of plasma membrane (GO:0005887)	13/1463	9.46E-03	8.31E-02	2.2677
microtubule (GO:0005874)	4/210	1.28E-02	9.25E-02	4.6668

Figure 33. Investigating similarities and differences in gene expression in APP/PS1 and APP^{NLF} astrocytes. (A) Log_2-fold change (FC) of the genes induced >1.5-fold in 12 and 18-month APP/PS1 astrocytes when examined in 18-months APP^{NLF} astrocytes, the upper and lower quartiles are marked by dotted lines. **(B)** Ontological analysis of genes in the lower quartile of **figure 33A**. **(C)** Ontological analysis of genes in the upper quartile of **figure 33A.**

I focused the remainder of my analysis on alterations to the 12-month APP/PS1 astrocyte translatome and 18-month APP^{NLF} translatome since these datasets displayed the most differentially expressed genes and so were best powered to investigate the alterations to the astrocyte translatome due to Aβ pathology.

4.2.5 Amyloidopathy Exacerbates Age-Dependent Reactive Changes in Astrocytes

Since the greatest known risk factor for developing Alzheimer's disease is age, I exploited the published dataset of the ageing astrocyte translatome (10 weeks vs 24 months) (Clarke et al. 2018) to discern whether astrocyte gene changes induced by amyloidopathy are enriched in genes which change during normal mouse ageing. I used the gene sets which were induced in the ageing cortex, hippocampus and striatum, as well as the set of genes common to all three regional sets. **Figure 34** illustrates that there was an enrichment in all regional age-dependent gene sets when interrogating the gene set induced >1.5 fold in the 12-month APP/PS1 astrocytes (expression cut-off 1FPKM, p_adj<0.05). This suggests that amyloidopathy prematurely induces astrocytic gene signatures that are normally found in old mice. Thus, supporting the proposal that the reduced number of differentially expressed genes in 18-month APP/PS1 vs WT dataset may be due to overlap with age-dependent changes in mice **(figure 24)**. Since only 71 genes were induced in APP^{NLF} astrocytes (p_adj<0.05), no fold change cut off was used when assessing for enrichment of age-dependent genes, nevertheless, this gene set was not enriched in age-dependent genes from any region. This is understandable since this gene set is very small. In the future, it would be interesting to do a similar analysis of age-dependent genes using our 6,12,18-month WT datasets. Additionally, it would be informative to compare genes which were repressed due to amyloidopathy with genes repressed due to ageing.

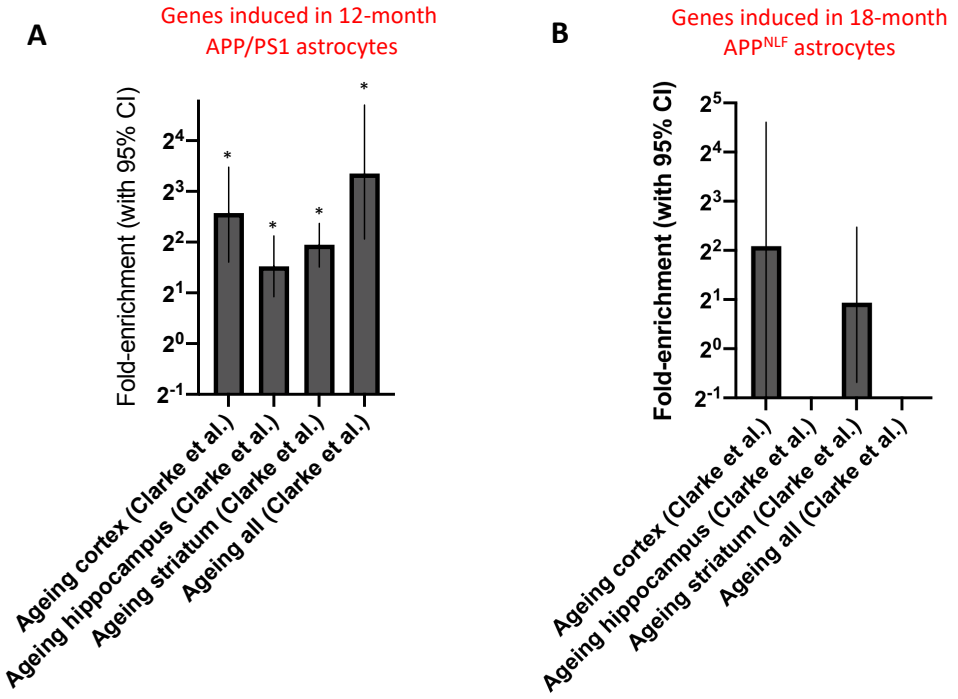

Figure 34. Enrichment analysis of genes induced in (A) 12-month APP/PS1 astrocytes (B) 18-month APP/PS1 astrocytes with ageing gene sets. Genes induced >1.5 fold in 12-month APP/PS1 astrocytes (expression cut-off 1FPKM, p_adj<0.05) or induced (without a fold change cut off, p_adj<0.05) in APP^{NLF} astrocytes were taken and enrichment analysis performed using the ageing translatome gene sets in the Clarke et al. (2018) published paper. Fold enrichment is shown. Error bars depict 95% confidence intervals of the fold enrichment. P values (left-to-right): <0.0001, <0.0001, <0.0001, <0.0001, 0.2164, >0.9999,0.2173,0.3625 (two-sided Fisher's exact test).

4.2.6 Changes in Astrocytes Due to Chronic Amyloidopathy Resemble Acutely Induced Reactive Profiles

Whilst reactive astrogliosis can be a product of chronic disease, it can also be induced very rapidly (<24 hours) by acute insults such as inflammatory stimuli or stroke (Zamanian et al. 2012). Recent studies have suggested that the expression profile of astrocytes in neurodegenerative disease more closely resemble a reactive profile induced by acute inflammation (LPS-activated microglia) rather than stroke (MCAO) (Liddelow et al. 2017). However, these conclusions were based on a putative marker gene C3 in end-stage disease. I wanted to investigate whether the expression profiles of astrocytes chronically exposed to amyloidopathy resembled the profiles of acutely induced reactive astrocytes. I initially carried out enrichment analysis of genes induced in the 12-month APP/PS1 astrocytes or 18-month APP^{NLF} astrocytes for genes which were defined as LPS-induced, MCAO-induced or pan-reactive in Liddelow et al (2017). Notably, these gene sets were small (12-13 genes) and when conducting the enrichment analysis, some genes were discarded due to low expression (<1FPKM). 8/11 (LPS/A1), 1/5 (MCAO/A2) and 7/10 (pan-reactive) genes were upregulated in APP/PS1 astrocytes. This meant that the APP/PS1 astrocytes were significantly enriched in A1 and pan-reactive genes ($p \leq 0.015$) **(figure 35A)**. None of the genes in these sets were present in the set of genes induced in 18-month APP^{NLF} astrocytes **(figure 35B)**. However, the gene sets defined in Liddelow et al. (2017) are very small and the rationale behind their inclusion was not stated. Therefore, we exploited the full transcriptional characterisation of these two reactive astrocyte phenotypes to define larger gene sets (Zamanian et al. 2012) (**see section 2.3.7.1** for in depth method)

Briefly, gene expression in each stimulation paradigm was ranked by fold-change. In order to be classed as LPS or MCAO induced, the gene had to be ranked in the top 100 genes for one stimulation paradigm, and at least 50 places lower for the other stimulation paradigm. In order to be classed as pan-reactive, we required the gene be ranked in the top 250 genes, and no more than 50 ranking positions between the two stimulation paradigms. **Figure 35C** is a representation of the expanded MCAO, LPS and pan-reactive gene sets.

Using the expanded gene sets, Aβ pathology in APP/PS1 astrocytes induced changes in astrocytic gene expression which were enriched in LPS-induced, MCAO-induced and pan-reactive gene sets **(figure 35D)**. Hence, the gene expression changes in astrocytes due to chronic amyloidopathy resemble both acutely induced reactive profiles. This finding is contrary to previous suggestions that AD pathology induces a reactive astrocyte profile that more closely resembles LPS-induced astrocytes. Genes induced in 18-month APP^{NLF} astrocytes were not enriched for the expanded LPS, MCAO or pan gene sets **(figure 35E)**.

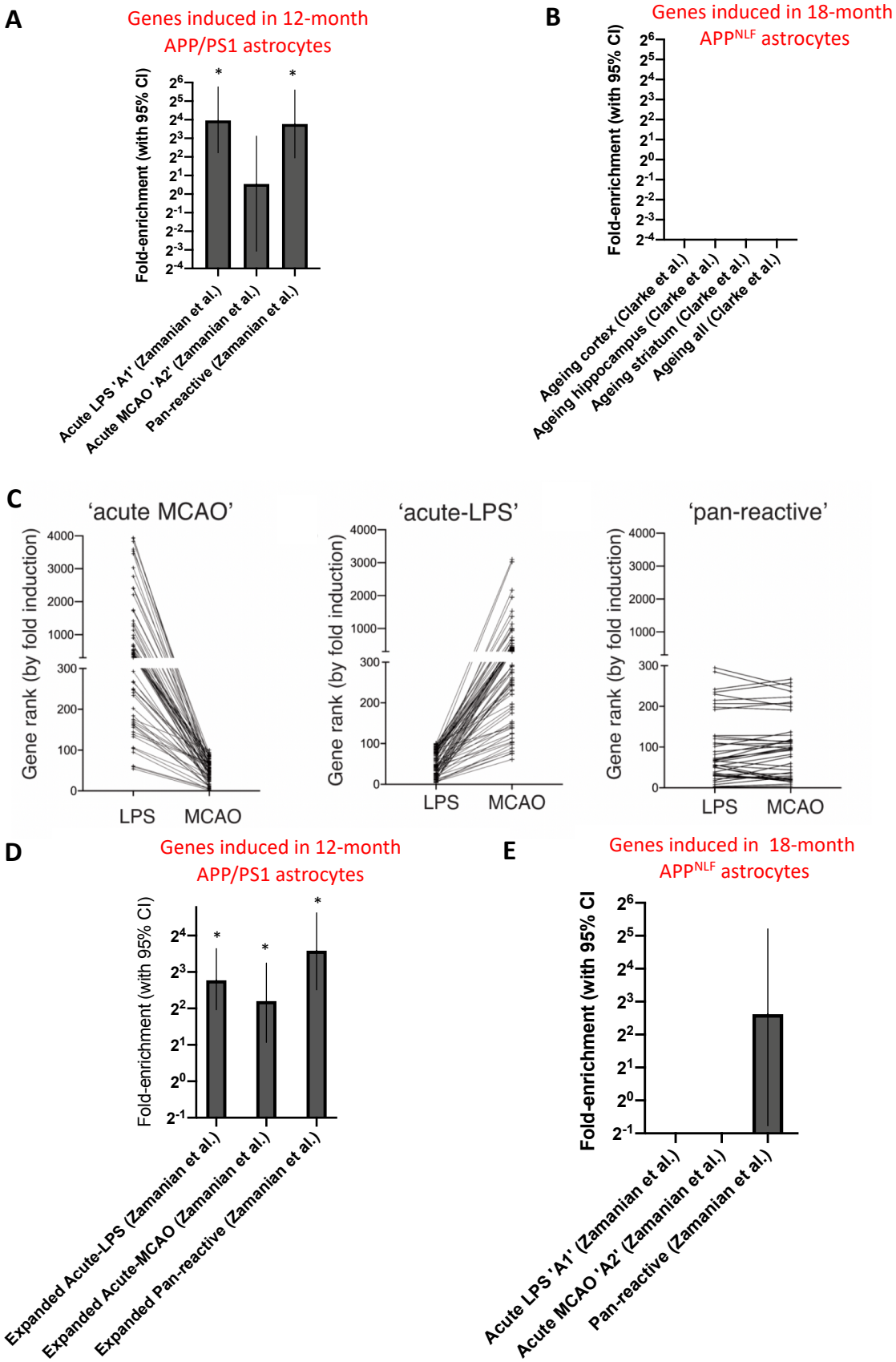
A
Genes induced in 12-month APP/PS1 astrocytes
Fold-enrichment (with 95% CI)
Acute LPS 'A1' (Zamanian et al.)
Acute MCAO 'A2' (Zamanian et al.)
Pan-reactive (Zamanian et al.)
B
Genes induced in 18-month APPNLF astrocytes
Fold-enrichment (with 95% CI)
Ageing cortex (Clarke et al.)
Ageing hippocampus (Clarke et al.)
Ageing striatum (Clarke et al.)
Ageing all (Clarke et al.)
C
'acute MCAO'
'acute-LPS'
'pan-reactive'
Gene rank (by fold induction)
LPS
MCAO
D
Genes induced in 12-month APP/PS1 astrocytes
Fold-enrichment (with 95% CI)
Expanded Acute-LPS (Zamanian et al.)
Expanded Acute-MCAO (Zamanian et al.)
Expanded Pan-reactive (Zamanian et al.)
E
Genes induced in 18-month APPNLF astrocytes
Fold-enrichment (with 95% CI)
Acute LPS 'A1' (Zamanian et al.)
Acute MCAO 'A2' (Zamanian et al.)
Pan-reactive (Zamanian et al.)

Figure 35. Enrichment of the small A1, A2 and pan-reactive gene sets described in Liddelow et al. (2017) in (A) 12-month APP/PS1 (B) 18-month APP^{NLF} astrocytes. Genes induced in 12-month APP/PS1 or 18-month APP^{NLF} astrocytes (expression cut-off 1FPKM, p_adj<0.05) were assessed for enrichment in A1, A2, and pan-reactive gene sets from Liddelow et al. (2017). Fold enrichment is shown. Error bars depict 95% confidence intervals of the fold enrichment. P values (left to right): <0.0001, 0.5471, 0.0001, >0.9999, >0.9999, >0.9999 (two-sided Fisher's exact test). **(C) Expanded LPS-induced, MCAO-induced and pan-reactive gene sets.** The microarray dataset from Zamanian et al. (2012) was used to curate expanded acute insult gene sets, see **section 2.3.7.1** for method of curation. The acute MCAO genes ranked in the top 100 MCAO-induced genes, median rank 49, and ranked >50 places lower in the 'acute LPS' gene set, median rank 41. The acute LPS genes ranked in the top 100 LPS-induced genes, median rank 47, and ranked >50 places lower in the 'acute MCAO' gene set, median rank 291. The pan-reactive genes were in the top 250 in both gene sets and had <50 ranking places between them, median 'acute LPS' ranking 66, median 'acute MCAO' ranking 92. The exact ranking position of each gene is shown. **Enrichment analysis using expanded A1/A2/pan reactive gene sets. (D)** Genes induced >1.5 fold in 12-month APP/PS1 astrocytes (expression cut-off 1FPKM, p_adj<0.05) or **(E)** induced in 18-month APP^{NLF} astrocytes (expression cut-off 1FPKM, p_adj<0.05) were taken and enrichment analysis performed using the expanded gene sets curated from the Zamanian et al (2012) paper **(see figure 34C).** Fold enrichment is shown. Error bars depict 95% confidence intervals of the fold enrichment. P values (left-to-right): <0.0001, 0.0006, <0.0001, >0.9999, >0.9999, 0.1569 (two-sided Fisher's exact test).

4.2.7 A Core Signature of Astrocytic Genes Regulated by Both Aβ and Tau Pathology

Amyloid pathology and reactive glia are not the only 'positive' pathological hallmarks of AD. The accumulation of hyperphosphorylated tau into neurofibrillary tangles is also considered a fundamental characteristic of AD and is thought to also induce reactive glia (Braak et al. 2006; Serrano-Pozo et al. 2011). Dr Zoeb Jiwaji, a member of the Hardingham lab, had previously curated a similar data set, investigating astrocyte translatome changes concomitant with tau pathology in $MAPT^{P301S}$ mice vs WT mice (both carrying the Aldh1l1_eGFP-RPL10a allele).

The $MAPT^{P301S}$ mice accumulate hyperphosphorylated filamentous tau, which drives progressive neurodegeneration in the spinal cord and upper cortical layers. Pathology begins around 3 months, and by 5 months mice physically deteriorate due to neurodegeneration (Allen et al. 2002; Yoshiyama et al. 2007). Dr Zoeb Jiwaji had shown that that substantial changes in gene expression occur in 5-month spinal cord $MAPT^{P301S}$ vs WT astrocytes. In the $MAPT^{P301S}$ cortex, where degeneration only takes place in upper layers, the number of significantly changed genes was lower, although, the fold-change (up and down) correlated well with the spinal cord data r=0.77 (Pearson correlation coefficient - data not shown). Hence, I decided to use the 5-month $MAPT^{P301S}$ spinal cord astrocyte dataset to compare with 12-month APP/PS1 neocortex astrocyte dataset.

The gene sets showed significant overlap of induced and repressed genes, $p<0.0001$ (Two sided Fisher's exact test). A 'core' set of 203 genes were significantly upregulated in both the APP/PS1 and $MAPT^{P301S}$ astrocytes, and a core set of 151 genes were significantly downregulated in both models **(figure 36A)**. As expected, the core induced gene set was strongly enriched in age-dependent genes and acutely-induced reactive astrocyte genes **(figure 37A)**.

Ontological analysis of the core upregulated genes revealed that GO Biological Processes were dominated by those associated with cytokine and inflammatory responses, as well as protein degradation **(figure 36B)**. GO Molecular Functions were dominated by proteases,

peptidases and protein binding classes **(figure 36B)**, while GO Cellular Components included lysosomal and luminal compartments of several types **(figure 36B)**. High ranking KEGG pathways included Lysosome, Apoptosis, and a number of inflammatory-associated pathways **(figure 36B, D)**.

Studying the core repressed genes overlapping the APP/PS1 and MAPT^{P301S} astrocytes revealed GO Biological Processes were dominated by mitochondrial oxidative phosphorylation and general protein synthesis **(figure 36C)**, GO Molecular Functions comprised mitochondrial enzymic activities **(figure 36C)**, and GO Cellular Components included mitochondrial protein classes and subclasses, as well as ribosomal proteins (notably *Rpl10a* was not one of the genes included in this category) **(figure 36C)**. KEGG pathways enriched in the downregulated genes included oxidative phosphorylation and ribosome (**Figure 36C, E)**. Collectively, these analyses suggest that both Aβ and tau induce potentially harmful alterations to astrocytes, such as mitochondrial and protein synthesis deficits, however, they also induce genes within pathways associated with protein degradation and clearance, which may represent a beneficial/protective response of astrocytes to proteinopathy. Alternatively, perhaps increased astrocyte phagocytosis/degradative pathways contribute to synapse loss in AD (Chung et al. 2015; Chung et al. 2013; Chung et al. 2016).

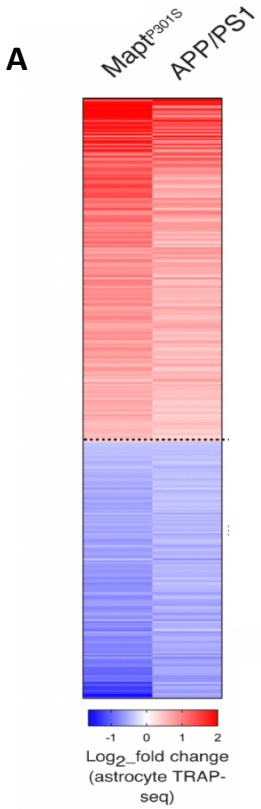

B Genes Induced by Aβ and Tau Pathology in Astrocytes

KEGG_2019_Mouse_table

Term	Overlap	P-value	Adjusted P-value	Odds Ratio
Lysosome	19/124	2.7966E-17	8.4737E-15	15.0221
Apoptosis	11/141	2.1969E-07	3.3283E-05	7.6484
Complement and coagulation cascades	8/88	3.2645E-06	1.9783E-04	8.9127
Osteoclast differentiation	8/128	5.1297E-05	1.7270E-03	6.1275
Phagosome	9/180	9.9528E-05	2.5131E-03	4.9020
TNF signaling pathway	7/110	1.3579E-04	3.1648E-03	6.2389
Sphingolipid metabolism	4/48	1.4397E-03	2.5660E-02	8.1699
Protein processing in endoplasmic reticulum	7/163	1.4449E-03	2.4322E-02	4.2103
JAK-STAT signaling pathway	7/164	1.4965E-03	2.3866E-02	4.1846

GO_Biological_Process_2018_table

Term	Overlap	P-value	Adjusted P-value	Odds Ratio
neutrophil degranulation (GO:0043312)	28/479	8.5750E-14	4.3758E-10	5.7309
neutrophil activation involved in immune response (GO:0002283)	28/483	1.0525E-13	2.6854E-10	5.6834
neutrophil mediated immunity (GO:0002446)	28/487	1.2892E-13	2.1929E-10	5.6368
cytokine-mediated signaling pathway (GO:0019221)	27/633	3.3966E-10	4.3332E-07	4.1818
proteolysis (GO:0006508)	18/291	1.2026E-09	1.2274E-06	6.0643
sphingolipid metabolic process (GO:0006665)	11/116	2.9312E-08	2.4930E-05	9.2968
cellular response to cytokine stimulus (GO:0071345)	20/456	4.9028E-08	3.5741E-05	4.3000
platelet degranulation (GO:0002576)	11/124	5.8743E-08	3.7471E-05	8.6970
cellular protein catabolic process (GO:0044257)	8/62	2.1536E-07	1.2211E-04	12.6502

GO_Molecular_Function_2018_table

Term	Overlap	P-value	Adjusted P-value	Odds Ratio
endopeptidase activity (GO:0004175)	21/354	1.0098E-10	1.1623E-07	5.8159
serine-type endopeptidase activity (GO:0004252)	14/196	1.4595E-08	8.3992E-06	7.0028
cysteine-type peptidase activity (GO:0008234)	9/65	1.9539E-08	7.4966E-06	13.5747
serine-type peptidase activity (GO:0008236)	14/220	6.2604E-08	1.8014E-05	6.2389
cysteine-type endopeptidase activity (GO:0004197)	9/81	1.3855E-07	3.1894E-05	10.8932
integrin binding (GO:0005178)	7/94	5.0098E-05	9.6104E-03	7.3008
peptidase activity, acting on L-amino acid peptides (GO:0070011)	9/185	1.2260E-04	2.0160E-02	4.7695
amyloid-beta binding (GO:0001540)	5/49	1.3920E-04	2.0027E-02	10.0040
collagen binding (GO:0005518)	5/52	1.8508E-04	2.3669E-02	9.4268

GO_Cellular_Component_2018_table

Term	Overlap	P-value	Adjusted P-value	Odds Ratio
lysosome (GO:0005764)	30/422	5.2173E-17	2.3269E-14	6.9696
lytic vacuole (GO:0000323)	21/183	2.4423E-16	5.4463E-14	11.2504
secretory granule lumen (GO:0034774)	24/317	2.1608E-14	3.2124E-12	7.4225
vacuolar lumen (GO:0005775)	15/161	1.0735E-10	1.1969E-08	9.1341
azurophil granule (GO:0042582)	14/154	6.3456E-10	5.6603E-08	8.9127
lysosomal lumen (GO:0043202)	11/86	1.1905E-09	8.8492E-08	12.5399
membrane raft (GO:0045121)	10/119	3.9607E-07	2.5235E-05	8.2386
ficolin-1-rich granule (GO:0101002)	12/184	4.3156E-07	2.4059E-05	6.3939
endoplasmic reticulum lumen (GO:0005788)	14/270	7.6343E-07	3.7832E-05	5.0835

C Genes repressed by Aβ and Tau Pathology in Astrocytes

KEGG_2019_Mouse_table

Term	Overlap	P-value	Adjusted P-value	Odds Ratio
Oxidative phosphorylation	28/134	9.9257E-33	3.0075E-30	27.4941
Thermogenesis	30/231	1.6245E-28	2.4610E-26	17.0882
Cardiac muscle contraction	11/78	1.7032E-11	7.3725E-10	18.5560
Retrograde endocannabinoid signaling	12/150	1.6799E-09	6.3625E-08	10.5263
Ribosome	12/170	6.9955E-09	2.3552E-07	9.2879

GO_Biological_Process_2018_table

Term	Overlap	P-value	Adjusted P-value	Odds Ratio
mitochondrial ATP synthesis coupled electron transport (GO:0042775)	22/85	4.1623E-28	2.1240E-24	34.0557
respiratory electron transport chain (GO:0022904)	22/94	4.9175E-27	1.2547E-23	30.7951
mitochondrial respiratory chain complex assembly (GO:0033108)	19/97	7.2088E-22	1.2262E-18	25.7732
mitochondrial electron transport, NADH to ubiquinone (GO:0006120)	12/46	7.4422E-16	9.4944E-13	34.3249
NADH dehydrogenase complex assembly (GO:0010257)	13/64	1.5767E-15	1.6092E-12	26.7270
mitochondrial respiratory chain complex I biogenesis (GO:0097031)	13/64	1.5767E-15	1.3410E-12	26.7270
mitochondrial respiratory chain complex I assembly (GO:0032981)	13/64	1.5767E-15	1.1494E-12	26.7270
mitochondrial transport (GO:0006839)	11/135	6.7712E-09	4.3192E-06	10.7212
mitochondrial electron transport, cytochrome c to oxygen (GO:0006123)	6/21	8.6176E-09	4.8862E-06	37.5940
peptide biosynthetic process (GO:0043043)	12/174	9.0951E-09	4.6412E-06	9.0744

GO_Molecular_Function_2018_table

Term	Overlap	P-value	Adjusted P-value	Odds Ratio
NADH dehydrogenase (ubiquinone) activity (GO:0008137)	12/43	2.9913E-16	3.4430E-13	36.7197
NADH dehydrogenase (quinone) activity (GO:0050136)	12/43	2.9913E-16	1.7215E-13	36.7197
ubiquinol-cytochrome-c reductase activity (GO:0008121)	5/8	1.3047E-09	5.0058E-07	82.2368
oxidoreductase activity, acting on diphenols... cytochrome as acceptor (GO:0016681)	5/8	1.3047E-09	3.7544E-07	82.2368
hydrogen ion transmembrane transporter activity (GO:0015078)	6/51	2.3704E-06	5.4567E-04	15.4799

GO_Cellular_Component_2018_table

Term	Overlap	P-value	Adjusted P-value	Odds Ratio
mitochondrial inner membrane (GO:0005743)	36/341	6.0740E-31	2.7090E-28	13.8910
mitochondrion (GO:0005739)	37/1026	1.1103E-15	2.4760E-13	4.7450
mitochondrial respiratory chain complex I (GO:0005747)	12/51	2.9396E-15	4.3702E-13	30.9598
cytosolic small ribosomal subunit (GO:0022627)	7/49	8.3798E-08	9.3435E-06	18.7970
small ribosomal subunit (GO:0015935)	7/53	1.4660E-07	1.3077E-05	17.3784
mitochondrial respiratory chain complex III (GO:0005750)	4/14	3.0251E-06	2.2487E-04	37.5940
cytosolic ribosome (GO:0022626)	8/124	4.8376E-06	3.0822E-04	8.4890
mitochondrial respiratory chain complex IV (GO:0005751)	4/17	7.0659E-06	3.9392E-04	30.9598
mitochondrial proton-transporting ATP synthase complex	4/22	2.1084E-05	1.0448E-03	23.9234
ribosome (GO:0005840)	6/76	2.4616E-05	1.0979E-03	10.3878

D Induced by Aβ and Tau Pathology in Astrocytes

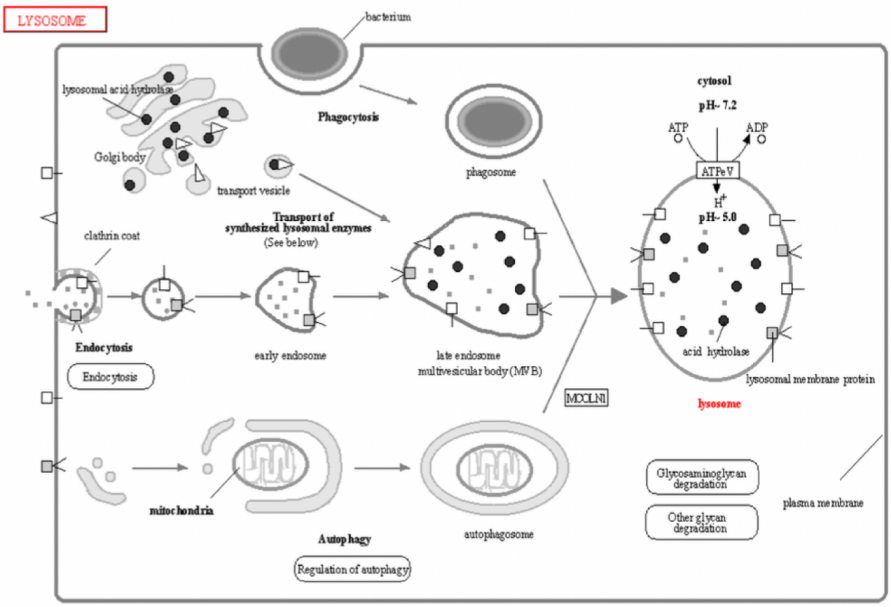

Lysosomal acid hydrolases: proteases, glycosidases, sulfatases, lipases

Arsa Daglb Ctsa Ctsb
Ctsc Ctsd Ctsh Ctsl
Ctss Ctsz Gba Fuca1
Hexa Hexb Ppt1 Psap

Lysosomal/Endosomal membrane

Atp6ap1 Itm2c Flot1 Gnb4
Lamp1 Laptm5 Ncstn

Endosomal/ lysosomal trafficking & fusion

Ap5b1 Mcoln1

E Repressed by Aβ and Tau Pathology in Astrocytes

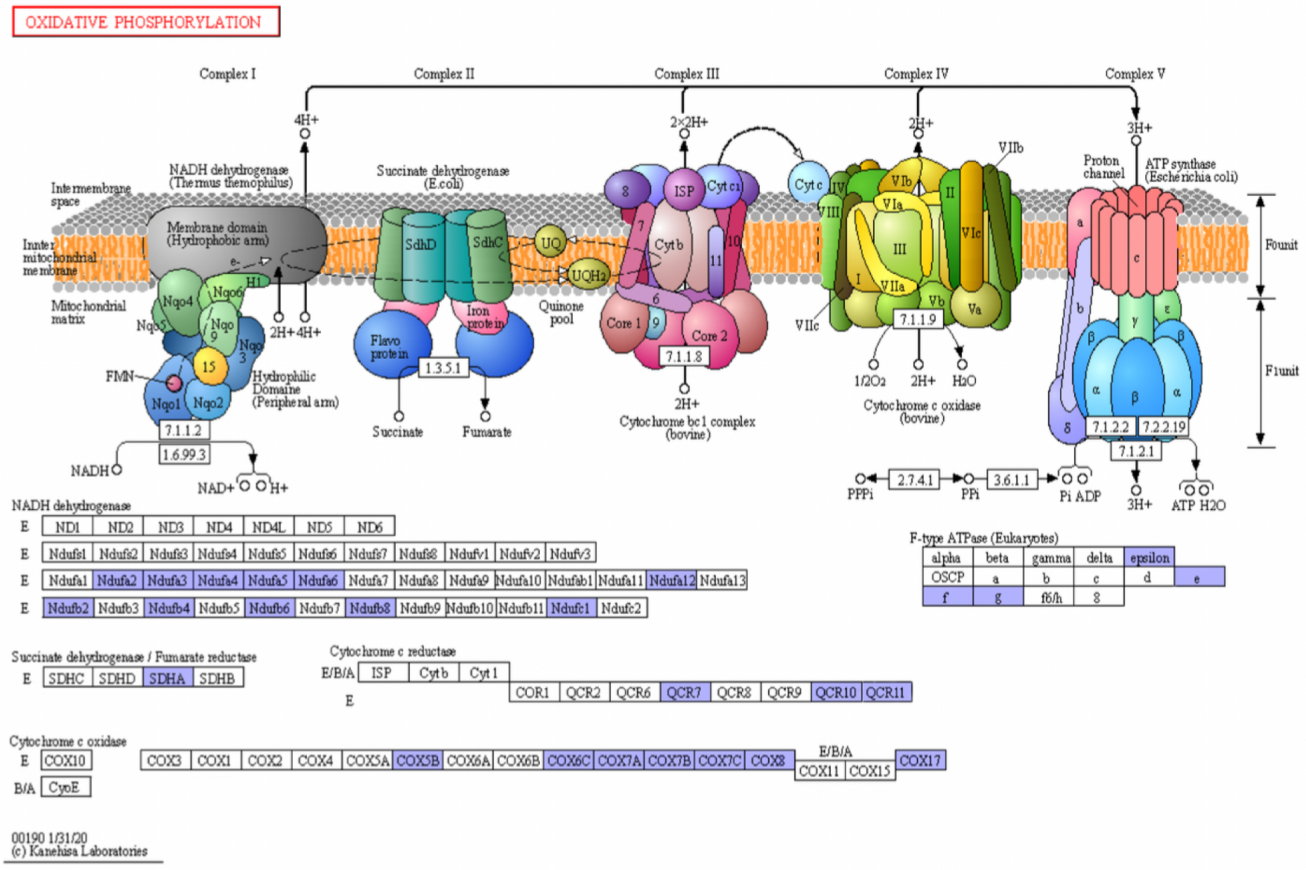

Figure 36. Aβ and tau pathology trigger a core set of gene expression changes in astrocytes. **(A)** heat map of genes induced (red) and repressed (blue) in both $MAPT^{P301S}$ and APP/PS1 mice. **(B, C)** Ontological analysis of genes induced **(B)** or repressed **(C)** in astrocytes in both APP/PS1 and $MAPT^{P301S}$ mice. For KEGG pathway analysis, disease pathways were omitted and number of genes required was ≥5. For KEGG and GO analysis the top 10 pathways are shown, unless fewer than 10 achieved an adjusted p-value cut-off of 0.05. **(D, E) Reproductions of the top KEGG Pathways induced and repressed by Aβ and tau pathology in astrocytes. (D)** The KEGG lysosome pathway with lysosomal genes induced in astrocytes in both the APP/PS1 and $MAPT^{P301S}$ models shaded in red. **(E)** The KEGG oxidative phosphorylation pathway, with genes repressed in astrocytes in both the APP/PS1 and $MAPT^{P301S}$ models shaded in blue.

4.2.8 Transcription Factor Analysis of Core Genes Induced by Aβ and Tau Pathology

I next wanted to understand whether the core genes changed by Aβ and tau pathology were enriched for genes regulated by a certain transcription factor, since a putative common regulator could pose as a druggable target. When interrogating the TFEA.ChiP platform (https://www.iib.uam.es/TFEA.ChIP/) and the ENCODE and ChEA consensus target genes from Chip-X database on the Enrichr platform (https://maayanlab.cloud/Enrichr/), transcription factor PU.1 (SPI1), a known inflammatory mediator (Prinz and Priller 2014), and Nuclear Factor Erythroid 2-Related Factor 2 (NFE2L2/NRF2), a master regulator of antioxidant, detoxification and proteostasis genes (Pajares et al. 2017; Shih et al. 2005; Nguyen et al. 2009), were enriched in both datasets **(figure 37B)**.

A Genes induced by Aβ and tau pathology in astrocytes

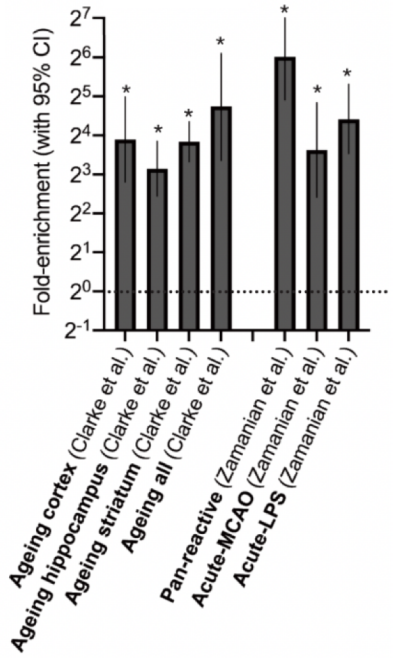

B Transcription factor analysis of genes induced by Aβ and tau pathology in astrocytes

TFEA.ChIP

TF	Accession	p.value	adj.p.value	Odds Ratio
NR2F2	GSE96124	1.2900E-09	1.4900E-06	2.9680
ARNTL	GSM1816455	3.9400E-08	2.2700E-05	2.2789
ZBTB48	GSE76496.27	4.5000E-07	9.7400E-05	4.7583
CTCF	wgEncodeEH003434	6.9500E-07	9.7400E-05	2.6266
CEBPB	wgEncodeEH001815	6.8600E-07	9.7400E-05	2.4187
NFE2L2 (NRF2)	GSE37589	2.7700E-07	9.7400E-05	2.1151
JUND	wgEncodeEH002164	1.0800E-06	1.2448E-04	2.3717
MYOD1	GSM1218849	1.4000E-06	1.2448E-04	2.2439
SPI1	wgEncodeEH001482	1.2900E-06	1.2448E-04	2.1310

ENCODE_and_ChEA_Consensus_TFs_from_ChIP-X_table

Term	P-value	Adjusted P-value	Odds Ratio
SPI1 CHEA	3.477E-06	3.616E-04	2.600
NFIC ENCODE	6.098E-04	3.171E-02	3.514
NFE2L2 (NRF2) CHEA	7.807E-04	2.706E-02	2.110

Figure 37. Enrichment analysis of genes induced by both Aβ and tau pathology. (A) Genes induced in astrocytes in APP/PS1 and MAPT^{P301S} astrocytes (expression cut off FPKM<1, p_adj<0.05) were subjected to enrichment analysis against the indicated gene sets. *p<0.0001 in all cases, (two-sided Fisher's exact test). **(B)** Enrichment analysis of genes induced in both MAPT^{P301S} and APP/PS1 mice for transcription factor targets using a survey of the TFEA.ChIP platform (left) and the ENCODE and ChEA Consensus target genes from ChIP-X performed in the Enrichr platform. SPI1 and NFE2L2/NRF2 were transcription factors highlighted in both enrichment analyses.

4.2.9 Comparison of Genes Induced by Aβ and Tau Pathology in Mouse Astrocytes to Human AD Astrocytes

Mouse models have proven invaluable for studying biological processes and the consequences of pathology found in humans. That being said, experimental findings in mouse models do not always translate to the human condition, as whilst the species are phylogenetically similar, mice and humans have evolved and adapted differently.

I wanted to compare the core gene set induced by Aβ and tau pathology in our mouse datasets to a human post-mortem dataset where both pathologies are present. I used the data from the Grubman et al. (2019) single nucleus RNA-seq study, looking at genes induced in astrocytes in AD relative to control. I performed an enrichment analysis on those genes with 1:1 orthologs in mouse, expressed > 10 FPKM (a higher than normal threshold since highly expressed genes are more likely to be detected in single cell RNA-seq).

Genes up-regulated in the translatome of both APP/PS1 and $MAPT^{P301S}$ astrocytes were enriched in genes induced in human AD astrocytes **(figure 38A)**. Furthermore, the core set of genes induced by both Aβ and tau pathology was also enriched ($p<0.0001$ in all cases, two-sided Fisher's exact test) **(figure 38A)**. Of the 126 genes expressed >10FPKM in either or both models, 68/126 were induced by Aβ pathology, 86/126 were induced by tau pathology and 28/126 were induced by both ($p\_adj<0.05$), **(figure 38B)**. Hence, there is significant association of genes induced in astrocytes by Aβ and tau pathology in mice over months, with those elevated in human astrocytes post-mortem after many years of patho-progression.

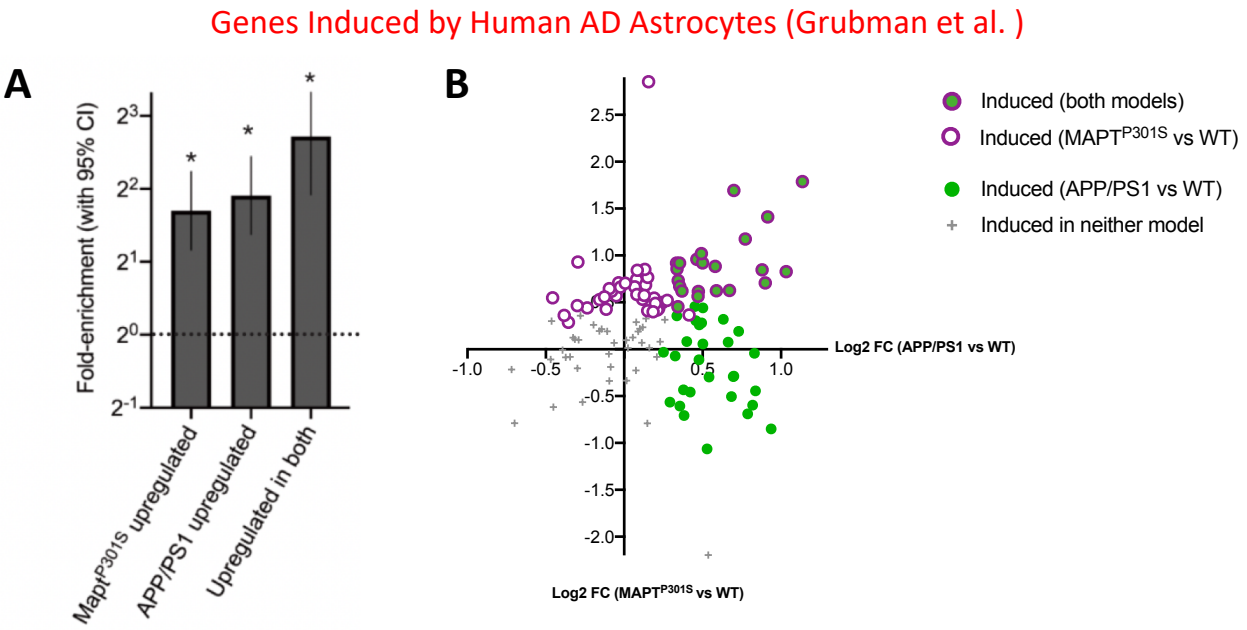

Figure 38. Comparison of genes induced in astrocytes in AD mouse models with genes induced in human AD astrocytes (A) Enrichment analysis of genes induced in human AD astrocytes (Grubman et al. 2019) for which a 1:1 ortholog exists (and >10FPKM cut off) for genes induced in APP/PS1 astrocytes, and MAPT^{P301S} astrocytes, or those induced in both models *p<0.0001 in all cases, (two-sided Fisher's exact test). **(B)** Genes induced in human AD astrocytes for which a 1:1 mouse ortholog exists and that are expressed >10 FPKM in APP/PS1 and MAPT^{P301S} astrocytes. Log_2-fold change in each gene is shown for both models (x-axis: APP/PS1 vs. WT; y-axis: MAPT^{P301S} vs. WT). For each gene, an indication of whether it is significantly (p_adj<0.05) induced in either, both or neither model is shown.

4.2.10 Astrocytes in Amyloidopathy and Tauopathy Mice Show Differential Enrichment in AD Risk Genes

Finally, GWAS have provided an understanding of genetic risk variants associated with human AD, and are somewhat responsible for the enthusiasm in glia research in AD, since many of the risk genes are expressed in glia (Karch and Goate 2015; Bertram and Tanzi 2009). Sierksma et al. (2020) recently published a paper where they looked at the enrichment of Aβ and tau-induced changes in gene expression in microglia for AD risk genes and sub-threshold risk loci, using the Marioni et al (2018) GWAS dataset (Marioni et al. 2018; Sierksma et al. 2020). I decided to deploy a similar technique looking at enrichment of AD risk genes in the amyloidopathy and tauopathy induced astrocyte translatome datasets.

There were 9938 genes expressed ≥ 1 FPKM, induced >1.5 fold (p_adj<0.05) in the TRAP-seq datasets for which a gene-level GWAS p-value was available. Using a Bonferroni-corrected cut-off of 0.05/9938 (i.e. 5.03E-06), induced genes in the APP/PS1 TRAP-seq data were significantly enriched in AD risk genes **(figure 39A)**. Furthermore, sequential relaxing of the p-value cut-offs to include more subthreshold risk genes maintained significant enrichment down to p=5E-03, with enrichment disappearing at the p=5E-02 cut-off. In contrast, a similar analysis of genes induced in $MAPT^{P301S}$ astrocytes did not achieve significance at any p-value cut-off **(figure 39B)**. However, despite not reaching significance the overlap at p=5.03E-06 for the $MAPT^{P301S}$ dataset (7/666) was similar to the APP/PS1 dataset (9/756). Hence, one should not read too much into the differences between Aβ and tau pathology. Nevertheless, this finding raises the possibility that astrocyte-centred genetic risk may influence their response to Aβ pathology, just as has been suggested for microglia (Sierksma et al. 2020).

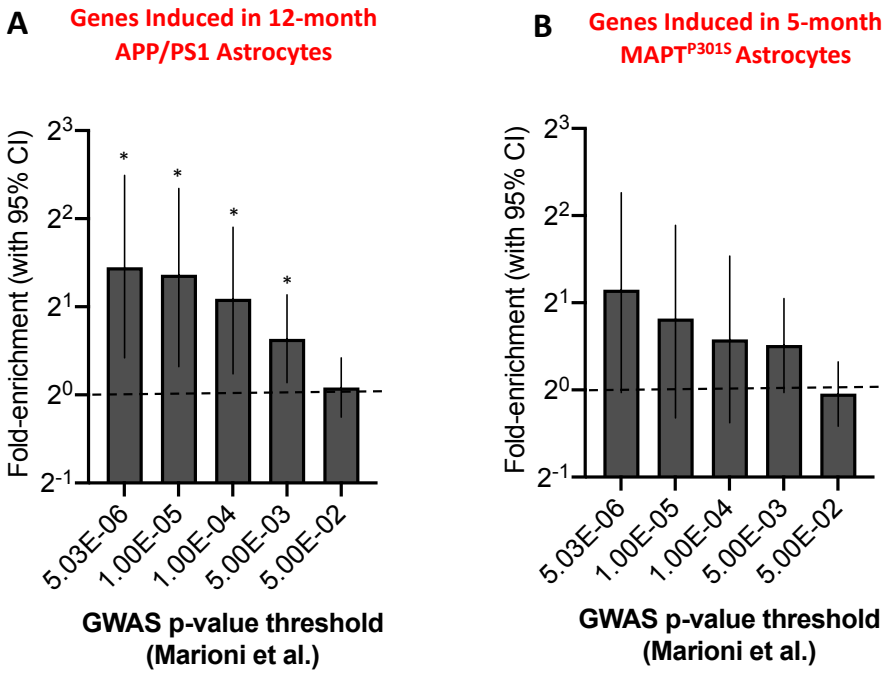

Figure 39. Enrichment analysis of Aβ and tau-induced changes in astrocytes for AD risk genes and sub-threshold risk loci. Genes induced >1.5 fold at 12 months in the APP/PS1 astrocytes **(A)**, and 5-month MAPT^{P301S} astrocytes **(B)** (expression cut-off 1FPKM, p_adj<0.05) were taken and enrichment analysis for human genes associated with late-onset AD was conducted. The analysis was conducted using the Marioni et al. (2018) GWAS dataset with differing p-value cut-offs. p-values (left to right): 0.011, 0.028, 0.017, 0.020, 0.0815,0.1943,0.2918,0.0748,0.8988 (two-sided Fisher's exact test).

4.3 Discussion

4.3.1 Summary of Findings

This chapter focused on investigating the effect of Aβ pathology on the astrocyte translatome. The APP^{NLF} and APP/PS1 amyloidopathy mouse models were subject to TRAP-seq. The 6 and 12-month APP^{NLF} and 6-month APP/PS1 astrocytes demonstrated none or few significant differentially expressed genes compared to corresponding WT astrocytes. However, there were non-significant indications of changes to astrocyte gene expression beginning early in amyloidopathy. Ontological analysis of genes changed concurrent with amyloidopathy revealed upregulation of genes involved in neuron and synaptic transmission maintenance, as well as pathways involved in protein degradation and the inflammatory response. Age-dependent genes and acutely-induced reactive astrocyte genes were induced concomitant with Aβ pathology. Comparison of astrocytic gene expression changes concurrent with amyloidopathy and tauopathy was performed using a previously curated $MAPT^{P301S}$ TRAP-seq dataset. The core genes upregulated by both pathologies revealed similar signatures to the amyloidopathy alone, with terms associated with proteolysis and the immune response being upregulated. Some of the genes induced by both pathologies may be regulated by NRF2, a master regulator of antioxidant, detoxification and proteostasis genes. Notably, the genes induced by Aβ, tau or both pathologies were enriched for genes changed in astrocytes extracted from human post-mortem AD, indicating translational relevance of results. An intriguing difference between the amyloidopathy and tauopathy datasets was that only the astrocytes exposed to amyloidopathy were significantly enriched for AD risk genes.

4.3.2 Amyloidopathy Induced Alterations in Astrocytes

The APP/PS1 astrocytes displayed more differentially expressed genes at all ages compared to the APP^{NLF} astrocytes. This was to be expected since the pathology in the transgenic APP/PS1 mouse develops quicker than in the knock-in APP^{NLF} model. Nevertheless, given synapse loss was significant around dense core plaques in 12-month APP^{NLF} mice, one might have expected to have seen more alterations in astrocyte phenotype at this age. Perhaps the relatively low plaque load in the APP^{NLF} mouse at this age meant that alterations in astrocytic gene expression in astrocytes surrounding plaques were lost when bulk sequencing

neocortical astrocytes. Future work where astrocytes surrounding plaques are laser capture microdissected and sequenced would identify if this is the case.

Interestingly, genes which are significantly induced >1.5 fold (p_adj<0.05) in 12 and 18-month astrocytes appear to increase in expression with age in APP^{NLF} astrocytes, indicating that although pathology in the APP^{NLF} mouse is slower to develop, directionality of gene expression alterations due to amyloid pathology appear somewhat conserved between the two models. Ontological analysis of genes changed due to chronic amyloidopathy indicate the astrocytes are upregulating protein degradative mechanisms, a potential protective mechanism in response to increased Aβ load. Additionally, the genes induced by amyloidopathy were enriched for processes involved in neuron development and synaptic transmission, again suggesting induction of protective mechanisms against the well documented amyloidopathy induced neurodegeneration (Liu et al. 2008) and synapse degeneration (Koffie et al. 2009). The presence of terms related to immune response activation may either be interpreted as protective or damaging, depending on the extent of activation and targets of phagocytosis. Whilst astrocytes appear to play an important role in mitigating aspects of pathology induced by Aβ, these protective mechanisms are not efficacious enough or are upregulated too late to halt disease progression. Astrocyte targeted therapeutics, which further bolster protein degradative pathways or support synaptic function, may provide meaningful improvements in AD, if given at an appropriate time point in the disease progression.

4.3.3 Astrocyte Responses to Aβ Pathology Overlap with Ageing

In this study, I found that genes induced in 12-month APP/PS1 astrocytes were significantly enriched in genes induced in 24-month WT mouse astrocytes, indicating an overlap of genes induced in amyloidopathy and ageing. This was further supported by comparison of the 12-month and 18-month APP/PS1 astrocyte TRAP-seq, where the 18-month APP/PS1 vs WT TRAP-seq demonstrated fewer differentially expressed genes compared to the 12-month APP/PS1 vs WT TRAP-seq, perhaps due to alterations in astrocyte gene expression induced by amyloidopathy overlapping with those changed due to ageing. Both ageing and AD are

associated with changes in cognition, functional connectivity, neurotransmission, as well as grey and white matter loss (Toepper 2017). However, there are clear differences in the details of these neurocognitive changes. For example, AD is characterised by an accentuated cholinergic dysfunction (Teipel et al. 2011), whereas ageing is associated with dopaminergic dysfunction (Li et al. 2010). This suggests that AD is not simply accelerated ageing. Nevertheless, both the ageing brain and AD involve compromised environments, be it metabolic, inflammatory, or other homeostatic functions. This could explain the overlapping molecular response of astrocytes to ageing and Aβ pathology, and is consistent with increasing age being the main risk factor for AD (Hou et al. 2019).

4.3.4 Aβ Pathology Induces Astrocytes to Adopt a Profile that Does Not Fit the Discrete A1/A2 Astrocyte Profiles

Defining the heterogeneity of astrocyte responses to different conditions has become a fundamental area of glia research. Liddelow et al (2017) described two reactive astrocyte profiles, derived from an earlier microarray study (Zamanian et al. 2012; Liddelow et al. 2017). One profile, made up of 12 genes, was induced acutely by LPS-activated inflammatory microglia (so-called A1) and was deemed neurotoxic. The other profile, also made up of 12 genes, was induced acutely by ischemia (so-called A2), and was proposed to be neuroprotective. 13 genes were reported to be expressed in both LPS-induced and MCAO-induced astrocytes, and were termed 'pan-reactive genes'.

The 12-month APP/PS1 astrocytes were significantly enriched in the Liddelow A1 and pan-reactive gene sets **(figure 35)**. However, these gene sets are small and the rationale behind their choice was not stated, and in some cases appeared unjustified. For example, *Cp* (Ceruloplasmin) was included in the pan-reactive set despite being the 12th highest induced gene by LPS and only 75th by MCAO, whereas *Gbp* was included in the A1 set even though it was the 26th highest induced gene in the MCAO set (and 8th in the LPS set). In a similar vein, *Cd44* (CD44 Antigen) was included in the pan-reactive set despite being only ranked 234th in the LPS set and 32nd in the MCAO set, whereas *Cd109* (CD109 Antigen) was included in the A2 set even though it was the 36th highest induced gene in the LPS set (and 15th in the MCAO set). We therefore exploited the full transcriptional characterisation of these two reactive

astrocyte phenotypes to define larger gene sets **(figure 35C)**. The expanded analyses showed significant enrichment in 12-month APP/PS1 astrocytes for all gene sets curated **(figure 35D**), with no evidence of preferential enrichment in the acute-LPS gene set. These results challenge the hypothesis made by Liddelow et al. that the majority of astrocytes in AD display A1 reactive profiles. Notably, their hypothesis was only based upon C3 immunoreactivity in end-stage disease (Liddelow et al. 2017).

The binary classification of reactive astrocytes into LPS-like ("A1") or stroke-like ("A2") appears to be unhelpful when investigating chronic disease pathology. Just as categorising microglia into M1 and M2 has fallen out of favour following routine use of genome-wide characterisation of transcriptomes (Nahrendorf and Swirski 2016), categorising astrocytes in such a manner is likely an over-simplification which will fall out of use. Nevertheless, defining the continuum of astrocyte profiles whilst considering stimulus, location, time, heterogeneity and the surrounding cell type reactions, will be invaluable when developing astrocyte targeted therapeutics. The analyses presented here highlight the reactive profiles of astrocytes when chronically exposed to Aβ pathology at early and later stages. Notably, the TRAP-seq was conducted on pooled astrocyte RNA, and so information on the heterogeneity and location of astrocytes was lost. In-situ single cell RNA-seq of astrocytes would provide valuable complementary information.

4.3.5 A Common Astrocyte Response Signature to Aβ and Tau Pathology

There was a substantial number of genes that were induced or repressed by both pathologies **(figure 36)**. Gene ontology analysis pointed towards activation of inflammatory pathways and upregulation of genes involved in protein degradation, potentially an adaptive/protective response to increased protein aggregates and/or debris in the extracellular milieu. In the context of genes downregulated by both Aβ and tau pathology, gene ontology analysis pointed to the repression of protein translation and mitochondrial oxidative phosphorylation. Defective translation could affect the ability of astrocytes to carry out their fundamental functions, leading to poor homeostatic support of neurons. Impaired astrocytic mitochondrial oxidative phosphorylation likely contributes to the overproduction of reactive oxygen species (ROS) which is found in AD and AD models (González-Reyes et al. 2017; Huang et al. 2016;

Hamel et al. 2008). Additionally, dysfunctional mitochondrial oxidative phosphorylation could lead to the inhibition of synaptic transmission, as it has been shown that use of fluoroacetate to selectively inhibit glial oxidative metabolism causes astrocytes to secrete adenosine, leading to synaptic inhibition (Canals et al. 2008). Whilst this mechanism was postulated to represent an energy-conserving neuroprotective response to prevent lethal depolarization, one can envisage that it would nevertheless alter circuit function and cognitive performance if maintained over a long period of time.

4.3.6 Therapeutically Targeting NRF2 in Astrocytes Early in AD.

The core gene set induced by Aβ and tau pathology in astrocytes was enriched in target genes of the transcription factors SPI1 and NRF2. The NRF2 pathway can be activated by conditions such as oxidative stress and is fundamental for antioxidant production, inflammatory regulation, xenobiotic detoxification, metabolic reprogramming, and proteostasis (Nguyen et al. 2009). Upregulation of genes downstream of NRF2 is likely an adaptive protective mechanism to the pathological insult. However, given the continued development of pathology in mouse and human, NRF2 activation appears to be too little, too late, to substantially alter disease trajectory. Indeed, this study shows that gene changes in astrocytes due to late-stage amyloidopathy begin much earlier in the course of pathology **(figure 30)**. Nevertheless, given the broad protective functions attributed to NRF2 activation, pharmacologically enhancing NRF2 activation at a suitably early time-point has the potential to mitigates some of the harmful components of AD.

NRF2 expression is thought to be epigenetically repressed in mature neurons (Bell et al. 2015). This emphasises the importance of this pathway in astrocytes to provide cell autonomous and non-cell-autonomous cytoprotection. An example benefit of enhancing astrocytic NRF2 includes promoting glutathione production and release into the extracellular space (Steele et al. 2013). This would enhance interstitial redox buffering, and provide cysteine-based precursors for non-astrocytic cells to use to enhance their own glutathione production and antioxidant capacity. In turn, fortified intraneuronal redox buffering could reduce tau phosphorylation and aggregation (Su et al. 2010), as well as repress ROS induced endoplasmic reticulum (ER) stress and unfolded protein response (UPR) over-activation (Uddin et al. 2020).

Additionally, ROS have been implicated in both causing chronic microglial and astrocytic activation, and being a product of chronic glial activation (Sheng et al. 2013; Ishii et al. 2017; Su et al. 2008). Hence, enhancing astrocytic NRF2 could suppress this self-amplifying cascade.

Therapies specifically targeting astrocytic NRF2 have yet to be investigated clinically. However, there is considerable pre-clinical research to suggest that NRF2 is an attractive therapeutic target. For example, Shih et al. (2005) demonstrated that dietary supplementation with the NRF2 inducer tert-butyl hydroquinone conferred neuroprotection to mice during mitochondrial stress (Shih et al. 2005). Additionally, Oksanen et al (2020) have shown that activation of NRF2 in Presenilin-1-mutated AD patient astrocytes reduced amyloid secretion, normalised cytokine release, increased secretion of the antioxidant glutathione, and finally increased the utilisation of glycolysis (Oksanen et al. 2020). Activation of NRF2 specifically in astrocytes in AD mouse models has yet to be published. However, this data supports trial of such strategies.

4.3.7 Relating Mouse Astrocyte Responses to Aβ and Tau Pathology to Human AD

The utility of mouse models is largely dependent on how well the findings translate to the human condition. Recently, there have been several papers highlighting the differences between mouse and human astrocytes, emphasising the smaller, less structurally complex nature of rodent astrocytes (Oberheim et al. 2009; Zhang et al. 2016). Hence, it was important to compare the responses of APP/PS1 and $MAPT^{P301S}$ astrocytes to human end-stage AD astrocytes. We utilised the largest reported gene set to date of differentially induced genes in human astrocytes from post-mortem AD brains (Grubman et al. 2019). Both pathologies in mice induced changes enriched in genes changed in human AD astrocytes **(figure 38)**. Whilst some genes induced in human AD were enriched in both the APP/PS1 and $MAPT^{P301S}$ astrocytes, other genes were only enriched in one of the models **(figure 38B)**. This is consistent with human AD being a combination of Aβ and tau pathology. Of note, there were genes that were induced in human AD that were not induced in either of the animal models. This could be due to species differences, different isolation methods impacting gene expression, or due to post-mortem astrocytes reflecting end-stage disease.

GWAS have identified several genes which are associated with increased risk of developing AD in humans. Many of these genes, such as *APOE*, *CLU* and *SORL1* are expressed in astrocytes (Karch and Goate 2015). An interesting distinction between the mouse astrocytes exposed to amyloidopathy and tauopathy was that only the amyloidopathy-induced astrocyte translatome was enriched in AD risk genes and subthreshold risk loci **(figure 39)**. A similar finding was reported to occur in mouse microglia exposed to amyloidopathy and tauopathy (Sierksma et al. 2020). These results could suggest that cumulative genetic risk is involved in determining the response of astrocytes to Aβ (direct or indirect e.g. via microglia). It remains to be seen how individual single nucleotide polymorphisms influence responses of genes to Aβ, and what the functional consequences are for astrocytes and microglia. However, it is possible that the glial response to Aβ is fundamental in determining the spectrum of outcomes of high Aβ load, ranging from aggressive AD to apparent tolerance of a high Aβ burden in the absence of cognitive symptoms.

4.3.8 Limitations and future work

The TRAP method used to isolate cell type specific mRNA has some limitations. Astrocyte ribosomes and translating mRNA were isolated by driving expression of an eGFP tagged ribosomal subunit using the *Aldh1l1* promoter. Whilst *Aldh1l1* is considered to be the best marker for distinguishing astrocytes from other cell types in the CNS (Srinivasan et al. 2016), *Aldh1l1* is lowly expressed in neurons, oligodendrocyte precursor cells, oligodendrocytes and microglia (Zhang et al. 2014). Hence, there is potential for off-target isolation and gene expression detection. We tried to mitigate this by checking the expression of genes that are considered to be cell type specific using qPCR and RNA-seq.

A second limitation of the TRAP method used was that astrocyte RNA from all over the neocortex was pooled. This would have masked any regional differences in the response of astrocytes to Aβ (or tau). Indeed, Bayrakartar et al (2020) has shown that even within one area of the brain, the somatosensory cortex, astrocyte gene expression can change dependent on the cortical layer (Bayraktar et al. 2020). Future work where astrocytes near to and further from the plaque are laser capture microdissected and single cell transcriptomic studies are conducted would not only help identify whether pathological alterations in astrocyte gene expression are occurring in a small subset of APP^{NLF} astrocytes near the plaques, it would also illuminate heterogeneity of astrocyte response to AD pathology.

An important limitation to consider with all transcriptomic studies is that mRNA levels may not correlate with protein levels. However, the TRAP methodology extracts actively translating mRNA, which we expect would correlate more closely with protein levels, and therefore the function of the astrocyte, when compared to total mRNA levels. In fact, the cellular abundance of proteins has been shown to be controlled at the level of translation (Schwanhäusser et al. 2011). A study comparing the astrocyte translatome and proteome in health and disease would illuminate how closely function can be inferred from the translatome and help to validate suggested alterations in pathways found in this research.

Another aspect to consider when assessing this research is that both the APP/PS1 and $MAPT^{P301S}$ mouse models are overexpression models. In the APP/PS1 mouse model, we cannot rule out the effect of high expression of APP cleavage products other than Aβ on differential astrocytic gene

expression. Furthermore, the MAPT^{P301S} mouse model contains a mutation that is not found in familial or sporadic AD, but in frontotemporal dementia. Despite this, the area most affected in the MAPT^{P301S} model is the spinal cord. This contrasts with human AD, where tau pathology develops from the entorhinal cortex to the rest of the brain. Despite the weaknesses in these transgenic mouse models, they are both useful tools to understand the impact of pathology on astrocytes. The enrichment of genes changed in human AD post-mortem astrocytes gives confidence in the models being somewhat useful to investigate the impact of Aβ and tau pathology on astrocytic gene expression. Nevertheless, in future studies it may be beneficial to use newer models of AD, such as the knock-in MAPT tauopathy model recently developed by Saito et al. (Saito et al. 2019), or the a model which contains both pathologies, and where pathology is found in similar areas of the mouse brain as in human AD.

Much of the analysis conducted involved ontological analysis of genes induced/repressed in each mouse model. Important aspects to consider when conducting ontological analyses are the fact that the data produced are only as good as the data that is entered, cut off thresholds are somewhat arbitrarily set and may not reflect biological significance, there are many different versions of ontological analyses, which may produce varying results, thus it may be useful to conduct analyses across multiple platforms to compare the output. Additionally, genes induced and repressed are often input separately into GO analyses to infer pathways induced and repressed. However, this may not accurately represent pathway dynamics where the balance of genes induced and repressed should ideally be considered together. To somewhat mitigate this, I also conducted IPA which does consider genes induced and repressed together in order to infer pathway dynamics. A further aspect to consider is sample source bias. This is where many of the terms returned by gene set enrichment analysis describes the sample rather than the condition, i.e. highlighting brain related GO/KEGG terms simply due to the sample being from the brain. I attempted to mitigate some of this risk by being stringent about the genes included in the GO analysis i.e. performing ontological analysis on genes robustly changed by amyloidopathy by looking at the intersection of genes changed in the 12 and 18-month APP/PS1 astrocytes. However, in the future it would be useful to select an astrocytic background set of genes against which to test for over-representation rather than all the genes annotated on the mouse genome.

Whilst time did not permit qPCR confirmation of select genes induced and repressed in each model, this will be an important step in validating results. Additionally, western blot analysis of protein expression would help to validate alterations to astrocyte phenotype. Conducting functional analysis such as a glutathione assay would validate functional consequences of alterations in gene expression.

Many of the gene set enrichment analyses presented here focused on the genes that were induced by Aβ pathology. However, there was also a substantial number of genes repressed. Analysis of this repressed dataset would further illuminate aspects of astrocyte dysfunction. In a similar vein, I focused on the similarities between astrocytic gene expression in an amyloidopathy and tauopathy model, in the future it would be informative to investigate the differences in astrocytic gene expression between the two models. This would help to dissect the impact of each pathology on astrocytic function and better target future therapeutics. Additionally, future work comparing genes induced in amyloidopathy and tauopathy astrocytes with those induced in astrocytes from other disease models would help to identify whether the similarities in altered gene expression in the amyloidopathy and tauopathy exposed astrocytes are simply markers of a stressed and pathological brain or whether they are common signatures specific to amyloidopathy and tauopathy exposed astrocytes. Irrespective of whether the gene alterations are specific to AD, this work contributes to our understanding pathology associated astrocytes and the development of future therapeutic targets. Experiments designed to bolster astrocyte expression of NRF2 in mouse models of AD and measure gene expression/pathological load/behaviour would develop our understanding of whether astrocytic NRF2 is a viable therapeutic target for AD.

4.4 Chapter Conclusion

In this chapter I have investigated alterations in the astrocyte translatome due to Aβ pathology. I used a dataset curated by Dr Zoeb Jiwaji on alterations in the astrocyte translatome due to tau pathology to address how astrocytes are affected by the two cardinal pathologies of AD. The APP/PS1 and APP^{NLF} mouse models of amyloidopathy were used, along with the $MAPT^{P301S}$ tauopathy mouse model. Amyloidopathy appeared to exacerbate age

dependent gene changes in astrocytes, as well as inducing a profile which resembled acutely induced reactive astrocytes. This highlighted an overlap of acute and chronic reactive astrocyte signatures. Both Aβ and tau pathology seemed to induce dysfunction of mitochondria and protein synthesis, and encourage an upregulation of inflammation and protein degradation. Interestingly, only astrocytes exposed to amyloidopathy were enriched in AD risk genes and subthreshold risk loci, which might indicate that the astrocyte response to Aβ is particularly involved in the development of AD. Finally, NRF2 emerged as a putative therapeutic target. However, more studies would need to be done to thoroughly investigate this.

Chapter 5

Single Cell Sequencing of Astrocytes from Mouse Models of AD

5.1 Chapter Introduction

In the last chapter, I used bulk RNA-sequencing of astrocytes from mouse models of AD and WT mice to identify pathways up and downregulated when exposed to amyloid pathology. Whilst this approach is powerful in identifying broad differences in astrocyte gene expression between sample conditions, information about the heterogeneity of gene expression in astrocytes is lost. Several studies have highlighted that astrocyte gene expression and therefore function is heterogenous, and can differ based on location in the brain (Batiuk et al. 2020), age (Clarke et al. 2018; Boisvert et al. 2018) and type of insult (Zamanian et al. 2012; Liddelow et al. 2017). Therefore, it seems likely that astrocytes exhibit heterogeneous gene expression in these AD models. Additionally, if any other cell types are pulled down in the TRAP experiments along with the astrocytes, they would influence the gene expression attributed to astrocytes. Single cell RNA-seq is a technique which allows us to address both of these issues.

Notably, single cell RNA-seq does have limitations, such as a dropout/low capture efficiency effect, whereby a transcript is expressed, but is not detected in the sequencing data due to a failure to capture or amplify it. Additionally, single cell RNA-seq data tends to be noisier/more variable compared to bulk RNA-seq data (Chen et al. 2019; Haque et al. 2017). Quality control measures can be implemented to mitigate technical noise, such as removing data likely originating from damaged cells with low amounts of ambient RNA, and normalisation of single cell sequencing data to remove non-biological variation such as differences in sequencing depth of the cell (Chen et al. 2019). Imputation methods to compensate for the dropout effect are being developed. The rationale behind imputation is that genes in the same subpopulation should have similar expression levels within a certain range of variability (Zhang and Zhang 2020). However, these were not implemented in this study as there is still uncertainty around the best method, and one must be conscious of the consequences on non-zero data. Bearing these limitations in mind, single cell sequencing of the astrocytes in mouse models of AD has the potential to meaningfully add to our understanding of the heterogeneity of amyloidopathy induced astrocyte dysfunction.

Grubman et al. (2019) published a study where they conducted single-nucleus RNA sequencing on entorhinal cortex samples from control and AD brains. They found that astrocytes separated into 8 sub-clusters. 2/8 were comprised of astrocytes from AD brains, and 6/8 were largely comprised of astrocytes form control brains. This demonstrates that within AD and control brains there is heterogeneity of astrocyte gene expression, and that there appears to be strong disease associated transcriptional changes in AD astrocytes. One AD astrocyte sub-cluster (termed a1) was enriched for genes related to the ribosome, mitochondria and neuron differentiation compared to other sub-clusters. Whereas the other AD sub-cluster (termed a2) was de-enriched for these processes, and was instead enriched for TGFβ signalling and immune responses (Grubman et al. 2019). This highlights a benefit of single cell RNA-seq in identifying heterogeneity in astrocyte response which might otherwise be missed in bulk RNA-seq due to alterations in these populations cancelling each other out. Notably, the a2 sub-cluster demonstrated an upregulation of C3, a proposed marker gene of neurotoxic astrocytes (Liddelow et al. 2017).

Habib et al. (2020) conducted single nucleus RNA-seq in the hippocampi from 7-month-old WT mice and 5xFAD mice. 5xFAD mice are a transgenic model of AD which overexpress APP and PSEN1, with 5 AD linked mutations. Amyloid pathology and gliosis begin around 2-months, and synapse loss around 4-months. Habib et al. identified 6 transcriptional sub-clusters of astrocytes (Habib et al. 2020). 5 of the sub-clusters contained both WT and AD astrocytes. However, sub-clusters 1 & 2 contained more WT astrocytes than AD astrocytes, and were found to lowly express *Gfap*. Sub-cluster 6 contained similar amounts of AD and WT astrocytes, and was found to highly express *Gfap*. This cluster was enriched for genes involved in metabolic pathways and inflammation, indicating the presence of activated astrocytes with and without AD pathology. Astrocytes in sub-cluster 4 were termed disease associated astrocytes (DAAs), since this cluster was only found in AD mice. DAAs expressed genes which were enriched for pathways involved in endocytosis, the complement cascade, ageing and the lysosome. The authors devised a computational procedure to infer transitions between cell states, which suggested that that cells in cluster 1 and 2 were the origin for cells in cluster 3, cells in cluster 3 & 5 undergo a transcription shift toward DAAs in cluster 4. Interestingly, Habib et al. noted that there was a reduction in the proportion of astrocytes in sub-clusters 1 & 2 and an increase in the proportion of DAAs at 4 months of age in the AD mouse model,

before manifestation of cognitive decline. Thus, indicating DAAs may contribute to the pathological progression of AD. Additionally, Habib et al. demonstrated DAA like cells begin to emerge in 13-14-month old mice, with increased abundance in 20-month mice. This supports our finding in the previous chapter of an overlap of amyloidopathy induced genes and age-dependent changes in astrocyte gene expression. Importantly, Habib et al. found astrocyte populations similar to the mouse low *Gfap*, intermediate and high *Gfap* transcriptional states in human astrocyte datasets, with more DAA like cells in individuals with AD. Therefore, suggesting that their results may be relevant to human physiology and disease.

Single cell RNA-sequencing currently involves the preparation of cells into a single cell suspension. Hence, a caveat to this technique is the loss of spatial resolution. Chen et al. (2020) used spatial transcriptomics (a technique which measures transcriptomic changes in hundreds of small tissue domains) in the APP^{NLGF} amyloidopathy mouse model, to identify 54 Aβ plaque induced genes (Chen et al. 2020). They attributed the plaque induced gene changes to cell types using in situ sequencing, which visualises select transcripts with cellular resolution. However, the authors note that currently, spatial transcriptomics does not provide single cell resolution and in-situ sequencing has low sensitivity. Computational approaches, such as Seurat (Satija et al. 2015), which integrates in situ hybridization data of 'landmark' genes that guide spatial assignment with single-cell RNA-sequencing data, may facilitate spatial reconstruction of single cell RNA-seq datasets and provide invaluable information in health and disease research.

In collaboration with the University of Edinburgh FACS facility, we conducted 10x Genomics single cell sequencing **(figure 40)** to investigate the heterogeneity of astrocyte phenotype in the knock-in APP^{NLF} and transgenic APP/PS1 amyloidopathy mouse models. This approach was chosen to shed light on whether the few differentially expressed genes found in the bulk RNA-sequencing of APP^{NLF} astrocytes is truly due to the astrocytes displaying few differences from WT astrocytes, or whether there are simply a small proportion of astrocytes with altered gene expression profiles. Additionally, preliminary comparison of responses in the transgenic

and knock-in models could be made. Perhaps in the future this dataset will be combined with in situ hybridization data in order to spatially reconstruct astrocyte gene expression.

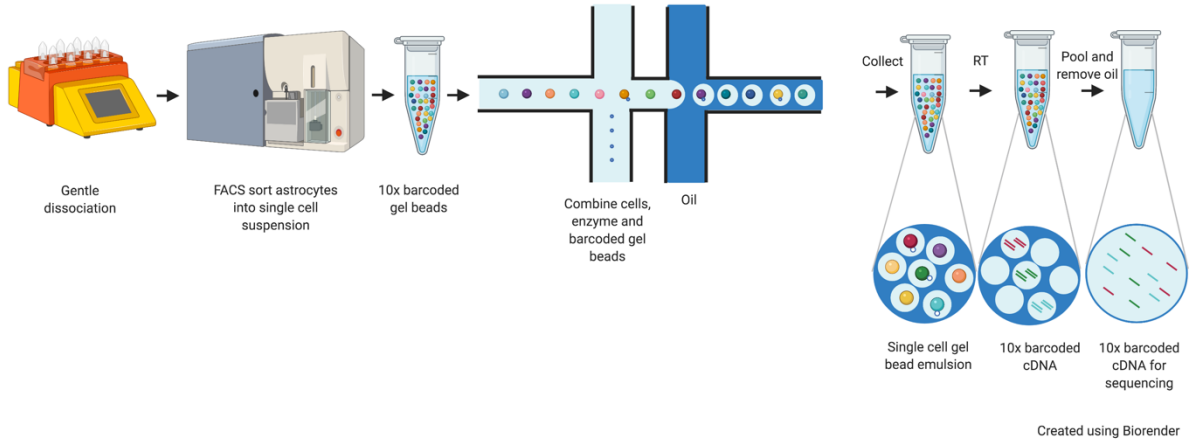

Figure 40. The process of 10x Genomics single cell sequencing. The neocortex from 12-month APP/PS1 and WT mice, 18-month APP/PS1, APP^{NLF} and WT mice (all carrying the Aldh1l1_eGFP-Rpl10a allele) were dissected out of 3-4 mice per genotype. The samples underwent gentle dissociation using the Miltenyi Biotec genleMACS Octo Dissociator. Green fluorescent protein (GFP) positive cells were isolated by fluorescence-activated cell sorting (FACS). Approximately 20,000 cells per genotype were isolated. Using the 10x Genomics microfluidic chip, cells were labelled with a barcoded gel bead. A gel bead emulsion was formed. Gel beads were then dissolved and the cells lysed, releasing mRNAs into solution. Reverse transcription within emulsion occured, leading to barcoded cDNA generation. Finally, library constructs were sequenced on an Illumina NextSeq 550.

5.2 Results

5.2.1 FACS Sorting GFP Positive Cells

Figure 41 illustrates an example of the gates set up to sort GFP positive cells. **Figure 41A** shows the gate set up to filter out debris. **Figure 41B** illustrates that DAPI positive cells were excluded and DAPI negative cells were carried forward. DAPI only permeates dead cells where the membrane has begun to breakdown. Hence, the gate allows live cells to be carried forward. Pulse width over area allows us to gate out cell clumps, and carry single cells forward with a 1:1 of width/area as in **figure 41C**. Gates in **figure 41D** and **E** are to gate on GFP positive cells and gate out autoflourescent cells and GFP negative cells. These gates were set using a control tissue sample without GFP positive cells, as well as a tissue sample with GFP positive cells.

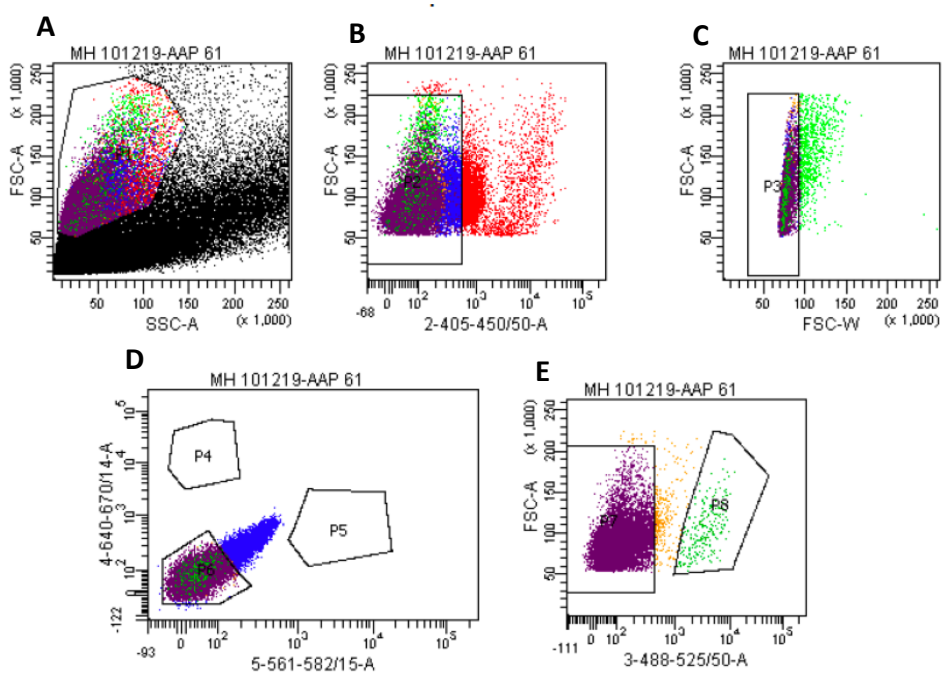

Figure 41. Fluorescence activated cell sorting of green fluorescent protein (GFP) positive cells. (A) Debris was gated out, **(B)** along with dead cells using DAPI, **(C)** clumps of cells and **(D, E)** auto-fluorescent cells, finally, selecting for GFP positive cells.

5.2.2 Defining the Astrocyte Population in 12-month APP/PS1 and WT Cells

Principle component analysis was run on the normalised and filtered feature-barcode matrices, computing the top 10 dimensions by default. Using this reduced representation of the matrices, the uniform manifold approximation and projection (UMAP) method was used to visualise the data in 2D space, each dot represents a cell. UMAP is a non-linear graph-based dimension reduction method. Unlike with t-SNE plots, UMAP defines local and global distances based on global data structure. Hence, the representation of the groups of cells remains the same when UMAP is re-run. Groups of cells were manually segmented based on position in UMAP space **(figure 42)**.

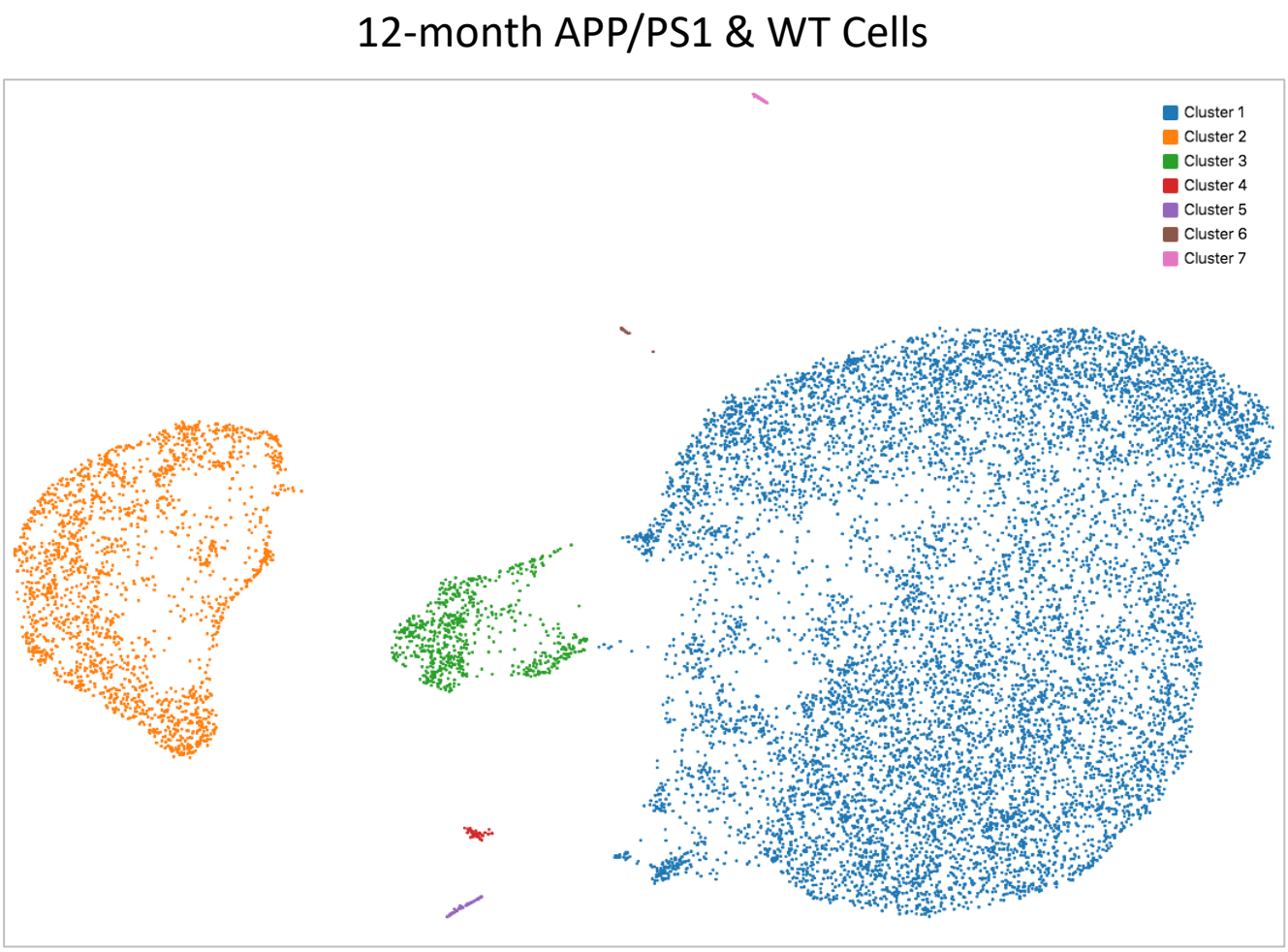

Figure 42. Uniform manifold approximation and projection (UMAP) method was used to visualise 12-month APP/PS1 and WT data in 2D space. Each dot represents a cell. Clusters were manually segmented based on position in UMAP space.

Differential gene expression revealed genes which were significantly enriched in each cluster vs the other clusters. Gene sets which were significantly enriched in each cluster were imported into the cell type specific expression analysis (CSEA) tool produced by the Dougherty lab in order to identify whether all of the clusters were likely to be astrocytes or whether other cell types had been sorted along with astrocytes, either due to GFP being lowly expressed by other cell types, or stray cells from FACS http://genetics.wustl.edu/jdlab/csea-tool-2/ (Dougherty et al. 2010). Using this tool was thought to be a quick and less biased method of identifying astrocyte clusters, compared to manually examining expression of genes of interest. However, there are several methods to identify cell types and future work will explore the most appropriate method for this dataset (Abdelaal et al. 2019). I remained blinded to whether clusters were present in both genotypes at this stage.

To produce the CSEA tool, the Dougherty lab performed TRAP on a number of different cell types by driving expression of eGFP-RPL10a with a cell type specific promoter. Immunohistochemistry was used to confirm specificity of eGFP expression. Microarray analysis was performed on mRNA extracted using the TRAP methodology. Gene lists which were enriched in each cell type/ region were constructed. Varying stringencies for enrichment were implemented, the least specific larger lists are represented by the largest hexagon in **figure 43**, the inner hexagons represent increasingly specific gene lists, constructed by varying the specificity threshold. The hexagons size is scaled to the size of the gene lists. I entered the set of genes significantly enriched in each cluster ($p\_adj<0.05$) relative to the other clusters into the tool. The tool uses Fisher's exact tests with Benjamini Hochberg corrected p values to indicate overlap of candidate gene list with cell type enrichment lists, and the results are represented by the varying colours of the hexagons. Notably, the tool included cell types originating outside of the brain, such as rods and cones, as well as cell types found inside the brain. Highlighting of the outer hexagons of these non-brain cell types was thought to occur due to non-specific gene overlap with cell types in the brain.

The tool revealed that in the 12-month APP/PS1 and WT sample, clusters 1 and 2 were enriched for astrocyte specific genes **(figure 43A, B)**. Notably, the tool indicated that astrocytes may be of cortical and cerebellar origin, even though they were only cortical

astrocytes. However, Dougherty et al. (2010) describe the considerable overlap of gene expression between astrocytes in these regions, hence region was ignored for the purposes of our analyses.

Cluster 3 appeared enriched for oligodendrocyte progenitor, oligodendrocyte and neuron specific genes **(figure 43C)**. Since this cluster is relatively large, this might indicate that some eGFP is expressed in these cells, rather than stray cells having been sorted. Indeed, the RNA transcriptome database https://www.brainrnaseq.org/ indicates that *Aldh1l1* is lowly expressed in oligodendrocyte progenitor cells and neurons (Zhang et al. 2014). In retrospect, this is something to bear in mind when assessing the bulk translatome data presented in the previous chapter. Alternatively, perhaps astrocytes are expressing genes normally associated with other cell types. Cluster 4 appeared enriched for oligodendrocyte transcripts, cluster 5 for immune cell transcripts (likely microglia), cluster 6 neuronal and oligodendrocyte progenitor transcripts, and cluster 7 for a mixture of cell type specific genes, in particular neuron and immune cell related genes. Hence, only clusters 1 and 2 were carried forward for downstream analysis. However, future work will investigate whether other clusters should be included in downstream analysis, for example by staining for oligodendrocyte progenitor cells and examining if markers colocalise with eGFP, as well as conducting more in-depth analysis of the genes which define each cluster and methods of cell type identification.

12-month APP/PS1 & WT Cells

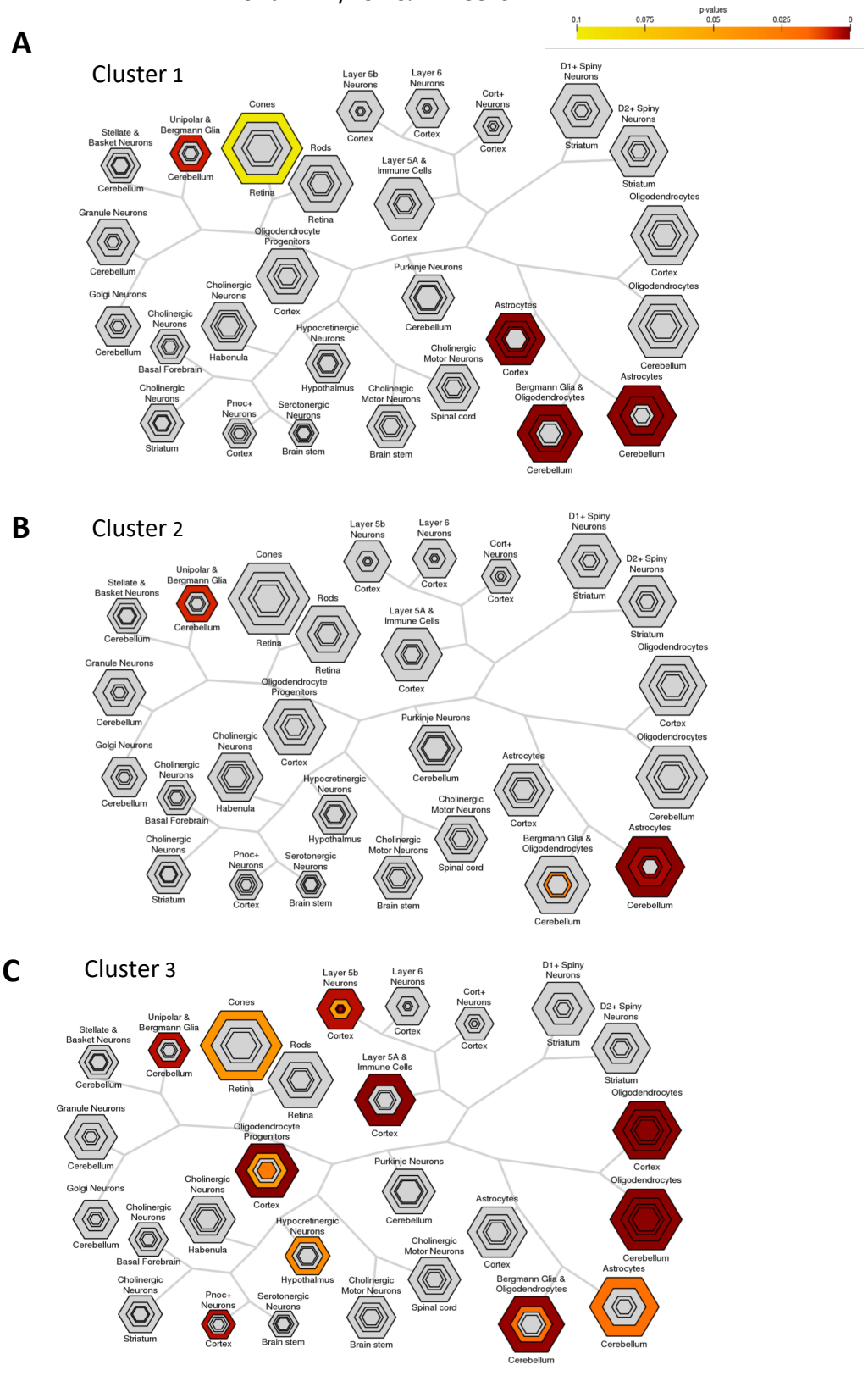

12-month APP/PS1 & WT Cells

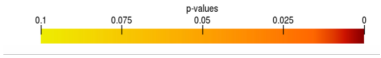

D Cluster 4

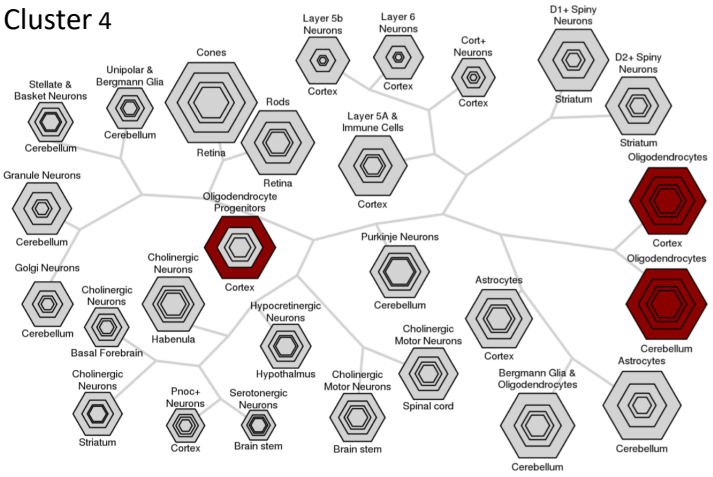

E Cluster 5

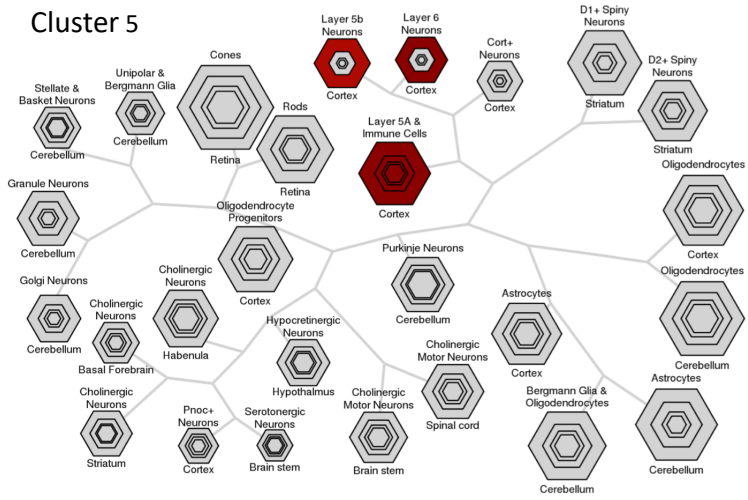

F Cluster 6

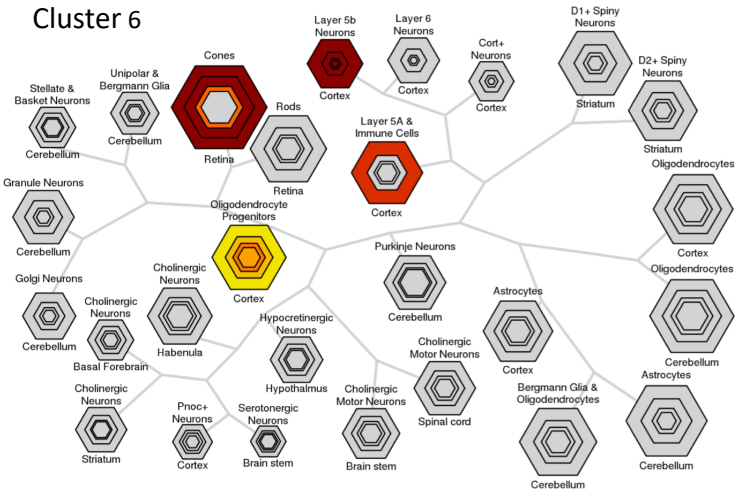

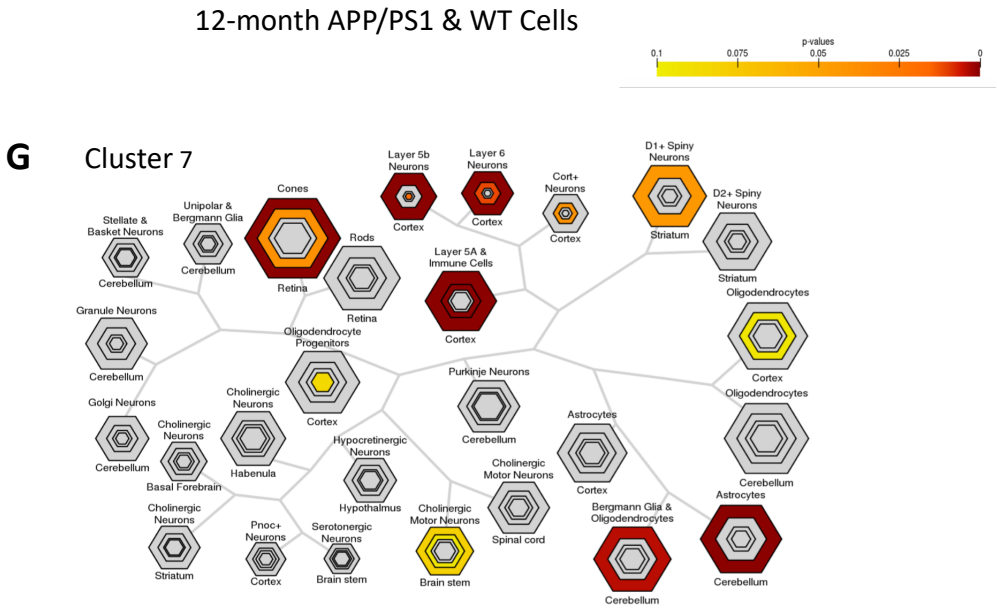

Figure 43. Investigating clusters enriched for astrocyte specific genes in the 12-month APP/PS1 and WT cells. The cell-type specific expression analysis tool (CSEA) provided by the Dougherty lab was used to identify whether clusters in **figure 42** were enriched for cell-type specific transcripts. This information allowed us to select clusters we believed to be astrocytes, so that we could investigate the heterogeneity of astrocyte gene expression with enhanced confidence of the cells included in the analysis. The Dougherty lab constructed gene lists which were enriched in each cell type/region. The least specific but largest gene list for that cell type is represented by the largest hexagon, the inner hexagons represent increasingly specific gene lists, constructed by varying a metric they coined as the specificity threshold (Dougherty et al. 2010). Genes which were significantly enriched ($p_{adj}<0.05$) in each cluster were entered as the candidate gene list. The tool uses Fisher's exact tests with Benjamini Hochberg corrected p values to indicate overlap of candidate gene list with cell type enrichment lists, and the results are represented by the varying colours of the hexagons. Clusters 1 and 2 appear enriched for astrocyte specific genes **(figure 43A, B)**, cluster 3 was enriched for oligodendrocyte progenitor, oligodendrocyte and neuronal genes **(figure 43C)**, cluster 4 for oligodendrocyte genes **(figure 43D)**, cluster 5 for immune cell related genes (likely microglia) **(figure 43E)**, cluster 6 for neuron and oligodendrocyte progenitor related genes **(figure 43F)**, and finally cluster 7 was enriched for genes from a mixture of cell types, in particular neuron and immune cell related genes.

5.2.3 Defining the Astrocyte Population in 18-month APP/PS1 and WT Cells

A similar workflow was performed on 18-month APP/PS1 and WT cells. **Figure 44** illustrates the UMAP representation of the data.

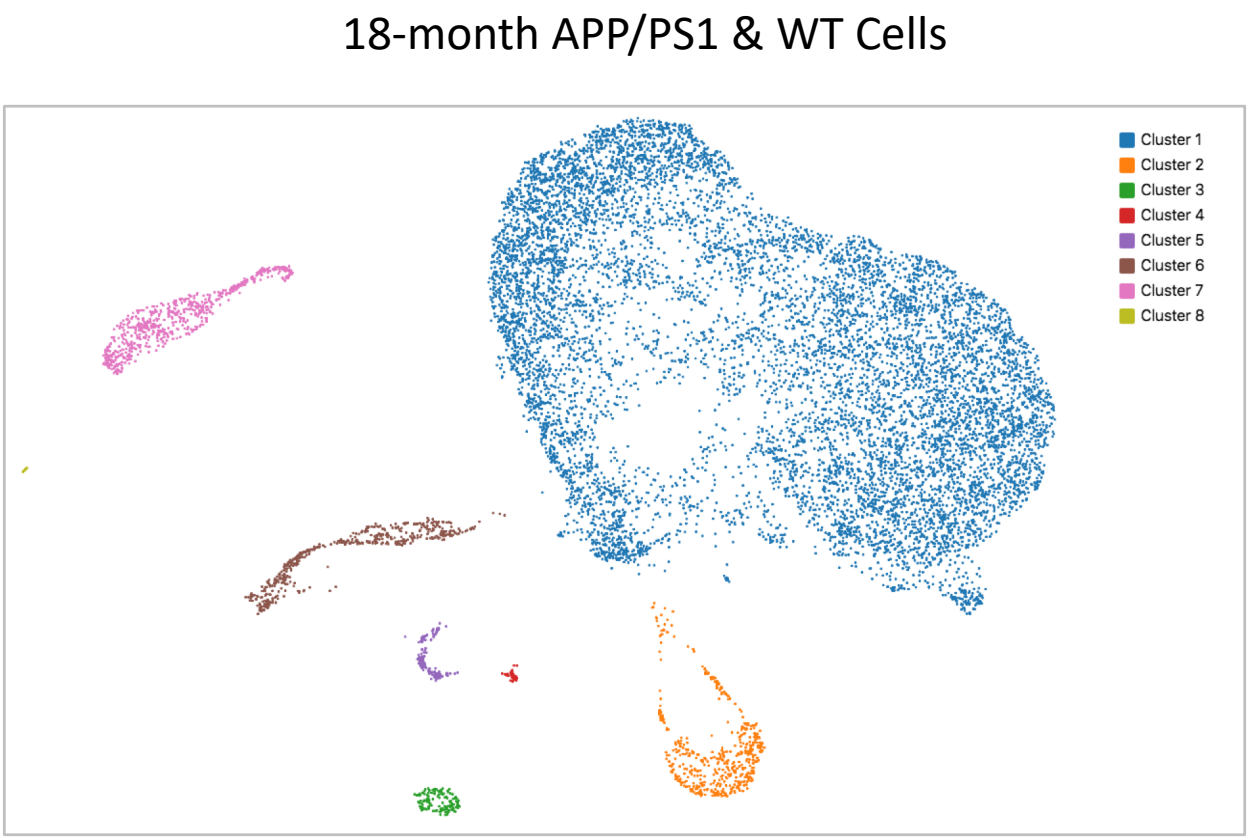

Figure 44. Uniform manifold approximation and projection (UMAP) method was used to visualise 18-month APP/PS1 and WT data in 2D space. Each dot represents a cell. Clusters were manually segmented based on position in UMAP space.

The CSEA tool was again used to identify clusters which were enriched for astrocyte specific genes. Clusters 1 and 7 appeared enriched for astrocyte specific genes **(figure 45A, G)**. Cluster 2 appeared enriched for oligodendrocyte progenitor and oligodendrocyte genes **(figure 45B)**. Cluster 3, for oligodendrocyte genes **(figure 45C)**. Clusters 4,5,6 and 8 for neuron and immune cell transcripts **(figure 45D, E, F, H)**. Hence, only clusters 1 and 7 were carried forward for downstream analysis.

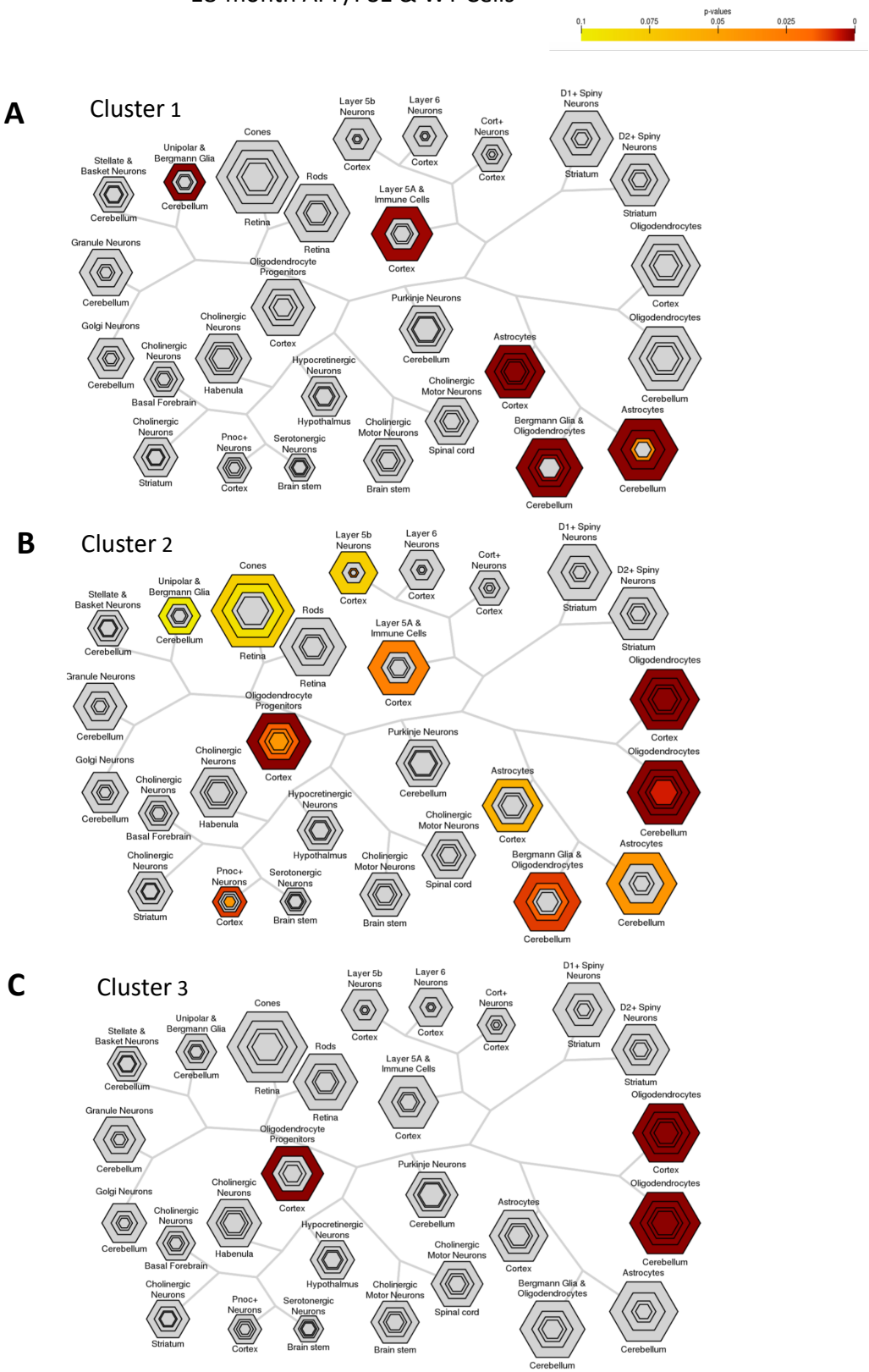
p-values
0.1
0.075
0.05
0.025
0
A
Cluster 1
Layer 5b Neurons
Cortex
Layer 6 Neurons
Cortex
Cort+ Neurons
Cortex
D1+ Spiny Neurons
Striatum
D2+ Spiny Neurons
Striatum
Cones
Retina
Rods
Retina
Unipolar & Bergmann Glia
Cerebellum
Stellate & Basket Neurons
Cerebellum
Layer 5A & Immune Cells
Cortex
Oligodendrocytes
Cortex
Granule Neurons
Cerebellum
Oligodendrocyte Progenitors
Cortex
Purkinje Neurons
Cerebellum
Oligodendrocytes
Cerebellum
Golgi Neurons
Cerebellum
Cholinergic Neurons
Basal Forebrain
Cholinergic Neurons
Habenula
Hypocretinergic Neurons
Hypothalmus
Astrocytes
Cortex
Cholinergic Motor Neurons
Spinal cord
Astrocytes
Cerebellum
Cholinergic Neurons
Striatum
Pnoc+ Neurons
Cortex
Serotonergic Neurons
Brain stem
Cholinergic Motor Neurons
Brain stem
Bergmann Glia & Oligodendrocytes
Cerebellum
B
Cluster 2
Layer 5b Neurons
Cortex
Layer 6 Neurons
Cortex
Cort+ Neurons
Cortex
D1+ Spiny Neurons
Striatum
D2+ Spiny Neurons
Striatum
Cones
Retina
Rods
Retina
Unipolar & Bergmann Glia
Cerebellum
Stellate & Basket Neurons
Cerebellum
Layer 5A & Immune Cells
Cortex
Oligodendrocytes
Cortex
Granule Neurons
Cerebellum
Oligodendrocyte Progenitors
Cortex
Purkinje Neurons
Cerebellum
Oligodendrocytes
Cerebellum
Golgi Neurons
Cerebellum
Cholinergic Neurons
Basal Forebrain
Cholinergic Neurons
Habenula
Hypocretinergic Neurons
Hypothalmus
Astrocytes
Cortex
Cholinergic Motor Neurons
Spinal cord
Astrocytes
Cerebellum
Cholinergic Neurons
Striatum
Pnoc+ Neurons
Cortex
Serotonergic Neurons
Brain stem
Cholinergic Motor Neurons
Brain stem
Bergmann Glia & Oligodendrocytes
Cerebellum
C
Cluster 3
Layer 5b Neurons
Cortex
Layer 6 Neurons
Cortex
Cort+ Neurons
Cortex
D1+ Spiny Neurons
Striatum
D2+ Spiny Neurons
Striatum
Cones
Retina
Rods
Retina
Unipolar & Bergmann Glia
Cerebellum
Stellate & Basket Neurons
Cerebellum
Layer 5A & Immune Cells
Cortex
Oligodendrocytes
Cortex
Granule Neurons
Cerebellum
Oligodendrocyte Progenitors
Cortex
Purkinje Neurons
Cerebellum
Oligodendrocytes
Cerebellum
Golgi Neurons
Cerebellum
Cholinergic Neurons
Basal Forebrain
Cholinergic Neurons
Habenula
Hypocretinergic Neurons
Hypothalmus
Astrocytes
Cortex
Cholinergic Motor Neurons
Spinal cord
Astrocytes
Cerebellum
Cholinergic Neurons
Striatum
Pnoc+ Neurons
Cortex
Serotonergic Neurons
Brain stem
Cholinergic Motor Neurons
Brain stem
Bergmann Glia & Oligodendrocytes
Cerebellum

D Cluster 4

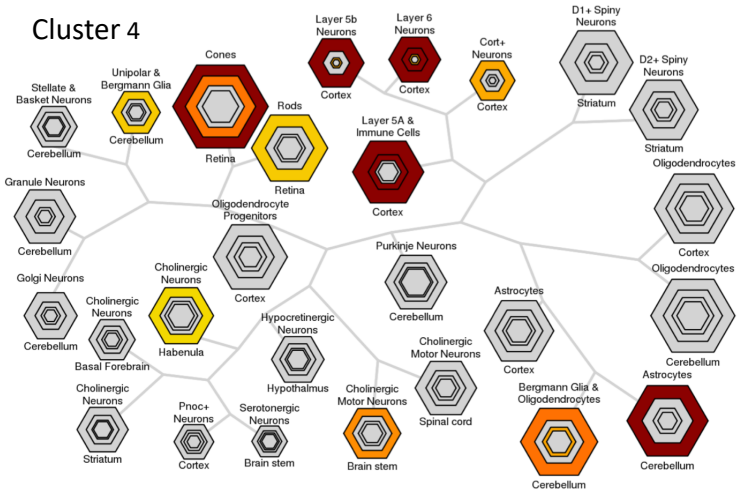

E Cluster 5

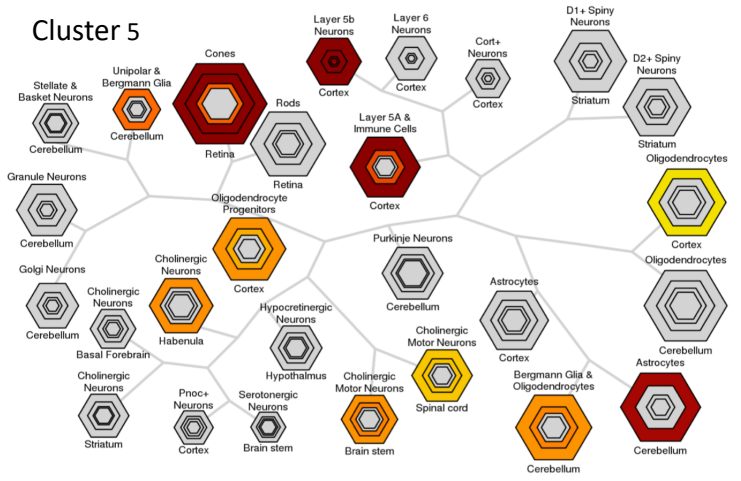

F Cluster 6

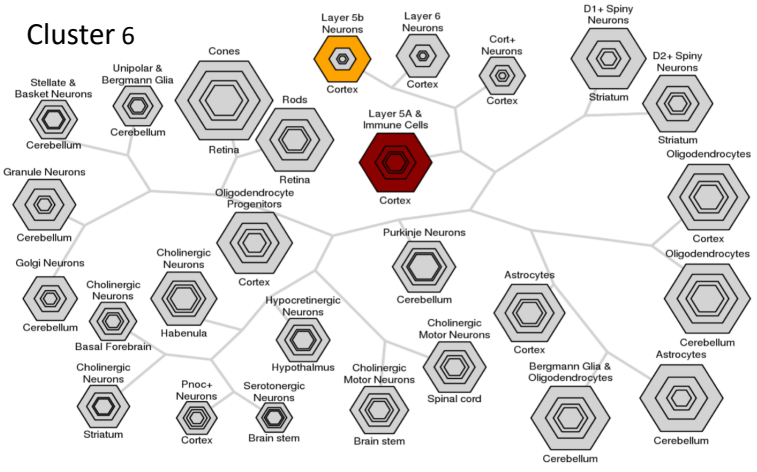

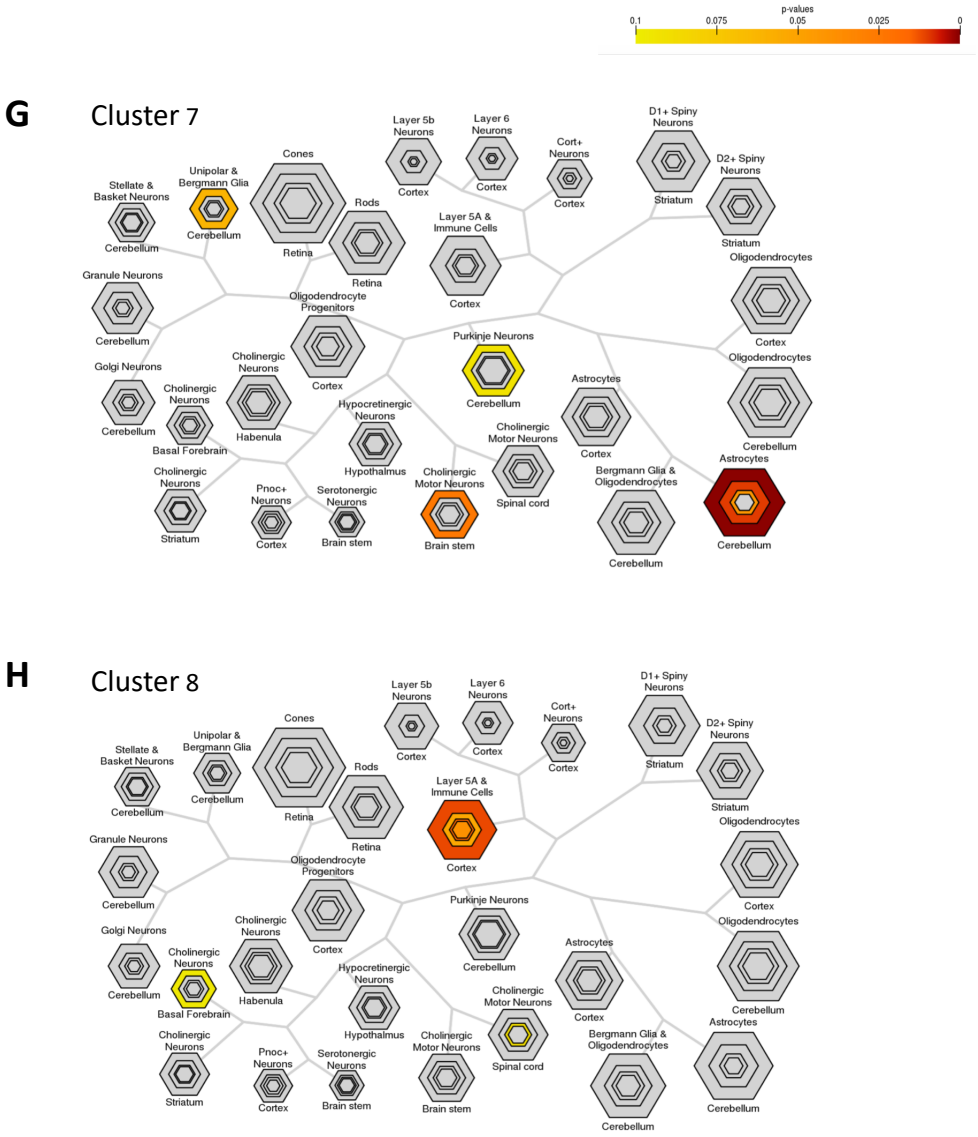

Figure 45. Investigating clusters enriched for astrocyte specific genes in 18-month APP/PS1 and WT cells. The cell type specific expression analysis tool (CSEA) provided by the Dougherty lab was used to identify whether clusters in figure 44 were enriched for cell type specific transcripts. This information allowed us to select clusters we believed to be astrocytes, so that we could investigate the heterogeneity of astrocyte phenotype with enhanced confidence of the cells included in the analysis. The Dougherty lab constructed gene lists which were enriched in each cell type/region. The least specific but largest gene list for that cell type is represented by the largest hexagon, the inner hexagons represent increasingly specific gene lists, constructed by varying a metric they coined as the specificity threshold (Dougherty et al. 2010). Genes which were significantly enriched ($p_{adj}<0.05$) in each cluster were entered as the candidate gene list. The tool uses Fisher's exact tests with Benjamini

Hochberg corrected p values to indicate overlap of candidate gene list with cell type enrichment lists, and the results are represented by the varying colours of the hexagons. **(A, G)** Clusters 1 and 7 appear enriched for astrocyte specific genes. **(B)** Cluster 2 appeared enriched for oligodendrocyte progenitor and oligodendrocyte genes. **(C)** Cluster 3, for oligodendrocyte genes. **(D, E, F, H)** Clusters 4,5,6 and 8 for neuron and immune cell transcripts.

5.2.4 Defining the Astrocyte Population in 18-month APP^{NLF} and WT Cells

Finally, a similar workflow was conducted for analysing the 18-month APP^{NLF} and WT single cell sequencing data. **Figure 46** illustrates the UMAP representation of the data.

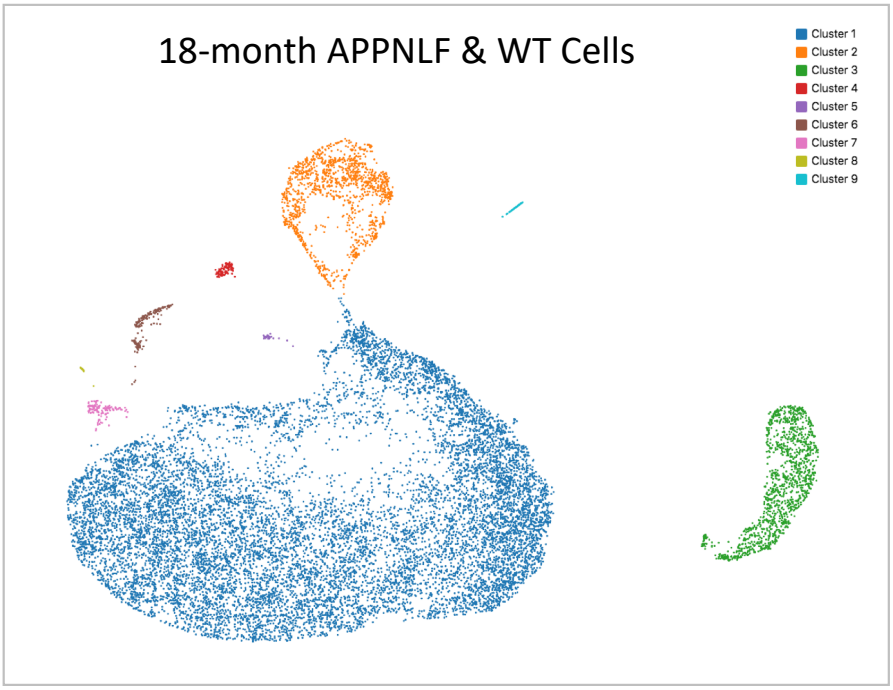

Figure 46. Uniform manifold approximation and projection (UMAP) method was used to visualise 18-month APP^{NLF} and WT data in 2D space. Each dot represents a cell. Clusters were manually segmented based on position in UMAP space.

Using the CSEA tool, it appeared that clusters 1,3 and 7 **(figure 47A, C, G)** were enriched in astrocyte specific genes and were not significantly enriched in genes related to other cell types. Cluster 2 was enriched in oligodendrocyte progenitor and oligodendrocyte genes **(figure 47B)**. Cluster 4 was enriched in oligodendrocyte genes **(figure 47D)**. Clusters 5,6 8 and

9 were enriched in a number of different cell types, including neuron and immune cell specific genes, as well as less specific oligodendrocyte and astrocyte genes **(figure 47E, F, H and I)**. Hence, only clusters 1,3 and 7 were carried forward for downstream analysis.

18-month APP^{NLF} & WT Cells

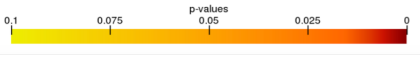

A Cluster 1

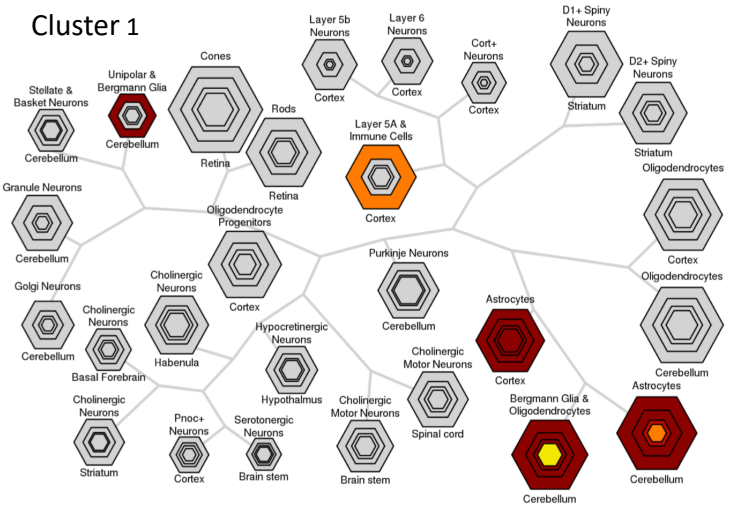

B Cluster 2

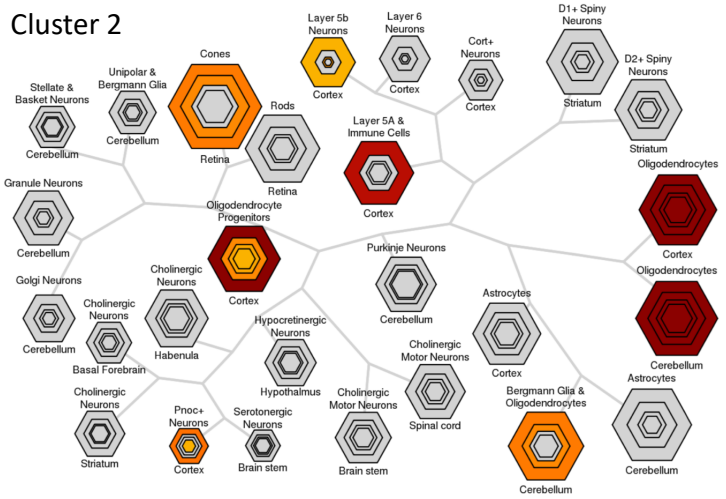

C Cluster 3

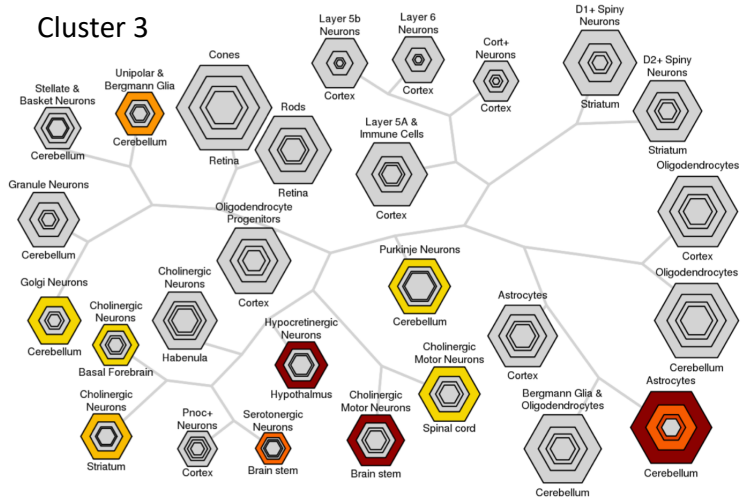

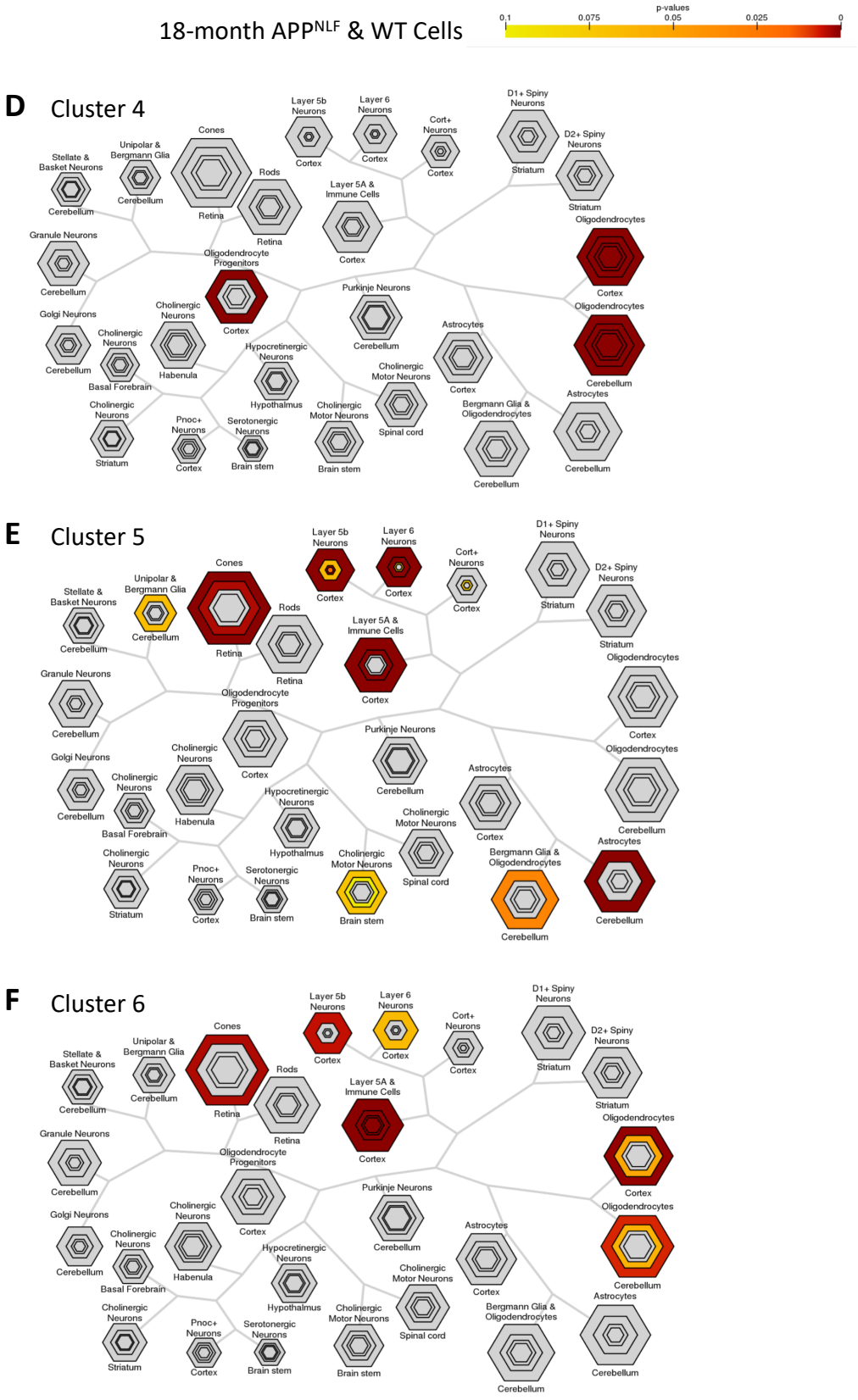
18-month APPNLF & WT Cells
p-values
0.1
0.075
0.05
0.025
0
D
Cluster 4
Layer 5b Neurons
Cortex
Layer 6 Neurons
Cortex
Cort+ Neurons
Cortex
D1+ Spiny Neurons
Striatum
D2+ Spiny Neurons
Striatum
Cones
Retina
Rods
Retina
Unipolar & Bergmann Glia
Cerebellum
Stellate & Basket Neurons
Cerebellum
Layer 5A & Immune Cells
Cortex
Oligodendrocytes
Cortex
Granule Neurons
Cerebellum
Oligodendrocyte Progenitors
Cortex
Purkinje Neurons
Cerebellum
Oligodendrocytes
Cerebellum
Golgi Neurons
Cerebellum
Cholinergic Neurons
Habenula
Cholinergic Neurons
Basal Forebrain
Hypocretinergic Neurons
Hypothalmus
Astrocytes
Cortex
Cholinergic Motor Neurons
Spinal cord
Cholinergic Neurons
Striatum
Pnoc+ Neurons
Cortex
Serotonergic Neurons
Brain stem
Cholinergic Motor Neurons
Brain stem
Bergmann Glia & Oligodendrocytes
Cerebellum
Astrocytes
Cerebellum
E
Cluster 5
Layer 5b Neurons
Cortex
Layer 6 Neurons
Cortex
Cort+ Neurons
Cortex
D1+ Spiny Neurons
Striatum
D2+ Spiny Neurons
Striatum
Cones
Retina
Rods
Retina
Unipolar & Bergmann Glia
Cerebellum
Stellate & Basket Neurons
Cerebellum
Layer 5A & Immune Cells
Cortex
Oligodendrocytes
Cortex
Granule Neurons
Cerebellum
Oligodendrocyte Progenitors
Cortex
Purkinje Neurons
Cerebellum
Oligodendrocytes
Cerebellum
Golgi Neurons
Cerebellum
Cholinergic Neurons
Habenula
Cholinergic Neurons
Basal Forebrain
Hypocretinergic Neurons
Hypothalmus
Astrocytes
Cortex
Cholinergic Motor Neurons
Spinal cord
Cholinergic Neurons
Striatum
Pnoc+ Neurons
Cortex
Serotonergic Neurons
Brain stem
Cholinergic Motor Neurons
Brain stem
Bergmann Glia & Oligodendrocytes
Cerebellum
Astrocytes
Cerebellum
F
Cluster 6
Layer 5b Neurons
Cortex
Layer 6 Neurons
Cortex
Cort+ Neurons
Cortex
D1+ Spiny Neurons
Striatum
D2+ Spiny Neurons
Striatum
Cones
Retina
Rods
Retina
Unipolar & Bergmann Glia
Cerebellum
Stellate & Basket Neurons
Cerebellum
Layer 5A & Immune Cells
Cortex
Oligodendrocytes
Cortex
Granule Neurons
Cerebellum
Oligodendrocyte Progenitors
Cortex
Purkinje Neurons
Cerebellum
Oligodendrocytes
Cerebellum
Golgi Neurons
Cerebellum
Cholinergic Neurons
Habenula
Cholinergic Neurons
Basal Forebrain
Hypocretinergic Neurons
Hypothalmus
Astrocytes
Cortex
Cholinergic Motor Neurons
Spinal cord
Cholinergic Neurons
Striatum
Pnoc+ Neurons
Cortex
Serotonergic Neurons
Brain stem
Cholinergic Motor Neurons
Brain stem
Bergmann Glia & Oligodendrocytes
Cerebellum
Astrocytes
Cerebellum

18-month APP^{NLF} & WT Cells

G Cluster 7

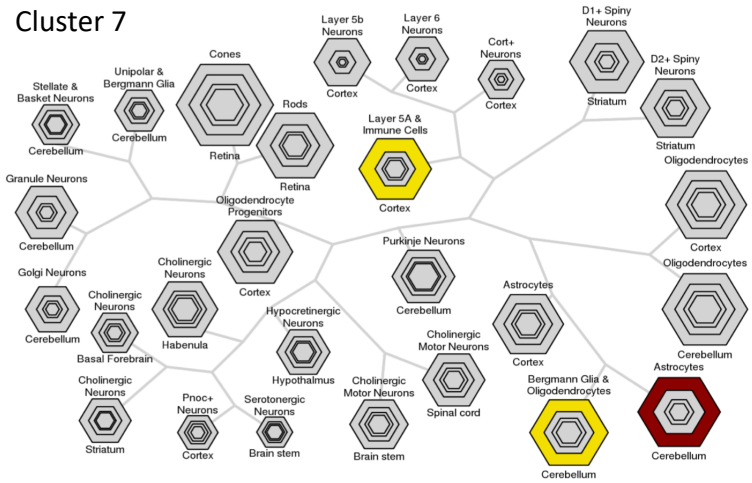

H Cluster 8

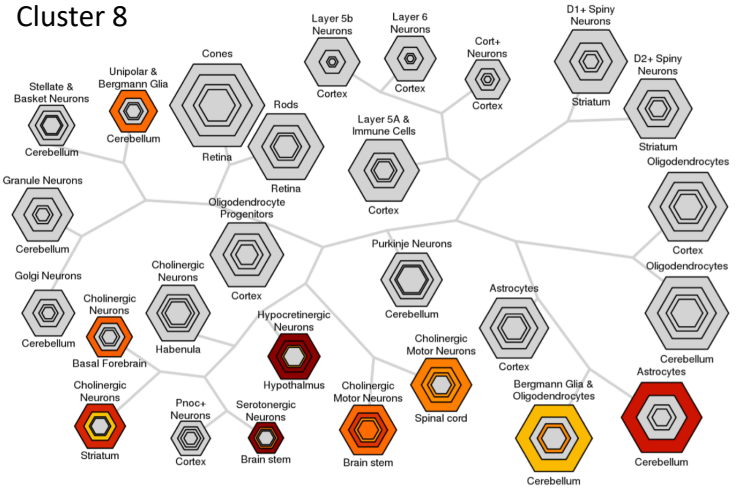

I Cluster 9

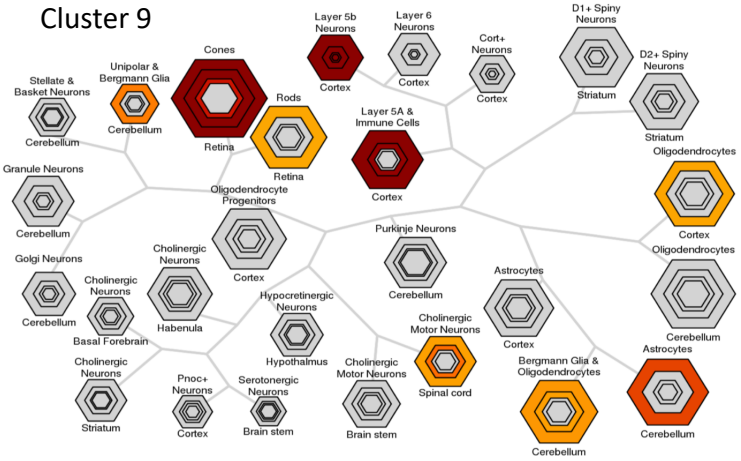

Figure 47. Investigating clusters enriched for astrocyte specific genes in 18-month APP^{NLF} and WT cells. The cell-type specific expression analysis tool (CSEA) provided by the Dougherty lab was used to identify whether clusters in figure 46 were enriched for cell-type specific transcripts. This information allowed us to select clusters we believed to be astrocytes, so that we could investigate the heterogeneity of astrocyte phenotype with enhanced confidence of the cells included in the analysis. The Dougherty lab constructed gene lists which were enriched in each cell type/ region. The least specific but largest gene list for that cell type is represented by the largest hexagon, the inner hexagons represent increasingly specific gene lists, constructed by varying a metric they coined as the specificity threshold (Dougherty et al. 2010). Genes which were significantly enriched (p_adj<0.05) in each cluster were entered as the candidate gene list. The tool uses Fisher's exact tests with Benjamini Hochberg corrected p values to indicate overlap of candidate gene list with cell type enrichment lists, and the results are represented by the varying colours of the hexagons. **(A, C, G)** Clusters 1 3 and 7 appear enriched for astrocyte specific genes. **(B)** Cluster 2 was enriched in oligodendrocyte progenitor and oligodendrocyte genes. **(D)** Cluster 4 was enriched in oligodendrocyte genes. **(E, F, H and I)** Clusters 5,6 8 and 9 were enriched in a number of different cell types, including neuron and immune cell specific genes, as well as less specific oligodendrocyte and astrocyte genes.

5.2.5 Investigating Heterogeneity of Astrocyte Gene Expression in Amyloidopathy Models

The groups of cells identified as likely being astrocytes using the CSEA tool were subject to K-means clustering, performed by Dr. Katie Emelianova, a post-doc in the Hardingham lab. K-means clustering generates K centroids and assigns each cell a cluster membership based on the nearest centroid (Mannor et al. 2010). The clustering quality metric termed the Davies-Bouldin Index, which calculates the ratio of 'within cluster' and 'between cluster' distances, was used to estimate the initial value of K (Petrovic 2006).

5.2.5.1 Pathology Associated Cluster in 12-month APP/PS1 and WT Astrocyte Sample

Using the Davies-Bouldin Index, the initial value of K in the 12-month APP/PS1 and WT astrocyte sample was set at 5. However, clusters 4 and 5 contained only 4 cells each, representing less than 0.1% of APP/PS1 or WT cells, and so K was set at 3 for downstream analysis. **Figure 48A** illustrates the UMAP visualisation of the 12-month APP/PS1 and WT cells. **Figure 48B** shows the proportion of APP/PS1 and WT cells in each cluster, data is represented in this way to account for genotype differences in the number of cells selected as astrocytes. A similar proportion of the WT and APP/PS1 astrocytes were present in cluster 1. A higher proportion of the WT astrocytes were in cluster 2 compared to APP/PS1 astrocytes. This is due to the fact that around 30% APP/PS1 astrocytes were in cluster 3, which only contained around 1.4% of WT astrocytes. Hence, cluster 3 could be seen as a pathology associated cluster of astrocytes.

A

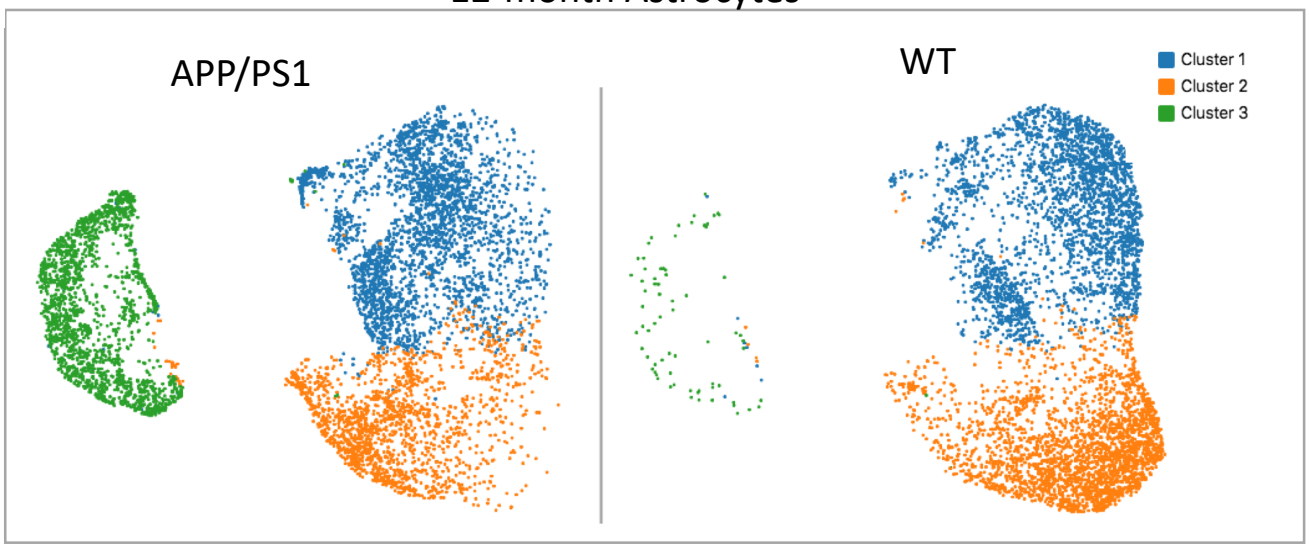
12-month Astrocytes
APP/PS1
WT
Cluster 1
Cluster 2
Cluster 3

B

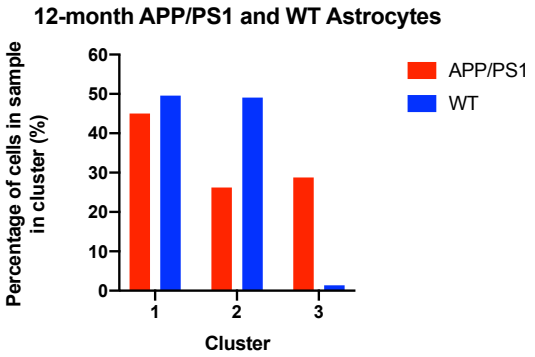
12-month APP/PS1 and WT Astrocytes
Percentage of cells in sample in cluster (%)
60
50
40
30
20
10
0
1
2
3
Cluster
APP/PS1
WT

C

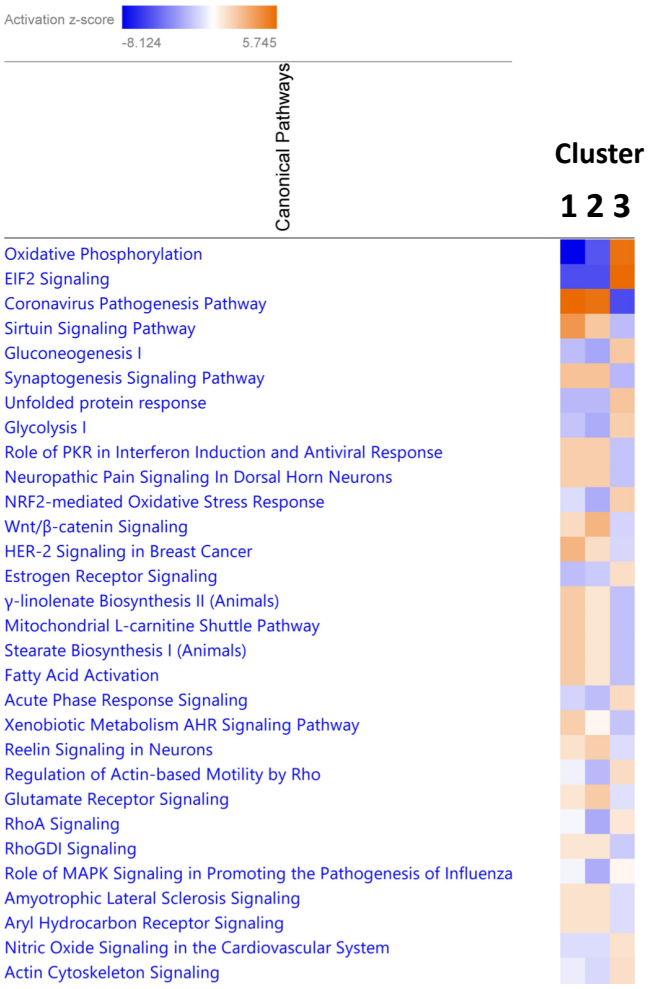
Activation z-score
-8.124
5.745
Canonical Pathways
Cluster
1 2 3
Oxidative Phosphorylation
EIF2 Signaling
Coronavirus Pathogenesis Pathway
Sirtuin Signaling Pathway
Gluconeogenesis I
Synaptogenesis Signaling Pathway
Unfolded protein response
Glycolysis I
Role of PKR in Interferon Induction and Antiviral Response
Neuropathic Pain Signaling In Dorsal Horn Neurons
NRF2-mediated Oxidative Stress Response
Wnt/β-catenin Signaling
HER-2 Signaling in Breast Cancer
Estrogen Receptor Signaling
γ-linolenate Biosynthesis II (Animals)
Mitochondrial L-carnitine Shuttle Pathway
Stearate Biosynthesis I (Animals)
Fatty Acid Activation
Acute Phase Response Signaling
Xenobiotic Metabolism AHR Signaling Pathway
Reelin Signaling in Neurons
Regulation of Actin-based Motility by Rho
Glutamate Receptor Signaling
RhoA Signaling
RhoGDI Signaling
Role of MAPK Signaling in Promoting the Pathogenesis of Influenza
Amyotrophic Lateral Sclerosis Signaling
Aryl Hydrocarbon Receptor Signaling
Nitric Oxide Signaling in the Cardiovascular System
Actin Cytoskeleton Signaling

Figure 48. 12-month APP/PS1 and WT astrocytes - single cell sequencing analysis. (A) Uniform manifold approximation and projection (UMAP) method was used to visualise the data in 2D space. K-means clustering of the data was performed, with K set at 3. **(B)** The percentage of cells in each sample in each cluster. **(C)** Ingenuity pathway analysis was performed on genes significantly enriched or de-enriched in each cluster relative to the other clusters. The top 30 pathways altered are shown. A positive activation z-score >2 (orange) indicates pathways are significantly enriched in that cluster relative to other clusters, a negative activation z-score <-2 (blue) indicates pathways are significantly de-enriched in that cluster relative to other clusters.

5.2.5.2 Pathology Associated Cluster in 18-month APP/PS1 and WT Astrocyte Sample

Using the Davies-Bouldin Index, the initial value of K was set at 4 for the 18-month APP/PS1 and WT astrocyte dataset. **Figure 49A** illustrates the UMAP visualisation of the 18-month APP/PS1 and WT cells. The immediately noticeable feature is that there were fewer cells in the APP/PS1 astrocyte sample than in the WT astrocyte sample (2751 vs 7747 cells respectively). Possible reasons for this discrepancy include fewer viable cells being sorted in the APP/PS1 model, or a larger number of sorted cells being discarded in clusters which were not enriched in astrocyte specific transcripts. Hence, it is useful to compare the proportion of cells in the sample in each cluster **(Figure 49B).** Clusters 1 and 2 collectively contain 95.5% of WT astrocytes and 88.5% of APP/PS1 cells. Intriguingly, just as in the 12-month APP/PS1 sample, cluster 3 was separated from the main body of astrocytes in the 18-month APP/PS1 and WT sample. The proportion of APP/PS1 astrocytes in cluster 3 was approximately double the proportion of WT astrocytes (11% vs 4.4% respectively), once again suggesting that this may be a pathology associated cluster. The proportion of WT astrocytes in the pathology associated cluster 3 is around 3 times larger in the 18-month astrocyte sample than in the 12-month astrocyte sample (4.4% vs 1.4% respectively). Whilst this is still a low percentage, it might indicate an upward trend of an ageing astrocyte phenotype overlapping with an amyloidopathy induced phenotype. It would be informative to conduct single cell RNA-seq analysis on 24-month astrocytes to confirm this trend, as well as to conduct clustering on all of the age groups together. Interestingly, the proportion of APP/PS1 astrocytes in this pathology associated cluster 3 is around 1/3 of that in the 12-month APP/PS1 sample (11.1% vs 28.8% respectively). It is unclear why this might be the case. However, perhaps astrocytes in this cluster are more vulnerable to dying when confronted with the effects of amyloid pathology and ageing. The proportion of APP/PS1 cells in cluster 4 is 10-fold higher than the proportion of WT cells in cluster 4 (0.4% vs 0.04% respectively). Since cluster 4 represented >0.1% of APP/PS1 cells, it was kept in the analysis.

A

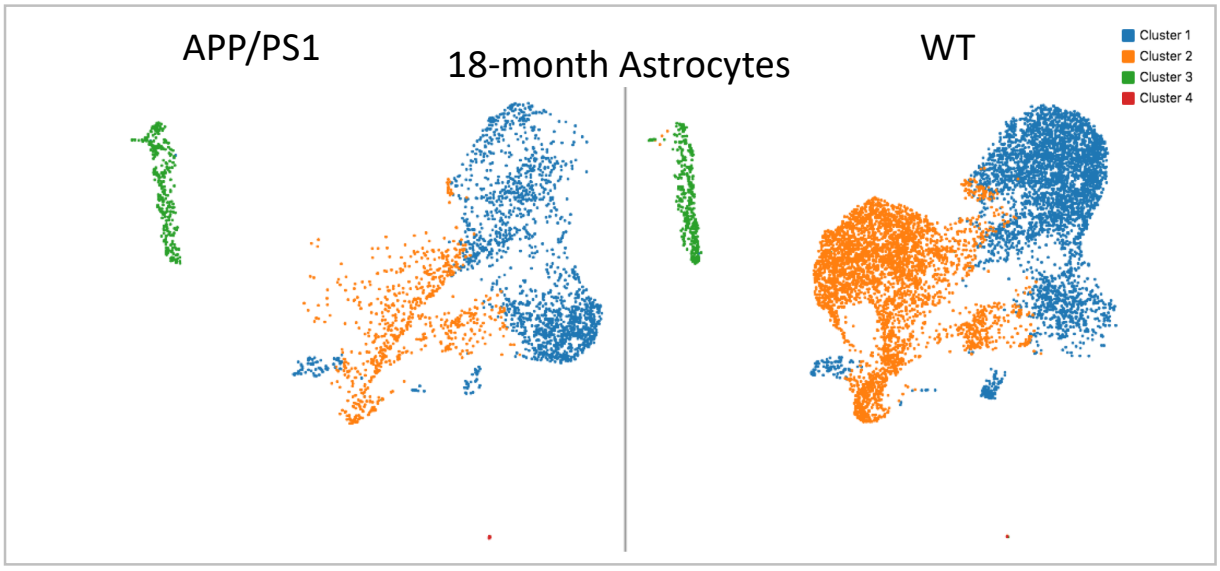
APP/PS1
18-month Astrocytes
WT
Cluster 1
Cluster 2
Cluster 3
Cluster 4

B

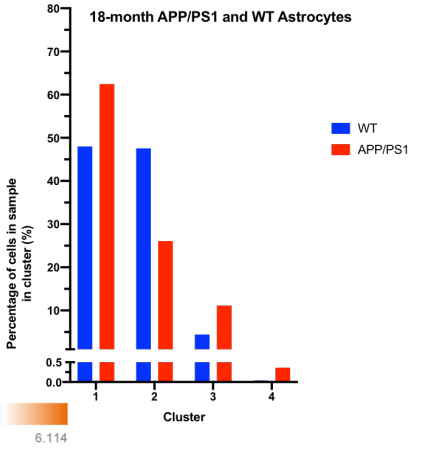
18-month APP/PS1 and WT Astrocytes
WT
APP/PS1
Percentage of cells in sample in cluster (%)
Cluster

C


Activation z-score
-7.699
6.114
Canonical Pathways
Cluster
1 2 3 4
EIF2 Signaling
Coronavirus Pathogenesis Pathway
Oxidative Phosphorylation
Neuropathic Pain Signaling In Dorsal Horn Neurons
γ-linolenate Biosynthesis II (Animals)
Gluconeogenesis I
Role of PKR in Interferon Induction and Antiviral Response
Sirtuin Signaling Pathway
Glycolysis I
Mitochondrial L-carnitine Shuttle Pathway
Fatty Acid Activation
Mouse Embryonic Stem Cell Pluripotency
Wnt/Ca+ pathway
TCA Cycle II (Eukaryotic)
Synaptogenesis Signaling Pathway
PCP pathway
RhoA Signaling
NRF2-mediated Oxidative Stress Response
Unfolded protein response
Xenobiotic Metabolism AHR Signaling Pathway
Necroptosis Signaling Pathway
Role of MAPK Signaling in Promoting the Pathogenesis of Influenza
Estrogen Receptor Signaling
BAG2 Signaling Pathway
Synaptic Long Term Potentiation
Signaling by Rho Family GTPases
Endocannabinoid Neuronal Synapse Pathway
Regulation of Actin-based Motility by Rho
HER-2 Signaling in Breast Cancer
Leukocyte Extravasation Signaling
Endoplasmic Reticulum Stress Pathway

Figure 49. 18-month APP/PS1 and WT astrocytes - single cell sequencing analysis. (A) Uniform manifold approximation and projection (UMAP) method was used to visualise the data in 2D. K-means clustering of the data was performed, with K set at 4. **(B)** The percentage of cells in each sample in each cluster. **(C)** Ingenuity pathway analysis was performed on genes significantly enriched or de-enriched in each cluster relative to the other clusters. The top 30 pathways altered are shown. A positive activation z-score >2 (orange) indicates pathways are significantly enriched in that cluster relative to other clusters, a negative activation z-score <-2 (blue) indicates pathways are significantly de-enriched in that cluster relative to other clusters.

5.2.5.3 Pathology Associated Cluster in 18-month APP^{NLF} and WT Astrocyte Sample

Using the Davies-Bouldin Index, the initial value of K was set at 2. **Figure 50A** illustrates the UMAP visualisation of the 18-month APP^{NLF} and WT cells. It should be noted that the WT cells in the 18-month APP/PS1 comparison were re-used in this APP^{NLF} comparison due to a failure of the 10x Genomics Chromium platform during experimentation. Once again, there appeared to be a cluster of astrocytes separated from the main body of astrocytes which contained more pathology exposed cells. Cluster 2 contained 14.5% of APP^{NLF} cells and 4.4% of WT cells, demonstrating ~3.5 times higher proportion of pathology exposed astrocytes than WT astrocytes. This is particularly noteworthy since few gene expression changes were found in the bulk RNA-seq analysis of 18-month APP^{NLF} astrocytes, nevertheless genes significantly induced >1.5 fold in 12 and 18-month APP/PS1 astrocytes vs WT astrocytes appeared to be changing in the same direction in the bulk translatomes of 18-month APP^{NLF} astrocytes. The single cell analysis presented here might indicate that these changes in gene expression were significant, but were lost due to the bulk of astrocytes in the APP^{NLF} model not displaying differences from the WT cells.

A

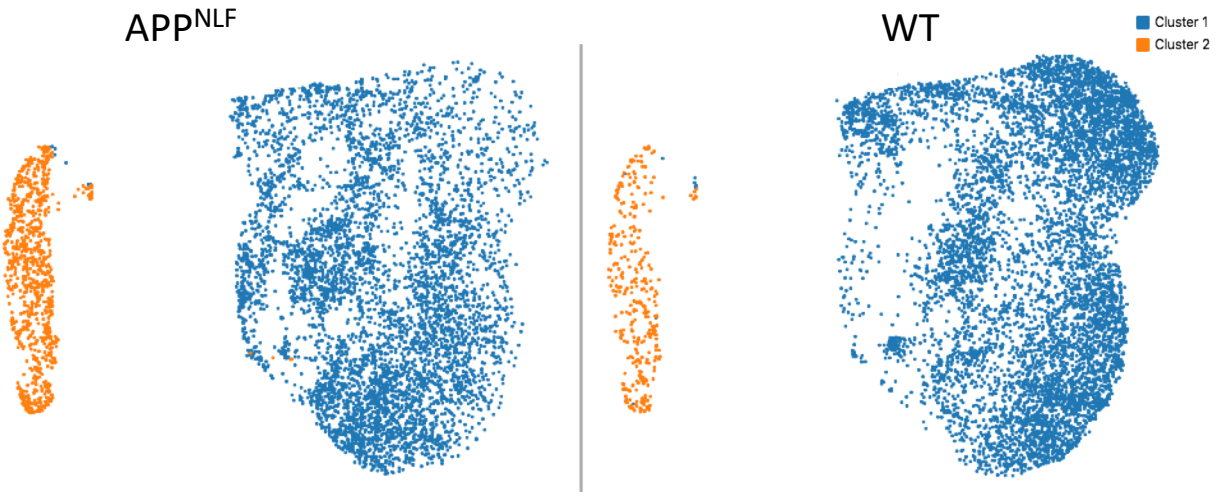
18-month Astrocytes
APPNLF
WT
Cluster 1
Cluster 2

B

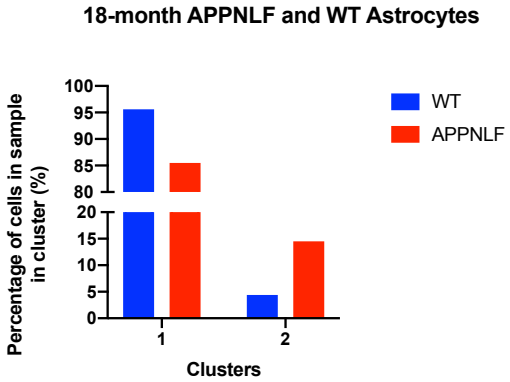
18-month APPNLF and WT Astrocytes
Percentage of cells in sample in cluster (%)
100
95
90
85
80
20
15
10
5
0
1
2
Clusters
WT
APPNLF

C

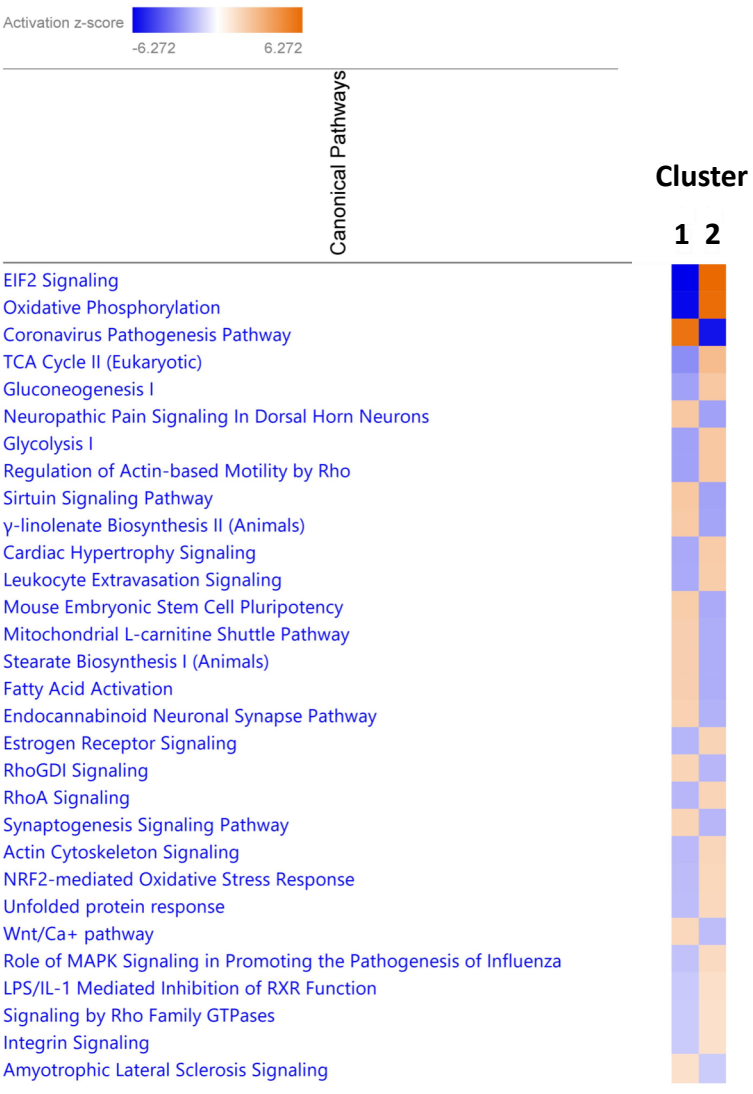
Activation z-score
-6.272
6.272
Canonical Pathways
Cluster
1 2
EIF2 Signaling
Oxidative Phosphorylation
Coronavirus Pathogenesis Pathway
TCA Cycle II (Eukaryotic)
Gluconeogenesis I
Neuropathic Pain Signaling In Dorsal Horn Neurons
Glycolysis I
Regulation of Actin-based Motility by Rho
Sirtuin Signaling Pathway
γ-linolenate Biosynthesis II (Animals)
Cardiac Hypertrophy Signaling
Leukocyte Extravasation Signaling
Mouse Embryonic Stem Cell Pluripotency
Mitochondrial L-carnitine Shuttle Pathway
Stearate Biosynthesis I (Animals)
Fatty Acid Activation
Endocannabinoid Neuronal Synapse Pathway
Estrogen Receptor Signaling
RhoGDI Signaling
RhoA Signaling
Synaptogenesis Signaling Pathway
Actin Cytoskeleton Signaling
NRF2-mediated Oxidative Stress Response
Unfolded protein response
Wnt/Ca+ pathway
Role of MAPK Signaling in Promoting the Pathogenesis of Influenza
LPS/IL-1 Mediated Inhibition of RXR Function
Signaling by Rho Family GTPases
Integrin Signaling
Amyotrophic Lateral Sclerosis Signaling

Figure 50. 18-month APP^{NLF} and WT astrocytes - single cell sequencing analysis. (A) Uniform manifold approximation and projection (UMAP) method was used to visualise the data in 2D space. K-means clustering of the data was performed, with K set at 2, chosen using the Davies-Bouldin Index. **(B)** The percentage of cells in each sample in each cluster. **(C)** Ingenuity pathway analysis was performed on genes significantly enriched or de-enriched in each cluster relative to the other clusters. The top 30 pathways altered are shown. A positive activation z-score (orange) indicates pathways are enriched in that cluster relative to other clusters, a negative activation z-score (blue) indicates pathways are de-enriched in that cluster relative to other clusters.

5.2.5.4 Robust Pathway Expression in Pathology Associated Clusters of Astrocytes

The presence of a pathology associated cluster across both age groups in the APP/PS1 model and in the APP^{NLF} model was particularly striking. In order to delve further into the pathways which were enriched in these pathology associated clusters relative to the other clusters in each dataset, IPA of the genes significantly enriched/de-enriched in each cluster relative to the other clusters was performed. Results were exported as heatmaps **(figure 48C, figure 49C and figure 50C)**. The top 30 pathways which were significantly enriched/de-enriched in the data are shown. IPA determines how many genes in each pathway demonstrate a positive or negative fold change and produces an activation z-score. An activation z-score of >2 indicates the pathway in question is significantly enriched in that cluster of astrocytes relative to the other clusters (orange), and an activation z score of < -2 indicates the pathway in question is significantly de-enriched in that cluster relative to other clusters.

IPA revealed a seemingly robust phenotype of the pathology associated cluster in all of the samples. In comparison to the other clusters in each sample, the pathology associated cluster was enriched for genes related to oxidative phosphorylation, eukaryotic initiation factor 2 (eIF2) signalling, the unfolded protein response, glycolysis and NRF2-mediated oxidative stress response, amongst other pathways. Additionally, in all the samples the pathology associated cluster was de-enriched for pathways such as the synaptogenesis signalling pathway relative to the other clusters in each sample. The magnitude of pathway enrichment/de-enrichment (activation z-score) in the pathology associated cluster relative to

the other clusters in each sample was also very similar. It would be interesting to re-cluster all of the samples in the same dataset to investigate this effect further.

5.2.5.5 Similar Genes Expressed in Pathology Associated Clusters of Astrocytes

In order to investigate whether similar genes were enriched/de-enriched in the pathology associated cluster in each of the samples, candidate genes involved in pathways of interest were highlighted using the 10x Genomics Loupe Browser. In the future, a broader and more in-depth analysis of the gene expression in each sample will be beneficial.

Figure 51 illustrates all of the clusters in all three samples express typical astrocytic genes *Clu* and *Apoe*, thus providing support for the selection of cells as being astrocytic. *Gfap* and *Vim* are genes typically associated with reactive astrocytes (Kamphuis et al. 2015). However, cells in all three samples showed low (or no) expression of these genes, even in the pathology associated cluster **(figure 52)**. The 10x Genomics kit involves 3'sequencing methods. Some have reported that full-length single cell RNA-seq approaches could be better for detecting lowly expressed transcripts, although they incur higher sequencing costs (Ziegenhain et al. 2017). Nevertheless, one would expect *Gfap* and *Vim* to be highly expressed in a portion of astrocytes compared to the rest of the astrocytes. This might indicate a technical issue with the single cell sequencing.

Figure 53 demonstrates that genes *Cox6c* (Cytochrome C Oxidase Subunit 6C), *Ndufa3* (NADH:ubiquinone Oxidoreductase Subunit A3), *Ndufa4* (Cytochrome C Oxidase Subunit NDUFA4), which are involved in oxidative phosphorylation, are all highly expressed in the pathology associated cluster in each of the samples (indicated by the black arrows). Whilst a thorough comparison of gene lists contributing to the pathways highlighted in each pathology associated cluster is necessary, this would suggest robust gene expression changes underlie the upregulation of oxidative phosphorylation in a subset of astrocytes in response to amyloidopathy. This finding is particularly interesting because genes *Cox6c*, *Ndufa3*, and *Ndufa4*, as well as the oxidative phosphorylation pathway in general, were shown to be downregulated in the 12-month APP/PS1 bulk astrocyte translatome analysis **(figure 36)**. Potential discrepancies between the bulk and single cell analysis may be due to the

differences between the transcriptome and translatome. Additionally, optimising the clustering of the cells may reveal a cluster which contains a higher proportion of the APP/PS1 cells than WT cells and which is de-enriched for oxidative phosphorylation. Oxidative phosphorylation is fundamental metabolic pathway for energy generation. Downregulation of genes related to oxidative phosphorylation, as indicated in the TRAP results, may cause metabolic stress and mitochondrial dysfunction. At the same time, overactivation of oxidative phosphorylation, which appears to be occurring in the pathology associated cluster of cells, can lead to excessive ROS generation. Hence, these pathology associated astrocytes may be contributing to neurodegeneration in AD through excessive ROS generation, or may be upregulating oxidative phosphorylation due to an energy demand caused by other astrocytes downregulating oxidative phosphorylation. In any case, this study highlights the benefit of single cell sequencing in identifying a subset of astrocytes with a different phenotype from the bulk analysis.

Genes induced in the bulk APP/PS1 translatome were enriched for GO Biological Process and KEGG pathway terms relating to protein degradation, lysosome and phagosome. **Figure 54** displays the expression of 3 genes involved in phagosome/lysosome processes, *Atp6ap1*, *Ctsd,* and *Fuca1*. The pathology associated clusters all appeared to express these genes highly in comparison to the other clusters of astrocytes. Additionally, the pathology associated clusters all highly expressed *Hsp90b1* (Heat Shock Protein 90 Beta Family Member 1), *Hspa5* (Heat Shock Protein Family A Member 5) and *Pdia6* (Protein Disulphide-Isomerase A6), proteins involved in the unfolded protein response **(figure 55)**. Interestingly, the pathology associated clusters did not express glutamate transporters *Slc1a2* and *Slc1a3* very highly **(figure 56)**. In fact, many of the cells appeared grey, either indicating an issue with the single cell sequencing, or indicating the expression was so low that it was not picked up by the single cell sequencing. Notably, impaired expression of glutamate transporters has been reported in a post-mortem study of human AD brains (Jacob et al. 2007), and human AD astrocytes (Grubman et al. 2019). Low astrocytic expression of glutamate transporters may contribute to excitotoxicity and synapse loss seen in AD.

The transcription factor analysis in the previous chapter indicated that genes induced in both the APP/PS1 and $MAPT^{P301S}$ mouse models were enriched for target genes of NRF2. *Nqo1*,

Gsta4 and *Prdx5* are all thought to be NRF2 target genes involved in antioxidant responses. These genes are all highly expressed in the pathology associated clusters and less so in the other clusters **(figure 57)**. These observations support the hypothesis that the pathology associated clusters are not only showing similar expression of genes in pathways enriched in those clusters, but also demonstrate similar reduced expression of genes in de-enriched pathways. A thorough comparison of the gene lists contributing to each pathway in the pathology associated clusters would help to prove this.

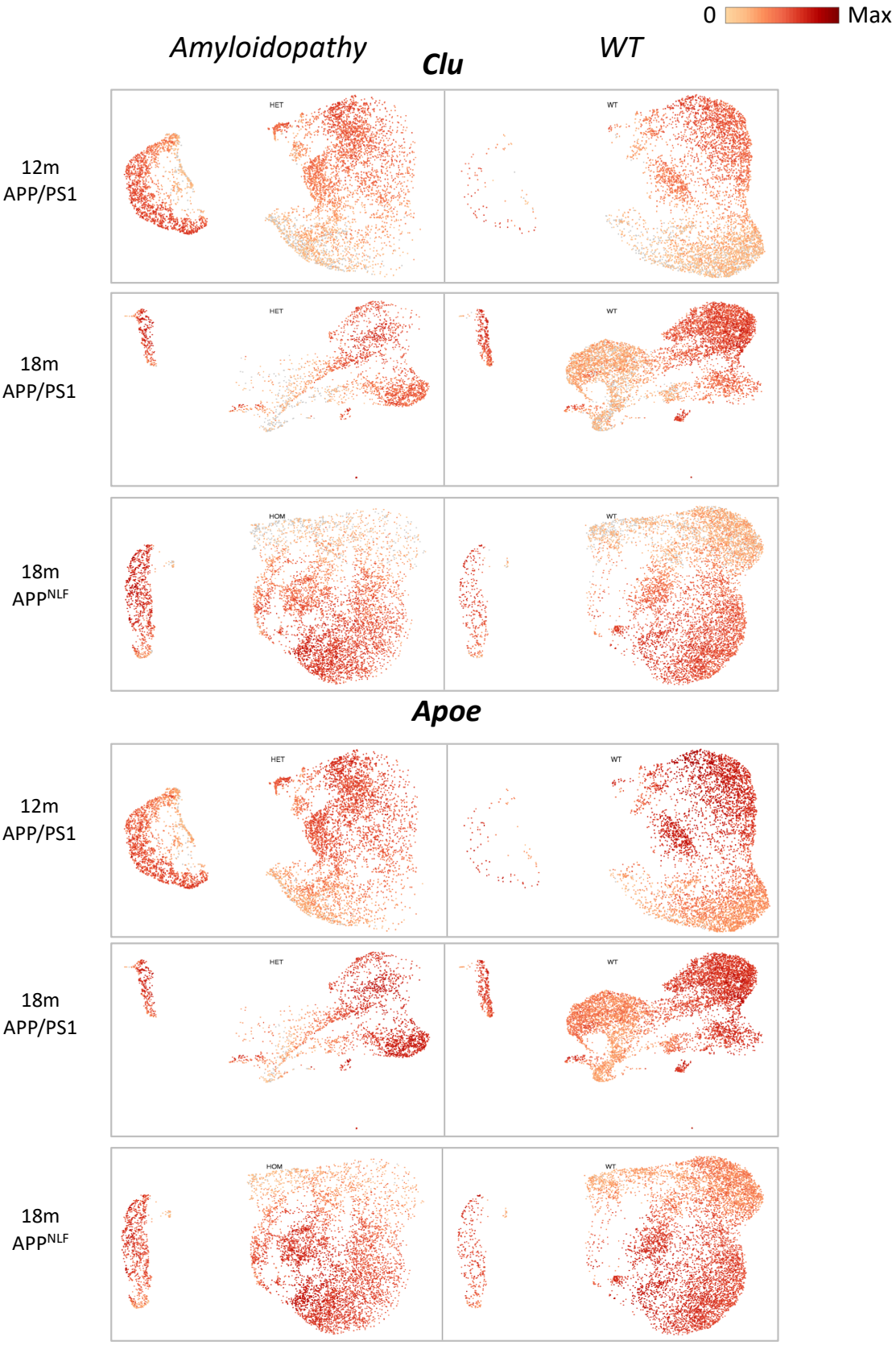
0
Max
Amyloidopathy
WT
Clu
12m APP/PS1
18m APP/PS1
18m APP^NLF
HET
WT
HOM
WT
Apoe
12m APP/PS1
18m APP/PS1
18m APP^NLF
HET
WT
HOM
WT

Figure 51. **Typical astrocyte genes expressed by all cells.** Uniform manifold approximation and projection (UMAP) representation of K-means clustered 12-month APP/PS1 and WT astrocytes, 18-month APP/PS1 and WT astrocytes, and 18-month APP^{NLF} and WT astrocytes. The 10x Genomics loupe browser in split view was used to visualise the amyloidopathy cells (left) and the WT cells (right). The normalised expression of candidate astrocyte expressed genes is shown. Total unique molecular identifier (UMI) counts for each cell were normalised towards the median of UMI counts for all cells. Then the count matrices were log-transformed, mean centred and scaled. All cells appear to express clusterin (*Clu*) and apolipoprotein E (*Apoe*).

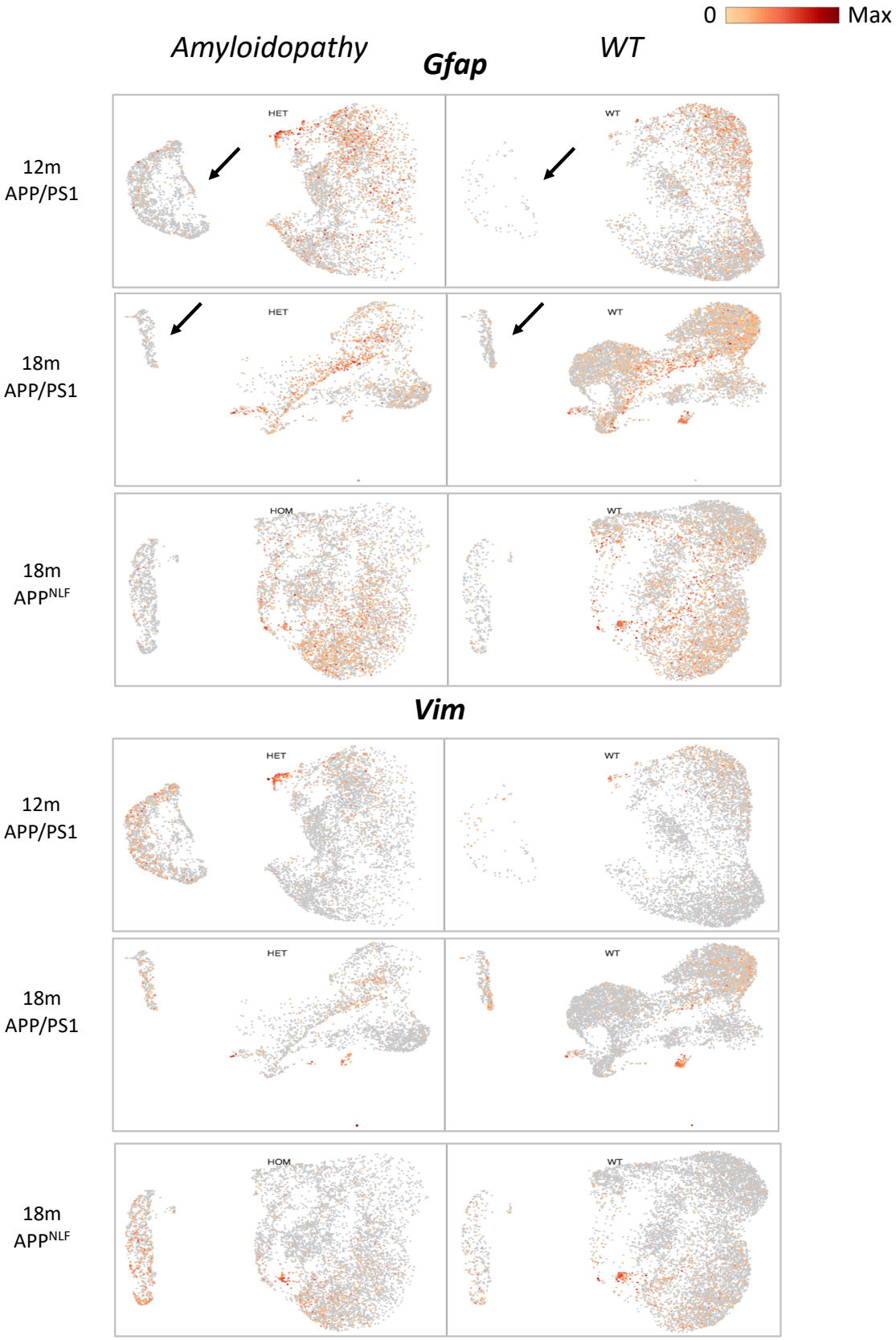

Figure 52. Reactive astrocyte genes lowly expressed in this single cell RNA-seq analysis. Uniform manifold approximation and projection (UMAP) representation of K-means clustered

12-month APP/PS1 and WT astrocytes, 18-month APP/PS1 and WT astrocytes, and 18-month APP^{NLF} and WT astrocytes. The 10x Genomics loupe browser in split view was used to visualise the amyloidopathy cells (left) and the WT cells (right). The normalised expression of candidate astrocyte expressed genes is shown. Total unique molecular identifier (UMI) counts for each cell were normalised towards the median of UMI counts for all cells. Then the count matrices were log-transformed, mean centred and scaled. The pathology associated cluster of astrocytes is indicated by black arrows. The astrocytes in this single cell RNA-seq analysis appear to not express or lowly express *Gfap* and *Vim*, genes classically associated with reactive astrocytes. Potentially highlighting technical issues with the single cell sequencing.

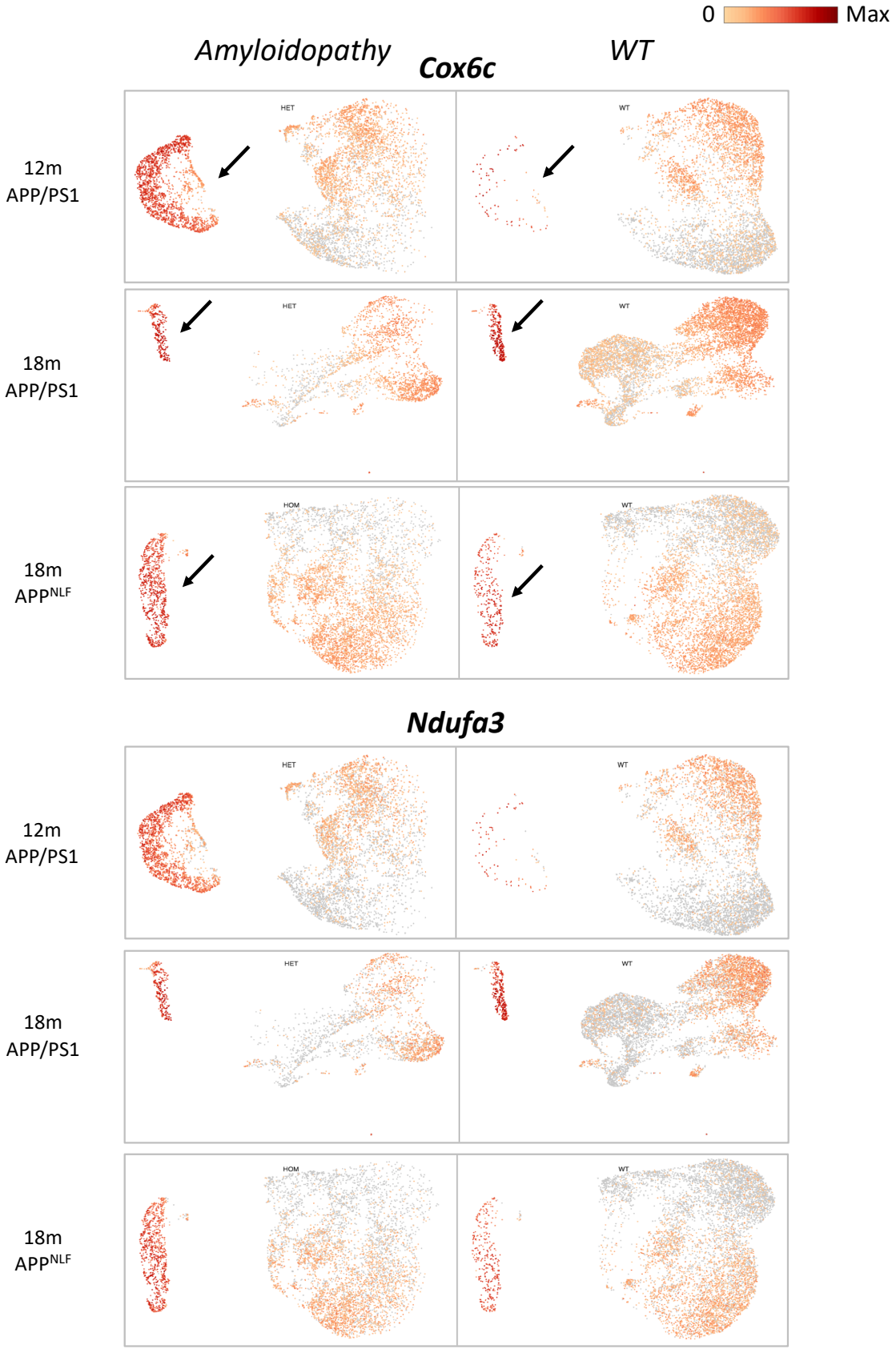
0
Max
Amyloidopathy
WT
Cox6c
12m
APP/PS1
18m
APP/PS1
18m
APPNLF
HET
WT
HOM
Ndufa3
12m
APP/PS1
18m
APP/PS1
18m
APPNLF
HET
WT
HOM

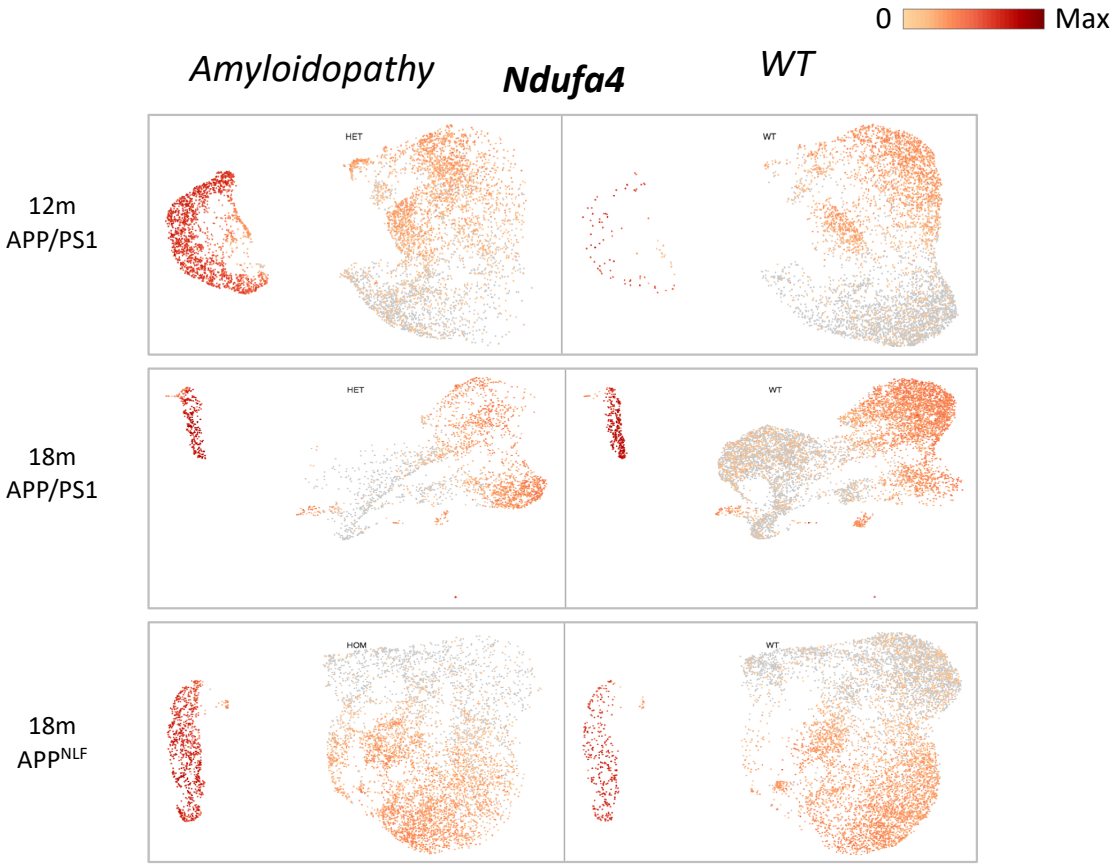

Figure 53. **Genes involved in oxidative phosphorylation are highly expressed in the pathology associated cluster.** Uniform manifold approximation and projection (UMAP) representation of K-means clustered 12-month APP/PS1 and WT astrocytes, 18-month APP/PS1 and WT astrocytes, and 18-month APP^{NLF} and WT astrocytes. The 10x Genomics loupe browser in split view was used to visualise the amyloidopathy cells (left) and the WT cells (right). The normalised expression of candidate astrocyte expressed genes is shown. Total unique molecular identifier (UMI) counts for each cell were normalised towards the median of UMI counts for all cells. Then the count matrices were log-transformed, mean centred and scaled. The pathology associated clusters of astrocytes (indicated by black arrows) appear to highly express *Cox6c*, *Ndufa3* and *Ndufa4*, genes involved in oxidative phosphorylation.

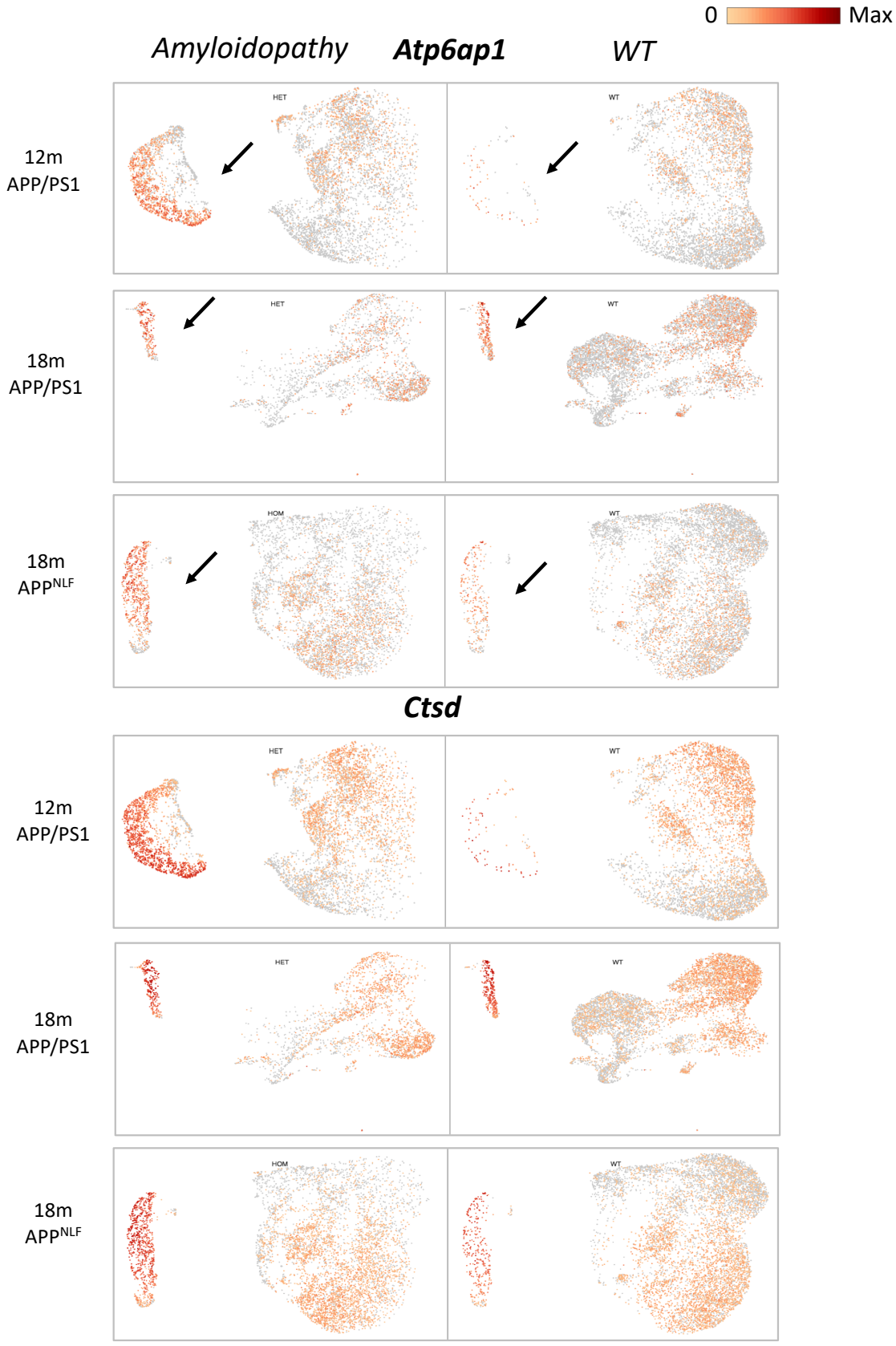
0
Max
Amyloidopathy
Atp6ap1
WT
12m APP/PS1
18m APP/PS1
18m APP^NLF
HET
WT
HOM
Ctsd
12m APP/PS1
18m APP/PS1
18m APP^NLF
HET
WT
HOM

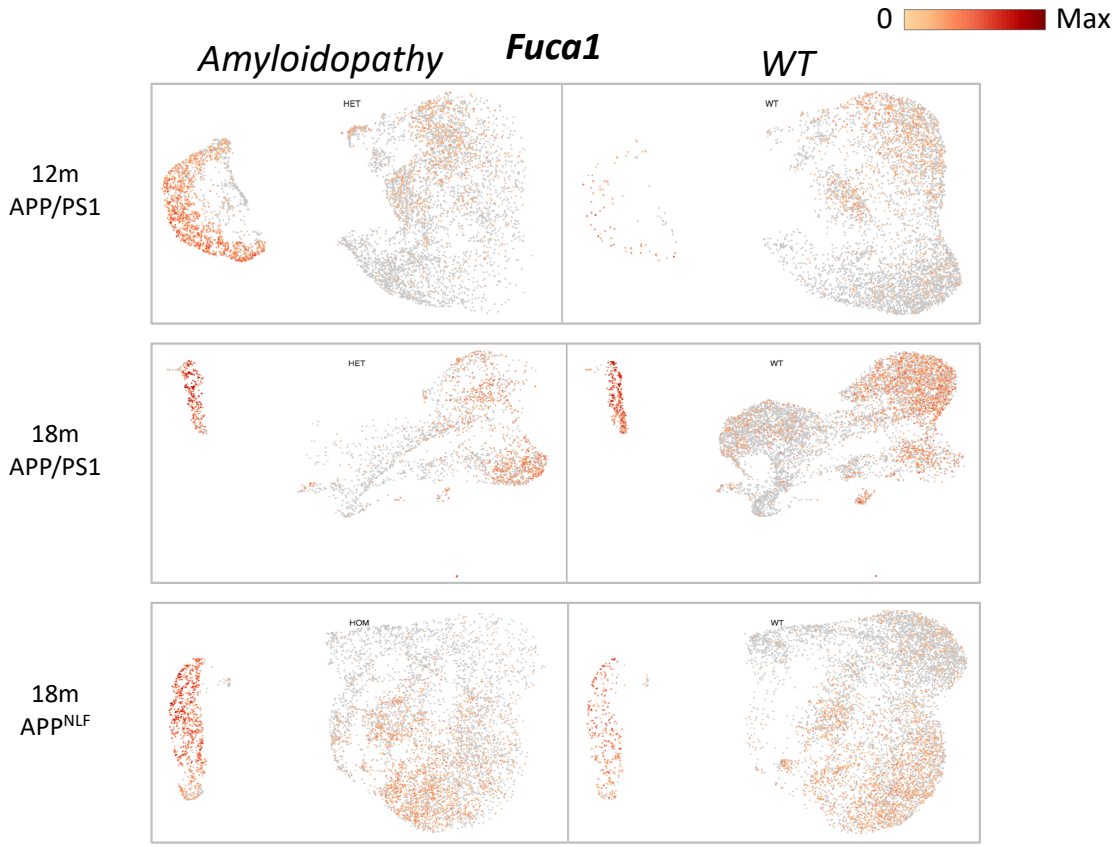

Figure 54. Genes involved in phagosome/lysosomal degradation are highly expressed in the pathology associated cluster. Uniform manifold approximation and projection (UMAP) representation of K-means clustered 12-month APP/PS1 and WT astrocytes, 18-month APP/PS1 and WT astrocytes, and 18-month APP^{NLF} and WT astrocytes. The 10x Genomics loupe browser in split view was used to visualise the amyloidopathy cells (left) and the WT cells (right). The normalised expression of candidate astrocyte expressed genes is shown. Total unique molecular identifier (UMI) counts for each cell were normalised towards the median of UMI counts for all cells. Then the count matrices were log-transformed, mean centred and scaled. The pathology associated clusters of astrocytes (indicated by black arrows) appear to highly express *Atp6ap1*, *Ctsd* and *Fuca1,* genes involved in autophagy.

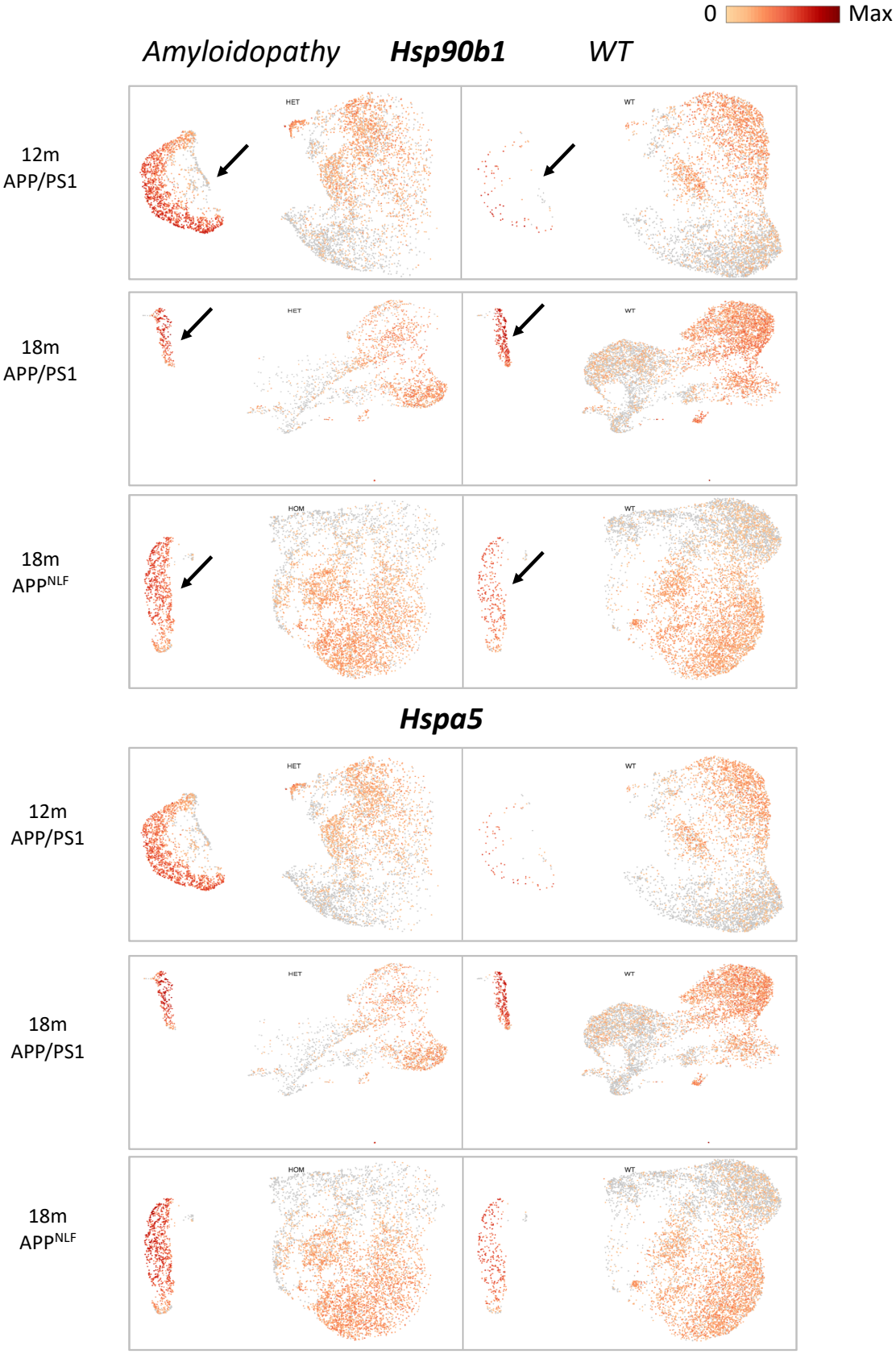
0
Max
Amyloidopathy
Hsp90b1
WT
12m
APP/PS1
18m
APP/PS1
18m
APPNLF
HET
WT
HOM
Hspa5
12m
APP/PS1
18m
APP/PS1
18m
APPNLF
HET
WT
HOM

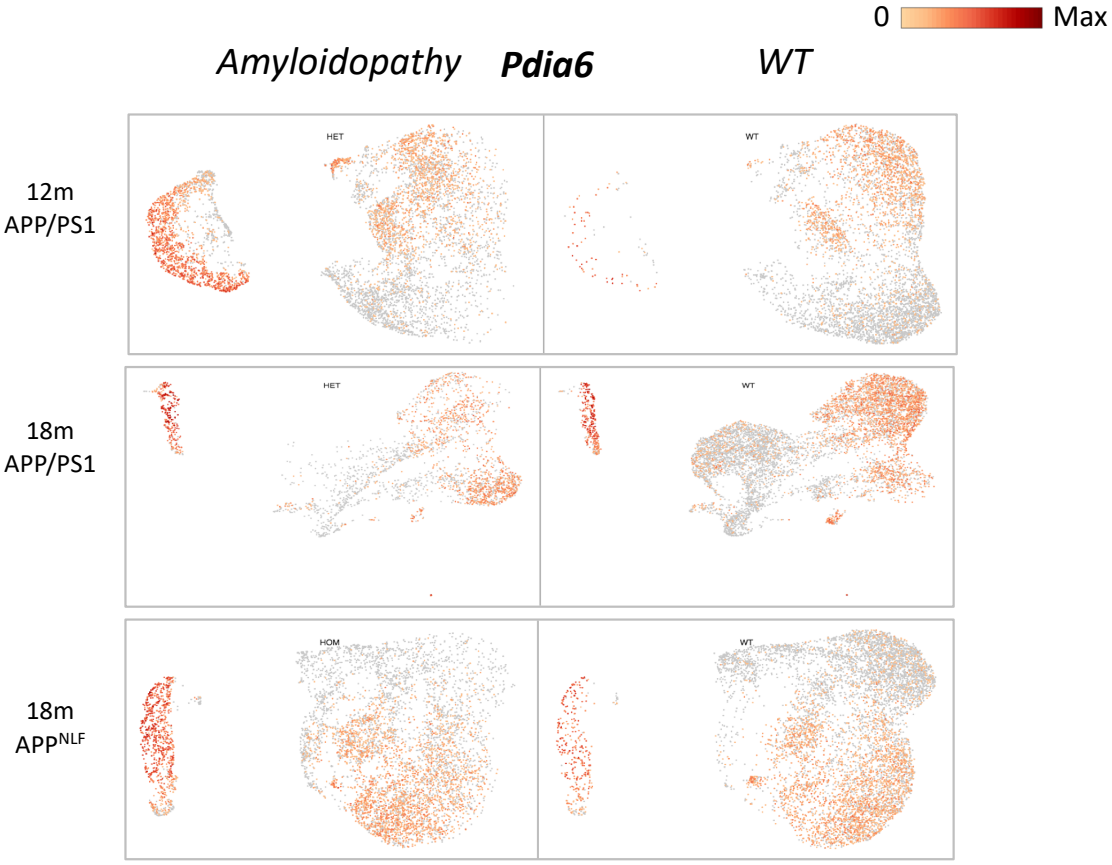

Figure 55. Genes involved in the unfolded protein response are highly expressed in the pathology associated cluster. Uniform manifold approximation and projection (UMAP) representation of K-means clustered 12-month APP/PS1 and WT astrocytes, 18-month APP/PS1 and WT astrocytes, and 18-month APP^{NLF} and WT astrocytes. The 10x Genomics loupe browser in split view was used to visualise the amyloidopathy cells (left) and the WT cells (right). The normalised expression of candidate astrocyte expressed genes is shown. Total unique molecular identifier (UMI) counts for each cell were normalised towards the median of UMI counts for all cells. Then the count matrices were log-transformed, mean centred and scaled. The pathology associated clusters of astrocytes (indicated by black arrows) appear to highly express *Hsp90b1*, *Hspa5* and *Pdia6,* genes involved in the unfolded protein response.

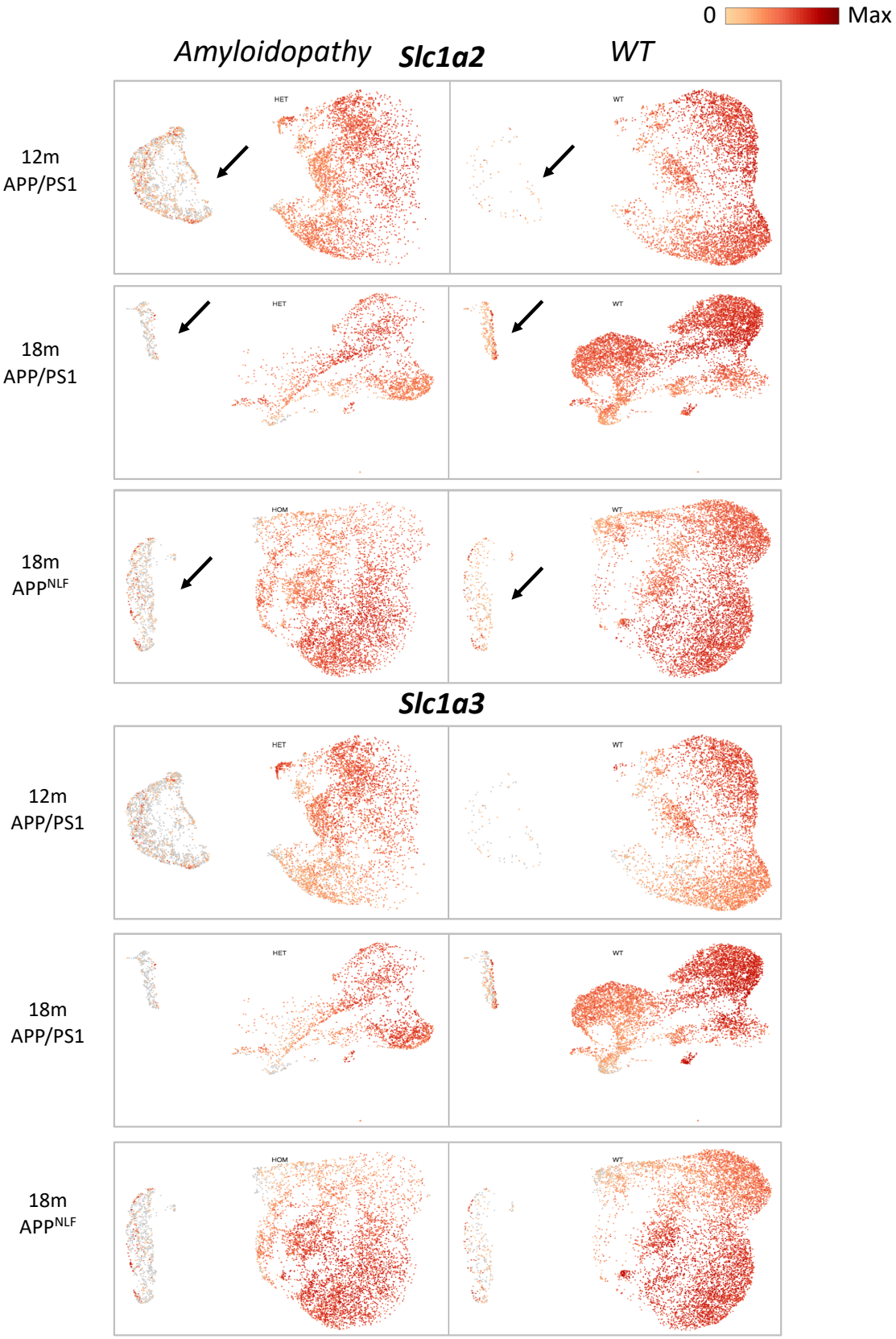
0
Max
Amyloidopathy
Slc1a2
WT
12m APP/PS1
18m APP/PS1
18m APPNLF
HET
WT
HOM
Slc1a3
12m APP/PS1
18m APP/PS1
18m APPNLF

Figure 56. **Glutamate transporter genes are lowly expressed in the pathology associated cluster.** Uniform manifold approximation and projection (UMAP) representation of K-means clustered 12-month APP/PS1 and WT astrocytes, 18-month APP/PS1 and WT astrocytes, and 18-month APP^{NLF} and WT astrocytes. The 10x Genomics loupe browser in split view was used to visualise the amyloidopathy cells (left) and the WT cells (right). The normalised expression of candidate astrocyte expressed genes is shown. Total unique molecular identifier (UMI) counts for each cell were normalised towards the median of UMI counts for all cells. Then the count matrices were log-transformed, mean centred and scaled. The pathology associated clusters of astrocytes (indicated by black arrows) appear to lowly express glutamate transporter genes *Slc1a2* and *Slc1a3* compared to the rest of the astrocytes in each sample.

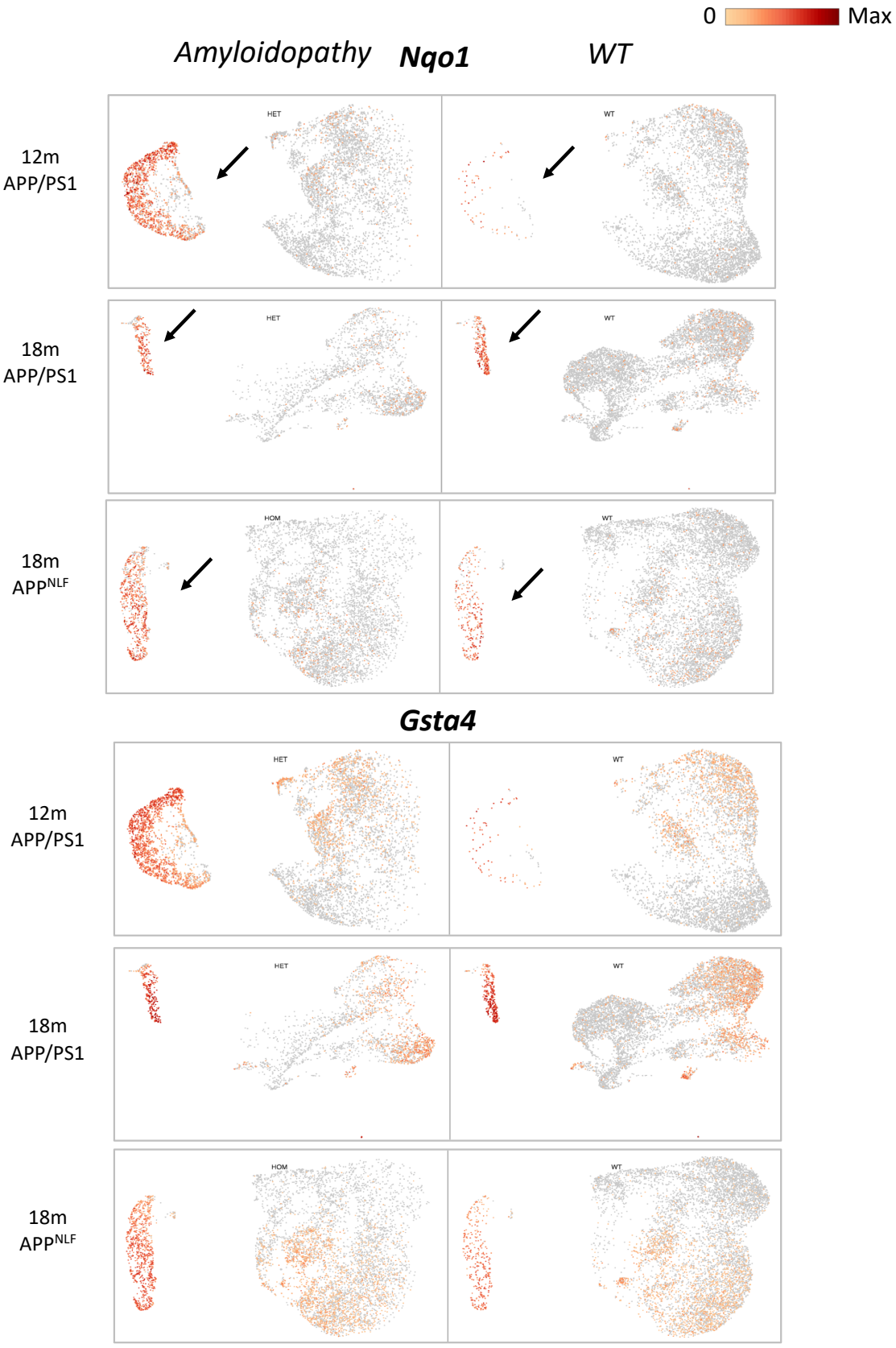
0
Max
Amyloidopathy
Nqo1
WT
12m APP/PS1
18m APP/PS1
18m APPNLF
HET
WT
HOM
Gsta4
12m APP/PS1
18m APP/PS1
18m APPNLF
HET
WT
HOM

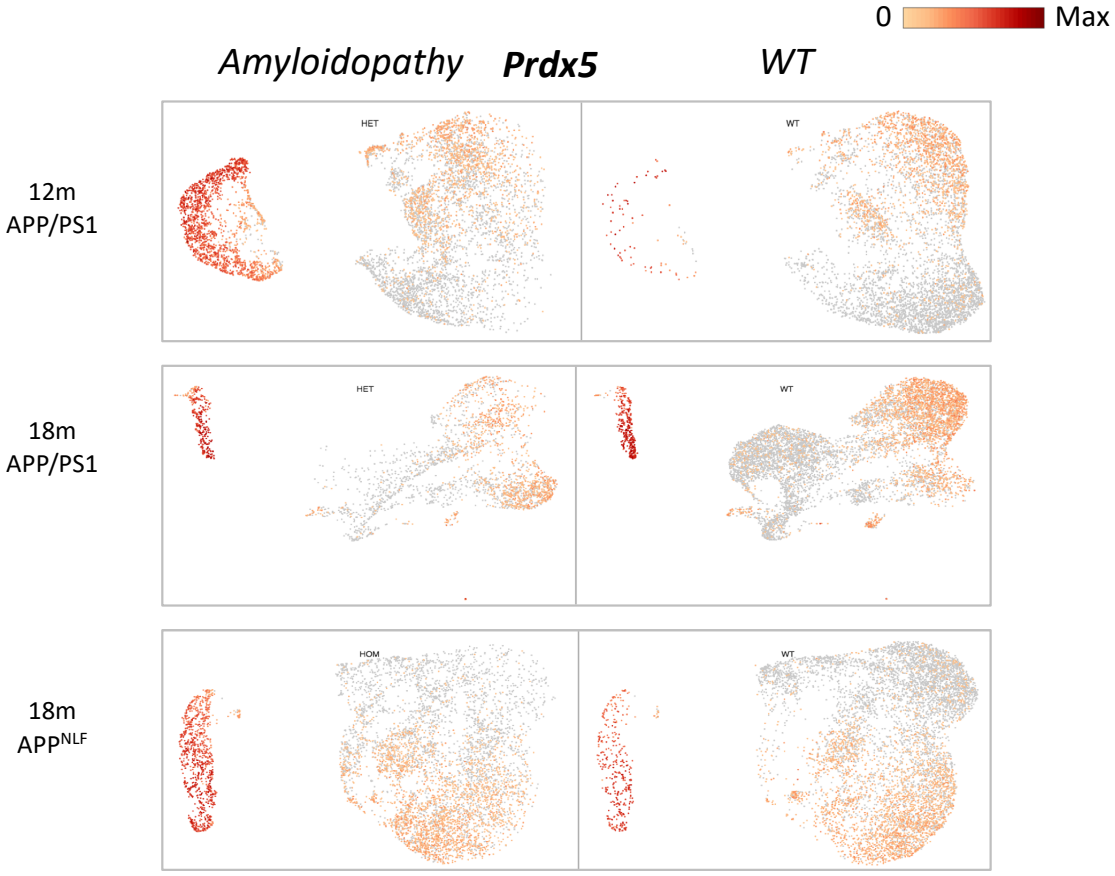

Figure 57. **NRF2 target genes are highly expressed in the pathology associated cluster.** Uniform manifold approximation and projection (UMAP) representation of K-means clustered 12-month APP/PS1 and WT astrocytes, 18-month APP/PS1 and WT astrocytes, and 18-month APP^{NLF} and WT astrocytes. The 10x Genomics loupe browser in split view was used to visualise the amyloidopathy cells (left) and the WT cells (right). The normalised expression of candidate astrocyte expressed genes is shown. Total unique molecular identifier (UMI) counts for each cell were normalised towards the median of UMI counts for all cells. Then the count matrices were log-transformed, mean centred and scaled. The pathology associated clusters of astrocytes (indicated by black arrows) appear to highly express NRF2 target genes *Nqo1*, *Gsta4* and *Prdx5*, compared to the rest of the astrocytes in each sample.

5.2.5.6 Clues as to the Location of the Pathology Associated Cluster of Astrocytes

Whilst the spatial information is lost when conducting single cell RNA-seq, Chen et al. (2020) had used spatial transcriptomics and in-situ sequencing to identify genes induced in cells in the immediate neighbourhood of Aβ plaques in APP^{NLGF} mice (i.e. in a ring with a radius of 50µm). Chen et al. report 57 plaque induced genes (coined PIGs), expressed in a coordinated manner between cell types (Chen et al. 2020). **Figure 58** illustrates that the pathology associated cluster of astrocytes in all three samples highly express candidate PIGs *Arpc1b*, *Man2b1*, and *Gpx4*, relative to other clusters in each sample, which might indicate that these pathology associated astrocytes are located around plaques. Notably, the pathology associated astrocytes were not enriched in *Gfap* or *C3* **(figure 52)** which are thought to be markers of reactive astrocytes, particularly around plaques (Liddelow et al. 2017; Kamphuis et al. 2015). Future experiments staining for Aβ plaques, astrocyte markers and markers of the pathology associated cluster would help to identify their location in proximity to plaques.

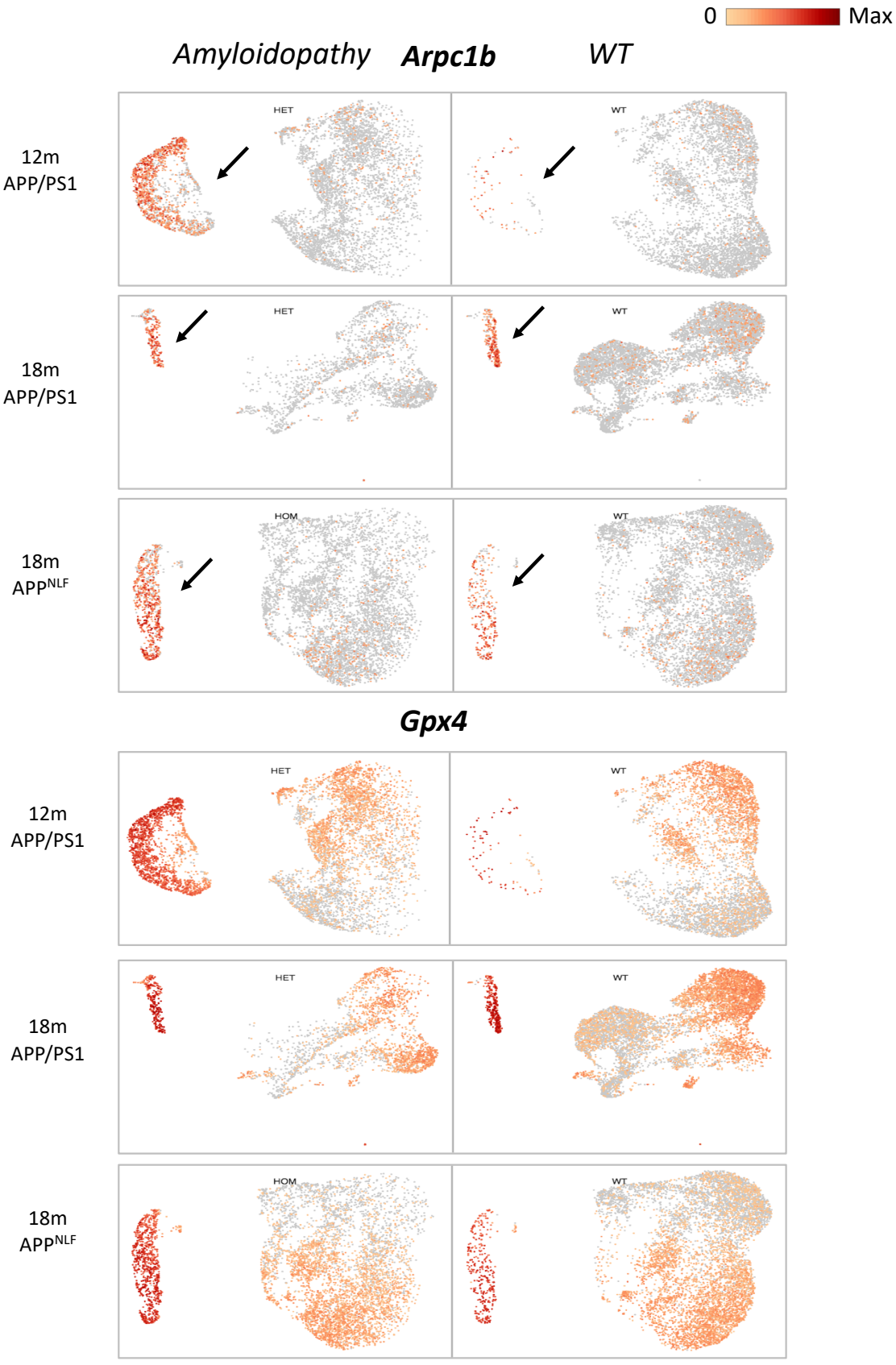
0
Max
Amyloidopathy
Arpc1b
WT
12m APP/PS1
18m APP/PS1
18m APPNLF
HET
HOM
WT
Gpx4
12m APP/PS1
18m APP/PS1
18m APPNLF
HET
HOM
WT

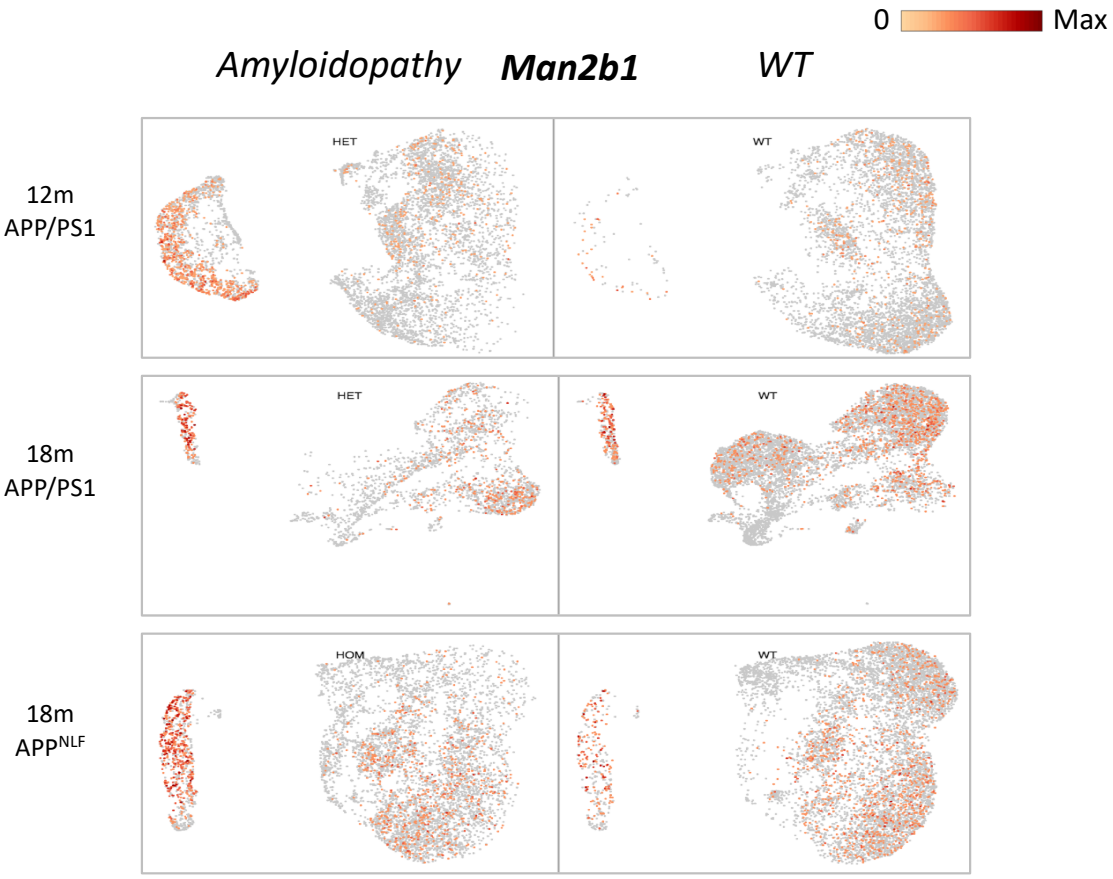

Figure 58. **Plaque induced genes identified by Chen et al. (2020) are highly expressed in the pathology associated cluster.** Chen et al. (2020) used spatial transcriptomics and in-situ sequencing to identify genes induced in cells in the immediate neighbourhood of Aβ plaques in APP^{NLGF} mice. *Arpc1b*, *Gpx4, and Man2b1* are candidate plaque induced genes from this study. Uniform manifold approximation and projection (UMAP) representation of K-means clustered 12-month APP/PS1 and WT astrocytes, 18-month APP/PS1 and WT astrocytes, and 18-month APP^{NLF} and WT astrocytes. The 10x Genomics loupe browser in split view was used to visualise the amyloidopathy cells (left) and the WT cells (right). The normalised expression of candidate astrocyte expressed genes is shown. Total unique molecular identifier (UMI) counts for each cell were normalised towards the median of UMI counts for all cells. Then the count matrices were log-transformed, mean centred and scaled. The pathology associated clusters of astrocytes (indicated by black arrows) appear to highly express plaque induced genes *Arpc1b*, *Gpx4, and Man2b1* compared to the rest of the astrocytes in each sample.

5.3 Discussion

5.3.1 Summary of Findings

This chapter investigated the heterogeneity of astrocyte response to amyloidopathy by performing K-means clustering on 12-month APP/PS1 and WT astrocytes, 18-month APP/PS1 and WT astrocytes, and 18-month APP^{NLF} and WT astrocytes. In all cases, a cluster of astrocytes which contained a higher proportion of the amyloidopathy exposed astrocytes than the WT astrocytes appeared separated from the larger body of astrocytes. This cluster was termed the 'pathology associated cluster'. IPA revealed robust pathway enrichment/de-enrichment in the pathology associated clusters of the different samples. Pathways related to oxidative phosphorylation, protein processing/degradation and NRF2-mediated oxidative stress response appeared enriched in the pathology associated cluster of astrocytes. Pathways related to synaptogenesis and synaptic function were downregulated in the pathology associated cluster relative to the other clusters in the samples. Investigation of candidate genes involved in pathways of interest revealed the pathology associated clusters demonstrated similar gene expression patterns irrespective of age or amyloidopathy model, suggesting a robust response to amyloidopathy in these astrocytes. High expression of plaque induced genes (taken from Chen et al. 2019) in the pathology associated cluster of astrocytes suggested that these astrocytes may be located around plaques.

5.3.2 A Preliminary Definition of the Astrocyte Population and Cluster Assignment

For the purposes of this initial exploration of the single cell datasets, manual segmentation of clusters based on position in UMAP space and the CSEA tool were used to identify clusters of cells likely to be astrocytes. Genes which were significantly enriched in each cluster, relative to the other clusters in the sample were input into the tool, which provided an easy way to identify the cell type enrichment in that cluster. Notably, Dougherty et al. (2010) had not included all of the cell types in the brain in their tool. Nevertheless, the main cell-types which we wanted to distinguish between, astrocytes, oligodendrocyte progenitors, oligodendrocytes, neurons and immunes cells were present. Using the tool was thought to provide a more unbiased method of cluster selection than looking for expression of candidate genes. Several automated methods to identify cell types in single cell RNA-seq have been

developed (Peyvandipour et al. 2020; Abdelaal et al. 2019). Hence, more sophisticated methods of defining the boundaries of clusters and assigning cell-types will be explored in the future.

In a similar vein, K-means clustering using the Davies-Bouldin Index to estimate the initial value of K was used in this first exploration of the single cell data. However, it is recognised that there are other methods of clustering (e.g. graph-based or hierarchical clustering) or other methods of estimating the optimal value of K (e.g. the elbow method, silhouette analysis). Future work exploring the most appropriate clustering of the data to avoid over or under clustering will be necessary.

5.3.3 Robust Phenotype of Pathology Associated Cluster of Astrocytes Across Time-Points and Models of Amyloidopathy

In all 3 astrocyte samples (12-month APP/PS1 and WT, 18-month APP/PS1 and WT, and 18-month APP^{NLF} and WT) there appeared to be a cluster of astrocytes, separated from the main body of astrocytes, which contained a higher proportion of the amyloidopathy exposed astrocytes than the WT astrocytes. IPA analysis revealed that the pathology associated cluster in each sample was enriched/de-enriched in remarkably similar pathways, and displayed a similar magnitude of enrichment/de-enrichment relative to the other clusters in each sample. Preliminary exploration of the data revealed all the pathology associated clusters highly expressed candidate genes involved in oxidative phosphorylation, phagosome/lysosomal degradation, the unfolded protein response and NRF2-mediated oxidative stress response, whilst showing low expression of glutamate transporters. Hence, it appears that similar alterations in gene expression underlie the similar pathway alterations of the pathology associated clusters in the 3 samples. Whilst a more thorough comparison of gene lists contributing to pathway enrichment in each sample, as well as assessment of expression values of genes in each sample is necessary, this preliminary analysis would suggest a robust phenotype of astrocytes in response to amyloidopathy, even across a transgenic and knock-in amyloidopathy model containing different genetic modifications. In the future, the data from both mouse models will be clustered together to investigate this further.

5.3.4 Comparison of the Bulk Translatome Sequencing and Single Cell Transcriptome Sequencing

Single cell RNA-seq is a powerful technique to identify heterogeneity of cellular responses, which are lost when assessing bulk transcriptomes/translatomes. Few gene expression changes were found in the bulk translatome analysis of 18-month APP^{NLF} astrocytes, nevertheless genes significantly induced >1.5 fold in 12-month APP/PS1 astrocytes appeared to be changing in the same direction in the 18-month APP^{NLF} astrocytes. The single cell analysis presented here might indicate that these changes in gene expression were significant, but were lost due to the bulk of astrocytes in the APP^{NLF} model not displaying differences from the WT cells. Perhaps in the 18-month APP^{NLF} model only astrocytes in the immediate vicinity of plaques display significant transcriptomic differences from WT astrocytes. Indeed, the pathology associated cluster highly expressed candidate PIGs chosen from Chen et al. (2020) compared to the other clusters of astrocytes **(figure 58)**, which might indicate they are located around Aβ plaques. Immunohistochemical staining of amyloid plaques, markers genes expressed in this pathology associated cluster and an astrocyte specific gene would help to provide information on the location of these astrocytes to prove this hypothesis.

IPA and GO analysis of the 12-month APP/PS1 bulk translatome indicated an upregulation of genes involved in synaptogenesis signalling **(figure 27)**, and a downregulation of genes involved in oxidative phosphorylation **(figure 36)**. Whereas, the phenotype of the pathology associated cluster in the single cell analysis appears to be enriched for genes related to oxidative phosphorylation and de-enriched for the synaptogenesis signalling pathway. More in-depth analysis of the genes which contribute to these pathways in the two experiments will be useful to understand these results.

A possible explanation for some of the contradictory phenotypes is that TRAP experiments assess the translatome, whereas single cell experiments assess the transcriptome. Perhaps genes involved in oxidative phosphorylation are upregulated in response to a metabolically compromised situation. However, they are not being actively translated, possibly due to a down regulation of translation machinery, as shown in **figure 36**. Alternatively, microRNAs

(miRNAs) are small regulatory RNAs which can bind to specific mRNAs and either cause them to not be translated or to be broken down (O'Brien et al. 2018). Perhaps miRNAs against oxidative phosphorylation genes such as *Cox6c*, *Ndufa3*, and *Ndufa4*, which overlapped between the two analyses, cause a downregulation of these genes in amyloidopathy exposed translatomes. Notably, the bulk translatome analysis does not include mitochondrial encoded genes. This might account for some discrepancy between the directionality of the oxidative phosphorylation pathways in the bulk translatome analysis and the pathology associated cluster in the single cell analysis. In the future, once could test this hypothesis by removing the mitochondrial encoded genes from the single cell pathway analysis.

Another possible explanation for the contradictory phenotypes between the TRAP and single cell data is that our current cell type selection/clustering method is masking amyloidopathy induced phenotypes found in the bulk RNA-seq dataset, and that the phenotype of the pathology associated cluster of astrocytes was diluted and not identified in the bulk analysis. Additionally, technical factors such as fewer than anticipated astrocytes sequenced, sequencing depth and dropout number (i.e. transcripts not detected in the sequencing data due to a failure to capture or amplify them) may be affecting the phenotypes found in the single cell RNA-seq. Future work defining the astrocyte population and clustering may prove to be insightful.

Notably, the bulk translatome analysis and single cell transcriptome analysis also demonstrated overlap of response to amyloidopathy. Genes induced in the bulk translatome of 12-month APP/PS1 astrocytes appeared enriched for NRF2 target genes **(figure 37)**. Likewise, the pathology associated clusters in the single cell transcriptome analyses highly expressed candidate NRF2 target genes **(figure 57)**. Transcription factor analysis of the genes highly expressed in the pathology associated clusters would help to illuminate if this cluster is enriched for NRF2 target gene expression.

Another similarity between the APP/PS1 bulk translatome analysis and the pathology associated clusters in the single cell transcriptome analysis is that terms related to protein processing and degradation were enriched in both. KEGG pathway analysis of the genes induced in the 12-month APP/PS1 astrocytes revealed enrichment for the terms lysosome,

phagosome and protein processing in the endoplasmic reticulum. The pathology associated clusters in the single cell analysis were enriched for genes involved in the unfolded protein response, and displayed high expression of candidate lysosome and phagosome genes. Upregulation of these genes is perhaps an adaptive protective response to the increased Aβ load in these animal models, but may also be contributing to the phagocytosis and loss of synapses around plaques in AD (Lee and Chung 2020). Interestingly, overactivation of the unfolded protein response in astrocytes has been shown to reduce astrocyte secretion of synaptogenic factors, leading to a failure to support synaptogenesis *in vitro* (Smith et al. 2020). Thus, providing an additional potential link between astrocyte dysfunction and the reduction in synapses seen in AD. Low expression of glutamate transporters in the pathology associated clusters of astrocytes likely also contributes to the excitotoxicity, synapse loss and neurodegeneration seen in AD.

5.3.5 Comparison of the Single Cell Transcriptome in AD Mouse Models and Human AD.

Grubman et al. (2019) conducted single-nucleus RNA sequencing on entorhinal cortex samples from control and Braak stages V-VI AD brains. In contrast to our results where there were a number of clusters which contained both WT and amyloidopathy exposed astrocytes, they found that AD and control astrocytes largely segregated into distinct clusters. This could be due to Grubman et al. focusing on the entorhinal cortex, whereas in this study we utilised astrocytes across the neocortex. Additionally, the fact that the astrocytes in human studies reflect end-stage disease, or that tau pathology in the human AD brains may also be impacting astrocyte phenotype, may be causing more distinction of clusters between the genotypes. Indeed, Habib et al. (2020) published a single nucleus sequencing study of astrocytes in the 5xFAD amyloidopathy mouse model where several clusters contained a mixed population of WT and pathology exposed astrocytes.

Grubman et al. reported 2 AD associated clusters of astrocytes. One of the AD astrocyte sub-clusters was enriched for genes related to the ribosome, mitochondria and neuron differentiation. This bears some similarity to the pathology associated clusters in our analysis which were enriched for eIF2a signalling and oxidative phosphorylation. Notably, the other

AD sub-cluster in the Grubman et al. study demonstrated high expression of the putative neurotoxic astrocyte marker gene C3, whereas this gene was not detected in our analysis, perhaps due to technical limitations.

Just as in this investigation, Habib et al. found a disease associated cluster of astrocytes in the 5xFAD mouse. This cluster expressed genes which were enriched for pathways involved in endocytosis, complement cascade, ageing and the lysosome. Hence the upregulation of lysosome related genes appears to robustly occur across 3 amyloidopathy mouse models, and both investigations suggest that amyloidopathy may exacerbate age dependent gene changes in astrocytes. Habib et al. reported an increase in the proportion of disease associated astrocytes at 4 months of age, before manifestation of cognitive decline, indicating the disease associated astrocytes may contribute to the pathological progression of AD. Conducting further single cell RNA-sequencing of APP^{NLF} and WT astrocytes at 6, 12 and 24 months would allow us to see if this effect replicates, and to test if an increasing proportion of WT astrocytes are present in the pathology associated cluster at 24-months. Furthermore, we would be able to perform single cell near-neighbour network embedding to identify astrocyte populations in pseudo time (Marques et al. 2018; Jäkel et al. 2019).

5.3.6 Limitations and Future Work

In this study, astrocytes were FACS sorted based on eGFP expression, which was driven by the *Aldh1l1* promoter. Whilst *Aldh1l1* is thought to be highly astrocyte specific, there might have been other cell types in the sequenced cells, although further investigation is needed. For example, immunohistochemical stains to investigate colocalisation of GFP with oligodendrocyte progenitor markers may help to identify whether these cells were erroneously sequenced. Further investigation of the best method to identify cell types in this dataset will also be conducted (Abdelaal et al. 2019; Peyvandipour et al. 2020). If a considerable amount of spurious cell types were sorted, in the future, using a combination of antibodies to gate in astrocytes and out other cell types, will allow more astrocytes to be sequenced and thus provide an improved understanding of astrocyte populations.

Capture efficiency can be a problem in single cell RNA-sequencing, whereby a transcript is expressed, however, it is not detected in the sequencing data due to a failure to capture or amplify it (Haque et al. 2017). Widespread capture inefficiencies would limit a comprehensive view of the population, especially given the reduced number of cells included in single cell sequencing compared to bulk RNA-sequencing. As the price of single cell sequencing reduces, it will be possible to sample more cells and at an increased depth, and thus further ensure samples are well represented.

The cell type selection tool created by Dougherty et al. (2010) was used in this study. Whilst this method provided a quick and easy way of identifying cells likely to be astrocytes. The tool highlighted that some of the clusters were somewhat enriched in non-brain cells or cells from non-cortical regions of the brain. This could be explained by there being common genes expressed in these cell types, or could indicate the tool is perhaps less useful than intended. Notably, the tool suggested large clusters of the GFP positive FACS sorted cells were closely related to oligodendrocytes (cluster 3 in figures 42 & 43, cluster 2 in figures 44 and 45 and cluster 2 in figures 46 and 47). However, it is possible that these clusters were in fact cells with a phenotype in between those typically associated with astrocytes or oligodendrocytes. Hence, we may have lost exciting information about astrocyte phenotypes by removing these cells from analysis. Nevertheless, the tool did provide a more unbiased means of determining cell type compared to the often-used method of picking favourite 'representable' gene(s). Additionally, upon pathology development, expression of genes which are associated with one cell type may change in another, such as the upregulation of TREM2 (a usually microglia associated gene) in astrocytes in response to amyloidopathy. Hence, to negate these issues it seemed wise to use the Dougherty tool which considers large lists of genes when assigning a likely cell type. In the future, it would be useful to use more widely used tools such as SingleR or Seurat to identify cell type. However, these tools require some programming expertise and so were not implemented in this analysis.

Additional limitations regarding the analysis include the need to further investigate the appropriate clustering for this data, and the need to validate that clusters are biologically meaningful. In particular, it will be necessary to cluster all of the cells together so that a meaningful comparison between genotypes and age groups can be conducted.

Additionally, a more in-depth analysis of genes highly expressed in each cluster will be conducted. This will be particularly interesting in the APP/PS1 samples, where at both 12 and 18-months, cluster 2 contained a lower proportion of the captured astrocytes.

Other technical limitations to bear in mind when conducting single cell sequencing include the possibility that tissue dissociation and FACS can cause alterations in the transcriptome of cells (Heiman et al. 2014). Whilst APP^{NLF} astrocytes displayed few differentially expressed genes compared to WT in the bulk TRAP-seq, in the single cell data there appeared to be a pathology associated cluster of astrocytes. The astrocytes in this cluster highly expressed candidate PIGs, which might indicate that this astrocyte profile was not found in the bulk TRAP-seq due to the relatively low plaque burden and surrounding reactive glial burden. However, an alternative explanation might be that FACS caused stress related gene expression artifacts. In order to investigate this further, it would be useful to conduct staining experiments with antibodies against astrocyte markers, marker genes of the pathology associated cluster, and plaques, in order to investigate whether these pathology associated astrocytes are present in the APP^{NLF} mouse, the location these astrocytes in relation to plaque pathology in both mouse models, and to confirm protein expression of marker genes. Finally, it would be interesting to further explore alterations in mitochondria in astrocytes exposed to Aβ. One could investigate the number of mitochondrial genes significantly up and down in pathology associated astrocytes as a proxy for whether mitochondrial function or density has altered, or perhaps conduct electron microscopy.

5.4 Chapter Conclusion

Whilst the single cell transcriptome analysis presented in this chapter is simply a preliminary exploration of the data, some interesting observations were made. Namely, there appeared to be a pathology associated cluster of astrocytes present in the 12 and 18-month APP/PS1 and WT sample, as well as the 18-month APP^{NLF} and WT sample. This pathology associated cluster appeared to be enriched/de-enriched in similar pathways compared to other pathology associated clusters in each sample, and similar genes appeared to underlie these pathway alterations. The pathology associated cluster was associated with increased

expression of the NRF2-mediated stress response, but also reduced expression of genes involved in synaptogenesis and synaptic function. Genes related to lysosome, phagosome, oxidative phosphorylation and the unfolded protein response were also enriched in the pathology associated cluster. These pathways are fundamental to healthy astrocyte function. However, if over activated can be damaging. Hence, the pathology associated cluster of astrocytes appeared to exhibit both beneficial and harmful phenotypes. The information gained in this study, along with further research defining pathology associated subsets of astrocytes could be used to specifically target pathological astrocytes with therapeutics to restore a healthy phenotype. If the therapeutic is given at an appropriate time-point, potentially prior to cognitive decline, this could provide a mechanism to alter the trajectory of Alzheimer's disease.

Chapter 6

General Discussion

6.1 Overview of Research Findings

In this thesis I investigate astrocyte dysfunction due to exposure to amyloidopathy using mouse models of AD. I utilised two amyloidopathy mouse models, the transgenic APP/PS1 and the knock-in APP^{NLF} mouse model (see section 1.5 on details of these models). **Figure 59** displays an overview of the research findings.

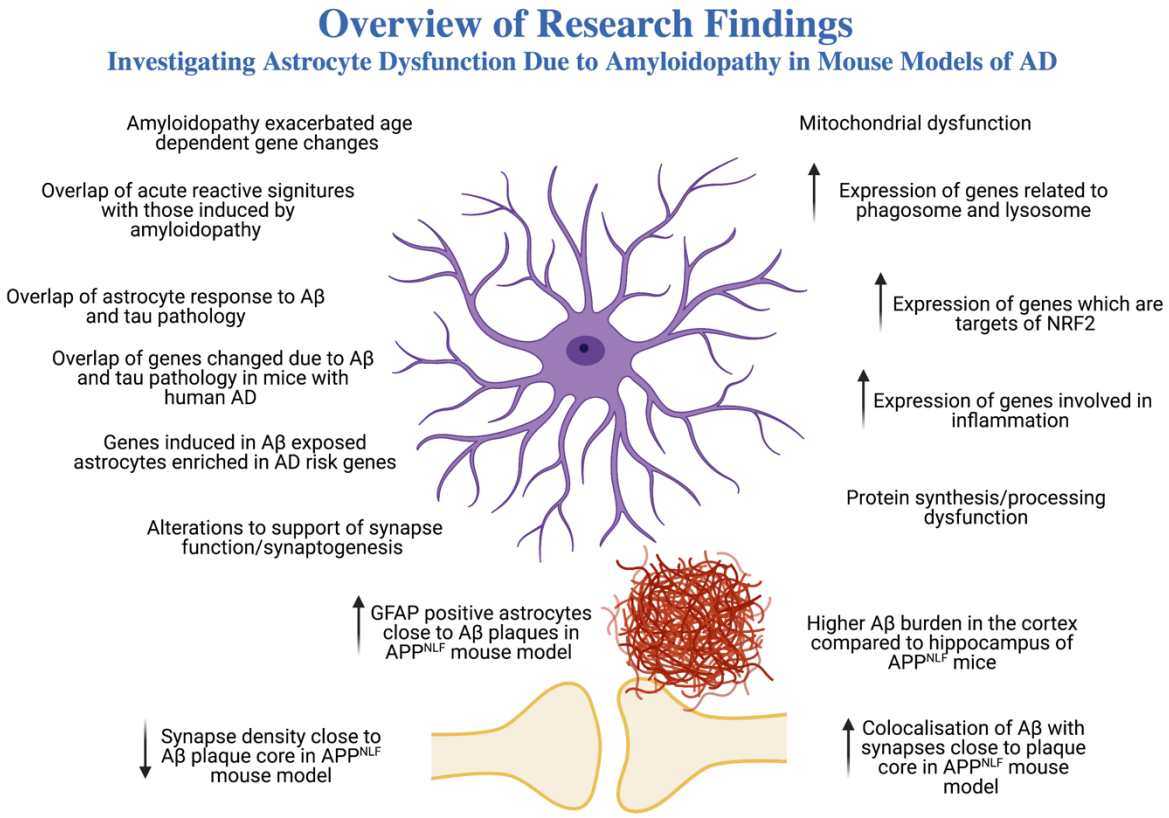

Figure 59. Overview of research findings. Created with BioRender.com.

Aβ plaques, synapse loss and astrogliosis are some of the major pathological hallmarks of AD and are thought to all contribute to, or be a consequence of astrocyte dysfunction in AD. Hence, I first investigated the extent to which the knock-in APP^{NLF} mouse model displayed these characteristics, since using the APP^{NLF} mouse to model AD would avoid potential artefacts caused by APP overexpression in other transgenic mouse models of AD. I used a high-resolution imaging technique to demonstrate synapse loss in the immediate vicinity (<10µm from the boundary of the plaque core) of Aβ plaques in the somatosensory cortex of HOM APP^{NLF} mice. I also showed that Aβ colocalisation with pre and post-synaptic puncta, and reactive astrocyte load (measured by GFAP staining) increased with reducing distance from the plaque core. These features had been documented before in other mouse models

of AD and in human post-mortem AD (Kamphuis et al. 2014; Ruan et al. 2009; Jackson et al. 2019; Koffie et al. 2012; Jackson et al. 2016; Koffie et al. 2009). However, this body of work helped confirm the utility of the APP^{NLF} mouse as a model of AD, and demonstrate that in the vicinity of plaques, a similar magnitude of synapse loss and astrogliosis occurs in the APP^{NLF} mouse as in other mouse models of AD and human AD.

Next, I investigated the impact of AD pathology on bulk astrocyte translatomes. I showed that few differences between WT and amyloidopathy exposed astrocytes could be found early in the disease pathology using bulk translatome sequencing. However, there were clear differences once Aβ pathology was widespread in the APP/PS1 mouse model. Amyloidopathy in the APP/PS1 mouse appeared to exacerbate age-dependent gene changes in astrocytes, and there was an overlap of acute reactive signatures with gene signatures caused by chronic exposure to amyloidopathy. However, astrocytes exposed to amyloidopathy did not display gene expression which fit distinctly into the A1/A2 astrocyte categories, suggesting that it may be more useful to think about astrocytes states as a continuum, with profiles beyond the A1/A2 categories. I utilised a $MAPT^{P301S}$ astrocyte translatome dataset, collected by a previous lab member, to show that Aβ and tau pathology cause some similar gene expression changes in astrocytes, namely an upregulation of genes related to protein processing and degradation, inflammation, and genes which appeared to be targets of the antioxidant master regulator NRF2. Additionally, Aβ and tau pathology appeared to both cause dysfunction of mitochondria and protein synthesis. Furthermore, both amyloidopathy and tauopathy exposed astrocytes demonstrated enrichment for genes changed in human post-mortem AD astrocytes, indicating some level of translatability of results in the mouse models to the human condition. An intriguing difference between amyloidopathy and tauopathy exposed astrocytes was that only astrocytes exposed to amyloidopathy were enriched for AD risk genes.

Few differences were seen in the APP^{NLF} astrocyte translatomes. Perhaps since the APP^{NLF} mouse takes longer to develop plaque pathology than the APP/PS1 mouse, and reactive astrocytes are often found encircling plaques, the reactive astrocyte load is also reduced in the APP^{NLF} mouse model. This could have led to translatome difference from WT being lost in the bulk sequencing. Nevertheless, genes induced in the APP/PS1 model also displayed a

positive fold change in the APP^{NLF} model, which might indicate overlap of response to amyloidopathy.

Preliminary analysis of single cell sequencing of astrocytes from APP/PS1 and APP^{NLF} mouse models revealed a pathology associated cluster of astrocytes in all of the samples. These astrocytes were significantly enriched for genes related to oxidative phosphorylation, protein processing/degradation and the NRF2-mediated stress response. Genes related to synaptogenesis and synaptic function were significantly de-enriched in these astrocytes, relative to the other astrocytes in the samples. Hence, there appeared to be a robust response of astrocytes to amyloidopathy, irrespective of mouse model. Thus, highlighting the benefit of single cell sequencing in identifying changes gene expression in small proportions of cells in the APP^{NLF} mouse.

Taken together, this study indicates that astrocyte phenotype is robustly perturbed by amyloidopathy in both of these mouse models. Astrocytes present both neuroprotective and neurotoxic alterations in gene expression in response to amyloidopathy. On the one hand, astrocyte upregulation of genes involved in protein processing and degradation could be viewed as adaptive protective responses to the build-up of amyloidopathy. However, excessive activation of the unfolded protein response has been associated with a reduced ability of astrocytes to support synaptogenesis (Smith et al. 2020), as well as increased apoptosis (Fribley et al. 2009). Additionally, enhanced astrocytic phagocytosis and lysosomal degradation may be involved in synapse loss in AD (Chung et al. 2013; Chung et al. 2015), indicating some of these adaptive protective responses may in fact be contributing to the pathology in AD. Mitochondrial dysfunction was also apparent in amyloidopathy exposed astrocytes. However, they appeared to also upregulate NRF2-mediated responses, perhaps to combat the increase in toxic free radicals caused by this mitochondrial dysfunction.

6.2 Contribution to Existing Knowledge

The studies outlined in this thesis add to our growing understanding of both animal models of AD and astrocyte dysfunction in AD. Saito et al. (2014) created the APP^{NLF} mouse model of AD to eliminate potential confounding effects of APP overexpression. However, they did not

quantify synapse pathology and astrogliosis around plaques. The initial body of work presented in this thesis filled that knowledge gap. Additionally, synapse loss results presented in this study were similar to those recently published by Sauerbeck et al. (2020), where they used a super-resolution imaging technique to quantify synapse pathology around plaques in APP^{NLF} mice. Replicability of results using different techniques and in different laboratories enhances the validity of the results presented here.

Orre et al. (2014) had conducted transcriptomic analysis of astrocytes from 15-18-month APP/PS1 mice. However, they had FACS isolated astrocytes and used a microarray to investigate gene expression. The TRAP-sequencing and single cell sequencing of APP/PS1 astrocytes presented in this study adds to this knowledge, illustrating alterations in astrocyte gene expression can be detected at 6 and 12-months. Additionally, TRAP-sequencing offers a number of benefits over FACS isolation and microarray analysis. TRAP is thought to cause fewer confounding alterations in astrocyte gene expression than dissociation of cells into single cell suspension. Additionally, RNA-sequencing offered the opportunity for improved sensitivity to detect alterations in genes expression, as well as the ability to detect changes in gene expression without pre-specification of the genes we were interested in. Notably, both studies illustrated upregulation of pathways involved in lysosome and phagosome processing, as well as inflammation. However, our study highlighted a mitochondrial dysfunction signature which was not highlighted in the Orre et al. study.

In this study, we also present translatome and transcriptome data for APP^{NLF} astrocytes, which to the best of our knowledge has not yet been published. The results of this investigation indicated that whilst there were significant alterations in APP^{NLF} astrocyte translatomes at 18-months, these were likely restricted to a subset of astrocytes, meaning few differences from WT were detected when bulk-sequencing. This work will help to inform researchers about the time points and experimental strategies to use for future experiments.

When comparing the APP^{NLF} and APP/PS1 amyloidopathy models, we showed that the APP^{NLF} mouse displayed a similar magnitude of plaque associated synapse loss as that found in the somatosensory cortex of APP/PS1 mice (Jackson et al. 2016). Furthermore, we demonstrated using single cell sequencing that astrocytes in the knock-in APP^{NLF} mouse model display similar

alterations in gene expression as transgenic APP/PS1 astrocytes, and similar directionality of genes induced when examining bulk translatomes. Notably, a thorough analysis of the differences between the two mouse models was not in the scope of this study, but is being conducted. Taken together, the knock-in APP^{NLF} mouse model bore resemblances to the transgenic APP/PS1 mouse model both in terms of synapse pathology and the response of astrocytes to amyloidopathy. This is important as there is a large resource difference (time and financial) between using the transgenic mouse model and the slower progressing knock-in mouse model. Additionally, there has been a lot of scientific data collected using transgenic mouse models, hence validation of results is encouraging. Future work investigating the differences between the two mouse models will help elucidate whether APP overexpression meaningfully impacts the results. Additionally, further examination of the single cell dataset is necessary to ensure that similarities between the APP/PS1 and APP^{NLF} astrocytes were not due to stress induced by FACS. Knock-in mouse models were created because disentangling the effects of Aβ from APP overexpression in the transgenic mouse models has not been possible. Even if our future analyses of astrocyte reaction in APP/PS1 and APP^{NLF} mice yield few differences, we would not be able to conclusively say that APP overexpression isn't affecting an aspect not measured. Hence, given unlimited resources, it is likely still better to use the knock-in APP^{NLF} mouse.

6.3 Limitations of Study and Future Directions of Research

A key limitation of the work carried out in the APP^{NLF} mouse model is that due to time restraints and the resources available, pathology was only quantified at 12-months, whereas bulk-translatome sequencing was carried out at 6, 12 and 18-months, and single cell sequencing was conducted at 18-months. In the future, it would be beneficial to quantify pathology at all of the time points used, so that alterations in astrocyte gene expression can be put in the context of pathology. To this point, astrogliosis was not quantified over the whole cortex, only in cropped images due to the thickness of tissue sections and imaging technique making it difficult to threshold. In future studies, tissue would be sectioned more thinly so that astrogliosis burden over the entire cortex can be measured and compared to other models of amyloidopathy.

The data gathered in this thesis suggests that astrocytes exhibit similar alterations in gene expression in the APP/PS1 and APP^{NLF} mouse models, however with different speeds of progression. 24-month old APP^{NLF} mice have more extensive plaque pathology, and thus one would hypothesise have more extensive reactive astrocyte load. Hence, conducting additional bulk translatome sequencing of 24- month old APP^{NLF} mice and comparing the data to the 12-month APP/PS1 translatome collected in this study would help to prove this point. Additionally, combining the APP/PS1 and APP^{NLF} single cell datasets and conducting more analysis of the pathology associated cluster could support this hypothesis. Due to time restraints, only a preliminary analysis of the single cell sequencing data is presented here. Future work will involve examining more sophisticated methods to identify cell types, cluster cells and assess gene enrichment. Subsequently, qPCR validation of genes highly expressed in the bulk and single cell sequencing experiments will be conducted. Immunohistochemistry experiments using antibodies against genes which define the pathology associated cluster of astrocytes, astrocyte specific genes and Aβ plaques would allow spatial information of these altered astrocytes to be collected. Furthermore, confirming the presence of this subset of astrocytes in human tissue would be extremely beneficial in demonstrating translatability of results.

Another intriguing result which has been suggested in this thesis and in other published work is that amyloidopathy exacerbates age dependent changes in astrocyte gene expression. Clustering the 12 and 18-month APP/PS1 and WT astrocytes together will be the first step in assessing this. Additionally, conducting single cell analysis on 24-month old mice may indicate further increases in the proportion of WT astrocytes in the pathology associated cluster and thus support this hypothesis.

Genes related to phagosome and lysosome function were upregulated in response to amyloidopathy and tauopathy. It would be interesting to conduct a functionnal synapse phagocytosis assays on AD patient stem cell derived astrocytes (or human astrocytes exposed to Aβ derived from human brains) in order to investigate whether these pathologically burdened astrocytes enhance phagocytosis of synapses as well as Aβ. Immunohistochemical staining using an astrocytes specific marker, a lysosomal marker and a synaptic protein marker might further indicate that enhanced astrocytic phagocytosis and lysosomal

processing is partially responsible for synapse loss in AD. An intriguing difference between the response of astrocytes to amyloidopathy and tauopathy was that only astrocytes exposed to amyloidopathy were enriched for AD risk genes. Further investigation of the link between AD risk genes and astrocyte response to amyloidopathy may highlight opportunities for astrocyte targeted preventative medicine.

The work carried out in this study has focused on the effects of amyloidopathy on astrocytic gene expression. However, it is possible that amyloidopathy affects the astrocyte phenotype indirectly, for example via microglia. Using the Sargasso method (Dando et al. 2016; Hasel et al. 2017), it is possible to identify which species RNA originated from. Hence, in vitro double cultures of mouse neurons and human astrocytes exposed to human derived Aβ oligomers, as well as triple cultures of mouse neurons, human astrocytes and rat microglia exposed human derived Aβ oligomers, may help to uncover the extent to which the alterations in astrocyte phenotype are due to the direct influence of Aβ on astrocytes, or due to the influence of Aβ on microglia which subsequently influences astrocyte phenotype.

The ultimate purpose of the investigations conducted in this thesis was to contribute to our understanding of AD pathogenesis and support the design of disease modifying therapeutics. In this study, I highlighted similarities between astrocyte response to amyloidopathy and tauopathy, the two cardinal pathological proteins in AD. In particular, there appeared to be an upregulation of NRF2 mediated antioxidant response in astrocytes exposed to both pathologies. However, the response is either too little and/or too late since pathology continues in both models. It would be interesting to investigate if boosting the astrocytic NRF2 mediated stress response further, at an earlier time point, or in conjunction with an Aβ-targeted therapeutic and an anti-inflammatory therapeutic, could alter the trajectory of pathology. Crossing conditional knock-in GFAP-NRF2 mice with amyloidopathy mice would facilitate this. Alternatively, creating an antibody-drug conjugate which binds to a marker of the pathology associated astrocytes, is engulfed and releases a drug combination which reduces neurotoxic phenotypes and increases neuroprotective phenotypes (e.g. with an antisense oligonucleotide against pro-inflammatory cytokines and mRNA for NRF2) would be an exciting research avenue. It may also be beneficial to investigate whether targeting other astrocytic dysfunctions uncovered in this study, such as the overactivation of the unfolded

protein response or mitochondrial dysfunction, can substantially alter the progression of pathology.

Taking these limitations and experimental ideas into consideration, whilst also considering resource limitations, the next steps in this project will be to:

- Re-examine the appropriate cells to include in the single cell analysis using more sophisticated methods such as Seurat, followed by clustering of the APP/PS1 and APP^{NLF} astrocytes together. Conduct differential gene expression analysis to re-determine the similarities and importantly examine the ***differences*** in gene expression in the two mouse models.
- Identify candidate pathology associate genes and stain for the proteins along with Aβ plaques using IHC in order to gain information of the location of astrocytes expressing these pathology associated genes and to verify that the pathology associated genes are not simply an artifact of cell sorting.
- Write a paper comparing synapse pathology and reactive astrocytes in the knock-in APP^{NLF} vs transgenic APP/PS1 mouse model, highlighting the appropriate time point to utilise the APP^{NLF} mouse model and examining the benefits and disadvantages of each mouse model.

6.4 Therapeutic Implications

The majority of clinical trials of disease modifying therapies for AD have failed (Mehta et al. 2017). These trials have included a wide variety of treatments, from anti-Aβ antibodies (Spencer and Masliah 2014), to antioxidants (Mecocci and Polidori 2012) and non-steroidal anti-inflammatory drugs (Wang et al. 2015). However, all showed little effect in altering the course of AD. Indeed, the overwhelming Aβ-targeted therapeutic failure has led some to believe the strategy should be abandoned (Herrup 2015). In this study, I highlight the consequences of Aβ pathology on astrocyte gene expression. However, it is clear that many cell types in the brain are affected by the gradual build-up of Aβ pathology over decades prior to clinical representation (Quintela-López et al. 2019; Navarro et al. 2018). Hence, it does not seem wise to disregard the wealth of research pointing at a central role of Aβ in AD.

Efforts to understand why the Aβ targeted therapeutics failed indicate that several therapeutics were either not selective enough for the noxious oligomeric form of Aβ, or were given too late in the disease pathology, such that downstream neuroinflammation and synapse loss had already begun. In some cases, it was found that participants without Aβ pathology were enrolled in the trial (Mehta et al. 2017; Cummings 2018). These failures have led to improvements in clinical trial design, placing emphasis on biomarker tracking, and the need to enrol patients in the earlier stages of the disease (Cummings 2018). Nevertheless, it may improve success of anti-Aβ treatments if they are combined with alternative therapeutic strategies which target some of the downstream consequences of Aβ.

In this study, I have highlighted a number of ways that astrocyte function appears to be altered (at least at the gene expression level) by exposure to Aβ. Designing therapeutics to correct each of those functions individually seems like an unlikely prospect, especially because other cell types in the brain are also dysfunctioning. However, altering the cellular environment to encourage proper functioning of glia may prove beneficial. In this study, and in other studies, astrocytes exposed to Aβ display pro-inflammatory and oxidative stress responses (Orre et al. 2014; Grubman et al. 2019; González-Reyes et al. 2017). This leads to a chronic feedforward cycle of reactive astrocytes releasing mediators of inflammation and oxidative stress, leading to further reactive astrocytes. Chronic inflammation and oxidative stress appear to also negatively impact the functioning of other cell types in the brain, such as microglia (Orre et al. 2014; Lue et al. 2001; McDonald et al. 1997; Meda et al. 1999) and oligodendrocytes (Lee et al. 2004; Cai and Xiao 2016; Jantaratnotai et al. 2003). Hence, the feedforward cycle of cellular dysfunction, inflammation and oxidative stress appear to be crucial elements of AD, in addition to the build-up of pathological proteins. Perhaps if anti-inflammatory, antioxidant and pathological protein-targeted therapeutics were given in combination, and at an early enough time point, this could alter the course of the disease.

Non-steroidal anti-inflammatory drugs (NSAIDs) are thought to modulate Aβ production, as well as microglial and astrocyte reaction (Lim et al. 2000; Weggen et al. 2001). Whilst meta-analyses of epidemiological studies indicate a reduced risk of developing AD with NSAID use (McGeer et al. 1996; Wang et al. 2015), meta-analyses of clinical trials have shown no statistical or clinical significance of the drugs (Miguel-Álvarez et al. 2015; Gupta et al. 2015).

However, these anti-inflammatory agents were given alone and many included AD patients with moderate disease (Aisen et al. 2003; Pasqualetti et al. 2009; Miguel-Álvarez et al. 2015). Hence, it is possible that the abundance of Aβ oligomers in the brain meant treatments were ineffective. Other anti-inflammatory agents such as the antibiotic minocycline and TNFα inhibitors have also been suggested as potential future therapeutics of AD (Chang et al. 2017; Sadick and Liddelow 2019). The previous clinical trials of antioxidants were beset by the same issues as the clinical trials of NSAIDs. Treatments were either given alone, or in combination with a symptomatic treatment and included patients with moderate AD (Mecocci and Polidori 2012).

The data presented in this thesis suggests that in response to amyloidopathy, a portion of astrocytes upregulate NRF2 mediated oxidative stress response. However, despite this, pathology continues. This information in conjunction with the previously failed clinical trials of anti-inflammatory and antioxidant treatments might suggest that antioxidant/anti-inflammatory approaches are not sufficient to alter disease progression. Alternatively, the data in this thesis might highlight once again the importance of amplifying these responses further in AD. Hence, a clinical trial of a combinatorial treatment targeting pathological proteins Aβ and tau, neuroinflammation, oxidative stress, and given at an early time point in the disease may prove to be disease altering.

Another aspect to consider is that the single cell sequencing in this study and other studies have revealed heterogeneity of cellular phenotypes in AD (Grubman et al. 2019; Mathys et al. 2019; Habib et al. 2020; Rangaraju et al. 2018). Just as targeting specific forms of noxious Aβ will likely improve therapeutic outcome due to increased target engagement with a specific dose, perhaps specifically targeting dysfunctioning glia will substantially improve therapeutic outcome. To do this, it will be necessary to identify the expression of marker proteins on dysfunctioning cell types. This will allow antibody-drug conjugates to be formulated to specifically target the dysfunctioning cell. Deciphering the appropriate drug/drug combination to enhance neuroprotective functions whilst diminishing neurotoxic functions of each cell type is an area in need of more research. However, for astrocytes, perhaps antisense oligonucleotides targeting pro-inflammatory cytokine mRNA, along with mRNA to boost antioxidant responses will prove beneficial, especially if given in addition to an Aβ-

targeted therapeutic. If the increase in phagosome and lysosome related genes which were identified in this study is an adaptive protective response to Aβ load, then perhaps targeting plaque proximal astrocytes and further boosting their phagocytic and protein degrative abilities will be useful.

Finally, it is imperative that we learn from previous clinical trial failures, ensuring therapeutics have good brain penetrance, are given at an appropriate time point, on biomarker confirmed patients and target a combination of the complex feedforward pathologies associated with AD. Furthermore, improved strategies to measure disease progression, for example using machine learning to develop digital biomarkers of AD, may help to diagnose patients earlier, enroll patients in clinical trials earlier, and track improvement with increased sensitivity, all of which will contribute to the development of a disease modifying AD therapeutic.

6.5 Thesis Conclusion

In this thesis, I have characterised pathology in the APP^{NLF} amyloidopathy mouse model, and investigated alterations in astrocyte gene expression due to amyloidopathy. These gene expression changes include both neuroprotective and neurotoxic astrocyte pathways. AD therapeutics have traditionally focused on targeting pathological proteins in AD. However, this has not yet led to disease modifying treatments, perhaps due to cell types in the brain already manifesting pathological alterations by the time patients are diagnosed. The work presented here will add to the body of research around the dysfunction of different cell types in the brain, and aid the design of astrocyte targeted therapeutics which boost neuroprotective pathways and reduce neurotoxic alterations in astrocyte function.

Bibliography

Abdelaal, T., Michielsen, L., Cats, D., et al. 2019. A comparison of automatic cell identification methods for single-cell RNA sequencing data. *Genome Biology* 20(1), p. 194.

Abdul, H.M., Sama, M.A., Furman, J.L., et al. 2009. Cognitive decline in Alzheimer's disease is associated with selective changes in calcineurin/NFAT signaling. *The Journal of Neuroscience* 29(41), pp. 12957–12969.

Adams, D.J., Arthur, C.P. and Stowell, M.H.B. 2015. Architecture of the synaptophysin/synaptobrevin complex: structural evidence for an entropic clustering function at the synapse. *Scientific Reports* 5, p. 13659.

Agarwal, A., Wu, P.-H., Hughes, E.G., et al. 2017. Transient opening of the mitochondrial permeability transition pore induces microdomain calcium transients in astrocyte processes. *Neuron* 93(3), p. 587–605.e7.

Aisen, P.S., Schafer, K.A., Grundman, M., et al. 2003. Effects of rofecoxib or naproxen vs placebo on Alzheimer disease progression: a randomized controlled trial. *The Journal of the American Medical Association* 289(21), pp. 2819–2826.

Aizenstein, H.J., Nebes, R.D., Saxton, J.A., et al. 2008. Frequent amyloid deposition without significant cognitive impairment among the elderly. *Archives of Neurology* 65(11), pp. 1509–1517.

Allen, B., Ingram, E., Takao, M., et al. 2002. Abundant tau filaments and nonapoptotic neurodegeneration in transgenic mice expressing human P301S tau protein. *The Journal of Neuroscience* 22(21), pp. 9340–9351.

Allen, N.J., Bennett, M.L., Foo, L.C., et al. 2012. Astrocyte glypicans 4 and 6 promote formation of excitatory synapses via GluA1 AMPA receptors. *Nature* 486(7403), pp. 410–414.

Anderson, C.M. and Swanson, R.A. 2000. Astrocyte glutamate transport: review of properties, regulation, and physiological functions. *Glia* 32(1), pp. 1–14.

Arranz, A.M. and De Strooper, B. 2019. The role of astroglia in Alzheimer's disease: pathophysiology and clinical implications. *Lancet Neurology* 18(4), pp. 406–414.

Baiardi, S., Abu-Rumeileh, S., Rossi, M., et al. 2019. Antemortem CSF Aβ42/Aβ40 ratio predicts Alzheimer's disease pathology better than Aβ42 in rapidly progressive dementias. *Annals of clinical and translational neurology* 6(2), pp. 263–273.

Bales, K.R., Du, Y., Dodel, R.C., Yan, G.M., Hamilton-Byrd, E. and Paul, S.M. 1998. The NF-kappaB/Rel family of proteins mediates Abeta-induced neurotoxicity and glial activation. *Brain research. Molecular brain research* 57(1), pp. 63–72.

Ballesteros-Yáñez, I., Benavides-Piccione, R., Elston, G.N., Yuste, R. and DeFelipe, J. 2006. Density and morphology of dendritic spines in mouse neocortex. *Neuroscience* 138(2), pp. 403–409.

Batiuk, M.Y., Martirosyan, A., Wahis, J., et al. 2020. Identification of region-specific astrocyte subtypes at single cell resolution. *Nature Communications* 11(1), p. 1220.

Bayés, A., Collins, M.O., Croning, M.D.R., van de Lagemaat, L.N., Choudhary, J.S. and Grant, S.G.N. 2012. Comparative study of human and mouse postsynaptic proteomes finds high compositional conservation and abundance differences for key synaptic proteins. *Plos One* 7(10), p. e46683.

Bayraktar, O.A., Bartels, T., Holmqvist, S., et al. 2020. Astrocyte layers in the mammalian

cerebral cortex revealed by a single-cell in situ transcriptomic map. *Nature Neuroscience* 23(4), pp. 500–509.
Bell, K.F.S., Al-Mubarak, B., Martel, M.-A., et al. 2015. Neuronal development is promoted by weakened intrinsic antioxidant defences due to epigenetic repression of Nrf2. *Nature Communications* 6, p. 7066.
Ben Haim, L., Ceyzériat, K., Carrillo-de Sauvage, M.A., et al. 2015. The JAK/STAT3 pathway is a common inducer of astrocyte reactivity in Alzheimer's and Huntington's diseases. *The Journal of Neuroscience* 35(6), pp. 2817–2829.
Bertram, L. and Tanzi, R.E. 2009. Genome-wide association studies in Alzheimer's disease. *Human Molecular Genetics* 18(R2), pp. R137-45.
Bialas, A.R. and Stevens, B. 2013. TGF-β signaling regulates neuronal C1q expression and developmental synaptic refinement. *Nature Neuroscience* 16(12), pp. 1773–1782.
Bloudek, L.M., Spackman, D.E., Blankenburg, M. and Sullivan, S.D. 2011. Review and meta-analysis of biomarkers and diagnostic imaging in Alzheimer's disease. *Journal of Alzheimer's Disease* 26(4), pp. 627–645.
Boisvert, M.M., Erikson, G.A., Shokhirev, M.N. and Allen, N.J. 2018. The Aging Astrocyte Transcriptome from Multiple Regions of the Mouse Brain. *Cell reports* 22(1), pp. 269–285.
Borchelt, D.R., Ratovitski, T., van Lare, J., et al. 1997. Accelerated amyloid deposition in the brains of transgenic mice coexpressing mutant presenilin 1 and amyloid precursor proteins. *Neuron* 19(4), pp. 939–945.
Bouvier, D.S., Jones, E.V., Quesseveur, G., et al. 2016. High resolution dissection of reactive glial nets in alzheimer's disease. *Scientific Reports* 6, p. 24544.
Braak, H., Alafuzoff, I., Arzberger, T., Kretzschmar, H. and Del Tredici, K. 2006. Staging of Alzheimer disease-associated neurofibrillary pathology using paraffin sections and immunocytochemistry. *Acta Neuropathologica* 112(4), pp. 389–404.
Brachya, G., Yanay, C. and Linial, M. 2006. Synaptic proteins as multi-sensor devices of neurotransmission. *BMC Neuroscience* 7 Suppl 1, p. S4.
Cahoy, J.D., Emery, B., Kaushal, A., et al. 2008. A transcriptome database for astrocytes, neurons, and oligodendrocytes: a new resource for understanding brain development and function. *The Journal of Neuroscience* 28(1), pp. 264–278.
Cai, Z. and Xiao, M. 2016. Oligodendrocytes and Alzheimer's disease. *The International journal of neuroscience* 126(2), pp. 97–104.
Canals, S., Larrosa, B., Pintor, J., Mena, M.A. and Herreras, O. 2008. Metabolic challenge to glia activates an adenosine-mediated safety mechanism that promotes neuronal survival by delaying the onset of spreading depression waves. *Journal of Cerebral Blood Flow and Metabolism* 28(11), pp. 1835–1844.
Carter, S.F., Chiotis, K., Nordberg, A. and Rodriguez-Vieitez, E. 2019. Longitudinal association between astrocyte function and glucose metabolism in autosomal dominant Alzheimer's disease. *European Journal of Nuclear Medicine and Molecular Imaging* 46(2), pp. 348–356.
Castano, E.M., Prelli, F., Wisniewski, T., et al. 1995. Fibrillogenesis in Alzheimer's disease of amyloid beta peptides and apolipoprotein E. *The Biochemical Journal* 306 (Pt 2), pp. 599–604.
Cerf, E., Gustot, A., Goormaghtigh, E., Ruysschaert, J.-M. and Raussens, V. 2011. High ability of apolipoprotein E4 to stabilize amyloid-β peptide oligomers, the pathological entities responsible for Alzheimer's disease. *The FASEB Journal* 25(5), pp. 1585–1595.
Chang, R., Yee, K.-L. and Sumbria, R.K. 2017. Tumor necrosis factor α Inhibition for Alzheimer's Disease. *Journal of central nervous system disease* 9, p. 1179573517709278.

Chen, G., Ning, B. and Shi, T. 2019. Single-Cell RNA-Seq Technologies and Related Computational Data Analysis. *Frontiers in genetics* 10, p. 317.
Chen, W.-T., Lu, A., Craessaerts, K., et al. 2019. Spatial and temporal transcriptomics reveal microglia-astroglia crosstalk in the amyloid-β plaque cell niche of Alzheimer's disease. *BioRxiv*.
Chen, W.-T., Lu, A., Craessaerts, K., et al. 2020. Spatial transcriptomics and in situ sequencing to study alzheimer's disease. *Cell* 182(4), p. 976–991.e19.
Chin, L.S., Li, L., Ferreira, A., Kosik, K.S. and Greengard, P. 1995. Impairment of axonal development and of synaptogenesis in hippocampal neurons of synapsin I-deficient mice. *Proceedings of the National Academy of Sciences of the United States of America* 92(20), pp. 9230–9234.
Christopherson, K.S., Ullian, E.M., Stokes, C.C.A., et al. 2005. Thrombospondins are astrocyte-secreted proteins that promote CNS synaptogenesis. *Cell* 120(3), pp. 421–433.
Chung, W.-S., Allen, N.J. and Eroglu, C. 2015. Astrocytes control synapse formation, function, and elimination. *Cold Spring Harbor Perspectives in Biology* 7(9), p. a020370.
Chung, W.-S., Clarke, L.E., Wang, G.X., et al. 2013. Astrocytes mediate synapse elimination through MEGF10 and MERTK pathways. *Nature* 504(7480), pp. 394–400.
Chung, W.-S., Verghese, P.B., Chakraborty, C., et al. 2016. Novel allele-dependent role for APOE in controlling the rate of synapse pruning by astrocytes. *Proceedings of the National Academy of Sciences of the United States of America* 113(36), pp. 10186–10191.
Clarke, L.E., Liddelow, S.A., Chakraborty, C., Münch, A.E., Heiman, M. and Barres, B.A. 2018. Normal aging induces A1-like astrocyte reactivity. *Proceedings of the National Academy of Sciences of the United States of America* 115(8), pp. E1896–E1905.
Cleary, J.P., Walsh, D.M., Hofmeister, J.J., et al. 2005. Natural oligomers of the amyloid-beta protein specifically disrupt cognitive function. *Nature Neuroscience* 8(1), pp. 79–84.
Colom-Cadena, M., Pegueroles, J., Herrmann, A.G., et al. 2017. Synaptic phosphorylated α-synuclein in dementia with Lewy bodies. *Brain: A Journal of Neurology* 140(12), pp. 3204–3214.
Corder, E.H., Saunders, A.M., Strittmatter, W.J., et al. 1993. Gene dose of apolipoprotein E type 4 allele and the risk of Alzheimer's disease in late onset families. *Science* 261(5123), pp. 921–923.
Cruts, M., Theuns, J. and Van Broeckhoven, C. 2012. Locus-specific mutation databases for neurodegenerative brain diseases. *Human Mutation* 33(9), pp. 1340–1344.
Cummings, J. 2018. Lessons Learned from Alzheimer Disease: Clinical Trials with Negative Outcomes. *Clinical and translational science* 11(2), pp. 147–152.
Cummings, J.L., Cohen, S., van Dyck, C.H., et al. 2018. ABBY: A phase 2 randomized trial of crenezumab in mild to moderate Alzheimer disease. *Neurology* 90(21), pp. e1889–e1897.
Curran, O.E., Qiu, Z., Smith, C. and Grant, S.G.N. 2020. The human and mouse synaptome architecture of excitatory synapses show conserved features. *BioRxiv*.
Dando, O., Heron, S. and Simpson, T.I. 2016. Statbio/Sargasso: Sargasso - A Python Tool To Disambiguate Mixed-Species Rna-Seq Reads According To Their Species Of Origin. *Zenodo*.
D'Andrea, M.R. and Nagele, R.G. 2010. Morphologically distinct types of amyloid plaques point the way to a better understanding of Alzheimer's disease pathogenesis. *Biotechnic & histochemistry : official publication of the Biological Stain Commission* 85(2), pp. 133–147.
DaRocha-Souto, B., Scotton, T.C., Coma, M., et al. 2011. Brain oligomeric β-amyloid but not total amyloid plaque burden correlates with neuronal loss and astrocyte inflammatory response in amyloid precursor protein/tau transgenic mice. *Journal of Neuropathology and*

Experimental Neurology 70(5), pp. 360–376.
Delaère, P., Duyckaerts, C., He, Y., Piette, F. and Hauw, J.J. 1991. Subtypes and differential laminar distributions of beta A4 deposits in Alzheimer's disease: relationship with the intellectual status of 26 cases. *Acta Neuropathologica* 81(3), pp. 328–335.
Delekate, A., Füchtemeier, M., Schumacher, T., Ulbrich, C., Foddis, M. and Petzold, G.C. 2014. Metabotropic P2Y1 receptor signalling mediates astrocytic hyperactivity in vivo in an Alzheimer's disease mouse model. *Nature Communications* 5, p. 5422.
Dhawan, G., Floden, A.M. and Combs, C.K. 2012. Amyloid-β oligomers stimulate microglia through a tyrosine kinase dependent mechanism. *Neurobiology of Aging* 33(10), pp. 2247–2261.
Dougherty, J.D., Schmidt, E.F., Nakajima, M. and Heintz, N. 2010. Analytical approaches to RNA profiling data for the identification of genes enriched in specific cells. *Nucleic Acids Research* 38(13), pp. 4218–4230.
Doyle, J.P., Dougherty, J.D., Heiman, M., et al. 2008. Application of a translational profiling approach for the comparative analysis of CNS cell types. *Cell* 135(4), pp. 749–762.
Duong, S., Patel, T. and Chang, F. 2017. Dementia: What pharmacists need to know. *Canadian pharmacists journal : CPJ = Revue des pharmaciens du Canada : RPC* 150(2), pp. 118–129.
Eng, L.F. and Ghirnikar, R.S. 1994. GFAP and astrogliosis. *Brain Pathology* 4(3), pp. 229–237.
Esparza, T.J., Zhao, H., Cirrito, J.R., et al. 2013. Amyloid-β oligomerization in Alzheimer dementia versus high-pathology controls. *Annals of Neurology* 73(1), pp. 104–119.
Ferreira, S.T. and Klein, W.L. 2011. The Aβ oligomer hypothesis for synapse failure and memory loss in Alzheimer's disease. *Neurobiology of Learning and Memory* 96(4), pp. 529–543.
Ferreira, S.T., Lourenco, M.V., Oliveira, M.M. and De Felice, F.G. 2015. Soluble amyloid-β oligomers as synaptotoxins leading to cognitive impairment in Alzheimer's disease. *Frontiers in Cellular Neuroscience* 9, p. 191.
Fisher, C.K., Smith, A.M., Walsh, J.R., Coalition Against Major Diseases and Abbott, Alliance for Aging Research, Alzheimer's Association, Alzheimer's Foundation of America, AstraZeneca Pharmaceuticals LP, Bristol-Myers Squibb Company, Critical Path Institute, CHDI Foundation, Inc., Eli Lilly and Company, F. Hoffmann-La Roche Ltd, Forest Research Institute, Genentech, Inc., GlaxoSmithKline, Johnson & Johnson, National Health Council, Novartis Pharmaceuticals Corporation, Parkinson's Action Network, Parkinson's Disease Foundation, Pfizer, Inc., sanofi-aventis. Collaborati 2019. Machine learning for comprehensive forecasting of Alzheimer's Disease progression. *Scientific Reports* 9(1), p. 13622.
Fribley, A., Zhang, K. and Kaufman, R.J. 2009. Regulation of apoptosis by the unfolded protein response. *Methods in Molecular Biology* 559, pp. 191–204.
Frost, G.R. and Li, Y.-M. 2017. The role of astrocytes in amyloid production and Alzheimer's disease. *Open biology* 7(12).
Fu, L., Sun, Y., Guo, Y., et al. 2018. Progressive spatial memory impairment, brain amyloid deposition and changes in serum amyloid levels as a function of age in appswe/ps1de9 mice. *Current Alzheimer research* 15(11), pp. 1053–1061.
Gabbouj, S., Ryhänen, S., Marttinen, M., et al. 2019. Altered Insulin Signaling in Alzheimer's Disease Brain - Special Emphasis on PI3K-Akt Pathway. *Frontiers in Neuroscience* 13, p. 629.
Galea, E., Morrison, W., Hudry, E., et al. 2015. Topological analyses in APP/PS1 mice reveal that astrocytes do not migrate to amyloid-β plaques. *Proceedings of the National Academy*

of Sciences of the United States of America 112(51), pp. 15556–15561.
Games, D., Adams, D., Alessandrini, R., et al. 1995. Alzheimer-type neuropathology in transgenic mice overexpressing V717F beta-amyloid precursor protein. *Nature* 373(6514), pp. 523–527.
Garcia-Alloza, M., Robbins, E.M., Zhang-Nunes, S.X., et al. 2006. Characterization of amyloid deposition in the APPswe/PS1dE9 mouse model of Alzheimer disease. *Neurobiology of Disease* 24(3), pp. 516–524.
Goate, A., Chartier-Harlin, M.C., Mullan, M., et al. 1991. Segregation of a missense mutation in the amyloid precursor protein gene with familial Alzheimer's disease. *Nature* 349(6311), pp. 704–706.
Gomez-Arboledas, A., Davila, J.C., Sanchez-Mejias, E., et al. 2018. Phagocytic clearance of presynaptic dystrophies by reactive astrocytes in Alzheimer's disease. *Glia* 66(3), pp. 637–653.
Gomez-Nicola, D. and Boche, D. 2015. Post-mortem analysis of neuroinflammatory changes in human Alzheimer's disease. *Alzheimer's research & therapy* 7(1), p. 42.
González-Reyes, R.E., Nava-Mesa, M.O., Vargas-Sánchez, K., Ariza-Salamanca, D. and Mora-Muñoz, L. 2017. Involvement of Astrocytes in Alzheimer's Disease from a Neuroinflammatory and Oxidative Stress Perspective. *Frontiers in Molecular Neuroscience* 10, p. 427.
Greber, B.J. and Ban, N. 2016. Structure and function of the mitochondrial ribosome. *Annual Review of Biochemistry* 85, pp. 103–132.
Griciuc, A., Serrano-Pozo, A., Parrado, A.R., et al. 2013. Alzheimer's disease risk gene CD33 inhibits microglial uptake of amyloid beta. *Neuron* 78(4), pp. 631–643.
Grubman, A., Chew, G., Ouyang, J.F., et al. 2019. A single-cell atlas of entorhinal cortex from individuals with Alzheimer's disease reveals cell-type-specific gene expression regulation. *Nature Neuroscience* 22(12), pp. 2087–2097.
Guerreiro, R. and Bras, J. 2015. The age factor in Alzheimer's disease. *Genome Medicine* 7, p. 106.
Gupta, P.P., Pandey, R.D., Jha, D., Shrivastav, V. and Kumar, S. 2015. Role of traditional nonsteroidal anti-inflammatory drugs in Alzheimer's disease: a meta-analysis of randomized clinical trials. *American Journal of Alzheimer's Disease and Other Dementias* 30(2), pp. 178–182.
Habib, N., McCabe, C., Medina, S., et al. 2020. Disease-associated astrocytes in Alzheimer's disease and aging. *Nature Neuroscience* 23(6), pp. 701–706.
Hagan.C 2017. When are mice considered old? [Online]. Available at: https://www.jax.org/news-and-insights/jax-blog/2017/november/when-are-mice-considered-old [Accessed: 24 January 2021].
Halassa, M.M., Fellin, T., Takano, H., Dong, J.-H. and Haydon, P.G. 2007. Synaptic islands defined by the territory of a single astrocyte. *The Journal of Neuroscience* 27(24), pp. 6473–6477.
Hamel, E., Nicolakakis, N., Aboulkassim, T., Ongali, B. and Tong, X.K. 2008. Oxidative stress and cerebrovascular dysfunction in mouse models of Alzheimer's disease. *Experimental Physiology* 93(1), pp. 116–120.
Han, X., Chen, M., Wang, F., et al. 2013. Forebrain engraftment by human glial progenitor cells enhances synaptic plasticity and learning in adult mice. *Cell Stem Cell* 12(3), pp. 342–353.
Haque, A., Engel, J., Teichmann, S.A. and Lönnberg, T. 2017. A practical guide to single-cell

RNA-sequencing for biomedical research and clinical applications. *Genome Medicine* 9(1), p. 75.
Hardingham, G.E., Fukunaga, Y. and Bading, H. 2002. Extrasynaptic NMDARs oppose synaptic NMDARs by triggering CREB shut-off and cell death pathways. *Nature Neuroscience* 5(5), pp. 405–414.
Hardy, J.A. and Higgins, G.A. 1992. Alzheimer's disease: the amyloid cascade hypothesis. *Science* 256(5054), pp. 184–185.
Hartlage-Rübsamen, M., Zeitschel, U., Apelt, J., et al. 2003. Astrocytic expression of the Alzheimer's disease beta-secretase (BACE1) is stimulus-dependent. *Glia* 41(2), pp. 169–179.
Hasel, P., Dando, O., Jiwaji, Z., et al. 2017. Neurons and neuronal activity control gene expression in astrocytes to regulate their development and metabolism. *Nature Communications* 8, p. 15132.
Hashimoto, T., Serrano-Pozo, A., Hori, Y., et al. 2012. Apolipoprotein E, especially apolipoprotein E4, increases the oligomerization of amyloid β peptide. *The Journal of Neuroscience* 32(43), pp. 15181–15192.
Head, D., Bugg, J.M., Goate, A.M., et al. 2012. Exercise engagement as a moderator of the effects of APOE genotype on amyloid deposition. *Archives of Neurology* 69(5), pp. 636–643.
Heiman, M., Kulicke, R., Fenster, R.J., Greengard, P. and Heintz, N. 2014. Cell type-specific mRNA purification by translating ribosome affinity purification (TRAP). *Nature Protocols* 9(6), pp. 1282–1291.
Heiman, M., Schaefer, A., Gong, S., et al. 2008. A translational profiling approach for the molecular characterization of CNS cell types. *Cell* 135(4), pp. 738–748.
Henstridge, C.M., Jackson, R.J., Kim, J.M., et al. 2015. Post-mortem brain analyses of the Lothian Birth Cohort 1936: extending lifetime cognitive and brain phenotyping to the level of the synapse. *Acta neuropathologica communications* 3, p. 53.
Herrup, K. 2015. The case for rejecting the amyloid cascade hypothesis. *Nature Neuroscience* 18(6), pp. 794–799.
Hertz, L. and Chen, Y. 2016. Importance of astrocytes for potassium ion (K+) homeostasis in brain and glial effects of K+ and its transporters on learning. *Neuroscience and Biobehavioral Reviews* 71, pp. 484–505.
Hölscher, C. 2019. Insulin signaling impairment in the brain as a risk factor in alzheimer's disease. *Frontiers in aging neuroscience* 11, p. 88.
Hong, S., Beja-Glasser, V.F., Nfonoyim, B.M., et al. 2016. Complement and microglia mediate early synapse loss in Alzheimer mouse models. *Science* 352(6286), pp. 712–716.
Hong, W., Wang, Z., Liu, W., et al. 2018. Diffusible, highly bioactive oligomers represent a critical minority of soluble Aβ in Alzheimer's disease brain. *Acta Neuropathologica* 136(1), pp. 19–40.
Hou, Y., Dan, X., Babbar, M., et al. 2019. Ageing as a risk factor for neurodegenerative disease. *Nature Reviews. Neurology* 15(10), pp. 565–581.
Howarth, C. 2014. The contribution of astrocytes to the regulation of cerebral blood flow. *Frontiers in Neuroscience* 8, p. 103.
Hsia, A.Y., Masliah, E., McConlogue, L., et al. 1999. Plaque-independent disruption of neural circuits in Alzheimer's disease mouse models. *Proceedings of the National Academy of Sciences of the United States of America* 96(6), pp. 3228–3233.
Hsiao, K., Chapman, P., Nilsen, S., et al. 1996. Correlative memory deficits, Abeta elevation, and amyloid plaques in transgenic mice. *Science* 274(5284), pp. 99–102.
Huang, W.-J., Zhang, X. and Chen, W.-W. 2016. Role of oxidative stress in Alzheimer's

disease. *Biomedical reports* 4(5), pp. 519–522.
Iliff, J.J., Wang, M., Liao, Y., et al. 2012. A paravascular pathway facilitates CSF flow through the brain parenchyma and the clearance of interstitial solutes, including amyloid β. *Science Translational Medicine* 4(147), p. 147ra111.
Ingelsson, M., Fukumoto, H., Newell, K.L., et al. 2004. Early Abeta accumulation and progressive synaptic loss, gliosis, and tangle formation in AD brain. *Neurology* 62(6), pp. 925–931.
Iram, T., Trudler, D., Kain, D., et al. 2016. Astrocytes from old Alzheimer's disease mice are impaired in Aβ uptake and in neuroprotection. *Neurobiology of Disease* 96, pp. 84–94.
Irwin, K., Sexton, C., Daniel, T., Lawlor, B. and Naci, L. 2018. Healthy aging and dementia: two roads diverging in midlife? *Frontiers in aging neuroscience* 10, p. 275.
Ishii, T., Takanashi, Y., Sugita, K., et al. 2017. Endogenous reactive oxygen species cause astrocyte defects and neuronal dysfunctions in the hippocampus: a new model for aging brain. *Aging Cell* 16(1), pp. 39–51.
Jack, C.R., Knopman, D.S., Jagust, W.J., et al. 2013. Tracking pathophysiological processes in Alzheimer's disease: an updated hypothetical model of dynamic biomarkers. *Lancet Neurology* 12(2), pp. 207–216.
Jackson, R.J., Rose, J., Tulloch, J., Henstridge, C., Smith, C. and Spires-Jones, T.L. 2019. Clusterin accumulates in synapses in Alzheimer's disease and is increased in apolipoprotein E4 carriers. *Brain Communications* 1(1), p. fcz003.
Jackson, R.J., Rudinskiy, N., Herrmann, A.G., et al. 2016. Human tau increases amyloid β plaque size but not amyloid β-mediated synapse loss in a novel mouse model of Alzheimer's disease. *The European Journal of Neuroscience* 44(12), pp. 3056–3066.
Jacob, C.P., Koutsilieri, E., Bartl, J., et al. 2007. Alterations in expression of glutamatergic transporters and receptors in sporadic Alzheimer's disease. *Journal of Alzheimer's Disease* 11(1), pp. 97–116.
Jäkel, S., Agirre, E., Mendanha Falcão, A., et al. 2019. Altered human oligodendrocyte heterogeneity in multiple sclerosis. *Nature* 566(7745), pp. 543–547.
Jankowsky, J.L., Fadale, D.J., Anderson, J., et al. 2004. Mutant presenilins specifically elevate the levels of the 42 residue beta-amyloid peptide in vivo: evidence for augmentation of a 42-specific gamma secretase. *Human Molecular Genetics* 13(2), pp. 159–170.
Jantaratnotai, N., Ryu, J.K., Kim, S.U. and McLarnon, J.G. 2003. Amyloid beta peptide-induced corpus callosum damage and glial activation in vivo. *Neuroreport* 14(11), pp. 1429–1433.
Jha, M.K., Jo, M., Kim, J.-H. and Suk, K. 2019. Microglia-Astrocyte Crosstalk: An Intimate Molecular Conversation. *The Neuroscientist* 25(3), pp. 227–240.
Jo, S., Yarishkin, O., Hwang, Y.J., et al. 2014. GABA from reactive astrocytes impairs memory in mouse models of Alzheimer's disease. *Nature Medicine* 20(8), pp. 886–896.
Johns, P. 2014. Dementia. In: *Clinical Neuroscience*. Elsevier, pp. 145–162.
Jones, V.C., Atkinson-Dell, R., Verkhratsky, A. and Mohamet, L. 2017. Aberrant iPSC-derived human astrocytes in Alzheimer's disease. *Cell death & disease* 8(3), p. e2696.
Jonsson, T., Atwal, J.K., Steinberg, S., et al. 2012. A mutation in APP protects against Alzheimer's disease and age-related cognitive decline. *Nature* 488(7409), pp. 96–99.
Kamphuis, W., Kooijman, L., Orre, M., Stassen, O., Pekny, M. and Hol, E.M. 2015. GFAP and vimentin deficiency alters gene expression in astrocytes and microglia in wild-type mice and changes the transcriptional response of reactive glia in mouse model for Alzheimer's disease. *Glia* 63(6), pp. 1036–1056.

Kamphuis, W., Mamber, C., Moeton, M., et al. 2012. GFAP isoforms in adult mouse brain with a focus on neurogenic astrocytes and reactive astrogliosis in mouse models of Alzheimer disease. *Plos One* 7(8), p. e42823.
Kamphuis, W., Middeldorp, J., Kooijman, L., et al. 2014. Glial fibrillary acidic protein isoform expression in plaque related astrogliosis in Alzheimer's disease. *Neurobiology of Aging* 35(3), pp. 492–510.
Karch, C.M. and Goate, A.M. 2015. Alzheimer's disease risk genes and mechanisms of disease pathogenesis. *Biological Psychiatry* 77(1), pp. 43–51.
Kay, K.R., Smith, C., Wright, A.K., et al. 2013. Studying synapses in human brain with array tomography and electron microscopy. *Nature Protocols* 8(7), pp. 1366–1380.
Keren-Shaul, H., Spinrad, A., Weiner, A., et al. 2017. A Unique Microglia Type Associated with Restricting Development of Alzheimer's Disease. *Cell* 169(7), p. 1276–1290.e17.
Khan, T.K. 2018. An algorithm for preclinical diagnosis of alzheimer's disease. *Frontiers in Neuroscience* 12, p. 275.
Knezevic, D. and Mizrahi, R. 2018. Molecular imaging of neuroinflammation in Alzheimer's disease and mild cognitive impairment. *Progress in Neuro-Psychopharmacology & Biological Psychiatry* 80(Pt B), pp. 123–131.
Koffie, R.M., Hashimoto, T., Tai, H.-C., et al. 2012. Apolipoprotein E4 effects in Alzheimer's disease are mediated by synaptotoxic oligomeric amyloid-β. *Brain: A Journal of Neurology* 135(Pt 7), pp. 2155–2168.
Koffie, R.M., Meyer-Luehmann, M., Hashimoto, T., et al. 2009. Oligomeric amyloid beta associates with postsynaptic densities and correlates with excitatory synapse loss near senile plaques. *Proceedings of the National Academy of Sciences of the United States of America* 106(10), pp. 4012–4017.
Kraft, A.W., Hu, X., Yoon, H., et al. 2013. Attenuating astrocyte activation accelerates plaque pathogenesis in APP/PS1 mice. *The FASEB Journal* 27(1), pp. 187–198.
Kucukdereli, H., Allen, N.J., Lee, A.T., et al. 2011. Control of excitatory CNS synaptogenesis by astrocyte-secreted proteins Hevin and SPARC. *Proceedings of the National Academy of Sciences of the United States of America* 108(32), pp. E440-9.
Kuleshov, M.V., Jones, M.R., Rouillard, A.D., et al. 2016. Enrichr: a comprehensive gene set enrichment analysis web server 2016 update. *Nucleic Acids Research* 44(W1), pp. W90-7.
Kulijewicz-Nawrot, M., Syková, E., Chvátal, A., Verkhratsky, A. and Rodríguez, J.J. 2013. Astrocytes and glutamate homoeostasis in Alzheimer's disease: a decrease in glutamine synthetase, but not in glutamate transporter-1, in the prefrontal cortex. *ASN Neuro* 5(4), pp. 273–282.
Lambert, M.P., Barlow, A.K., Chromy, B.A., et al. 1998. Diffusible, nonfibrillar ligands derived from Abeta1-42 are potent central nervous system neurotoxins. *Proceedings of the National Academy of Sciences of the United States of America* 95(11), pp. 6448–6453.
Le Prince, G., Delaere, P., Fages, C., et al. 1995. Glutamine synthetase (GS) expression is reduced in senile dementia of the Alzheimer type. *Neurochemical Research* 20(7), pp. 859–862.
Lee, J.-T., Xu, J., Lee, J.-M., et al. 2004. Amyloid-beta peptide induces oligodendrocyte death by activating the neutral sphingomyelinase-ceramide pathway. *The Journal of Cell Biology* 164(1), pp. 123–131.
Lee, S.Y. and Chung, W.-S. 2020. The roles of astrocytic phagocytosis in maintaining homeostasis of brains. *Journal of Pharmacological Sciences*.
Levy-Lahad, E., Wijsman, E.M., Nemens, E., et al. 1995. A familial Alzheimer's disease locus

on chromosome 1. *Science* 269(5226), pp. 970–973.
Li, S.-C., Lindenberger, U. and Bäckman, L. 2010. Dopaminergic modulation of cognition across the life span. *Neuroscience and Biobehavioral Reviews* 34(5), pp. 625–630.
Lian, H., Litvinchuk, A., Chiang, A.C.-A., Aithmitti, N., Jankowsky, J.L. and Zheng, H. 2016. Astrocyte-Microglia Cross Talk through Complement Activation Modulates Amyloid Pathology in Mouse Models of Alzheimer's Disease. *The Journal of Neuroscience* 36(2), pp. 577–589.
Liddelow, S.A., Guttenplan, K.A., Clarke, L.E., et al. 2017. Neurotoxic reactive astrocytes are induced by activated microglia. *Nature* 541(7638), pp. 481–487.
Liebmann, T., Renier, N., Bettayeb, K., Greengard, P., Tessier-Lavigne, M. and Flajolet, M. 2016. Three-Dimensional Study of Alzheimer's Disease Hallmarks Using the iDISCO Clearing Method. *Cell reports* 16(4), pp. 1138–1152.
Lim, G.P., Yang, F., Chu, T., et al. 2000. Ibuprofen suppresses plaque pathology and inflammation in a mouse model for Alzheimer's disease. *The Journal of Neuroscience* 20(15), pp. 5709–5714.
Liu, P., Reichl, J.H., Rao, E.R., et al. 2017. Quantitative Comparison of Dense-Core Amyloid Plaque Accumulation in Amyloid-β Protein Precursor Transgenic Mice. *Journal of Alzheimer's Disease* 56(2), pp. 743–761.
Liu, Y., Yoo, M.-J., Savonenko, A., et al. 2008. Amyloid pathology is associated with progressive monoaminergic neurodegeneration in a transgenic mouse model of Alzheimer's disease. *The Journal of Neuroscience* 28(51), pp. 13805–13814.
Lue, L.F., Rydel, R., Brigham, E.F., et al. 2001. Inflammatory repertoire of Alzheimer's disease and nondemented elderly microglia in vitro. *Glia* 35(1), pp. 72–79.
Ma, J., Yee, A., Brewer, H.B., Das, S. and Potter, H. 1994. Amyloid-associated proteins alpha 1-antichymotrypsin and apolipoprotein E promote assembly of Alzheimer beta-protein into filaments. *Nature* 372(6501), pp. 92–94.
Ma, Q.-L., Yang, F., Rosario, E.R., et al. 2009. Beta-amyloid oligomers induce phosphorylation of tau and inactivation of insulin receptor substrate via c-Jun N-terminal kinase signaling: suppression by omega-3 fatty acids and curcumin. *The Journal of Neuroscience* 29(28), pp. 9078–9089.
Mahmoud, S., Gharagozloo, M., Simard, C. and Gris, D. 2019. Astrocytes Maintain Glutamate Homeostasis in the CNS by Controlling the Balance between Glutamate Uptake and Release. *Cells* 8(2).
Mannor, S., Jin, X., Han, J., et al. 2010. K-Means Clustering. In: Sammut, C. and Webb, G. I. eds. *Encyclopedia of machine learning*. Boston, MA: Springer US, pp. 563–564.
Marioni, R.E., Harris, S.E., Zhang, Q., et al. 2018. GWAS on family history of Alzheimer's disease. *Translational psychiatry* 8(1), p. 99.
Marques, S., van Bruggen, D., Vanichkina, D.P., et al. 2018. Transcriptional Convergence of Oligodendrocyte Lineage Progenitors during Development. *Developmental Cell* 46(4), p. 504–517.e7.
Martins, I.C., Kuperstein, I., Wilkinson, H., et al. 2008. Lipids revert inert Abeta amyloid fibrils to neurotoxic protofibrils that affect learning in mice. *The EMBO Journal* 27(1), pp. 224–233.
Mathys, H., Davila-Velderrain, J., Peng, Z., et al. 2019. Single-cell transcriptomic analysis of Alzheimer's disease. *Nature* 570(7761), pp. 332–337.
Mc Donald, J.M., Savva, G.M., Brayne, C., et al. 2010. The presence of sodium dodecyl sulphate-stable Abeta dimers is strongly associated with Alzheimer-type dementia. *Brain: A*

Journal of Neurology 133(Pt 5), pp. 1328–1341.
McDonald, D.R., Brunden, K.R. and Landreth, G.E. 1997. Amyloid fibrils activate tyrosine kinase-dependent signaling and superoxide production in microglia. *The Journal of Neuroscience* 17(7), pp. 2284–2294.
McGeer, P.L., Schulzer, M. and McGeer, E.G. 1996. Arthritis and anti-inflammatory agents as possible protective factors for Alzheimer's disease: a review of 17 epidemiologic studies. *Neurology* 47(2), pp. 425–432.
Mecocci, P. and Polidori, M.C. 2012. Antioxidant clinical trials in mild cognitive impairment and Alzheimer's disease. *Biochimica et Biophysica Acta* 1822(5), pp. 631–638.
Meda, L., Baron, P., Prat, E., et al. 1999. Proinflammatory profile of cytokine production by human monocytes and murine microglia stimulated with β-amyloid[25–35]. *Journal of Neuroimmunology* 93(1–2), pp. 45–52.
Meda, L., Baron, P. and Scarlato, G. 2001. Glial activation in Alzheimer's disease: the role of Abeta and its associated proteins. *Neurobiology of Aging* 22(6), pp. 885–893.
Mehta, D., Jackson, R., Paul, G., Shi, J. and Sabbagh, M. 2017. Why do trials for Alzheimer's disease drugs keep failing? A discontinued drug perspective for 2010-2015. *Expert Opinion on Investigational Drugs* 26(6), pp. 735–739.
Merlini, M., Meyer, E.P., Ulmann-Schuler, A. and Nitsch, R.M. 2011. Vascular β-amyloid and early astrocyte alterations impair cerebrovascular function and cerebral metabolism in transgenic arcAβ mice. *Acta Neuropathologica* 122(3), pp. 293–311.
Micheva, K.D., Busse, B., Weiler, N.C., O'Rourke, N. and Smith, S.J. 2010. Single-synapse analysis of a diverse synapse population: proteomic imaging methods and markers. *Neuron* 68(4), pp. 639–653.
Micheva, K.D. and Smith, S.J. 2007. Array tomography: a new tool for imaging the molecular architecture and ultrastructure of neural circuits. *Neuron* 55(1), pp. 25–36.
Miguel-Álvarez, M., Santos-Lozano, A., Sanchis-Gomar, F., et al. 2015. Non-steroidal anti-inflammatory drugs as a treatment for Alzheimer's disease: a systematic review and meta-analysis of treatment effect. *Drugs & Aging* 32(2), pp. 139–147.
Miñano-Molina, A.J., España, J., Martín, E., et al. 2011. Soluble oligomers of amyloid-β peptide disrupt membrane trafficking of α-amino-3-hydroxy-5-methylisoxazole-4-propionic acid receptor contributing to early synapse dysfunction. *The Journal of Biological Chemistry* 286(31), pp. 27311–27321.
Mitew, S., Kirkcaldie, M.T.K., Dickson, T.C. and Vickers, J.C. 2013. Altered synapses and gliotransmission in Alzheimer's disease and AD model mice. *Neurobiology of Aging* 34(10), pp. 2341–2351.
Morel, L., Chiang, M.S.R., Higashimori, H., et al. 2017. Molecular and functional properties of regional astrocytes in the adult brain. *The Journal of Neuroscience* 37(36), pp. 8706–8717.
Morizawa, Y.M., Hirayama, Y., Ohno, N., et al. 2017. Reactive astrocytes function as phagocytes after brain ischemia via ABCA1-mediated pathway. *Nature Communications* 8(1), p. 28.
Mormino, E.C. and Papp, K.V. 2018. Amyloid accumulation and cognitive decline in clinically normal older individuals: implications for aging and early alzheimer's disease. *Journal of Alzheimer's Disease* 64(s1), pp. S633–S646.
Mota, S.I., Ferreira, I.L. and Rego, A.C. 2014. Dysfunctional synapse in Alzheimer's disease - A focus on NMDA receptors. *Neuropharmacology* 76 Pt A, pp. 16–26.
Mullan, M., Crawford, F., Axelman, K., et al. 1992. A pathogenic mutation for probable Alzheimer's disease in the APP gene at the N-terminus of beta-amyloid. *Nature Genetics*

1(5), pp. 345–347.
Mulligan, S.J. and MacVicar, B.A. 2004. Calcium transients in astrocyte endfeet cause cerebrovascular constrictions. *Nature* 431(7005), pp. 195–199.
Nahrendorf, M. and Swirski, F.K. 2016. Abandoning M1/M2 for a network model of macrophage function. *Circulation Research* 119(3), pp. 414–417.
Navarro, V., Sanchez-Mejias, E., Jimenez, S., et al. 2018. Microglia in alzheimer's disease: activated, dysfunctional or degenerative. *Frontiers in aging neuroscience* 10, p. 140.
Nguyen, T., Nioi, P. and Pickett, C.B. 2009. The Nrf2-antioxidant response element signaling pathway and its activation by oxidative stress. *The Journal of Biological Chemistry* 284(20), pp. 13291–13295.
Nielsen, H.M., Mulder, S.D., Beliën, J.A.M., Musters, R.J.P., Eikelenboom, P. and Veerhuis, R. 2010. Astrocytic A beta 1-42 uptake is determined by A beta-aggregation state and the presence of amyloid-associated proteins. *Glia* 58(10), pp. 1235–1246.
Norris, C.M., Kadish, I., Blalock, E.M., et al. 2005. Calcineurin triggers reactive/inflammatory processes in astrocytes and is upregulated in aging and Alzheimer's models. *The Journal of Neuroscience* 25(18), pp. 4649–4658.
Oberheim, N.A., Takano, T., Han, X., et al. 2009. Uniquely hominid features of adult human astrocytes. *The Journal of Neuroscience* 29(10), pp. 3276–3287.
O'Brien, J., Hayder, H., Zayed, Y. and Peng, C. 2018. Overview of microrna biogenesis, mechanisms of actions, and circulation. *Frontiers in endocrinology* 9, p. 402.
Oddo, S., Caccamo, A., Shepherd, J.D., et al. 2003. Triple-transgenic model of Alzheimer's disease with plaques and tangles: intracellular Abeta and synaptic dysfunction. *Neuron* 39(3), pp. 409–421.
Oksanen, M., Hyötyläinen, I., Trontti, K., et al. 2020. NF-E2-related factor 2 activation boosts antioxidant defenses and ameliorates inflammatory and amyloid properties in human Presenilin-1 mutated Alzheimer's disease astrocytes. *Glia* 68(3), pp. 589–599.
Olabarria, M., Noristani, H.N., Verkhratsky, A. and Rodríguez, J.J. 2011. Age-dependent decrease in glutamine synthetase expression in the hippocampal astroglia of the triple transgenic Alzheimer's disease mouse model: mechanism for deficient glutamatergic transmission? *Molecular Neurodegeneration* 6, p. 55.
Olabarria, M., Noristani, H.N., Verkhratsky, A. and Rodríguez, J.J. 2010. Concomitant astroglial atrophy and astrogliosis in a triple transgenic animal model of Alzheimer's disease. *Glia* 58(7), pp. 831–838.
Olsen, M., Aguilar, X., Sehlin, D., et al. 2018. Astroglial Responses to Amyloid-Beta Progression in a Mouse Model of Alzheimer's Disease. *Molecular imaging and biology : MIB : the official publication of the Academy of Molecular Imaging* 20(4), pp. 605–614.
Orre, M., Kamphuis, W., Osborn, L.M., et al. 2014. Isolation of glia from Alzheimer's mice reveals inflammation and dysfunction. *Neurobiology of Aging* 35(12), pp. 2746–2760.
Pajares, M., Cuadrado, A. and Rojo, A.I. 2017. Modulation of proteostasis by transcription factor NRF2 and impact in neurodegenerative diseases. *Redox biology* 11, pp. 543–553.
Pasqualetti, P., Bonomini, C., Dal Forno, G., et al. 2009. A randomized controlled study on effects of ibuprofen on cognitive progression of Alzheimer's disease. *Aging Clinical and Experimental Research* 21(2), pp. 102–110.
Pawley, J.B. ed. 1995. *Handbook of Biological Confocal Microscopy* . New York: Plenum Press.
Pekny, M. and Pekna, M. 2004. Astrocyte intermediate filaments in CNS pathologies and regeneration. *The Journal of Pathology* 204(4), pp. 428–437.

Perez-Nievas, B.G. and Serrano-Pozo, A. 2018. Deciphering the astrocyte reaction in alzheimer's disease. *Frontiers in aging neuroscience* 10, p. 114.
Petrovic, S. 2006. A Comparison Between the Silhouette Index and the Davies-Bouldin Index in Labelling IDS Clusters. *Citeseer*.
Peyvandipour, A., Shafi, A., Saberian, N. and Draghici, S. 2020. Identification of cell types from single cell data using stable clustering. *Scientific Reports* 10(1), p. 12349.
Pfrieger, F.W. 2003. Role of cholesterol in synapse formation and function. *Biochimica et Biophysica Acta (BBA) - Biomembranes* 1610(2), pp. 271–280.
Piaceri, I., Nacmias, B. and Sorbi, S. 2013. Genetics of familial and sporadic Alzheimer's disease. *Frontiers in bioscience (Elite edition)* 5, pp. 167–177.
Pickett, E.K., Herrmann, A.G., McQueen, J., et al. 2019. Amyloid beta and tau cooperate to cause reversible behavioral and transcriptional deficits in a model of alzheimer's disease. *Cell reports* 29(11), p. 3592–3604.e5.
Pickett, E.K., Koffie, R.M., Wegmann, S., et al. 2016. Non-Fibrillar Oligomeric Amyloid-β within Synapses. *Journal of Alzheimer's Disease* 53(3), pp. 787–800.
Poskanzer, K.E. and Yuste, R. 2016. Astrocytes regulate cortical state switching in vivo. *Proceedings of the National Academy of Sciences of the United States of America* 113(19), pp. E2675-84.
Potokar, M., Jorgačevski, J. and Zorec, R. 2016. Astrocyte aquaporin dynamics in health and disease. *International Journal of Molecular Sciences* 17(7).
Prince, M, Knapp, M, Guerchet, M, et al. 2014. Dementia UK: Second edition – Overview . *Alzheimer's Society 2014*.
Prinz, M. and Priller, J. 2014. Microglia and brain macrophages in the molecular age: from origin to neuropsychiatric disease. *Nature Reviews. Neuroscience* 15(5), pp. 300–312.
Quintanilla, R.A., Orellana, D.I., González-Billault, C. and Maccioni, R.B. 2004. Interleukin-6 induces Alzheimer-type phosphorylation of tau protein by deregulating the cdk5/p35 pathway. *Experimental Cell Research* 295(1), pp. 245–257.
Quintela-López, T., Ortiz-Sanz, C., Serrano-Regal, M.P., et al. 2019. Aβ oligomers promote oligodendrocyte differentiation and maturation via integrin β1 and Fyn kinase signaling. *Cell death & disease* 10(6), p. 445.
Rangaraju, S., Dammer, E.B., Raza, S.A., et al. 2018. Identification and therapeutic modulation of a pro-inflammatory subset of disease-associated-microglia in Alzheimer's disease. *Molecular Neurodegeneration* 13(1), p. 24.
Ries, M. and Sastre, M. 2016. Mechanisms of aβ clearance and degradation by glial cells. *Frontiers in aging neuroscience* 8, p. 160.
Risher, W.C., Patel, S., Kim, I.H., et al. 2014. Astrocytes refine cortical connectivity at dendritic spines. *eLife* 3.
Robinson, S.R. 2000. Neuronal expression of glutamine synthetase in Alzheimer's disease indicates a profound impairment of metabolic interactions with astrocytes. *Neurochemistry International* 36(4–5), pp. 471–482.
Rockenstein, E.M., McConlogue, L., Tan, H., Power, M., Masliah, E. and Mucke, L. 1995. Levels and alternative splicing of amyloid beta protein precursor (APP) transcripts in brains of APP transgenic mice and humans with Alzheimer's disease. *The Journal of Biological Chemistry* 270(47), pp. 28257–28267.
Rogaev, E.I., Sherrington, R., Rogaeva, E.A., et al. 1995. Familial Alzheimer's disease in kindreds with missense mutations in a gene on chromosome 1 related to the Alzheimer's disease type 3 gene. *Nature* 376(6543), pp. 775–778.

Rouach, N., Koulakoff, A., Abudara, V., Willecke, K. and Giaume, C. 2008. Astroglial metabolic networks sustain hippocampal synaptic transmission. *Science* 322(5907), pp. 1551–1555.
Ruan, L., Kang, Z., Pei, G. and Le, Y. 2009. Amyloid deposition and inflammation in APPswe/PS1dE9 mouse model of Alzheimer's disease. *Current Alzheimer research* 6(6), pp. 531–540.
Sadick, J.S. and Liddelow, S.A. 2019. Don't forget astrocytes when targeting Alzheimer's disease. *British Journal of Pharmacology* 176(18), pp. 3585–3598.
Saito, T., Matsuba, Y., Mihira, N., et al. 2014. Single App knock-in mouse models of Alzheimer's disease. *Nature Neuroscience* 17(5), pp. 661–663.
Sakakibara, Y., Sekiya, M., Saito, T., Saido, T.C. and Iijima, K.M. 2019. Amyloid-β plaque formation and reactive gliosis are required for induction of cognitive deficits in App knock-in mouse models of Alzheimer's disease. *BMC Neuroscience* 20(1), p. 13.
Sakers, K., Lake, A.M., Khazanchi, R., et al. 2017. Astrocytes locally translate transcripts in their peripheral processes. *Proceedings of the National Academy of Sciences of the United States of America* 114(19), pp. E3830–E3838.
Salarinasab, S., Salimi, L., Alidadiani, N., et al. 2020. Interaction of opioid with insulin/IGFs signaling in Alzheimer's disease. *Journal of Molecular Neuroscience* 70(6), pp. 819–834.
Sarnat, H.B. 2013. Clinical neuropathology practice guide 5-2013: markers of neuronal maturation. *Clinical Neuropathology* 32(5), pp. 340–369.
Satija, R., Farrell, J.A., Gennert, D., Schier, A.F. and Regev, A. 2015. Spatial reconstruction of single-cell gene expression data. *Nature Biotechnology* 33(5), pp. 495–502.
Sauerbeck, A.D., Gangolli, M., Reitz, S.J., et al. 2020. SEQUIN Multiscale Imaging of Mammalian Central Synapses Reveals Loss of Synaptic Connectivity Resulting from Diffuse Traumatic Brain Injury. *Neuron*.
Savage, M.J., Kalinina, J., Wolfe, A., et al. 2014. A sensitive aβ oligomer assay discriminates Alzheimer's and aged control cerebrospinal fluid. *The Journal of Neuroscience* 34(8), pp. 2884–2897.
Schmechel, D.E., Saunders, A.M., Strittmatter, W.J., et al. 1993. Increased amyloid beta-peptide deposition in cerebral cortex as a consequence of apolipoprotein E genotype in late-onset Alzheimer disease. *Proceedings of the National Academy of Sciences of the United States of America* 90(20), pp. 9649–9653.
Schneider, L. 2020. A resurrection of aducanumab for Alzheimer's disease. *Lancet Neurology* 19(2), pp. 111–112.
Schwanhäusser, B., Busse, D., Li, N., et al. 2011. Global quantification of mammalian gene expression control. *Nature* 473(7347), pp. 337–342.
Sekar, S., McDonald, J., Cuyugan, L., et al. 2015. Alzheimer's disease is associated with altered expression of genes involved in immune response and mitochondrial processes in astrocytes. *Neurobiology of Aging* 36(2), pp. 583–591.
Selkoe, D.J. 1991. The molecular pathology of Alzheimer's disease. *Neuron* 6(4), pp. 487–498.
Selkoe, D.J. and Hardy, J. 2016. The amyloid hypothesis of Alzheimer's disease at 25 years. *EMBO Molecular Medicine* 8(6), pp. 595–608.
Sengupta, U., Nilson, A.N. and Kayed, R. 2016. The Role of Amyloid-β Oligomers in Toxicity, Propagation, and Immunotherapy. *EBioMedicine* 6, pp. 42–49.
Serrano-Pozo, A., Frosch, M.P., Masliah, E. and Hyman, B.T. 2011. Neuropathological alterations in Alzheimer disease. *Cold Spring Harbor perspectives in medicine* 1(1), p.

a006189.
Serrano-Pozo, A., Gómez-Isla, T., Growdon, J.H., Frosch, M.P. and Hyman, B.T. 2013. A phenotypic change but not proliferation underlies glial responses in Alzheimer disease. *The American Journal of Pathology* 182(6), pp. 2332–2344.
Serrano-Pozo, A., Mielke, M.L., Gómez-Isla, T., et al. 2011. Reactive glia not only associates with plaques but also parallels tangles in Alzheimer's disease. *The American Journal of Pathology* 179(3), pp. 1373–1384.
Serrano-Pozo, A., Muzikansky, A., Gómez-Isla, T., et al. 2013. Differential relationships of reactive astrocytes and microglia to fibrillar amyloid deposits in Alzheimer disease. *Journal of Neuropathology and Experimental Neurology* 72(6), pp. 462–471.
Shankar, G.M., Bloodgood, B.L., Townsend, M., Walsh, D.M., Selkoe, D.J. and Sabatini, B.L. 2007. Natural oligomers of the Alzheimer amyloid-beta protein induce reversible synapse loss by modulating an NMDA-type glutamate receptor-dependent signaling pathway. *The Journal of Neuroscience* 27(11), pp. 2866–2875.
Shankar, G.M., Li, S., Mehta, T.H., et al. 2008. Amyloid-beta protein dimers isolated directly from Alzheimer's brains impair synaptic plasticity and memory. *Nature Medicine* 14(8), pp. 837–842.
Sheng, M. and Kim, E. 2011. The postsynaptic organization of synapses. *Cold Spring Harbor Perspectives in Biology* 3(12).
Sheng, W.S., Hu, S., Feng, A. and Rock, R.B. 2013. Reactive oxygen species from human astrocytes induced functional impairment and oxidative damage. *Neurochemical Research* 38(10), pp. 2148–2159.
Sherrington, R., Froelich, S., Sorbi, S., et al. 1996. Alzheimer's disease associated with mutations in presenilin 2 is rare and variably penetrant. *Human Molecular Genetics* 5(7), pp. 985–988.
Sherrington, R., Rogaev, E.I., Liang, Y., et al. 1995. Cloning of a gene bearing missense mutations in early-onset familial Alzheimer's disease. *Nature* 375(6534), pp. 754–760.
Shi, Q., Chowdhury, S., Ma, R., et al. 2017. Complement C3 deficiency protects against neurodegeneration in aged plaque-rich APP/PS1 mice. *Science Translational Medicine* 9(392).
Shih, A.Y., Imbeault, S., Barakauskas, V., et al. 2005. Induction of the Nrf2-driven antioxidant response confers neuroprotection during mitochondrial stress in vivo. *The Journal of Biological Chemistry* 280(24), pp. 22925–22936.
Siemers, E.R., Sundell, K.L., Carlson, C., et al. 2016. Phase 3 solanezumab trials: Secondary outcomes in mild Alzheimer's disease patients. *Alzheimer's & Dementia* 12(2), pp. 110–120.
Sierksma, A., Lu, A., Mancuso, R., et al. 2020. Novel Alzheimer risk genes determine the microglia response to amyloid-β but not to TAU pathology. *EMBO Molecular Medicine* 12(3), p. e10606.
Simpson, J.E., Ince, P.G., Lace, G., et al. 2010. Astrocyte phenotype in relation to Alzheimer-type pathology in the ageing brain. *Neurobiology of Aging* 31(4), pp. 578–590.
Simpson, J.E., Ince, P.G., Shaw, P.J., et al. 2011. Microarray analysis of the astrocyte transcriptome in the aging brain: relationship to Alzheimer's pathology and APOE genotype. *Neurobiology of Aging* 32(10), pp. 1795–1807.
Smith, H.L., Freeman, O.J., Butcher, A.J., et al. 2020. Astrocyte Unfolded Protein Response Induces a Specific Reactivity State that Causes Non-Cell-Autonomous Neuronal Degeneration. *Neuron* 105(5), p. 855–866.e5.
Sondag, C.M., Dhawan, G. and Combs, C.K. 2009. Beta amyloid oligomers and fibrils

stimulate differential activation of primary microglia. *Journal of Neuroinflammation* 6, p. 1.
Soreq, L., UK Brain Expression Consortium, North American Brain Expression Consortium, et al. 2017. Major shifts in glial regional identity are a transcriptional hallmark of human brain aging. *Cell reports* 18(2), pp. 557–570.
Spencer, B. and Masliah, E. 2014. Immunotherapy for Alzheimer's disease: past, present and future. *Frontiers in aging neuroscience* 6, p. 114.
Sperling, R.A., Jack, C.R., Black, S.E., et al. 2011. Amyloid-related imaging abnormalities in amyloid-modifying therapeutic trials: recommendations from the Alzheimer's Association Research Roundtable Workgroup. *Alzheimer's & Dementia* 7(4), pp. 367–385.
Spires, T.L., Meyer-Luehmann, M., Stern, E.A., et al. 2005. Dendritic spine abnormalities in amyloid precursor protein transgenic mice demonstrated by gene transfer and intravital multiphoton microscopy. *The Journal of Neuroscience* 25(31), pp. 7278–7287.
Srinivasan, R., Lu, T.-Y., Chai, H., et al. 2016. New transgenic mouse lines for selectively targeting astrocytes and studying calcium signals in astrocyte processes in situ and in vivo. *Neuron* 92(6), pp. 1181–1195.
Stanley, M., Macauley, S.L. and Holtzman, D.M. 2016. Changes in insulin and insulin signaling in Alzheimer's disease: cause or consequence? *The Journal of Experimental Medicine* 213(8), pp. 1375–1385.
Steele, M.L., Fuller, S., Patel, M., Kersaitis, C., Ooi, L. and Münch, G. 2013. Effect of Nrf2 activators on release of glutathione, cysteinylglycine and homocysteine by human U373 astroglial cells. *Redox biology* 1, pp. 441–445.
Su, B., Wang, X., Lee, H.-G., et al. 2010. Chronic oxidative stress causes increased tau phosphorylation in M17 neuroblastoma cells. *Neuroscience Letters* 468(3), pp. 267–271.
Su, B., Wang, X., Nunomura, A., et al. 2008. Oxidative stress signaling in Alzheimer's disease. *Current Alzheimer research* 5(6), pp. 525–532.
Tarnanas, I., Tsolaki, A., Wiederhold, M., Wiederhold, B. and Tsolaki, M. 2015. Five-year biomarker progression variability for Alzheimer's disease dementia prediction: Can a complex instrumental activities of daily living marker fill in the gaps? *Alzheimer's & Dementia : Diagnosis, Assessment & Disease Monitoring* 1(4), pp. 521–532.
Teipel, S.J., Meindl, T., Grinberg, L., et al. 2011. The cholinergic system in mild cognitive impairment and Alzheimer's disease: an in vivo MRI and DTI study. *Human Brain Mapping* 32(9), pp. 1349–1362.
Terry, R.D., Masliah, E., Salmon, D.P., et al. 1991. Physical basis of cognitive alterations in Alzheimer's disease: synapse loss is the major correlate of cognitive impairment. *Annals of Neurology* 30(4), pp. 572–580.
Thermo Fisher Scientific - UK 2020. Methods to Check RNA Integrity | Thermo Fisher Scientific - UK [Online]. Available at: https://www.thermofisher.com/uk/en/home/references/ambion-tech-support/rna-isolation/tech-notes/is-your-rna-intact.html [Accessed: 2 July 2020].
Toepper, M. 2017. Dissociating Normal Aging from Alzheimer's Disease: A View from Cognitive Neuroscience. *Journal of Alzheimer's Disease* 57(2), pp. 331–352.
Tsai, H.-H., Li, H., Fuentealba, L.C., et al. 2012. Regional astrocyte allocation regulates CNS synaptogenesis and repair. *Science* 337(6092), pp. 358–362.
Uddin, M.S., Tewari, D., Sharma, G., et al. 2020. Molecular mechanisms of ER stress and UPR in the pathogenesis of alzheimer's disease. *Molecular Neurobiology* 57(7), pp. 2902–2919.
Vasile, F., Dossi, E. and Rouach, N. 2017. Human astrocytes: structure and functions in the healthy brain. *Brain Structure & Function* 222(5), pp. 2017–2029.

Verghese, P.B., Castellano, J.M., Garai, K., et al. 2013. ApoE influences amyloid-β (Aβ) clearance despite minimal apoE/Aβ association in physiological conditions. *Proceedings of the National Academy of Sciences of the United States of America* 110(19), pp. E1807-16.
Verkhratsky, A. and Kirchhoff, F. 2007. NMDA Receptors in glia. *The Neuroscientist* 13(1), pp. 28–37.
Verkhratsky, A., Parpura, V., Rodriguez-Arellano, J.J. and Zorec, R. 2019. Astroglia in alzheimer's disease. *Advances in Experimental Medicine and Biology* 1175, pp. 273–324.
Verkhratsky, A., Rodrigues, J.J., Pivoriunas, A., Zorec, R. and Semyanov, A. 2019. Astroglial atrophy in Alzheimer's disease. *Pflugers Archiv: European Journal of Physiology* 471(10), pp. 1247–1261.
Villemagne, V.L., Burnham, S., Bourgeat, P., et al. 2013. Amyloid β deposition, neurodegeneration, and cognitive decline in sporadic Alzheimer's disease: a prospective cohort study. *Lancet Neurology* 12(4), pp. 357–367.
Wang, J., Dickson, D.W., Trojanowski, J.Q. and Lee, V.M. 1999. The levels of soluble versus insoluble brain Abeta distinguish Alzheimer's disease from normal and pathologic aging. *Experimental Neurology* 158(2), pp. 328–337.
Wang, J., Tan, L., Wang, H.-F., et al. 2015. Anti-inflammatory drugs and risk of Alzheimer's disease: an updated systematic review and meta-analysis. *Journal of Alzheimer's Disease* 44(2), pp. 385–396.
Wang, Z., Gerstein, M. and Snyder, M. 2009. RNA-Seq: a revolutionary tool for transcriptomics. *Nature Reviews. Genetics* 10(1), pp. 57–63.
Weggen, S. and Beher, D. 2012. Molecular consequences of amyloid precursor protein and presenilin mutations causing autosomal-dominant Alzheimer's disease. *Alzheimer's research & therapy* 4(2), p. 9.
Weggen, S., Eriksen, J.L., Das, P., et al. 2001. A subset of NSAIDs lower amyloidogenic Abeta42 independently of cyclooxygenase activity. *Nature* 414(6860), pp. 212–216.
White, J.A., Manelli, A.M., Holmberg, K.H., Van Eldik, L.J. and Ladu, M.J. 2005. Differential effects of oligomeric and fibrillar amyloid-beta 1-42 on astrocyte-mediated inflammation. *Neurobiology of Disease* 18(3), pp. 459–465.
Wildsmith, K.R., Holley, M., Savage, J.C., Skerrett, R. and Landreth, G.E. 2013. Evidence for impaired amyloid β clearance in Alzheimer's disease. *Alzheimer's research & therapy* 5(4), p. 33.
Wilhelmsson, U., Bushong, E.A., Price, D.L., et al. 2006. Redefining the concept of reactive astrocytes as cells that remain within their unique domains upon reaction to injury. *Proceedings of the National Academy of Sciences of the United States of America* 103(46), pp. 17513–17518.
Wisniewski, K.E., Wisniewski, H.M. and Wen, G.Y. 1985. Occurrence of neuropathological changes and dementia of Alzheimer's disease in Down's syndrome. *Annals of Neurology* 17(3), pp. 278–282.
Wu, L., Rosa-Neto, P., Hsiung, G.-Y.R., et al. 2012. Early-onset familial Alzheimer's disease (EOFAD). *The Canadian Journal of Neurological Sciences. Le Journal Canadien des Sciences Neurologiques* 39(4), pp. 436–445.
Wu, Z., Guo, Z., Gearing, M. and Chen, G. 2014. Tonic inhibition in dentate gyrus impairs long-term potentiation and memory in an Alzheimer's [corrected] disease model. *Nature Communications* 5, p. 4159.
Yamada, T., Kawamata, T., Walker, D.G. and McGeer, P.L. 1992. Vimentin immunoreactivity in normal and pathological human brain tissue. *Acta Neuropathologica* 84(2), pp. 157–162.

Yao, H., Coppola, K., Schweig, J.E., Crawford, F., Mullan, M. and Paris, D. 2019. Distinct signaling pathways regulate TREM2 phagocytic and nfκb antagonistic activities. *Frontiers in Cellular Neuroscience* 13, p. 457.
Yao, Y., Chen, Z.-L., Norris, E.H. and Strickland, S. 2014. Astrocytic laminin regulates pericyte differentiation and maintains blood brain barrier integrity. *Nature Communications* 5, p. 3413.
Yiannopoulou, K.G. and Papageorgiou, S.G. 2013. Current and future treatments for Alzheimer's disease. *Therapeutic advances in neurological disorders* 6(1), pp. 19–33.
Yoshiyama, Y., Higuchi, M., Zhang, B., et al. 2007. Synapse loss and microglial activation precede tangles in a P301S tauopathy mouse model. *Neuron* 53(3), pp. 337–351.
Zamanian, J.L., Xu, L., Foo, L.C., et al. 2012. Genomic analysis of reactive astrogliosis. *The Journal of Neuroscience* 32(18), pp. 6391–6410.
Zanetti, O., Solerte, S.B. and Cantoni, F. 2009. Life expectancy in Alzheimer's disease (AD). *Archives of Gerontology and Geriatrics* 49 Suppl 1, pp. 237–243.
Zeppenfeld, D.M., Simon, M., Haswell, J.D., et al. 2017. Association of Perivascular Localization of Aquaporin-4 With Cognition and Alzheimer Disease in Aging Brains. *JAMA neurology* 74(1), pp. 91–99.
Zhang, L. and Zhang, S. 2020. Comparison of Computational Methods for Imputing Single-Cell RNA-Sequencing Data. *IEEE/ACM Transactions on Computational Biology and Bioinformatics* 17(2), pp. 376–389.
Zhang, Y., Chen, K., Sloan, S.A., et al. 2014. An RNA-sequencing transcriptome and splicing database of glia, neurons, and vascular cells of the cerebral cortex. *The Journal of Neuroscience* 34(36), pp. 11929–11947.
Zhang, Y., Sloan, S.A., Clarke, L.E., et al. 2016. Purification and Characterization of Progenitor and Mature Human Astrocytes Reveals Transcriptional and Functional Differences with Mouse. *Neuron* 89(1), pp. 37–53.
Zhang, Z., Ma, Z., Zou, W., et al. 2019. The appropriate marker for astrocytes: comparing the distribution and expression of three astrocytic markers in different mouse cerebral regions. *BioMed research international* 2019, p. 9605265.
Zhao, J., Davis, M.D., Martens, Y.A., et al. 2017. APOE ε4/ε4 diminishes neurotrophic function of human iPSC-derived astrocytes. *Human Molecular Genetics* 26(14), pp. 2690–2700.
Zhao, J., O'Connor, T. and Vassar, R. 2011. The contribution of activated astrocytes to Aβ production: implications for Alzheimer's disease pathogenesis. *Journal of Neuroinflammation* 8, p. 150.
Zhu, F., Cizeron, M., Qiu, Z., et al. 2018. Architecture of the mouse brain synaptome. *Neuron* 99(4), p. 781–799.e10.
Ziegenhain, C., Vieth, B., Parekh, S., et al. 2017. Comparative Analysis of Single-Cell RNA Sequencing Methods. *Molecular Cell* 65(4), p. 631–643.e4.
Zimmer, E.R., Parent, M.J., Souza, D.G., et al. 2017. [18F]FDG PET signal is driven by astroglial glutamate transport. *Nature Neuroscience* 20(3), pp. 393–395.